Doctoral Thesis

Design of Novel Polydiacetylene Microstructures with Reversible multi-Modal Optical Signals

Jongwon Oh

School of Energy and Chemical Engineering
(Chemical Engineering)

Ulsan National Institute of Science and Technology

2021

Design of Novel Polydiacetylene Microstructures with Reversible multi-Modal Optical Signals

Jongwon Oh

School of Energy and Chemical Engineering
(Chemical Engineering)

Ulsan National Institute of Science and Technology

Design of Novel Polydiacetylene Microstructures with Reversible multi-Modal Optical Signals

A thesis/dissertation submitted to
Ulsan National Institute of Science and Technology
in partial fulfillment of the
requirements for the degree of
Doctor of Philosophy

Jongwon Oh

06.10.2021 of submission
Approved by

Advisor

Jiseok Lee

Design of Novel Polydiacetylene Microstructures with Reversible multi-Modal Optical Signals

Jongwon Oh

This certifies that the thesis of Jongwon Oh is approved.

06.10.2021 of submission

Signature

Advisor: Jiseok Lee

Thesis Committee Member #1: Sang Kyu Kwak

Thesis Committee Member #2: Hyunhyub Ko

Thesis Committee Member #3: Chang Young Lee

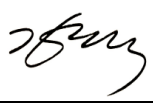

Thesis Committee Member #4: Jungwook Kim

Abstract

Photonic systems having interesting optical properties through the interaction with light have attracted much attention in various fields such as optical sensors, smart windows, dynamic gratings, and light control devices. In particular, metasurface holograms, one of the metamaterial-based systems with non-naturally occurring optical properties, have received great interest due to the reproducibility of full-color three-dimensional (3D) images through the manipulation of light. However, most metasurface holograms can provide an only static holographic signal. In order to overcome this limitation, many researchers have focused on responsive systems that modulate diffractive colors in response to environmental changes. These responsive systems correspond to dynamic holograms because they can control the phase of light and provide a variety of holographic signals through periodic variations of their structural properties. However, these dynamic systems have limitations in that they cannot reversibly display 3D holograms of complex shapes and they usually provide only a single holographic signal. In this dissertation, we intend to develop dynamic holograms capable of simultaneously expressing multiple holographic signals including structural color change and 3D holograms in a single architecture, based on three strategies: a. the organic synthesis of photocurable diacetylene, b. periodic photopatterning by DMD lithography, c. the contraction and swelling of the crosslinked network.

In chapter 2, we report a polydiacetylene (PDA) organogel that reversibly displays 3 modes of holograms in a single architecture. Using dithering mask lithography, we realized two-dimensional patterns with varying crosslinking density on a conjugated polydiacetylene. In protic solvents, the organogel contracts anisotropically to develop optical and structural heterogeneities along the third dimension, displaying holograms in the form of three-dimensional full parallax signals, both in fluorescence and bright-field microscopy imaging. In aprotic solvents, these heterogeneities diminish as organogels expand, recovering the two-dimensional periodicity to display a third hologram mode based on iridescent structural colors. Our study presents a next-generation hologram manufacturing method for multi-level encryption technologies.

Moreover, we developed practical PDA based-chemosensors for the detection of toxic molecules. Although the unique optical signaling properties of PDA have been exploited in diverse bio-chemosensors, the practical application of most PDA sensor systems is limited by their instability in harsh environments and fluorescence signal weakness. In chapter 3, a universal design principle for a highly stable PDA sensor system with a practical dual signaling capability is developed to detect cyanide (CN) ions, which are commonly found in drinking water. Effective metal intercalation and enhanced hydrophobic intermolecular interactions between PDA-metal supramolecules are used to construct highly stacked PDA-metal nanoplates that feature unusual optical stability upon exposure to strong acids, bases, organic solvents, and thermal/mechanical stresses, and can selectively detect CN anions, concomitantly undergoing a specific supramolecular structure change. To realize the practical

dual signaling capability of the PDA sensor system, upconverting nanocrystals (UCNs) are incorporated into highly stacked PDA-metal nanoplates, and practical dual signaling (orthogonal changes in luminescence and visible color) is demonstrated using a portable detection system. The presented universal design principle is expected to be suitable for the development of other highly stable and selective PDA sensor systems with practical dual signaling capability.

In chapter 4, PDA/UCNs sensor system has been developed for selective dual signaling of Chemical Warfare Agents (CWAs) gases such as G-series nerve agent simulant and blood agent. Rationally utilizing the orthogonal reaction mechanisms of the G-agent simulant and the blood agent (ClCN), oxime and benzaldehyde modified diacetylene monomers capable of rapid recognition of CWAs gases were synthesized. PDA/UCNs embedded fiber patch having dual signaling capability was realized by interweaving the color change of PDAs and the anti-stoke shift based optical properties of UCNs. PDA/UCNs nanocomposite fiber patches selectively display blue-to-red color and yellow to red luminescence change upon exposure to CWAs gases. These results present a provisional design principle of a rapid and selective PDA/UCNs-based CWAs gas detection system that can be used at night.

Contents

List of Tables

List of Figures

Chapter 1

efficiency[22] and (b) helicity multiplexed broadband properties[23]. These holograms are fabricated using a thin layer of (c) plasmonic[24] or (d-e) dielectric structures[25,26]. Reprinted with permission from refs. 22, 23, 24, 25 and 26, respectively. Copyright © 2015 Springer Nature, Copyright © 2015 Springer Nature, Copyright © 2016 American Chemical Society, Copyright © 2016 American Chemical Society, and Copyright © 2020 WILEY-VCH Verlag GmbH & Co. KGaA, Weinheim, respectively.

Fig. 1.6. a-d, Dynamic structural color systems displaying multiple optical signals upon external stimuli such as (a) thermal stress[27,28], (b) chemical molecules[29,30], (c) magnetic force[31,32], and (d) mechanical stress[33,34]. Reprinted with permission from refs. 27, 28, 29, 30, 31, 32, 33, and 34, respectively. Copyright © 2012 WILEY-VCH Verlag GmbH & Co. KGaA, Weinheim, Copyright © 2019 Springer Nature, Copyright © 2018 WILEY-VCH Verlag GmbH & Co. KGaA, Weinheim, Copyright © 2017 WILEY-VCH Verlag GmbH & Co. KGaA, Weinheim, Copyright © 2009 Springer Nature, Copyright © 2017 American Chemical Society, and Copyright © 2018 Springer Nature, respectively.

Fig. 1.7. a-d, Fabrication of dynamic structural color systems through a variety of methods such as (a) block copolymer[35], (b) self-assembled nanoparticles[38], (c) liquid crystal[40], and (d) photolithography[42]. Reprinted with permission from refs. 35, 38, 40 and 42, respectively. Copyright © 2012 American Chemical Society, Copyright © 2007 WILEY-VCH Verlag GmbH & Co. KGaA, Weinheim, Copyright 2015 © The Royal Society of Chemistry, Copyright © 2000 Springer Nature, respectively.

Fig. 1.8. a,b, Methods of realizing 3D optical heterogeneity in polymer matrices through (a) two photon-initiated polymerization[44,45] and (b) holographic lithography[42,46]. Reprinted with permission from refs. 42,44, 45, and 46, respectively. Copyright © 1999 Springer Nature, Copyright © 2008 American Chemical Society, Copyright © 2000 Springer Nature, Copyright © 2019 American Chemical Society, and Copyright © 2012 WILEY-VCH Verlag GmbH & Co. KGaA, Weinheim, respectively.

Fig. 1.9. Polymerization of diacetylene (DA) monomers and optical properties of polydiacetylene (PDA).

Fig. 1.10. Ideal arrangement of DA monomers in crystalline state for photo-polymerization.

Fig. 1.11. a-e, Responsive PDA systems displaying color transition and fluorescence emission upon external stimuli such as (a) thermal stress[57,58], (b) light[51], (c) mechanical stress[60], (d) pH[63], and (e) biomolecule[70]. Reprinted with permission from refs. 57, 58, 59, 60, 63, and 70, respectively. Copyright © 2014 WILEY-VCH Verlag GmbH & Co. KGaA, Weinheim, Copyright © 2013 American Chemical Society, Copyright © 2018 American Chemical Society, Copyright © 2014 WILEY-VCH Verlag GmbH & Co. KGaA, Weinheim, Copyright © 2019 Elsevier Inc., Copyright © 2016 Elsevier Inc., respectively.

Fig. 1.12. Energy profiles according to the twist angle of PDA models[71]. Reprinted with permission

Chapter 2

Fig. 2.6. Fabrication of 2,4-hexadiyn-1,6-diacrylate (HD-DA) and 1,6-hexanediol diacrylate (HDDA) organogel microstructures according to the 365 nm UV exposure. a,b, Bright-field microscope images of crosslinked HD-DA (a) and HDDA (b) microstructures according to the 365 nm UV irradiation time. Scale bar is 50 μm. Copyright © 2021 Springer Nature.

Fig. 2.7. Analysis of photo-chemical reactions of hydroxy-ethyl acrylate (HEA) and propargyl acrylate (PA) using ^{13}C NMR spectroscopy. a, ^{13}C NMR spectra of HEA and PI (1:0.15 molar ratio) in DMSO-d solvent according to the exposure time of 365 nm UV light. The molar concentration of HEA is 433 mM and that of PI is 65.6 mM. **b,** Comparison of the peaks corresponding to carbon atoms of acrylate according to the exposure time of 365 nm UV light. **c,** ^{13}C NMR spectra of PA and PI (1:0.15 molar ratio) in DMSO-d solvent according to the exposure time of 365 nm UV light. The molar concentration of PA is 433 mM and that of PI is 65.6 mM. **d,e,** Comparison of the peaks corresponding to carbon atoms of acrylate (d) and diacetylene (e) according to the exposure time of 365 nm UV light. Copyright © 2021 Springer Nature.

Fig. 2.8. Analysis of photo-chemical reactions of 2,4-hexadiyn-1,6-diol (HD-DO) using ^{13}C NMR spectroscopy. a, ^{13}C NMR spectra of HD-DO and PI (1:0.15 molar ratio) in DMSO-d solvent according to the exposure time of 365 nm UV light. The molar concentration of HD-DO is 433 mM and that of PI is 65.6 mM. **b,** Comparison of the peaks corresponding to carbon atoms of diacetylene according to the exposure time of 365 nm UV light. Copyright © 2021 Springer Nature.

Fig. 2.9. Analysis of photo-chemical reactions of 2,4-hexadiyn-1,6-diacrylate (HD-DA) using ^{13}C NMR spectroscopy. a, ^{13}C NMR spectra of HD-DA and PI (1:0.15 molar ratio) in DMSO-d solvent according to the exposure time of 365 nm UV light. The molar concentration of HD-DA is 433 mM and that of PI is 65.6 mM. **b,c,** Comparison of the peaks corresponding to carbon atoms acrylate (b) and diacetylene (c) according to the exposure time of 365 nm UV light. Copyright © 2021 Springer Nature.

Fig. 2.10. Analysis of photo-chemical reactions of 2,4-hexadiyn-acrylate (HDA) using ^{13}C NMR spectroscopy. a, ^{13}C NMR spectra of pure HDA with 634 mM of PI (1:0.15 molar ratio) according to the exposure time of 365 nm UV light. **b,c,** Comparison of the peaks corresponding to carbon atoms of acrylate (b) and diacetylene (c) according to the exposure time of 365 nm UV light. Copyright © 2021 Springer Nature.

Fig. 2.11. Analysis of photo-chemical reactions of 2,4-hexadiyn-1,6-diacrylate (HD-DA) with equimolar PI using ^{13}C NMR spectroscopy. a, ^{13}C NMR spectra of HD-DA and PI (1: 1 molar ratio) in DMSO-d solvent according to the exposure time of 365 nm UV light. The molar concentration of HD-DA is 433 mM and that of PI is 433 mM. **b,c,** Comparison of the peaks corresponding to carbon atoms acrylate (b) and diacetylene (c) according to the exposure time of 365 nm UV light. Copyright ©

Fig. 2.19. CGMD simulation for contraction and expansion of PDA organogel structure. Final configurations of PDA organogel structure in ACN and MeOH solvents obtained from CGMD simulation. Solvent beads are omitted for clarity. Copyright © 2021 Springer Nature.

Fig. 2.20. Radius of gyration and molecular structure of PDA in solvent. a, Radius of gyration of PDA in ACN and MeOH solvents obtained from CGMD simulation. **b,** Representative molecular structure of PDA in ACN and MeOH. Structure of PDA was shown stretched and folded in ACN and MeOH, respectively. Green and pink colored beads represent C_3H_2–O and C_3H_4=O group. Copyright © 2021 Springer Nature.

Fig. 2.21. Coarse-grained (CG) model of PDA (left) and configuration of PDA organogel structure in ACN/MeOH solvents (right). Light blue dashed box shows the CG model, composed of 30 diacetylenes. Configuration of PDA organogel in ACN (transparent color) and MeOH (solid color) are shown. Solvents are omitted for clarity. *V* is volume of organogel. Copyright © 2021 Springer Nature.

Fig. 2.22. a, Probability distribution of torsion angle of PDA backbone in ACN/MeOH. Solvents were changed sequentially from ACN (ACN 1) to MeOH and back to ACN (ACN 2). **b,** AAMD simulation models of molecular structures of PDA monomer in ACN/MeOH solvents. Blue and red dashed boxes show the torsion angle of PDA backbone. Torsion angle is measured with yellow highlighted carbon atoms. **c,** HOMO isosurfaces and relative energies of PDA molecules from Fig. 2.22b. Relative energies are calculated based on the MeOH case. The green and orange colored isosurfaces represent the positive and negative values of *p*-orbital phase, respectively. Copyright © 2021 Springer Nature.

Fig. 2.23. HOMO-LUMO gap and torsion angle of PDA molecule from **Fig. 2.22b** to investigate *p*-orbital twist by solvent exchange. Copyright © 2021 Springer Nature.

Fig. 2.24. Raman spectroscopy of PDA organogel microstructure upon a solvent exchange. a-c, Full spectral range (a) and magnified regions (b and c) of Raman shift in PDA organogel microstructure. Copyright © 2021 Springer Nature.

Fig. 2.25. Raman spectra of PDA structure. a,b, Calculated results of Raman spectra of PDA structures for C=C (a) and C≡C (b) frequency regions. The PDA structures are obtained from MD simulation under two types of solvent (*i.e.*, ACN and MeOH). The Raman spectra are calculated under the condition of 298.15 K and 785 nm incident light with Lorentzian broadening (20.0 cm^{-1}). Note that blue and red colored arrows indicate the frequencies of Raman active vibrational modes in the crosslinked PDA ring structure. All Raman active vibrational modes are stretching modes (right hand side of Raman spectra). Copyright © 2021 Springer Nature.

Fig. 2.26. Effect of torsion angle on Raman spectra of PDA. a,b, Calculated results of Raman spectra

of PDA structures for C=C (a) and C≡C (b) frequency regions. The PDA structures are constructed according to the two types of torsion angle (*i.e.*, 180º and 90º). The Raman spectra are calculated under the condition of 298.15 K and 785 nm incident light with Lorentzian broadening (20 cm^{-1}). Note that black and red colored arrows indicate the frequencies of Raman active vibrational modes in the crosslinked PDA ring structure. All Raman active vibrational modes are stretching modes (right hand side of Raman spectra). Copyright © 2021 Springer Nature.

Fig. 2.27. a, Probability distribution of torsion angle of twisted PDA backbone with different number of acrylate conversion sites. **b,** HOMO isosurfaces and HOMO-LUMO gaps of PDA molecules with low (left) and high (right) volume contraction rate. Isosurface value of HOMO is 0.007 $e/Å^3$. The green and orange colored isosurfaces represent the positive and negative values of *p*-orbital phase, respectively. Copyright © 2021 Springer Nature.

Fig. 2.28. Volume and fluorescence emission intensity change of the conjugated PDA organogel microstructures with different stiffness. PDA organogels were further stiffened with interpenetrating network using 1,6-hexanediol diacrylate. **a,** Chemical structure of 1,6-hexanediol diacrylate. **b,c,** Bright-field (b) and fluorescence (c) microscopy images of six PDA/1,6-hexanediol diacrylate microstructures with different crosslinking density upon a solvent exchange. **d,** Fluorescence intensity ratio (I_{MeOH}/I_{ACN}) of conjugated organogel microstructures upon solvent exchange according to a crosslinking density of 1,6-hexanediol diacrylate controlled by the exposure number of 365 nm UV light. Scale bar is 25 μm. Copyright © 2021 Springer Nature.

Fig. 2.29. Comparison of contraction simulation result with confocal microscopy image. 3D simulation result (left) shows predicted deformed shape, and each cut plane of simulation result (middle) is matched to confocal microscopy image of contracted gel in MeOH (right). Scale bar is 25um. Copyright © 2021 Springer Nature.

Fig. 2.30. a,b, Organogel crosslinked without dithering pattern into a disk shape and shrunk in MeOH was (a) imaged using epi-fluorescence microscope and (b) simulated using FEA to predict fluorescence expressions resulting from network densification (left), torsional angle reduction (middle), and their combination (right, $\beta = 2$). Copyright © 2021 Springer Nature.

Fig. 2.31. Bright-field microscopy images of PDA organogel microstructure (left) composed of 2D arrays of highly crosslinked rods in a square dithering pattern (right, light areas) embedded in lightly crosslinked matrix (right, dark areas). Copyright © 2021 Springer Nature.

Fig. 2.32. Refractive indices change of rod and matrix in conjugated PDA organogel microstructure upon solvent exchange. a,b, Refractive indices of rod and matrix when exposed to

ACN (a) and water (b). Copyright © 2021 Springer Nature.

Fig. 2.33. Confocal microscopy image of rod and matrix in conjugated PDA organogel microstructure. a, Square–patterned dithering mask composed of 72 white pixels. **b,** Orthogonal confocal microscopy image of the square–patterned PDA organogel microstructure (Carl zeiss LSM 780, 63×). Scale bar is 10 μm. Copyright © 2021 Springer Nature.

Fig. 2.34. Structural color of the patterned PDA organogel. Structural color of the patterned PDA organogel array was changed as the viewing angle is varied (from left to right, left panel) or as the solvent is exchanged between ACN and water. The spectral change of structural color with different viewing angle is also shown (right panel). Copyright © 2021 Springer Nature.

Fig. 2.35. Schematic of the imaging setup for structural color of dithering mask patterned organogel microstructure. Copyright © 2021 Springer Nature.

Fig. 2.36. Diffraction from square dithering mask-patterned PDA organogel microstructure. a, Schematic of the diffraction efficiency measuring system. Transmitted and diffracted light were collected by the objective lens (20×/0.75 NA, Olympus) and relayed to the CMOS (CM3-U3-31S4M, Point Grey) camera placed at the Fourier plane by a 4-f lens pair system comprising L1 (f = 250 mm) and L2 (f = 100 mm). An iris was placed at a conjugate image plane to selectively measure light diffracted from a single PDA organogel microstructure. **b,** Diffraction efficiency of the first order diffracted light ($\eta = \sum I_{1st_o rder} / I_{incident}$) of a PDA organogel microstructure upon immersion to ACN was measured with respect to 405, 532 and 649 nm wavelengths. Here $I_{1st_o rder}$ is the intensity of the ± 1 diffracted orders in the *x* and *y* directions, and $I_{incident}$ is the intensity of light that is transmitted through empty regions of the sample where there were no PDA organogel structures and only the immersion solvents. **c,d,** Captured diffraction intensity patterns of a PDA organogel microstructure under exposure to ACN (c) and water (d). Diffracted intensity patterns for 649, 532 and 405 nm laser beams were assigned to the RGB colormap, respectively and displayed in a log scale. Insets show a magnified view of a single diffraction order. Copyright © 2021 Springer Nature.

Fig. 2.37. Confocal microscopy images of dithering mask patterned conjugated PDA organogel microstructure. a,b, Hexagon dithering mask patterned PDA organogel microstructure at bottom when exposed to ACN (a) and water (b). **c,d,** Orthogonal confocal microscopy images of hexagon dithering mask patterned PDA organogel microstructure when exposed to ACN (c) and water (d). Scale bar is 10 μm. Copyright © 2021 Springer Nature.

Fig. 2.38. FEA results showing the structure of PDA organogel with arrays of highly crosslinked rods in a square dithering pattern. When organogel contracted in water, a three-dimensional view

(left) and a cross-sectional view (bottom) demonstrated deflection of rods towards the center, which were initially aligned along the thickness direction as shown in a cross-sectional view (top). Copyright © 2021 Springer Nature.

Fig. 2.39. Bright-field (top row) and fluorescence microscopy images (bottom row) of dithering mask patterned PDA microstructure fabricated by five types of masks (rhombus, square, hexagon, and horizontal and vertical line, from left to right) when they were exposed to ACN and water. Scale bar is 50 μm. Copyright © 2021 Springer Nature.

Fig. 2.40. a, Bright-field micrographs (top row), widefield fluorescence micrographs (middle row), and 3D reconstructed confocal fluorescence micrographs (bottom row) of PDA organogels patterned with a hexagon dithering mask. Organogels exposed to water were observed at varying angles (blue arrows indicate viewing angles). **b,** The series of brightfield micrographs showing the temporal evolution of 3D focused light above the physical structure of PDA organogels patterned with a hexagonal dithering mask during the solvent exchange to water. Copyright © 2021 Springer Nature.

Fig. 2.41. FEA results showing that solvent exchange shrank the organogel patterned with a square dithering mask. Color map indicates volumetric strain. Copyright © 2021 Springer Nature.

Fig. 2.42. Comparison of confocal microscopy image of dithering mask patterned conjugated PDA organogel microstructure with deformed model structure by FEA. Orthogonal confocal microscopy image (left) of square dithering mask patterned PDA organogel upon exposure to water. Deformed structure modeled by FEA (right) shows bending of rods (red) and contraction of matrix (blue). Scale bar is 10 μm. Copyright © 2021 Springer Nature.

Fig. 2.43. Line profile of initial fluorescence intensity of uniform PDA organogel. Uniform organogels which have same UV dose of rod and matrix in dithering mask patterned PDA organogel microstructure. Inset shows fluorescence image of uniform rod gel (left) and matrix gel (right). Copyright © 2021 Springer Nature.

Fig. 2.44. Fluorescence expression predicted for the patterned organogel in FEA results after normalization by the maximum value. A relative contribution of network densification and torsional angle reduction to the fluorescence expression was adjusted separately for rod and matrix to match the fluorescence image shown in **Fig. 2.39**. Copyright © 2021 Springer Nature.

Fig. 2.45. Bright-field and fluorescence microscopy images of dithering mask patterned PDA microstructures having different crosslinking densities upon an exposure of ACN and MeOH. a-c, Rhombus (a), square (b), and hexagon (c) dithering mask were used to fabricate the PDA microstructure. Crosslinking densities was controlled by changing exposure time of 365 nm UV light.

Scale bar is 50 μm. Copyright © 2021 Springer Nature.

Fig. 2.46. Bright-field and fluorescence microscopy images of PDA organogel microstructures upon exposure to solvents. a-c, Rhombus (a), square (b), and hexagon (c) dithering mask were used to fabricate the PDA microstructure. Scale bar is 50 μm. Copyright © 2021 Springer Nature.

Fig. 2.47. Changing of signal shape with varying contraction level. Modeled fluorescence signals show the strongest intensity at the center of the organogel, and intensity about 0.7 shows along the cross shape. Radius of strong center and width of the cross get larger with higher crosslinking density, lower contraction level. Copyright © 2021 Springer Nature.

Fig. 2.48. Light propagation simulations. a, The 3D organogel structure was divided into N=90 layers. The local volumetric strain upon exposure to water, obtained by finite element analysis, was used to reconstruct the refractive index distribution of each layer *L*. The incident beam $E_{\mathrm{in},1}(x,y)$ was modeled by the condenser NA. Propagation of light through the respective layers was calculated using the angular spectrum method. To simulate the bright-field transmitted light, the intensity of the optical field obtained for the individual plane waves per incident angle, which ranged between ±17.4° to cover the full illumination numerical aperture (NA) of 0.3, were incoherently summed. **b,** The observed fluorescence pattern within the organogel structure was calculated by multiplying the degree of fluorescence expression per layer with the illumination intensity per layer. The degree of fluorescence expression was calculated through FEA simulations as described in the main text. The illumination intensity per layer was calculated using the angular spectrum method as in Fig. 2.48 (a). Copyright © 2021 Springer Nature.

Fig. 2.49. a,b, (a) Expected fluorescence intensity based on fluorescence expression and illumination intensity (inset: fluorescence micrograph) and (**b**) expected bright-field transmitted light distribution (inset: bright-field micrograph) for Fig. 2.41. Copyright © 2021 Springer Nature.

Fig. 2.50. Bright-field, fluorescent and structural color change of dithering mask patterned PDA organogel microparticle. a,b, Bright-field (a) and fluorescence (b) microscopy images of hexagon patterned PDA organogel microparticles when they were exposed to ACN (left) and water (right). **c,** Structural color change of hexagon patterned PDA organogel microparticles upon a solvent exchange from ACN (top) to water (bottom). Scale bar is 100 μm for (a) and (b), and 1 mm for (c). Copyright © 2021 Springer Nature.

Fig. 2.51. Bright-field and fluorescent pattern change of dithering mask patterned 1,6-hexanediol diacrylate microstructures. Bright-field and fluorescence microscopy image of dithering mask patterned fluorescein o-acrylate attached 1,6-hexanediol diacrylate microstructure with upon exposure

Fig. 2.60. Microarray consisting of organogels patterned with horizontal lines on the right of the red dotted line and vertical lines on the other side display selective structural color depending on the direction of incident light. Copyright © 2021 Springer Nature.

Fig. 2.61. Structural color turn on-off according to the direction of incident light. a, Horizontal lined dithering mask pattern image. **b,c,** Bright-field microscopy images of horizontal lined dithering mask patterned PDA organogel microstructure upon exposure to ACN by 20× (b) and 100 × (c) objective. **d,** Vertical lined dithering mask pattern image. **e,f,** Bright-field microscopy images of vertical lined dithering mask patterned PDA organogel microstructure upon exposure to ACN by 20× (e) and 100 × (f) objective. **g,** Schematic of selective patterning of horizontal and vertical lined dithering mask patterned microarray. **h,** Selective structural color and iridescence according to the direction of incident light. Scale bar: 100 μm (b) and (e), 10 μm (c) and (f) and is 1 mm (h). Copyright © 2021 Springer Nature.

Fig. 2.62. Dynamic flip-flop structural color systems displaying letter changes from T to E and T to S. Copyright © 2021 Springer Nature.

Fig. 2.63. Schematic of letter transition according to the direction of incident light. a, Fabrication of letter transition systems using four types of dithering masks. Hexagon dithering mask pattern (green dot) represents always on. Vertical (blue dot) and horizontal (red dot) dithering mask represents selective on-off of structural color according to the 90 angle of incident light. Black dot dithering mask represent no structural color. **b,** Letters transition from T to S according to the direction of incident light and their iridescence color upon the observation angle. **c,** Fabrication of letter transition systems using three types of dithering masks. Hexagon dithering mask pattern (green dot) represents always on. Vertical line dithering mask (blue dot) represents selective on-off of structural color according to the 90 angle of incident light. Black dot dithering mask represent no structural color. **d,** Letters transition from T to E according to the direction of incident light and their iridescence color upon the observation angle. Scale bar is 1mm. Copyright © 2021 Springer Nature.

Fig. 2.64. Cryptographic letter system using patterned PDA microstructure. Selective patterning of conjugated PDA organogel for structural color and 1,6-hexanediol diacrylate organogel for blank results in hidden letter encryption. Structural colored letter “S” was displayed upon exposure to ACN. Scale bars are 1 mm (left) and 100 μm (right). Copyright © 2021 Springer Nature.

Fig. 2.65. Free-standing flexible films with embedded holographic lettering fabricated using conventional biocompatible PEG-DA resin. Copyright © 2021 Springer Nature.

Fig. 2.66. a, A schematic diagram of encryption process that generates a specific dithering pattern in

Chapter 3

Chapter 4

(Diameter: 100 μm). Copyright © 2021 IOP Publishing.

Fig. 4.3. a, CCD images (top), averaged colors and color standard names (middle), and H values on the color wheel (bottom) of PCDA-OX coated fiber patch after exposure to ClCN (1720 ppm) and DMMP (390 ppm) gases. **b,** CCD images (top), averaged colors and color standard names (middle), and H values on the color wheel (bottom) of PCDA-BA coated fiber patch after exposure to DMMP (390 ppm) and ClCN (1720 ppm) gases. Copyright © 2021 IOP Publishing.

Fig. 4.4. a, SEM images and **b,** luminescence change of UCNs after exposure to ClCN (1720 ppm) and DMMP (390 ppm) gases. **c,** Luminescence spectra change of UCNs coated fiber patch before and after exposure to ClCN (1720 ppm) and DMMP (390 ppm) gases. **d,e,** Luminescence overlap of UCNs with (d) blue phase PCDA-OX and (e) red phase PCDA-OX. **f,** Color (top) and luminescence (bottom) change of PCDA-OX/UCNs fiber patch upon exposure to ClCN (1720 ppm) and DMMP (390 ppm) gases. **g,** Color (top) and luminescence (bottom) change of PCDA-BA/UCNs fiber patch upon exposure to ClCN (1720 ppm) and DMMP (390 ppm) gases. **h,** Luminescence spectra change of PCDA-OX/UCNs fiber patch before and after exposure to DMMP (390 ppm) gas. Scale bar is 1 μm for (A) and 5 mm for (F). Copyright © 2021 IOP Publishing.

Chapter 1. Introduction

1.1 Bio-inspired Photonics

Natural species exhibit various optical signals such as structural color, surface pattern change, and color change by pigment through different sophisticated mechanisms. For example, the *Morpho butterfly* shows brilliant colors through its complex structural variations at the nanometer scale, and the *Mimic octopus* exhibits the alteration of surface patterns in response to environmental changes. Inspired by optical signals of nature species, the advanced polymer system that controls light propagation has been much attention. By reproducing complex structural variation in *Morpho butterfly wings,* the structural color systems have been achieved in a variety of types such as angle-independent structural reflectors[1], photonic microcapsule[2], and structural color hydrogel[3] (**Fig. 1.1.1**). These polymer systems display a selective reflectance at a specific wavelength via diffraction originated from structural variations of periodic micro/nanostructure. Also, many researchers have tried to develop the photonic system displaying a variety of optical signals through the interaction with light (**Fig. 1.1.2 and Fig. 1.1.3**). As a result, the polymer systems which alters absorption[4-7], emission[8,9], and surface wrinkle patterns[10,11] upon environmental perturbations have been reported for diverse applications such as optical sensor, smart windows, dynamic gratings, and light control devices.

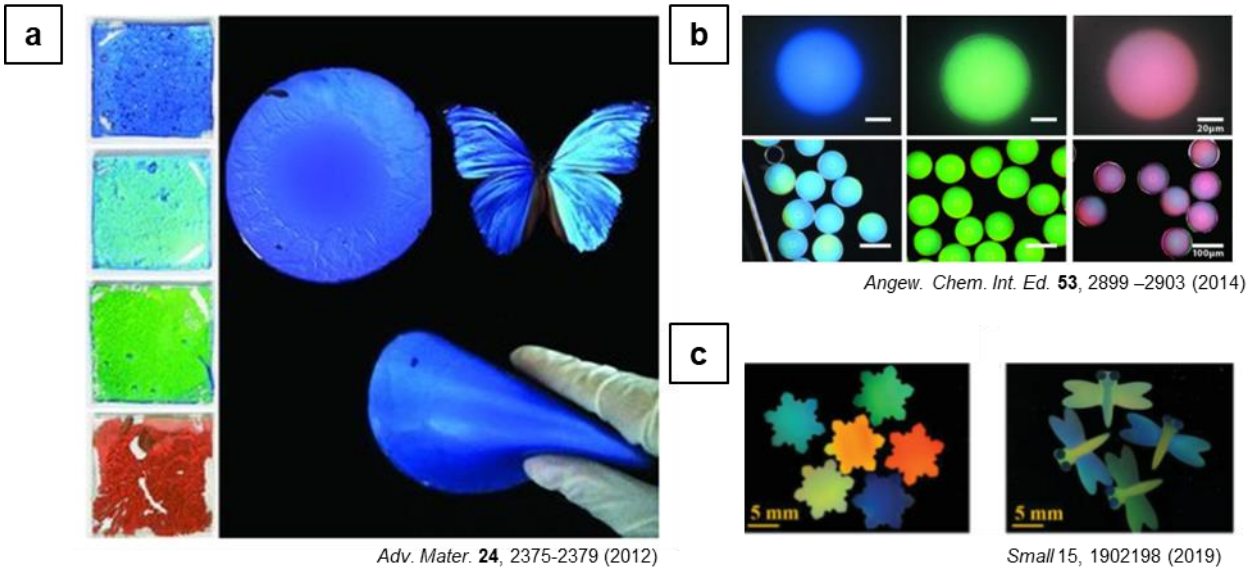

Fig. 1.1. a-c, Introduction of bio-inspired structural color systems in various types such as (a) angle-independent film[1], (b) photonic microcapsule[2], and (c) photonic hydrogel[3]. Reprinted with permission from refs. 1,2, and 3. Copyright © 2012 WILEY-VCH Verlag GmbH & Co. KGaA, Weinheim, Copyright © 2014 WILEY-VCH Verlag GmbH & Co. KGaA, Weinheim, Copyright © 2019 WILEY-VCH Verlag GmbH & Co. KGaA, Weinheim, respectively.

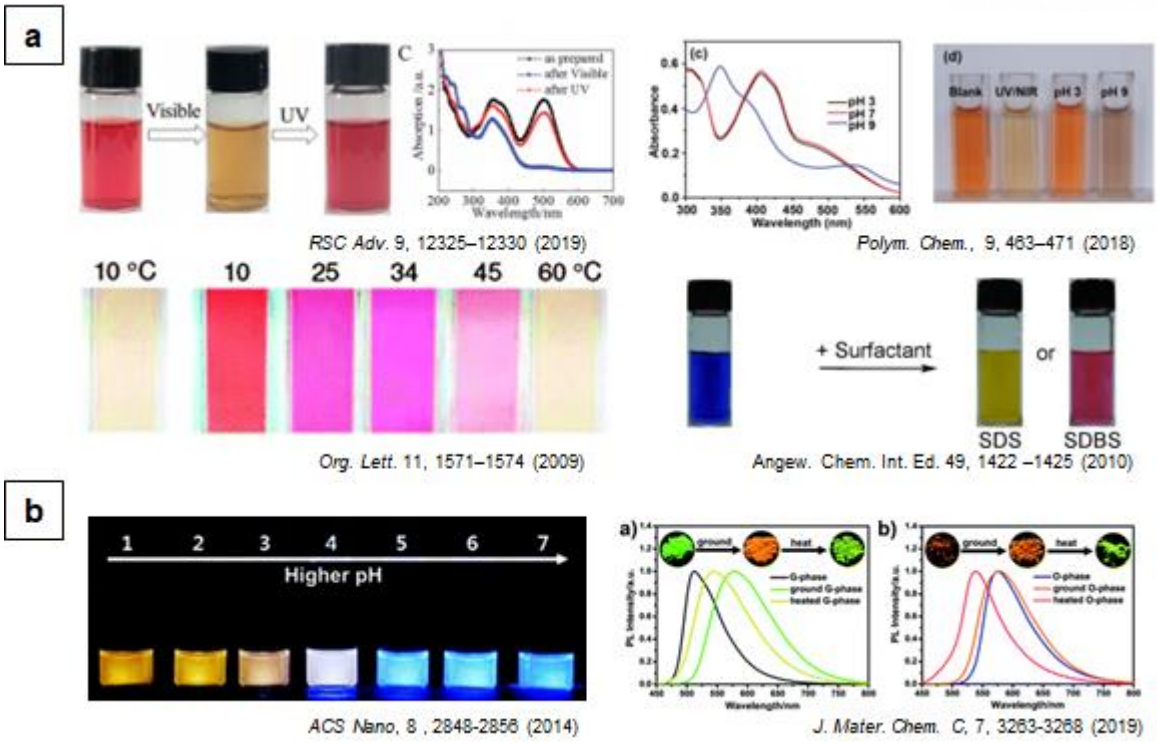

Fig. 1.2. a,b, Introduction of photonic systems which alter optical signals such as (a) absorption[4-7] and (b) emission[8,9] in response to external stimuli. Reprinted with permission from refs. 4, 5, 6, 7, 8, and 9. Copyright © 2019 The Royal Society of Chemistry, Copyright 2018 © The Royal Society of Chemistry, Copyright © 2009 American Chemical Society, Copyright © 2010 WILEY-VCH Verlag GmbH & Co. KGaA, Weinheim, Copyright © 2014 American Chemical Society, Copyright 2019 © The Royal Society of Chemistry, respectively.

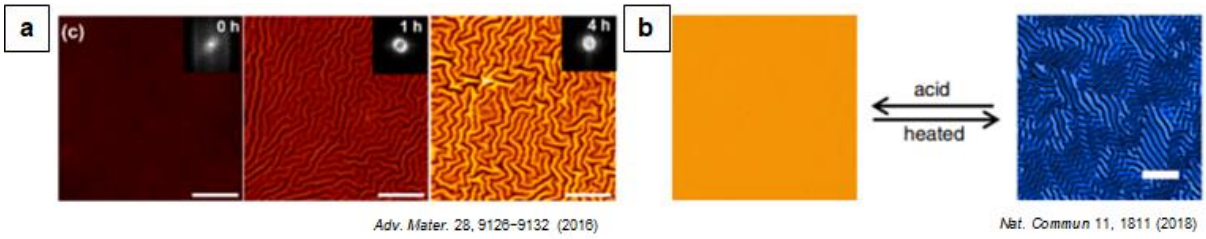

Fig. 1.3. a,b, Introduction of photonic systems which control the surface wrinkle pattern in response to external stimuli such as (a) thermal stress[10] and (b) near-infrared light[11]. Reprinted with permission from refs. 10 and 11, respectively. Copyright © 2016 WILEY-VCH Verlag GmbH & Co. KGaA, Weinheim, Copyright © 2018 Springer Nature, respectively.

1.2 Optical metamaterials

1.2.1 Introduction of optical metamaterials

In addition to the development of photonic systems that mimic natural species, researchers have also paid much attention to the realization of materials with novel optical properties that did not exist in the natural world. The materials with unprecedented optical properties were called metamaterials because the prefix “meta” means “beyond conventional materials in nature”. These metamaterials refer to a metal or dielectric material artificially designed in a periodic arrangement with a spacing substantially smaller than the wavelength of light or electromagnetic waves. These artificial structures generate electromagnetic responses, resulting in unusual optical properties including negative refractive index[12-15], hyperbolic dispersion[16,17], perfect absorption[18,19], artificial chirality[20,21], and holograms[22-26]. The metamaterials systems have been developed through a variety of methods such as e-beam lithography, interference lithography, 3D printing, and block copolymer self-assembly.

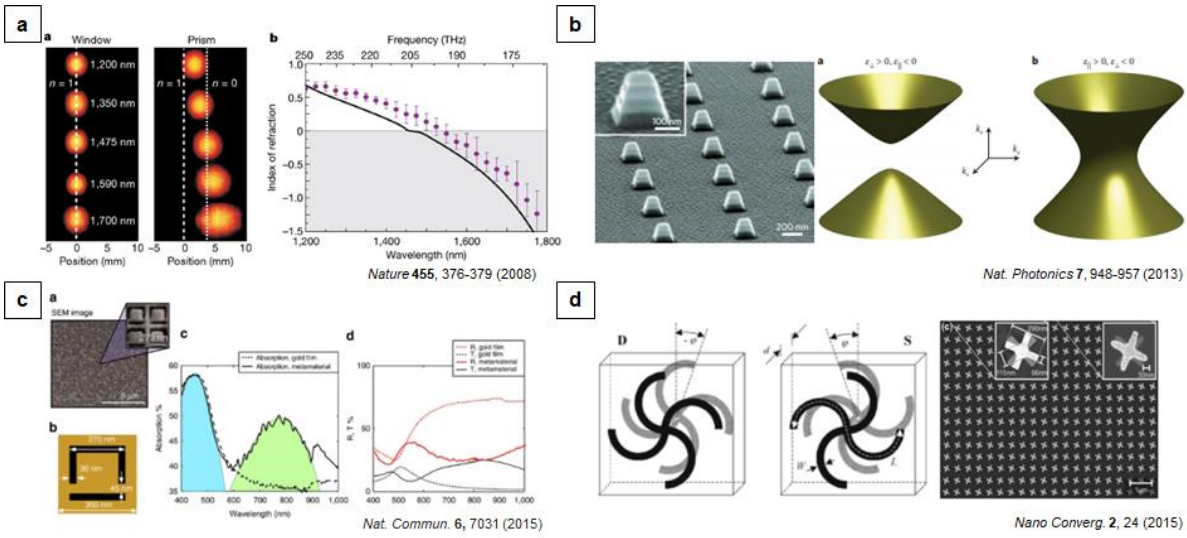

Fig. 1.4. a-d, Introduction of metamaterials system with unusual optical properties such as (a) negative refractive index[12], (b) hyperbolic dispersion[16], (c) perfect absorption[19], and (d) artificial chirality[20]. Reprinted with permission from refs. 12, 16, 19, and 20, respectively. Copyright © 2018 Springer Nature, Copyright © 2013 Springer Nature, Copyright © 2015 Springer Nature, Copyright © 2019 American Chemical Society, and Copyright © 2015 American Chemical Society, respectively.

1.2.2 Metasurface holograms

Holography, first introduced in 1948 by Denis Gabor, is broadly defined as recording and reconstruction of both the amplitude and phase of light, and holograms refer to reconstructed images recorded by holography techniques. These holography techniques have been utilized for diverse

applications such as 3D displays, data storage, and optical sensors. In particular, with the development of nanofabrication technology, the metasurface holograms composed of ultrathin 2D metamaterials have attracted considerable attention for their capabilities of generating three-dimensional (3D) full-color holographic images with unprecedented spatial resolution, high precision, and low noise. Recently, Guoxing Zheng and coworkers successfully developed metasurface hologram system composed of a ground metal plane, a dielectric spacer layer, and a top layer of antennas[22]. The system reconstructed elaborate 3D holographic images via high diffraction efficiency (80%). Also, Dandan Wen and coworkers realized a polarization multiplexed optical device by the introduction of three layers containing silver nanorods (top), SiO_2/silver background layer (middle), and Si substrate (bottom)[23]. In addition, various plasmonic or dielectric materials have been utilized for ultrathin 2D metasurface, and the plasmonic/dielectric metasurface generated full-color holographic images with complex shape by manipulating the amplitude and phase of light[24-26].

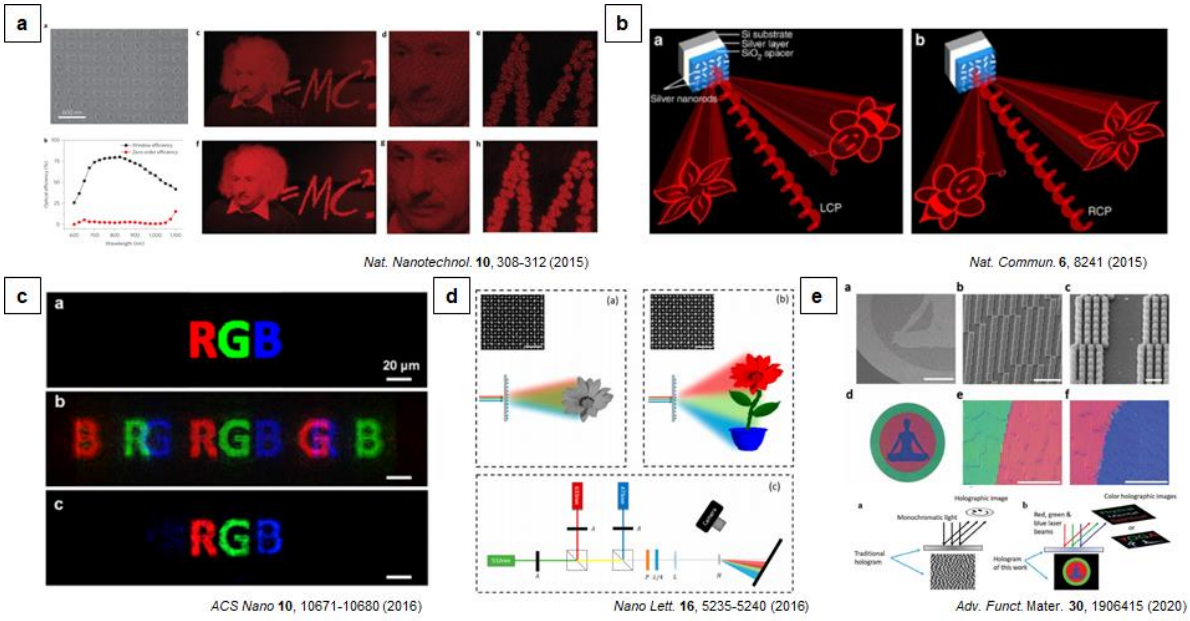

Fig. 1.5. a-e, Introduction of metasurface holograms and its applications having (a) high diffraction efficiency[22] and (b) helicity multiplexed broadband properties[23]. These holograms are fabricated using a thin layer of (c) plasmonic[24] or (d-e) dielectric structures[25,26]. Reprinted with permission from refs. 22, 23, 24, 25 and 26, respectively. Copyright © 2015 Springer Nature, Copyright © 2015 Springer Nature, Copyright © 2016 American Chemical Society, Copyright © 2016 American Chemical Society, and Copyright © 2020 WILEY-VCH Verlag GmbH & Co. KGaA, Weinheim, respectively.

1.3 Polymer based-hologram systems

1.3.1 Dynamic holograms using responsive polymer

However, most of the conventional metasurface holograms can provide only static holographic

signals because their phase and magnitude profiles were fixed during the fabrication process. To realize holograms which provide a variety of signals by altering their phase and magnitude profile, the responsive polymers have been exploited. Many researchers have developed a dynamic structural color system capable of providing multiple signals upon external stimuli such as thermal stress[27,28], chemical molecules[29,30], magnetic force[31,32], and mechanical stress[33,34]. The structural color arises from the periodic refractive index distribution of inter-domains, and the color signal changes because the phase and magnitude profile are altered as the spacing of inter-domains varies. These systems can be fabricated using block copolymer[35-37], self-assembled nanoparticles[38,39], liquid crystals[40,41], and lithographic patterning[42,43]. Because hologram is broadly defined as *any entity that can control the amplitude and phase of light*, these dynamic structural color systems which alter their phase profile of light in response to external stimuli could be known as dynamic holograms.

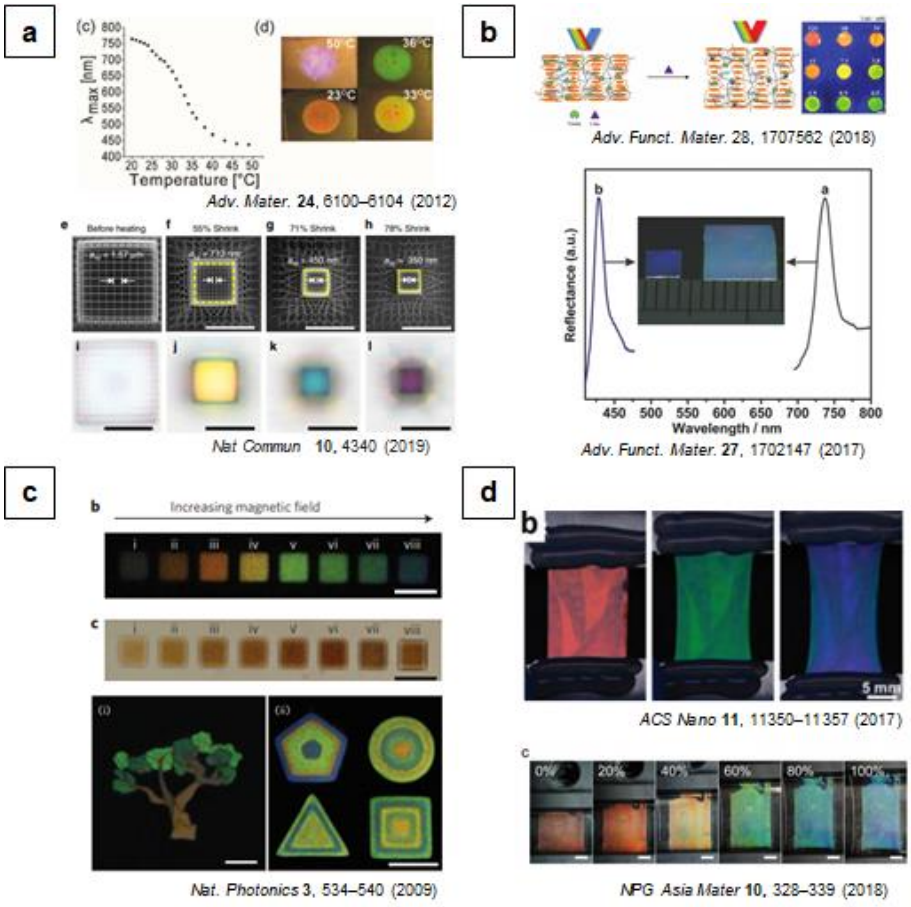

Fig. 1.6. a-d, Dynamic structural color systems displaying multiple optical signals upon external stimuli such as (a) thermal stress[27,28], (b) chemical molecules[29,30], (c) magnetic force[31,32], and (d) mechanical stress[33,34]. Reprinted with permission from refs. 27, 28, 29, 30, 31, 32, 33, and 34, respectively. Copyright © 2012 WILEY-VCH Verlag GmbH & Co. KGaA, Weinheim, Copyright © 2019 Springer Nature, Copyright © 2018 WILEY-VCH Verlag GmbH & Co. KGaA, Weinheim, Copyright © 2017 WILEY-VCH Verlag GmbH & Co. KGaA, Weinheim, Copyright © 2009 Springer Nature, Copyright © 2017 American Chemical Society, and Copyright © 2018 Springer Nature, respectively.

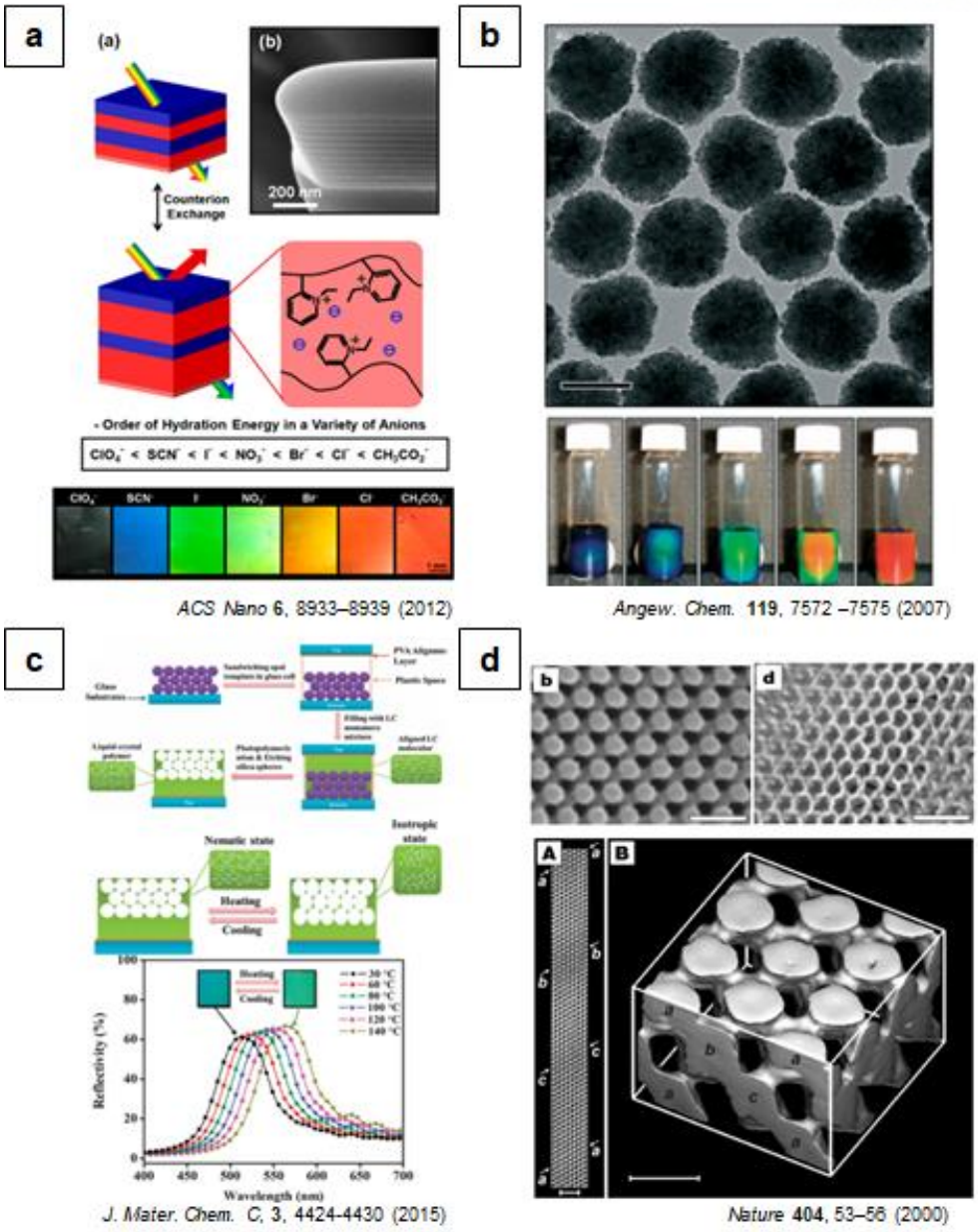

Fig. 1.7. a-d, Fabrication of dynamic structural color systems through a variety of methods such as (a) block copolymer[35], (b) self-assembled nanoparticles[38], (c) liquid crystal[40], and (d) photolithography[42]. Reprinted with permission from refs. 35, 38, 40 and 42, respectively. Copyright © 2012 American Chemical Society, Copyright © 2007 WILEY-VCH Verlag GmbH & Co. KGaA, Weinheim, Copyright 2015 © The Royal Society of Chemistry, Copyright © 2000 Springer Nature, respectively.

1.3.2 The limitations of dynamic structural color systems

The above-mentioned structural color systems provide optical signals such as color variations when the responsive polymer is actuated by external stimuli. However, they cannot display complex-shaped signals other than diffractive color change because the interdomain spacing is altered consistently when exposed to environmental changes. Therefore, these dynamic structural color systems have low

encryption capabilities and are difficult to be applied to multi-level security systems. Also, those systems that show simple color signals are far from true 3D holograms.

1.3.3 The motivation for dynamic 3D holograms

Therefore, researchers have devoted enormous efforts to realize 3D polymer holograms with complex shapes. They tried to develop complex-shaped holograms through the formation of 3D optical heterogeneities in polymer matrices using lithographic techniques such as two photon-initiated polymerization[44,45] and holographic lithography[42,46] (**Fig. 1.8**). However, the technology requires expensive equipment and complicated processes, and the corresponding structures are difficult to mass-produce, therefore, a more efficient method of implementing 3D optical heterogeneity is needed. Furthermore, if novel materials that express optical signals in response to change is introduced to the photonic system, the system can provide various types of optical signals in addition to holograms caused by the optical heterogeneity. As a result, it is expected to take one step closer to true dynamic 3D holograms.

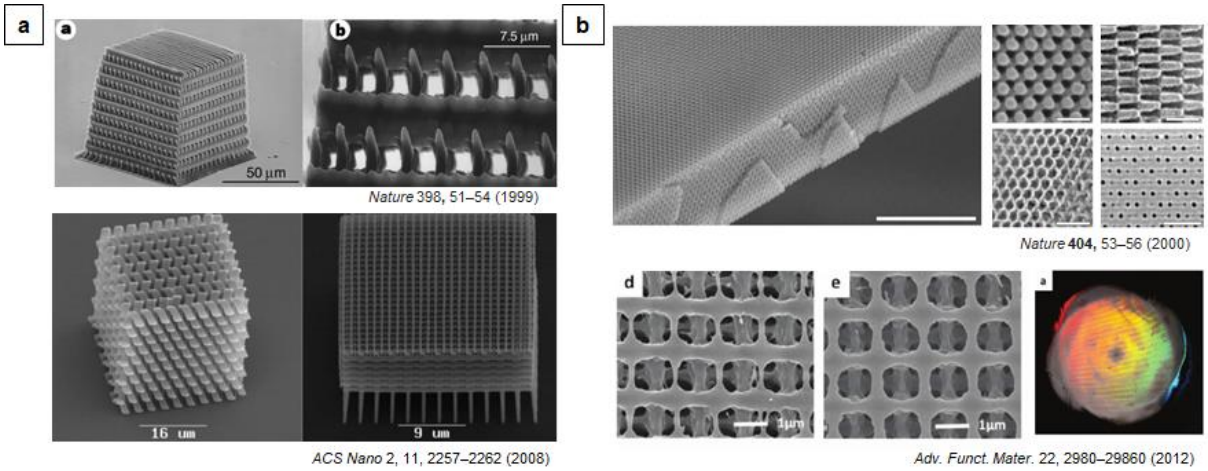

Fig. 1.8. a,b, Methods of realizing 3D optical heterogeneity in polymer matrices through (a) two photon-initiated polymerization[44,45] and (b) holographic lithography[42,46]. Reprinted with permission from refs. 42,44, 45, and 46, respectively. Copyright © 1999 Springer Nature, Copyright © 2008 American Chemical Society, Copyright © 2000 Springer Nature, Copyright © 2019 American Chemical Society, and Copyright © 2012 WILEY-VCH Verlag GmbH & Co. KGaA, Weinheim, respectively.

1.4 Polydiacetylene (PDA)

1.4.1 Self-assembly and photopolymerization of diacetylene monomers

Among novel materials that express optical signals in response to external stimuli, polydiacetylene (PDA), one of the conjugated polymers, have received great attention due to their unique properties such as blue-to-red color transition and fluorescence emission. Polydiacetylene is formed by 1,4-

topochemical polymerization of diacetylenes through 254 nm UV irradiation when diacetylene monomers are positioned in an ideal arrangement through the self-assembly process. Especially, in the crystalline structure, the ideal arrangement corresponds to a C1-C1 repeat distance of 4.9 Å and a C1-C4 distance of 3.5Å, and a tilt angle of 45°[47,48] (**Fig. 1.10**). Then, photopolymerization of self-assembled diacetylene at 254 nm UV light forms a delocalized π-system consisting of an alternative carbon double bond and carbon triple bond, resulting in a blue phase PDA with strong absorption at 650 nm. These PDA systems have been fabricated in diverse forms such as vesicles[49,50], mono/bilayer[51,52], single crystals[53,54], and polymer composites[55,56].

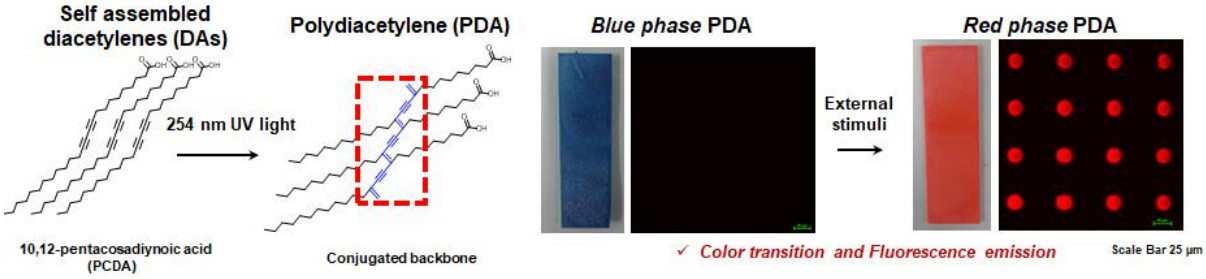

Fig. 1.9. Polymerization of diacetylene (DA) monomers and optical properties of polydiacetylene (PDA).

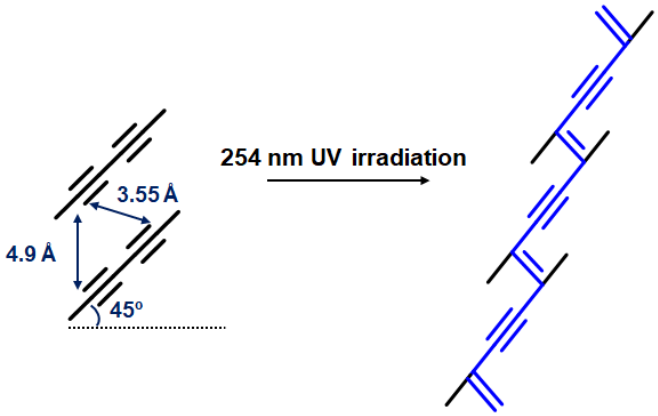

Fig. 1.10. Ideal arrangement of DA monomers in crystalline state for photo-polymerization.

1.4.2 Optical properties of PDA

PDA exhibits unique optical properties such as color transition and fluorescent emission upon environmental perturbations such as thermal stress[57,58], light[59], mechanical stress[60], pH[61-63], chemical molecules[64-67], and biomolecules[68-70] (**Fig. 1.11**). Upon external stimuli, PDA having a delocalized network of π electron undergoes blue-to-red transition due to the conformational changes of conjugated backbone. Furthermore, these red phase PDA exhibits red emission.

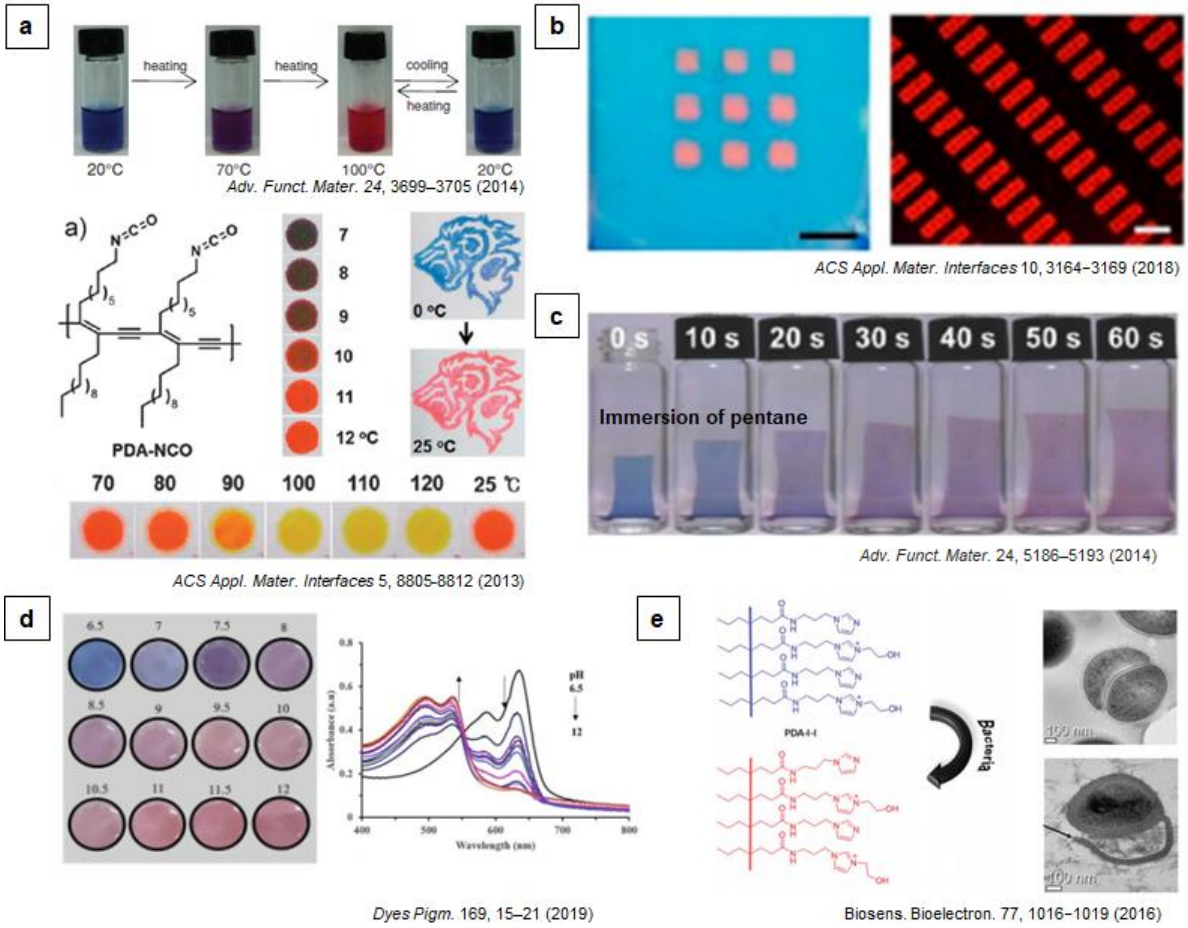

Fig. 1.11. a-e, Responsive PDA systems displaying color transition and fluorescence emission upon external stimuli such as (a) thermal stress[57,58], (b) light[51], (c) mechanical stress[60], (d) pH[63], and (e) biomolecule[70]. Reprinted with permission from refs. 57, 58, 59, 60, 63, and 70, respectively. Copyright © 2014 WILEY-VCH Verlag GmbH & Co. KGaA, Weinheim, Copyright © 2013 American Chemical Society, Copyright © 2018 American Chemical Society, Copyright © 2014 WILEY-VCH Verlag GmbH & Co. KGaA, Weinheim, Copyright © 2019 Elsevier Inc., Copyright © 2016 Elsevier Inc., respectively.

Many researchers have attempted to investigate the exact mechanism of these chromatic transitions and fluorescence emissions in PDA. Although these origins of optical signal changes have been fully not understood, it is believed that the transition of electronic structures in the conjugated backbone induces optical signals change. A recently reported study on the electronic and physical properties of PDA through density functional theory (DFT) calculations also supported the fact that chromogenic transitions are caused by the transition of electronic structure[71]. When the model structures with different torsional angles were analyzed, the models with large torsional angles (90˚) corresponding to red phase PDA exhibited the higher energy (**Fig. 1.12**).

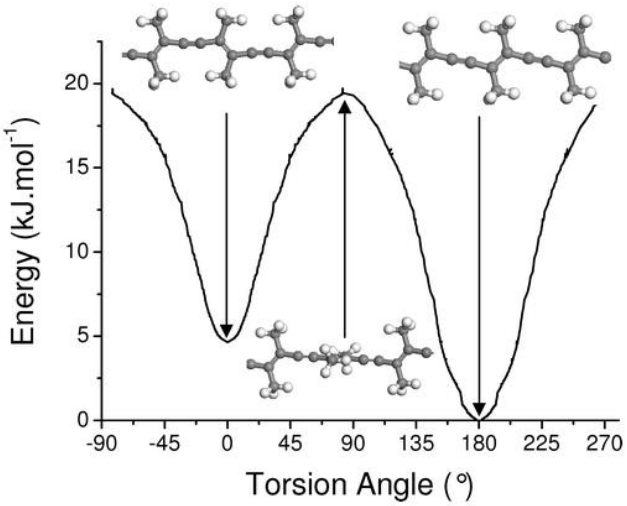

Fig. 1.12. Energy profiles according to the twist angle of PDA models[71]. Reprinted with permission from ref. 71. Copyright © 2009 American Chemical Society.

1.4.3 PDA sensors

These color change and emission characteristics enable PDA to be utilized for sensor applications. In particular, PDA sensors are manufactured in the form of attaching a probe unit to the end, and have been widely used as chemosensors for detecting specific molecules. These PDA sensory systems can detect specific molecules through color transition and fluorescent emission because their conjugated backbone undergoes partial *p* orbital twisting by the repulsion between probe-target complexes (**Fig. 1.13**). Based on these properties and sensing mechanisms, Lee and co-workers successfully developed colorimetric and fluorescent PDA chemosensors for the detection of various toxic molecules such as potassium[64], mercury[65], melamine[66], and nerve agents[67] (**Fig. 1.14**).

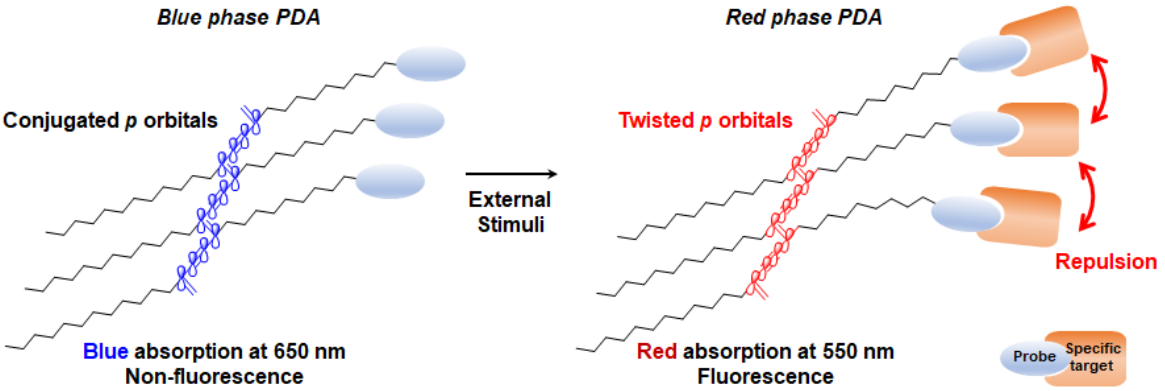

Fig. 1.13. Mechanism of PDA based-chemosensor with probe unit for detection of specific target.

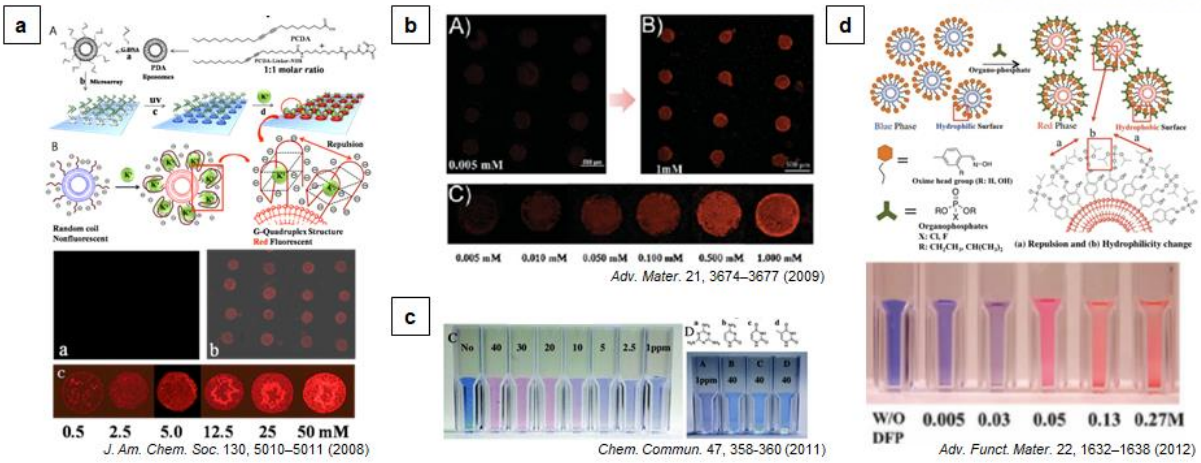

Fig. 1.14. a-d, Illustration and optical properties of various kinds of PDA-based chemosensor for detection of (a) potassium[64], (b) mercury[65], (c) melamine[66], and (d) nerve agents[67]. Reprinted with permission from refs. 64, 65, 66, and 67, respectively. and Copyright © 2008 American Chemical Society, Copyright © 2009 WILEY-VCH Verlag GmbH & Co. KGaA, Weinheim, Copyright © 2011 The Royal Society of Chemistry, Copyright © 2009 WILEY-VCH Verlag GmbH & Co. KGaA, Weinheim, respectively.

1.5 References

1 Chung, K. *et al.* Flexible, angle-independent, structural color reflectors inspired by morpho butterfly wings. *Adv. Mater.* **24**, 2375-2379 (2012).

2 Park, J. G. *et al.* Full-spectrum photonic pigments with non-iridescent structural colors through colloidal assembly. *Angew. Chem. Int. Ed.* **53**, 2899-2903 (2014).

3 Zhang, Y. et al. Super-Elastic Magnetic Structural Color Hydrogels. *Small* **15**, e1902198 (2019).

4 Gan, M. K., Xiao, T. L., Liu, Z. Y. & Wang, Y. Layered photochromic films stacked from spiropyran-modified montmorillonite nanosheets. *RSC Adv.* **9**, 12325-12330 (2019).

5 Li, Q. W., Cao, Z. Q. & Wang, G. J. Diazonaphthoquinone-based amphiphilic polymer assemblies for NIR/UV light- and pH-responsive controlled release. *Polym. Chem-Uk* **9**, 463-471 (2018).

6 Shiraishi, Y., Miyamoto, R. & Hirai, T. Spiropyran-Conjugated Thermoresponsive Copolymer as a Colorimetric Thermometer with Linear and Reversible Color Change. *Org. Lett.* **11**, 1571-1574 (2009).

7 Chen, X. *et al.* Thin-Film Formation of Imidazolium-Based Conjugated Polydiacetylenes and Their Application for Sensing Anionic Surfactants. *Angew. Chem. Int. Ed.* **49**, 1422-1425 (2010).

8 Paek, K., Yang, H., Lee, J., Park, J. & Kim, B. J. Efficient Colorimetric pH Sensor Based on Responsive Polymer-Quantum Dot Integrated Graphene Oxide. *ACS Nano* **8**, 2848-2856 (2014).

9 Shao, B. *et al.* Luminescent switching and structural transition through multiple external stimuli based on organic molecular polymorphs. *J. Mater. Chem. C* **7**, 3263-3268 (2019).

10 Hou, H. H., Yin, J. & Jiang, X. S. Reversible Diels-Alder Reaction To Control Wrinkle Patterns: From Dynamic Chemistry to Dynamic Patterns. *Adv. Mater.* **28**, 9126-9132 (2016).

11 Ma, T. et al. Dynamic wrinkling pattern exhibiting tunable fluorescence for anticounterfeiting applications. *Nat. Commun* **11**, 1811 (2020).

12 Valentine, J. *et al.* Three-dimensional optical metamaterial with a negative refractive index. *Nature* **455**, 376-379 (2008).

13 Smith, D. R., Pendry, J. B. & Wiltshire, M. C. K. Metamaterials and negative refractive index. *Science* **305**, 788-792 (2004).

14 Kaina, N., Lemoult, F., Fink, M. & Lerosey, G. Negative refractive index and acoustic superlens from multiple scattering in single negative metamaterials. *Nature* **525**, 77-81 (2015).

15 Grigorenko, A. N. Negative refractive index in artificial metamaterials. *Opt. Lett.* **31**, 2483-2485 (2006).

16 Poddubny, A., Iorsh, I., Belov, P. & Kivshar, Y. Hyperbolic metamaterials. *Nat. Photonics* **7**, 948-957 (2013).

17 Kruk, S. S. *et al.* Magnetic hyperbolic optical metamaterials. *Nat. Commun.* **7**, 11329 (2016).

18 Zhong, S. M., Ma, Y. G. & He, S. L. Perfect absorption in ultrathin anisotropic epsilon-near-zero metamaterials. *Appl. Phys. Lett.* **105**, 023504 (2014).

19 Roger, T. *et al.* Coherent perfect absorption in deeply subwavelength films in the single-photon regime. *Nat. Commun.* **6**, 7031 (2015).

20 Oh, S. S. & Hess, O. Chiral metamaterials: enhancement and control of optical activity and circular dichroism. *Nano Converg.* **2**, 24 (2015).

21 Zhou, J. F. *et al.* Terahertz chiral metamaterials with giant and dynamically tunable optical activity. *Phys. Rev. B* **86**, 035448 (2012).

22 Zheng, G. X. *et al.* Metasurface holograms reaching 80% efficiency. *Nat. Nanotechnol.* **10**, 308-312 (2015).

23 Wen, D. D. *et al.* Helicity multiplexed broadband metasurface holograms. *Nat. Commun.* **6**, 8241 (2015).

24 Wan, W. W., Gao, J. & Yang, X. D. Full-Color Plasmonic Metasurface Holograms. *ACS Nano* **10**, 10671-10680 (2016).

25 Wang, B. *et al.* Visible-Frequency Dielectric Metasurfaces for Multiwavelength Achromatic and Highly Dispersive Holograms. *Nano Lett.* **16**, 5235-5240 (2016).

26 Wen, D. D., Cadusch, J. J., Meng, J. & Crozier, K. B. Multifunctional Dielectric Metasurfaces Consisting of Color Holograms Encoded into Color Printed Images. *Adv. Funct. Mater.* **30**, 1906415 (2020).

27 Chiappelli, M. C. & Hayward, R. C. Photonic Multilayer Sensors from Photo-Crosslinkable Polymer Films. *Adv. Mater.* **24**, 6100-6104 (2012).

28 Liu, Y. J. *et al.* Structural color three-dimensional printing by shrinking photonic crystals. *Nat. Commun.* **10**, 4340 (2019).

29 Xiao, F. B. *et al.* Smart Photonic Crystal Hydrogel Material for Uranyl Ion Monitoring and Removal in Water. *Adv. Funct. Mater.* **27**, 1702147 (2017).

30 Noh, K. G. & Park, S. Y. Biosensor Array of Interpenetrating Polymer Network with Photonic Film Templated from Reactive Cholesteric Liquid Crystal and Enzyme-Immobilized Hydrogel Polymer. *Adv. Funct. Mater.* **28**, 1707562 (2018).

31 Zhang, Y. L. *et al.* Super-Elastic Magnetic Structural Color Hydrogels. *Small* **15**, 1902198 (2019).

32 Kim, H. *et al.* Structural colour printing using a magnetically tunable and lithographically fixable photonic crystal. *Nat. Photonics* **3**, 534-540 (2009).

33 Lee, G. H. *et al.* Chameleon-Inspired Mechanochromic Photonic Films Composed of Non-Close-Packed Colloidal Arrays. *ACS Nano* **11**, 11350-11357 (2017).

34 Park, T. H. *et al.* Block copolymer structural color strain sensor. *NPG Asia Mater.* **10**, 328-339 (2018).

35 Lim, H. S., Lee, J. H., Walish, J. J. & Thomas, E. L. Dynamic Swelling of Tunable Full-Color Block Copolymer Photonic Gels via Counterion Exchange. *ACS Nano* **6**, 8933-8939 (2012).

36 Park, T. H. *et al.* Thermo-Adaptive Block Copolymer Structural Color Electronics. *Adv. Funct. Mater.* **31**, 2008548 (2021).

37 Kang, H. S. *et al.* Printable and Rewritable Full Block Copolymer Structural Color. *Adv. Mater.* **29**, 1700084 (2017).

38 Ge, J. P., Hu, Y. X. & Yin, Y. D. Highly tunable superparamagnetic colloidal photonic crystals. *Angew. Chem. Int. Edit.* **46**, 7428-7431 (2007).

39 Lei, Q. L., Ni, R. & Ma, Y. Q. Self-Assembled Chiral Photonic Crystals from a Colloidal Helix Racemate. *ACS Nano* **12**, 6860-6870 (2018).

40 Xing, H. H., Li, J., Guo, J. B. & Wei, J. Bio-inspired thermal-responsive inverse opal films with dual structural colors based on liquid crystal elastomer. *J. Mater. Chem. C* **3**, 4424-4430 (2015).

41 Lim, C., Bae, S., Jeong, S. M. & Ha, N. Y. Manipulation of Structural Colors in Liquid-Crystal Helical Structures Deformed by Surface Controls. *ACS Appl. Mater. Inter.* **10**, 12060-12065 (2018).

42 Campbell, M., Sharp, D. N., Harrison, M. T., Denning, R. G. & Turberfield, A. J. Fabrication of photonic crystals for the visible spectrum by holographic lithography. *Nature* **404**, 53-56 (2000).

43 Liang, G. F., Chen, X., Wen, Z. Q., Chen, G. & Guo, L. J. Super-resolution photolithography

using dielectric photonic crystal. *Opt. Lett.* **44**, 1182-1185 (2019).

44 Cumpston, B. H. *et al.* Two-photon polymerization initiators for three-dimensional optical data storage and microfabrication. *Nature* **398**, 51-54 (1999).

45 Ovsianikov, A. *et al.* Ultra-Low Shrinkage Hybrid Photosensitive Material for Two-Photon Polymerization Microfabrication. *ACS Nano* **2**, 2257-2262 (2008).

46 Li, J., Liang, G. Q., Zhu, X. L. & Yang, S. Exploiting Nanoroughness on Holographically Patterned Three-Dimensional Photonic Crystals. *Adv. Funct. Mater.* **22**, 2980-2986 (2012).

47 Baughman, R. H. Solid-State Synthesis of Large Polymer Single-Crystals. *J. Polym. Sci. Pol. Phys.* **12**, 1511-1535 (1974).

48 Lauher, J. W., Fowler, F. W. & Goroff, N. S. Single-crystal-to-single-crystal topochemical polymerizations by design. *Accounts Chem. Res.* **41**, 1215-1229 (2008).

49 Jung, Y. K., Kim, T. W., Park, H. G., Soh, H. T. Specific Colorimetric Detection of Proteins Using Bidentate Aptamer-Conjugated Polydiacetylene (PDA) Liposomes. *Adv. Funct. Mater.* **20**, 3092-3097 (2010).

50 Wang, D.-E., Wang, Y., Tian, C., Zhang, L., Han, X., Tu, Q., Yuan, M., Chen, S., Wang, J. Polydiacetylene Liposome-Encapsulated Alginate Hydrogel Beads for Pb^{2+} Detection with Enhanced Sensitivity. *J. Mater. Chem. A* **3**, 21690-21698 (2015).

51 Charych, D. H., Nagy, J. O., Spevak, W., Bednarski, M. D. Direct Colorimetric Detection of a Receptor-Ligand Interaction by a Polymerized Bilayer Assembly. *Science* **261**, 585-588 (1993).

52 Cheng, Q., Stevens, R. C. Coupling of an Induced Fit Enzyme to Polydiacetylene Thin Films: Colorimetric Detection of Glucose. *Adv. Mater.* **9**, 481-483 (1997).

53 Jo, S., Suzuki, S. & Yoshimura, M. Effect of solid-state polymerization on crystal morphology of a type of polydiacetylene single crystal obtained by physical vapor transport technique. *Thin Solid Films* **554**, 154-157 (2014).

54 Jo, S., Yoshikawa, H., Fujii, A. & Takenaga, M. Preparation of polydiacetylene single crystals based on physical vapor growth technique. *Synthetic Met* **150**, 223-226 (2005).

55 Seo, S., Lee, J., Kwon, M. S., Seo, D., Kim, J. Stimuli-Responsive Matrix-Assisted Colorimetric Water Indicator of Polydiacetylene Nanofibers. *ACS Appl. Mater. Interfaces* **7**, 20342-20348 (2015).

56 Tu, M.-C., Cheema, J. A., Yildiz, U. H., Palaniappan, A., Liedberg, B. Vapor Phase Solvatochromic Responses of Polydiacetylene Embedded Matrix Polymers. *J. Mater. Chem. C* **5**, 1803-1809 (2017).

57 Park, I. S., Park, H. J. & Kim, J. M. A Soluble, Low-Temperature Thermochromic and Chemically Reactive Polydiacetylene. *ACS Appl. Mater. Inter.* **5**, 8805-8812 (2013).

58 Lee, S. *et al.* Construction and Molecular Understanding of an Unprecedented, Reversibly Thermochromic Bis-Polydiacetylene. *Adv. Funct. Mater.* **24**, 3699-3705 (2014).

59 Lee, J., Seo, S. & Kim, J. Rapid Light-Driven Color Transition of Novel Photoresponsive Polydiacetylene Molecules. *ACS Appl. Mater. Inter.* **10**, 3164-3169 (2018).

60 Park, D. H., Hong, J., Park, I. S., Lee, C. W. & Kim, J. M. A Colorimetric Hydrocarbon Sensor Employing a Swelling-Induced Mechanochromic Polydiacetylene. *Adv. Funct. Mater.* **24**, 5186-5193 (2014).

61 Kew, S. J. & Hall, E. A. H. pH response of carboxy-terminated colorimetric polydiacetylene vesicles. *Anal. Chem.* **78**, 2231-2238 (2006).

62 Won, S. H., Lee, J. U. & Sim, S. J. Fluorogenic pH-Sensitive Polydiacetylene (PDA) Liposomes as a Drug Carrier. *J Nanosci. Nanotechno.* **13**, 3792-3800 (2013).

63 Jannah, F. & Kim, J. M. pH-sensitive colorimetric polydiacetylene vesicles for urease sensing. *Dyes and Pigments* **169**, 15-21 (2019).

64 Lee, J., Kim, H. J. & Kim, J. Polydiacetylene liposome arrays for selective potassium detection. *J. Am. Chem. Soc.* **130**, 5010-5011 (2008).

65 Lee, J., Jun, H. & Kim, J. Polydiacetylene-Liposome Microarrays for Selective and Sensitive Mercury(II) Detection. *Adv. Mater.* **21**, 3674-3677 (2009).

66 Lee, J., Jeong, E. J. & Kim, J. Selective and sensitive detection of melamine by intra/inter liposomal interaction of polydiacetylene liposomes. *Chem. Commun.* **47**, 358-360 (2011).

67 Lee, J., Seo, S. & Kim, J. Colorimetric Detection of Warfare Gases by Polydiacetylenes Toward Equipment-Free Detection. *Adv. Funct. Mater.* **22**, 1632-1638 (2012).

68 Scindia, Y., Silbert, L., Volinsky, R., Kolusheva, S. & Jelinek, R. Colorimetric detection and fingerprinting of bacteria by glass-supported lipid/polydiacetylene films. *Langmuir* **23**, 4682-4687 (2007).

69 West, M. R., Hanks, T. W. & Watson, R. T. Polydiacetylene-Based Liposomes: An "Optical Tongue" for Bacteria Detection and Identification. *J. Chem. Educ.* **86**, 373-375 (2009).

70 Lee, S. *et al.* Sensing and antibacterial activity of imidazolium-based conjugated polydiacetylenes. *Biosens Bioelectron* **77**, 1016-1019, doi:10.1016/j.bios.2015.10.090 (2016).

71 Filhol, J. S. *et al.* Polymorphs and Colors of Polydiacetylenes: A First Principles Study. *J. Am. Chem. Soc.* **131**, 6976-6988 (2009).

Chapter 2 Dynamic Multimodal Holograms of Conjugated Organogels via Dithering mask lithography

This chapter includes the published contents:

J. Oh, D. Baek, T. K. Lee, D. Kang, H. Hwang, E. M. Go, I. Jeon, Y. You, C. Son, D. Kim, M. Whang, K. Nam, M. Jang, J.-H. Park, S. K. Kwak*, J. Kim*, and J. Lee*. *Nature Materials* **20**, 385-394 (2021).

---

2. 1 Introduction

Responsive polymer matrices containing one- to three-dimensional periodic patterns of optical properties are of interest because they have applications in optical sensors and displays. In response to various external stimuli[1-4], these matrices are used to dynamically control light propagation and modulate optical properties such as refractive index and absorption and emission spectra[5-11]. The periodic patterns that give rise to the optical properties in these matrices are typically created using lithographic patterning and self-assembly of nano- and micro-particles, block copolymer, and liquid crystals[12-17].

While optical systems such as waveguides or holographic gratings[18, 19] are created using stimuli-responsive polymer matrices, they are almost exclusively used in photonic crystals, wherein active coloration forms from changes in the peak wavelength of Bragg diffraction as the uniform inter-domain spacing is varied consistently throughout the entire system[20-26]. Therefore, these typical photonic crystals and polymer-based hologram systems cannot reversibly display varying hologram shapes, they were restricted in their functionalities to mostly spectroscopic changes. However, if the optical periodicity in the polymer matrices was made heterogeneous, one may modulate light propagation in more complex ways to realize varying types of optical signals, for example dynamically shape-changing holograms used for sophisticated encryption technologies. Although two-photon or holographic lithography can be used to create complicated 3D optical heterogeneities in polymer matrices[27,28], these methods are not widely accessible because they involve expensive precision instruments and fabrication requires extreme care and time. This has limited the exploration of light propagation through polymer matrices with complex 3D optical heterogeneities that could potentially display a rich variety of optical signals besides structural colors.

Here, we describe the use of conventional 2D photo-lithography to create a dynamic optical system that reversibly displays three modes of holograms in a single architecture through a solvent exchange.

We used dithering mask lithography to pattern conjugated polydiacetylene (PDA) organogels with varying crosslinking density in two dimensions, forming 2D periodic refractive index variations that displayed structural color via diffraction. When immersed in protic solvents such as water or methanol (MeOH), the PDA organogels shrank anisotropically because their bottom surface was attached to a glass substrate (**Fig. 2.1a**). Anisotropic shrinkage caused the 2D optical periodicity of the organogels to vary along the thickness direction, resulting in the disappearance of structural colors and the appearance of unusual 3D full parallax holographic signals that are unique to the shape of individual dithering masks (**Fig. 2.1b**). We conducted multiscale simulations to mechanistically describe the emergence of these unique light signals. Unlike typical optical systems displaying a single-mode hologram, our system realizes multi-modal holograms in a cost-effective and scalable manner. Such a robust system will find ample applications in multi-level anti-counterfeiting and encryption technologies.

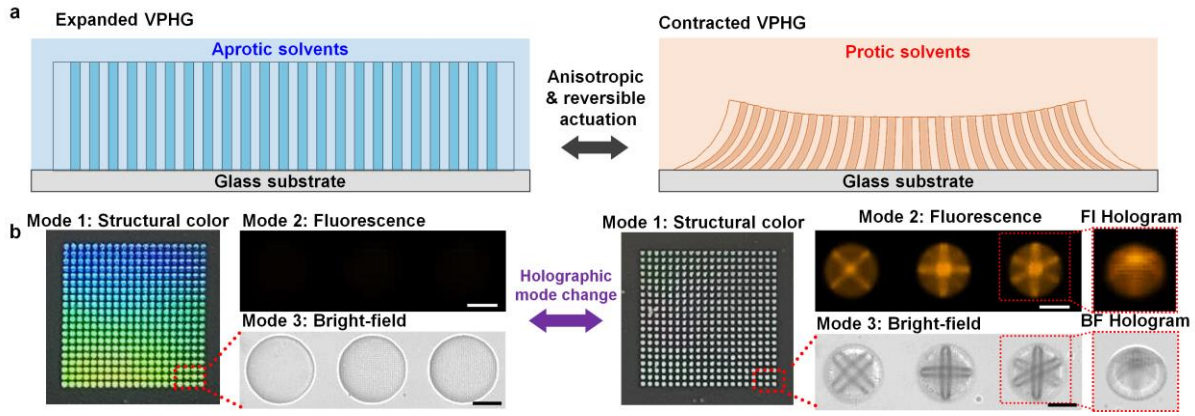

Fig. 2.1. Architecture and multi-modal hologram of responsive conjugated PDA organogel formed via dithering mask lithography. a, Depending on immersion solvent, PDA organogels acting as volume phase holographic gratings (VPHG) undergo anisotropic actuation between expanded state and contracted state, and **b,** display either iridescent structural colors (left panel) or 3D full parallax bright-field and fluorescence signals (right panel, rhombus, square, and hexagon dithering masks were used, from left to right). Copyright © 2021 Springer Nature.

2. 2 Results and discussion

To create a multi-modal holographic system, disk-shaped PDA organogels attached to glass substrates via silane chemistry were fabricated inside polydimethylsiloxane (PDMS) channels (**Fig. 2.2a and Fig. 2.3**). The pregel solution containing diacrylic acetylene liquid monomer, 2,4-hexadiyne-1,6-diacrylate (HD-DA), and the photo-initiator were injected into the channels. Using an optical microscope equipped with a digital micro-mirror device (DMD), 365 nm ultraviolet (UV) light with or

without two-dimensional patterns was irradiated to the pregel solution, and the free-radical acrylic polymerization proceeded to form the crosslinked network (**Fig. 2.2b and Fig. 2.4**).

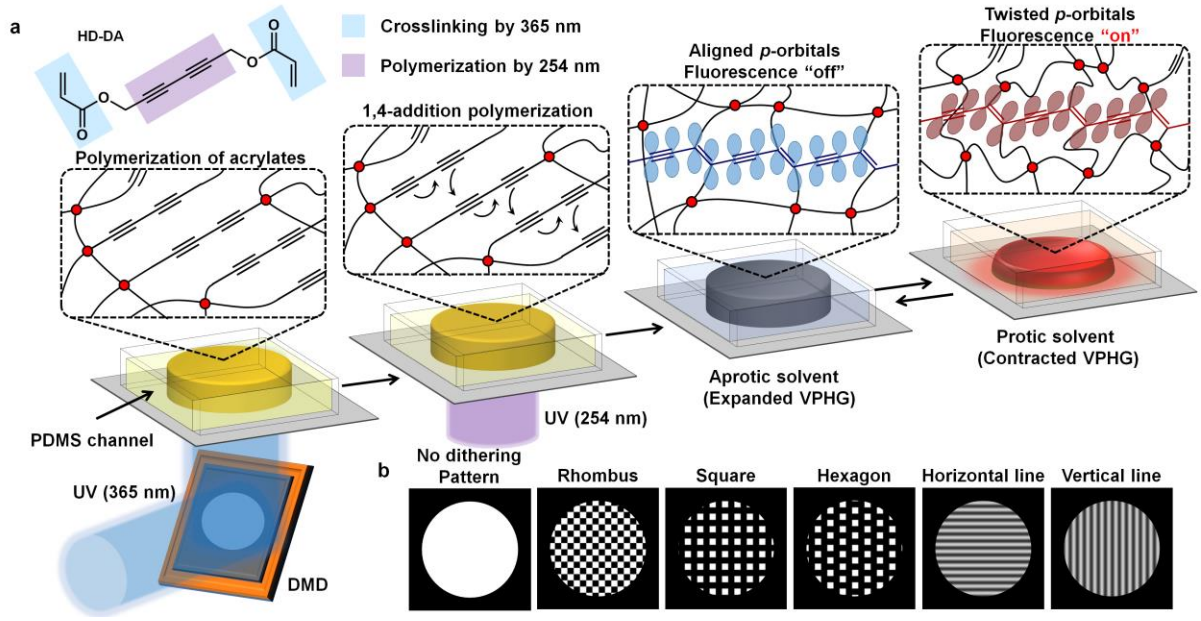

Fig. 2.2. a, Schematic showing fabrication of conjugated PDA organogels. Two-dimensionally patterned 365 nm UV light delivered via a digital micro-mirror device (DMD) converts HD-DA monomers into crosslinks. Solvent exchange expands and anisotropically contracts the organogels to respectively turn fluorescence off and on. **b,** Dithering masks used in this study. Copyright © 2021 Springer Nature.

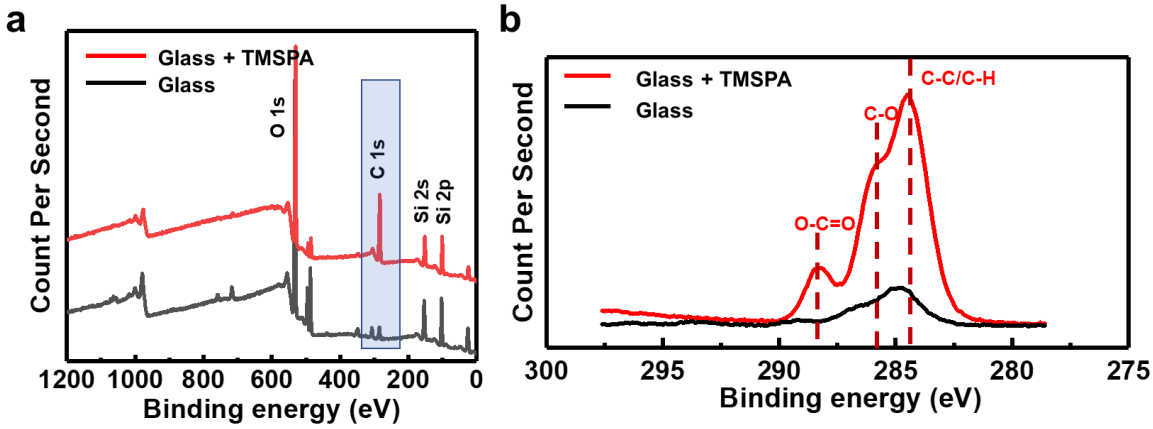

Fig. 2.3. Surface analysis of acrylated silane coated glass slide. a,b XPS survey (a) and C 1s core level spectra (b) of glass (black) and 3-(trimethoxysilyl)propyl acrylate (TMSPA) coated glass (red). Copyright © 2021 Springer Nature.

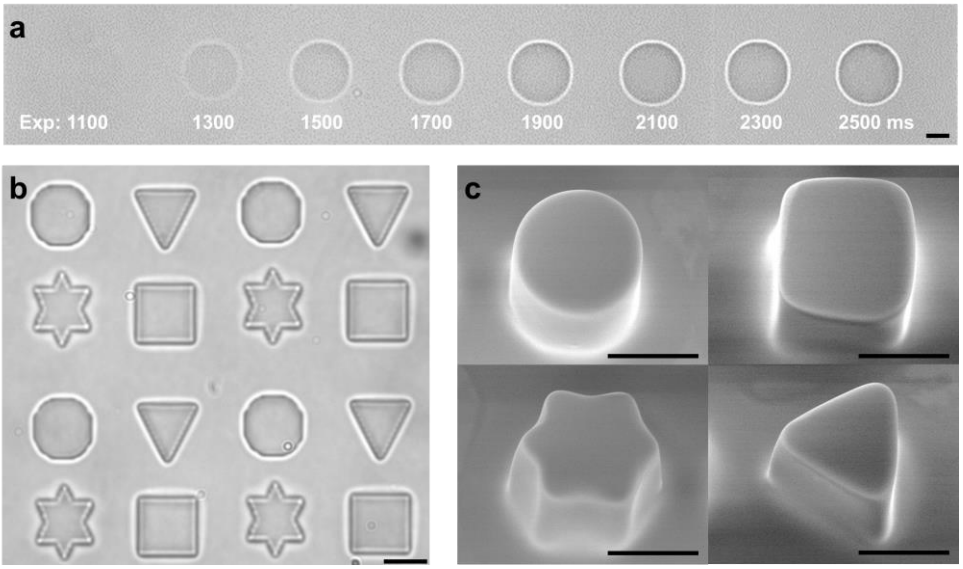

Fig. 2.4. Fabrication of conjugated PDA organogel microstructure. **a,** Bright-field microscopy images of crosslinked HD-DA microstructures according to 365 nm UV exposure time. **b,c,** Bright-field microscopy images (b) and SEM images (c) of multiple shaped PDA microstructures. Scale bar is 20 μm. Copyright © 2021 Springer Nature.

Photocrosslinking of HD-DA through acrylate polymerization under 365 nm UV light

We photo-crosslinked HD-DA resin mixed with photo-initiator, and 10 vol.% of the photo-initiator (Darocur 1173) used in the study was exceptionally high when compared to the 0.1–1.0 vol.% of the same photo-initiator typically used in previous studies to polymerize diacrylate monomers[29-31]. From the preliminary results shown in **Fig. 2.5**, however, we found that the pregel solution containing at least 10 vol.% of the photo-initiator should be irradiated with UV_{365} for ~2000 ms to clearly display the optical features showing the formation of the crosslinked structure. We also found that the pregel solution containing a lower vol.% photo-initiator and irradiated with UV_{365} for an extended time produced diffuse boundaries, while the pregel solution containing a higher vol.% photo-initiator produced overly polymerized structures, as determined microscopically. Based on these results, we optimized the volume ratio of the photo-initiator and the irradiation time to 10 vol.% and 2300 ms, respectively. We infer that such an excess amount of photo-initiator is necessary for the stabilization of the acrylic radical using diacetylene, which is known to significantly retard the acrylate polymerization in a conceptually similar manner to the atom transfer radical polymerization (ATRP)[32]. As shown in **Fig. 2.6**, diacetylene tethered with the electron-withdrawing group in our study slows down the acrylate polymerization by as much as 10^3 times, when compared to the polymerization of 1,6-hexanediol diacrylate. To compensate for the substantially lower rate of polymerization owing to the stabilization of active radicals, we used an excess amount of photo-initiator for the acrylate polymerization of HD-DA.

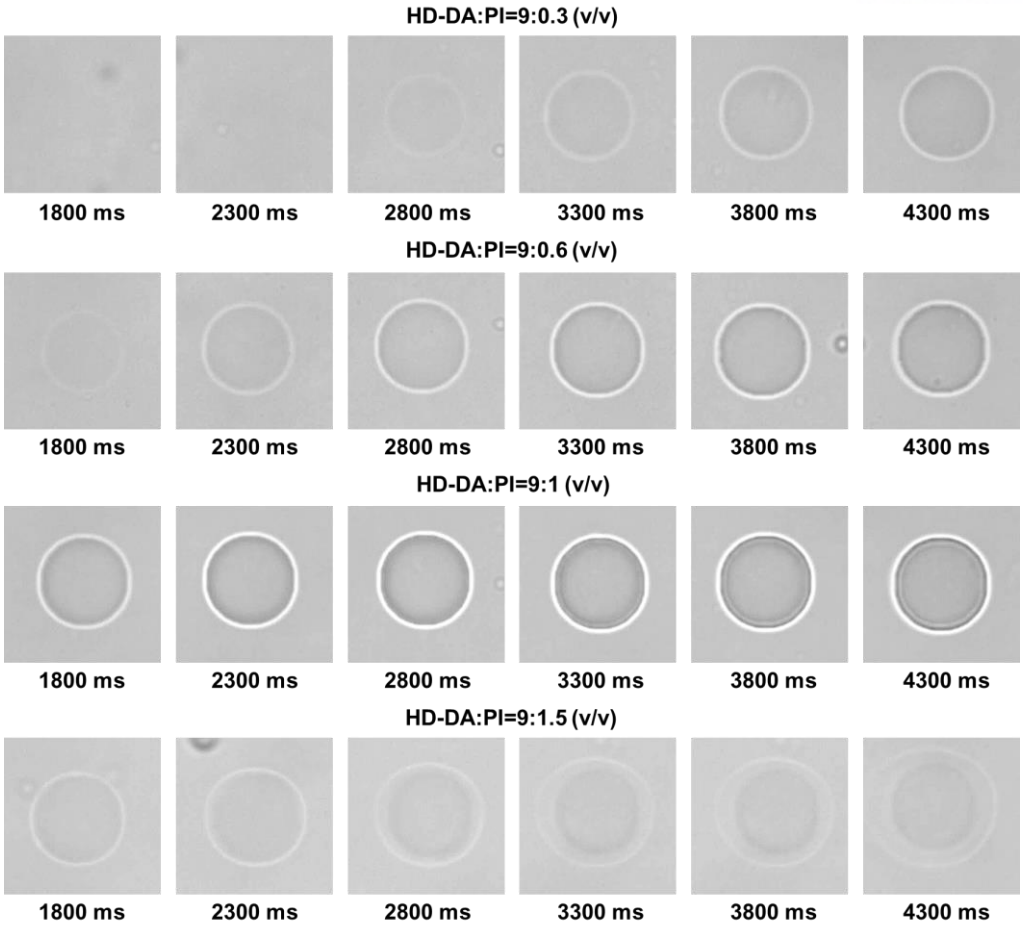

Fig. 2.5. Fabrication of crosslinked HD-DA microstructures according to the amount of photo-initiator (PI). Bright-field images of crosslinked HD-DA microstructures by changing 365 nm UV exposure time using HD-DA monomer solution with different amounts of PI. Scale bar is 50 μm. Copyright © 2021 Springer Nature.

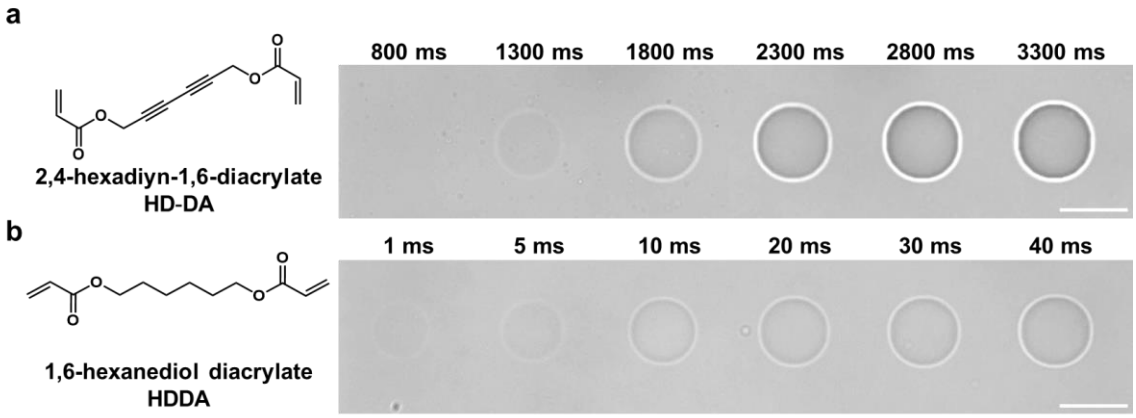

Fig. 2.6. Fabrication of 2,4-hexadiyn-1,6-diacrylate (HD-DA) and 1,6-hexanediol diacrylate (HDDA) organogel microstructures according to the 365 nm UV exposure. a,b, Bright-field microscope images of crosslinked HD-DA (a) and HDDA (b) microstructures according to the 365 nm UV irradiation time. Scale bar is 50 μm. Copyright © 2021 Springer Nature.

Analysis of photo-chemical reactions between acrylate and diacetylene group through ^{13}C NMR spectroscopy and DFT calculations

To investigate the photo-chemical reactions of monomers having mono-alkyne, diacetylene, and acrylate, we performed solution-state ^{13}C NMR analysis for the radical polymerization of monomers. For the solution-based reactions, we prepared four monomer solutions containing 66 mM of the photo-initiator and 433 mM of either 2-hydroxyethyl acrylate (HEA), propargyl acrylate (PA), 2,4-hexadiyn-1,6-diol (HD-DO), or 2,4-hexadiyn-1,6-diacrylate (HD-DA). We also prepared a pure liquid-phase 2,4-hexadiyn acrylate (HDA) monomer with 634 mM of the photo-initiator, which has the same composition used throughout the study, in addition, we used mono-acrylic HDA instead of di-acrylic HD-DA. Finally, we prepared a monomer solution containing HD-DA and a photo-initiator of the same molar concentration (433 mM). As shown in **Fig. 2.7**, the terminal mono-alkyne in PA participated considerably in the free-radical polymerization. For the solution-phase reactions of PA, the peaks corresponding to carbon atoms of acrylate (C5 and C6) and terminal mono-alkyne (C1) both reduced substantially with increasing doses of UV.

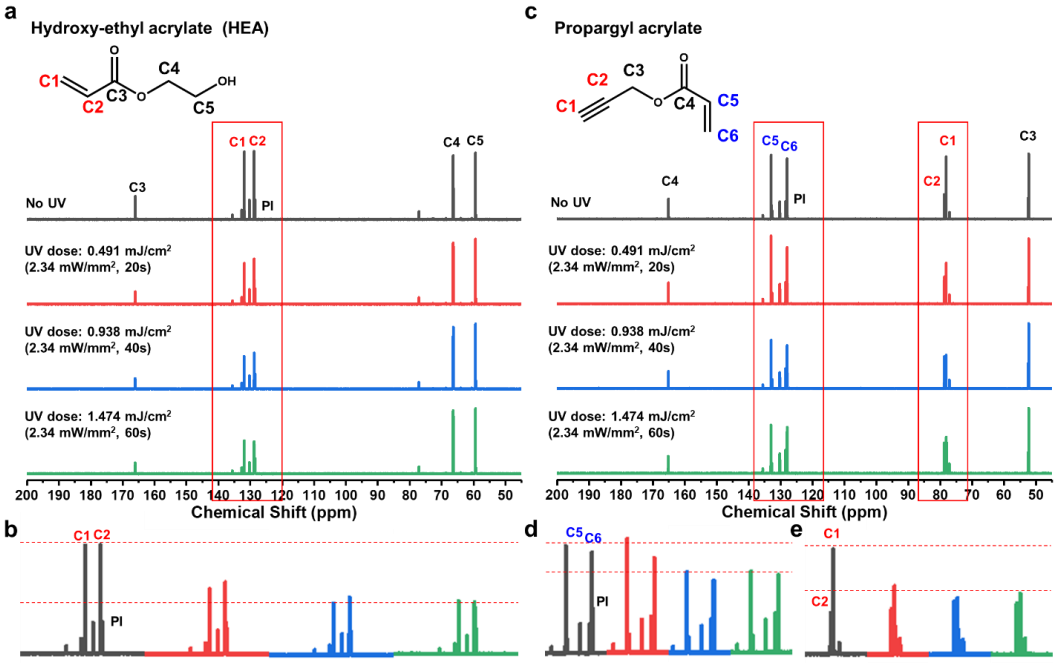

Fig. 2.7. Analysis of photo-chemical reactions of hydroxy-ethyl acrylate (HEA) and propargyl acrylate (PA) using ^{13}C NMR spectroscopy. a, ^{13}C NMR spectra of HEA and PI (1:0.15 molar ratio) in DMSO-d solvent according to the exposure time of 365 nm UV light. The molar concentration of HEA is 433 mM and that of PI is 65.6 mM. **b,** Comparison of the peaks corresponding to carbon atoms of acrylate according to the exposure time of 365 nm UV light. **c,** ^{13}C NMR spectra of PA and PI (1:0.15 molar ratio) in DMSO-d solvent according to the exposure time of 365 nm UV light. The molar concentration of PA is 433 mM and that of PI is 65.6 mM. **d,e,** Comparison of the peaks corresponding

to carbon atoms of acrylate (d) and diacetylene (e) according to the exposure time of 365 nm UV light. Copyright © 2021 Springer Nature.

With respect to the diacetylene, however, from the NMR analysis, it was concluded that under our experimental conditions, the diacetylene participation in radical polymerization is largely limited (**Figs. 2.8 and 2.9**). For both solution-phase reactions of HD-DO and HD-DA, peaks corresponding to carbon atoms of diacetylene (C1 and C2) remained unchanged, whereas those corresponding to carbon atoms of acrylate of HD-DA (C5 and C6) reduced significantly. In particular, for the solution-phase reaction of HD-DA, the dose of UV_{365} was further increased up to ~ 15 mJ/cm^2, above which the bulk polymer network was observed. Under this condition, we found that the conversion of acrylate reached ~40%, which was not fully consumed, but that of diacetylene was unnoticeable. Similar results to ours have been reported previously using the diacetylene end-tethered with aryl groups[32]. In those studies, the radical initiator initiated diacetylene polymerization and diacetylene did not form bonds with propagating acrylic radicals[32-34]. From the NMR analysis, we concluded that under our experimental conditions, the diacetylene participation in radical polymerization is largely limited.

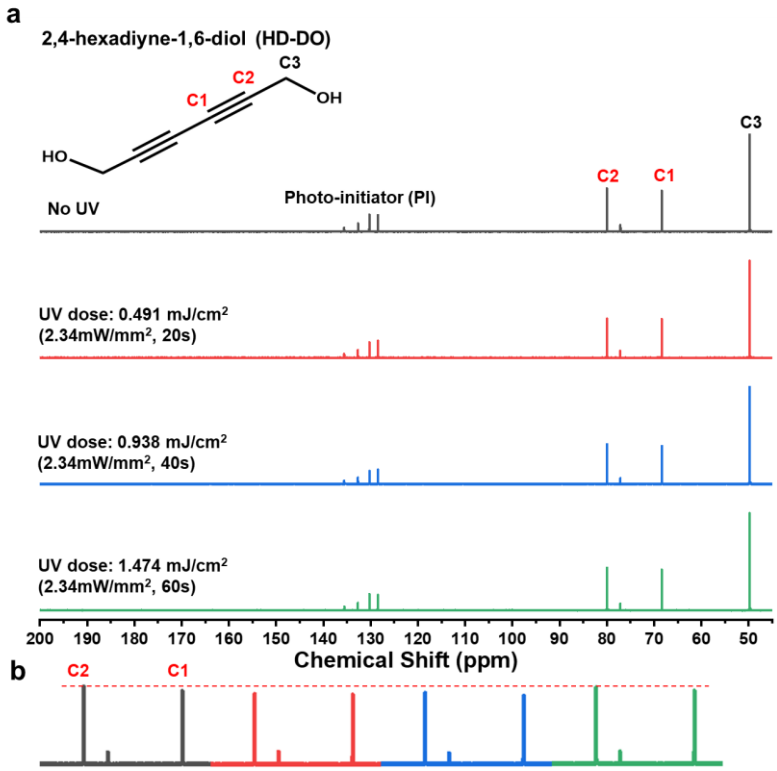

Fig. 2.8. Analysis of photo-chemical reactions of 2,4-hexadiyn-1,6-diol (HD-DO) using ^{13}C NMR spectroscopy. a, ^{13}C NMR spectra of HD-DO and PI (1:0.15 molar ratio) in DMSO-d solvent according to the exposure time of 365 nm UV light. The molar concentration of HD-DO is 433 mM and that of PI is 65.6 mM. **b,** Comparison of the peaks corresponding to carbon atoms of diacetylene according to the exposure time of 365 nm UV light. Copyright © 2021 Springer Nature.

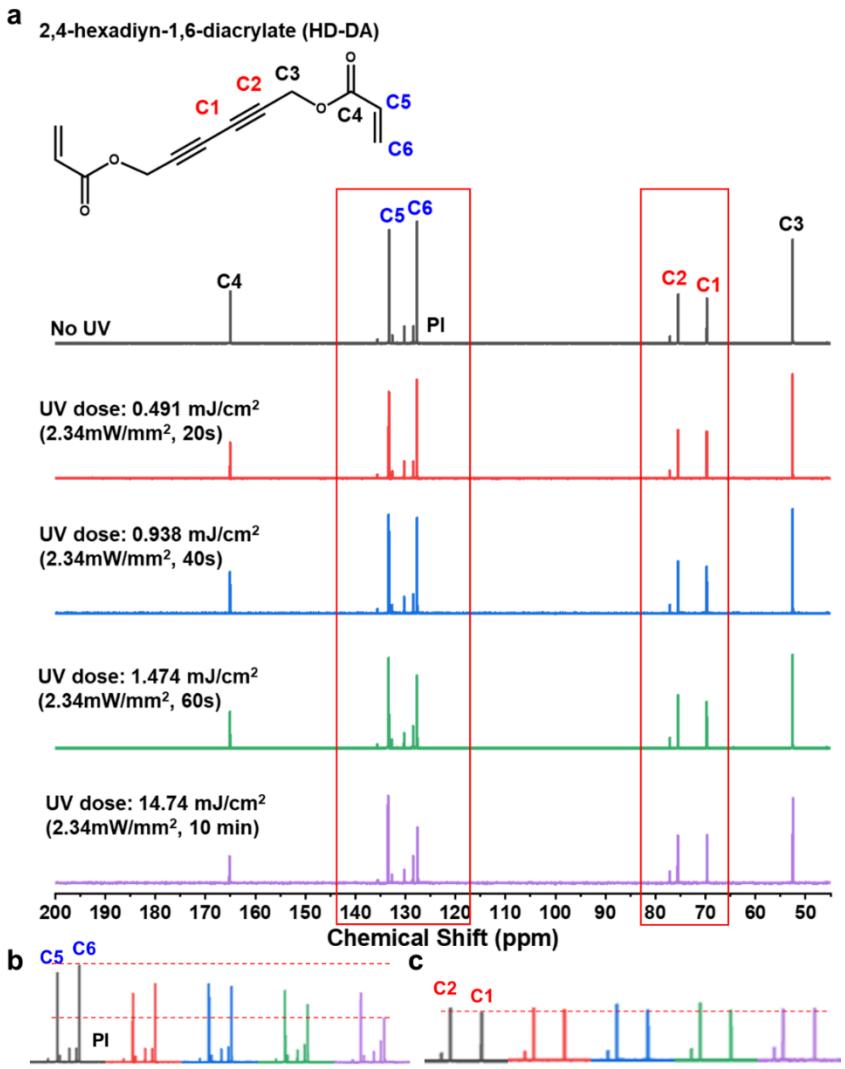

Fig. 2.9. Analysis of photo-chemical reactions of 2,4-hexadiyn-1,6-diacrylate (HD-DA) using ^{13}C NMR spectroscopy. a, ^{13}C NMR spectra of HD-DA and PI (1:0.15 molar ratio) in DMSO-d solvent according to the exposure time of 365 nm UV light. The molar concentration of HD-DA is 433 mM and that of PI is 65.6 mM. **b,c,** Comparison of the peaks corresponding to carbon atoms acrylate (b) and diacetylene (c) according to the exposure time of 365 nm UV light. Copyright © 2021 Springer Nature.

Next, similar to the pure liquid-phase HD-DA used to create organogels, as described in the manuscript, the pure liquid-phase HDA was irradiated with UV_{365} and was analyzed for the conversion (**Fig. 2.10**). Consistent with the solution-phase reactions of HD-DO and HD-DA, we found that the conversion of diacetylene (C2–C5) was negligible, whereas that of acrylate (C8–C9) was clearly observed. When we compared the NMR spectra of HEA, PA, HDA, and HD-DA irradiated with UV_{365}, we found that the acrylate conversion was lower when diacetylene was present. A previous study using electron spin resonance (ESR) spectroscopy, which allows for direct observation of transient propagating radicals, revealed that diacetylene stabilizes methacrylic radicals, thereby retarding

methacrylate polymerization[32]. We presumed that similar radical stabilization occurred in our cases as well. In addition, when an equimolar amount of photo-initiator to HD-DA was used in the solution-phase reaction of HD-DA, we observed a negligible conversion of acrylate as well as diacetylene (**Fig. 2.11**). Similar results of a significant reduction in monomer conversion with excessive radical initiators have been reported previously[35-36].

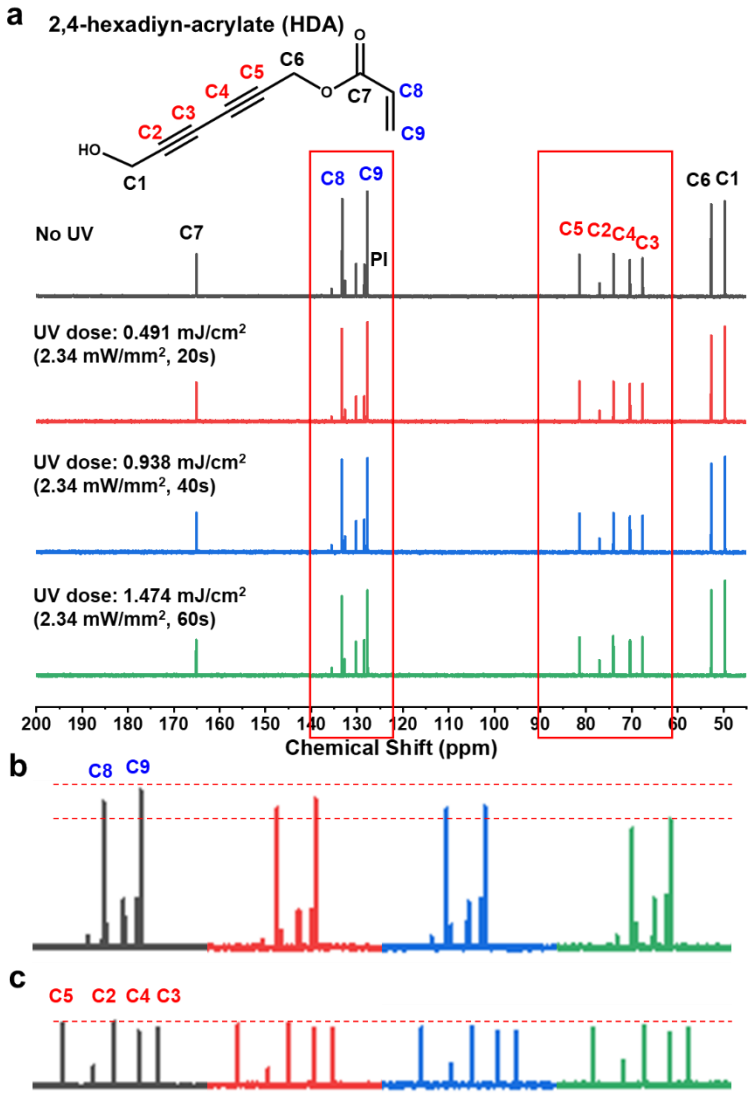

Fig. 2.10. Analysis of photo-chemical reactions of 2,4-hexadiyn-acrylate (HDA) using ^{13}C NMR spectroscopy. a,^{13}C NMR spectra of pure HDA with 634 mM of PI (1:0.15 molar ratio) according to the exposure time of 365 nm UV light. **b,c,** Comparison of the peaks corresponding to carbon atoms of acrylate (b) and diacetylene (c) according to the exposure time of 365 nm UV light. Copyright © 2021 Springer Nature.

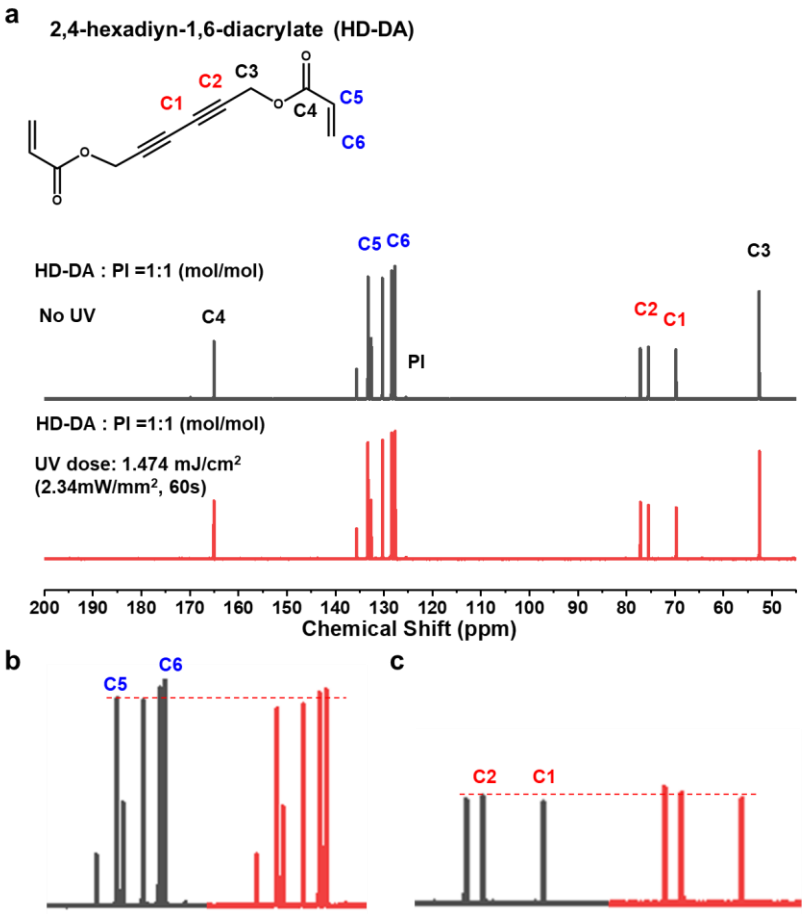

Fig. 2.11. Analysis of photo-chemical reactions of 2,4-hexadiyn-1,6-diacrylate (HD-DA) with equimolar PI using ^{13}C NMR spectroscopy. a, ^{13}C NMR spectra of HD-DA and PI (1: 1 molar ratio) in DMSO-d solvent according to the exposure time of 365 nm UV light. The molar concentration of HD-DA is 433 mM and that of PI is 433 mM. **b,c,** Comparison of the peaks corresponding to carbon atoms acrylate (b) and diacetylene (c) according to the exposure time of 365 nm UV light. Copyright © 2021 Springer Nature.

We next sought to understand why diacetylene was rarely converted using density functional theory (DFT) calculations. The reaction pathways of the acrylate radical with acrylate or diacetylene were investigated, which was the initial step of radical polymerization of HD-DA. We found that the reaction of the acrylate radical with the acrylate site showed much lower activation energy compared to the reactions with the diacetylene site (**Fig. 2.12**). Moreover, we calculated the relative reactivity of the acrylate and diacetylene sites with their activation energies through the Boltzmann distribution (R) (*i.e.*, the reaction rate constant). The equation *R* is as follows:

$$(4) R \approx e^{((-\Delta G_a)/(k_B T))}$$

where ΔG_a is the activation energy (*i.e.*, $\Delta G_a = \Delta G_{TS\ at\ 298.15\ K} - \Delta G_{reactant\ at\ 298.15\ K}$), k_B is the Boltzmann

constant (*i.e.*, 8.6173 × 10^{-5} eV/K), and *T* is the temperature (*i.e.*, 298.15 K). Through **Table 2.1**, we found that the reactivity of $acrylate_{radical}$+diacetylene was ~3×10^{-6} times less than that of $acrylate_{radical}$+acrylate.

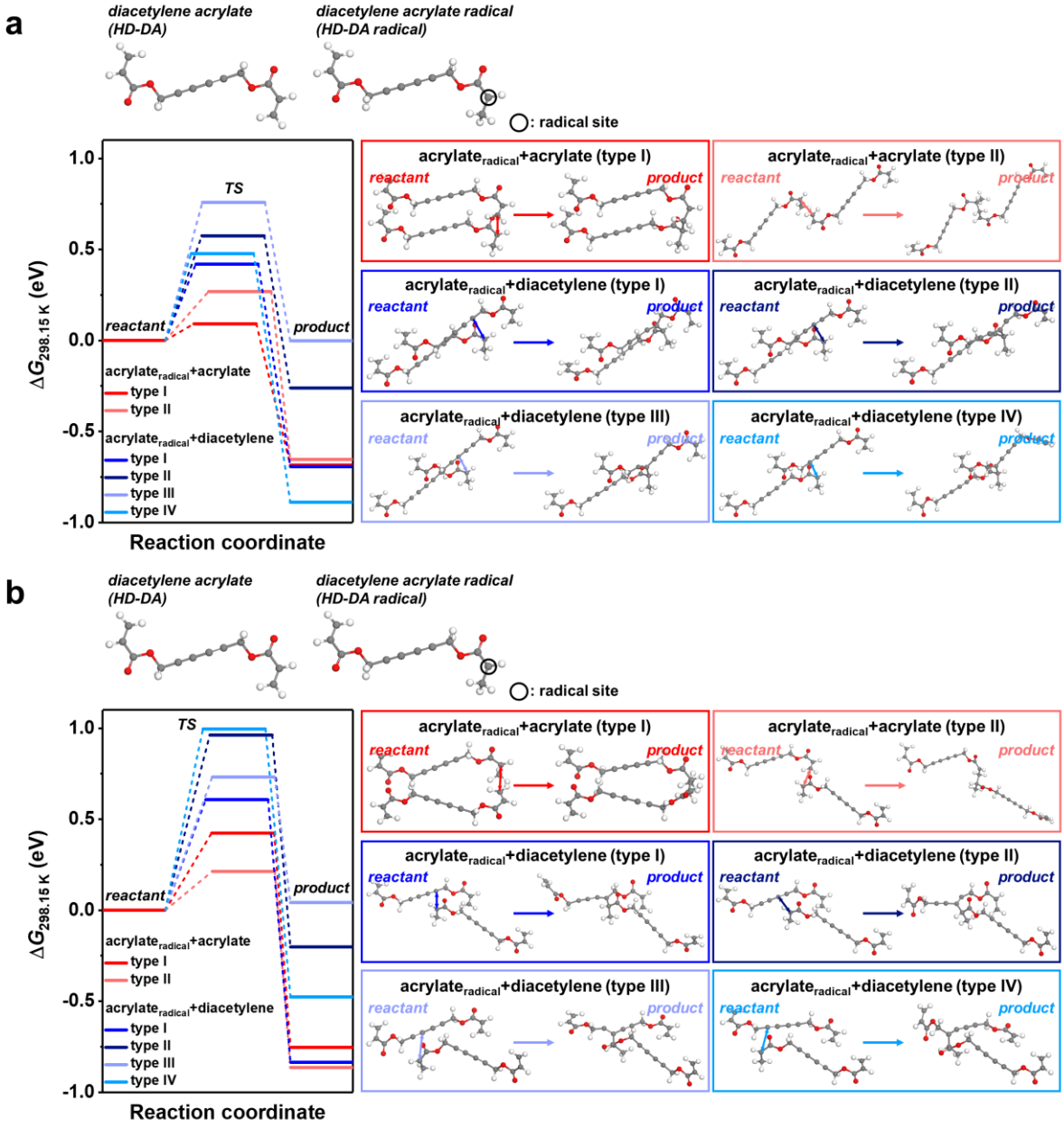

Fig. 2.12. Investigation of reaction pathways of polymerization of HD-DA. a,b, Reaction pathways of polymerization of HD-DA molecules containing acrylate radical and acrylate according to the reaction sites (*i.e.*, acrylate site and four sites of diacetylene) and the directions of reaction (*i.e.*, perpendicular (a) and side (b) directions to the principle axis of HD-DA monomer). Relative Gibbs free energies (Δ*G*) were calculated at 1 atm and 298.15 K. Copyright © 2021 Springer Nature.

Table 2.1. Activation energy and reaction rate constant (*R*) of acrylate with acrylate radical and diacetylene with acrylate radical. Note that the activation energy of each reaction is the case of the lowest activation energy in Fig. 2.12. The ratio of rate constant between two competing reactions, R_2/R_1, where the subscripts 1 and 2 indicate $acrylate_{radical}$ + acrylate reaction and $acrylate_{radical}$ + diacetylene reaction, respectively. Copyright © 2021 Springer Nature.

Reaction (HD-DA)	Activation energy (eV)	Reaction rate constant (*R*)	R_2/R_1
1. $acrylate_{radical}$ + acrylate	0.0908	2.919×10^{-2}	2.789×10^{-6}
2. $acrylate_{radical}$ + diacetylene	0.4194	8.141×10^{-8}	

To better understand the substantially lower reactivity of the diacetylene site, we estimated the partial atomic charges of carbon atoms of HD-DA using Mulliken charge analysis. The acrylate site (C6 atom of vinyl group in **Fig. 2.13** = -0.178 *e*) showed greater negative charge compared to the acetylene site (C1 and C2 atoms of acetylene group in **Fig. 2.13** = +0.119 *e* and +0.006 *e*). Because radical species react more favorably with the carbon atom possessing a greater negative charge[37], the diacetylene is much less likely to react with acrylate radical species. Therefore, the acrylate radical polymerization of HD-DA occurs at the acrylate site dominantly, which is consistent with the results of our NMR measurements. This reactivity difference originates from the atomic charges of carbon atoms in the acrylate and diacetylene sites of HD-DA.

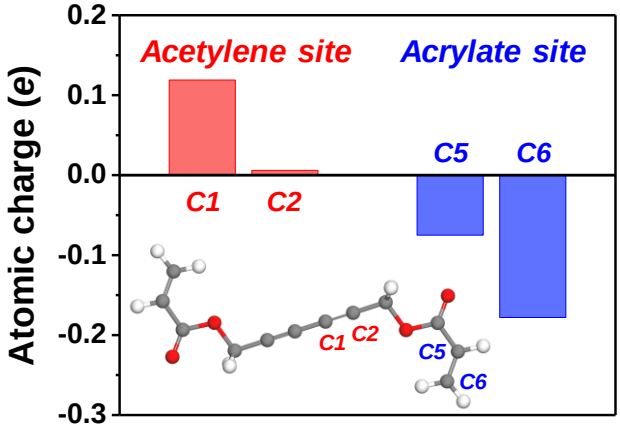

Fig. 2.13. Atomic charges of carbon atoms of acetylene and acrylate sites in HD-DA molecule. Copyright © 2021 Springer Nature.

Based on the ^{13}C NMR analysis and DFT calculations, we confirmed that diacetylene groups of HD-DA rarely participated in the free-radical polymerization of acrylate as similarly reported in previous studies[32-34].

Further irradiation of 254 nm UV light initiated 1,4-addition photo-polymerization of diacetylenes and created π-conjugated PDA backbones inside the crosslinked network[38-40]. Using all-atom molecular dynamics (AAMD) simulations, we found that the inter-atomic distance between carbon atoms of adjacent diacetylene groups in the crosslinked network became sufficiently close enough (~ 3.9 Å) to proceed the 1,4-addition polymerization of diacetylene[41] (**Fig. 2.14**), suggesting that the structural characteristics of HD-DA have allowed PDA to be macroscopically photo-patterned in a liquid-phase without having to form the self-assembly structure as required in previous studies[42-44].

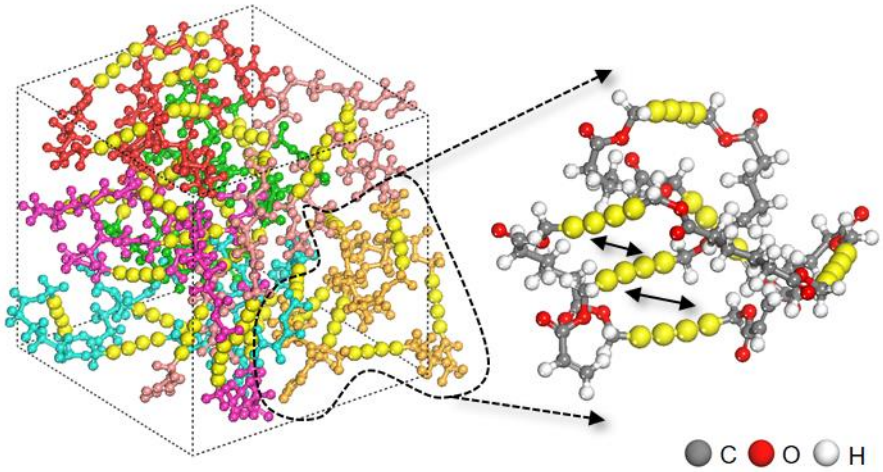

Fig. 2.14. Structure of conjugated PDA. Molecular structures estimated from the AAMD simulation for HD-DA monomers proceeded with the acrylic polymerization. The four carbon atoms in diacetylene were in yellow, and the arrows indicate the inter-atomic distance between C(1) and C(4) of the adjacent diacetylene. Copyright © 2021 Springer Nature.

Solvent effects on the chain conformation and electronic properties of PDA structure

Volume expansion ratio – defined as the volume ratio of PDA organogels in the equilibrium swelling to as-prepared state – decreased as the polarity or hydrogen bond ability (α) of the immersion solvent increased. For example, when we exchanged the solvent inside the PDMS channel from aprotic acetonitrile (ACN) to protic MeOH, the volume of PDA organogels crosslinked without dithering patterns decreased to 28 %. Interestingly, when irradiated by the peak wavelength of 488 nm, PDA organogels contract in solvents with higher α such as MeOH and water emitted strong fluorescence signals that were enhanced near the center and circumferential areas of the disk (**Figs. 2.15-2.17**). Such enhanced fluorescence signals were reversibly switched off in aprotic solvents such as dimethylsulfoxide (DMSO) and ACN.

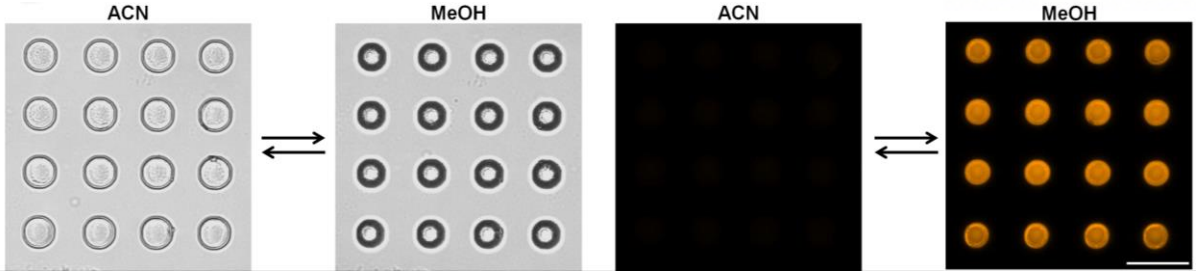

Fig. 2.15. Bright-field (left) and fluorescence (right) microscopy images show reversible volume and fluorescence intensity change of disk-shaped PDA organogel microstructure crosslinked without dithering pattern upon exposure to ACN and MeOH. Scale bar is 50 μm. Copyright © 2021 Springer Nature.

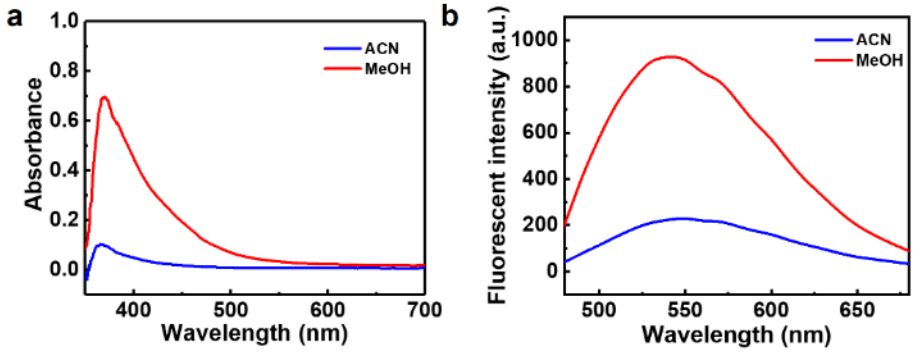

Fig. 2.16. Characterization of conjugated PDA organogel upon exposure to ACN and MeOH. a,b, UV-Vis spectra (a) and fluorescence emission spectra (b) of PDA organogels immersed in ACN and MeOH. Copyright © 2021 Springer Nature.

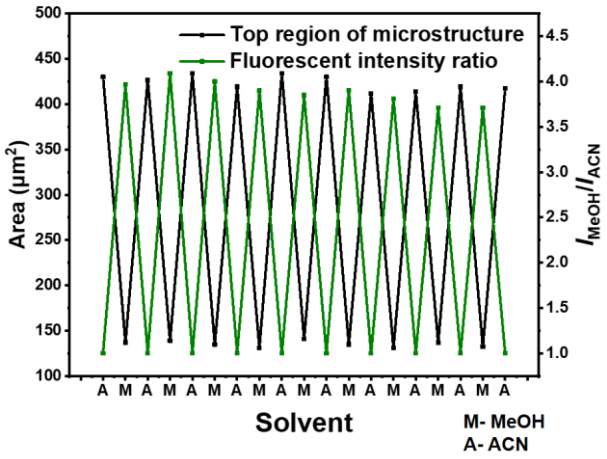

Fig. 2.17. Reversible fluorescence emission of the conjugated PDA organogel microstructure upon a solvent exchange. Comparison of an area of top region of PDA microstructure and their fluorescence intensity according to the types of immersion solvents. The fluorescence intensity ratio (I_{MeOH}/I_{ACN}) is inversely proportional to the area of top region in the PDA microstructure. Copyright © 2021 Springer Nature.

Fluorescence signals of PDA microstructure in various solvents

The conjugated PDA organogel microstructure in the PDMS microfluidic device was exposed to various aprotic and protic solvents with different hydrogen bond abilities (α) (**Table 2.2**). As shown in **Fig. 2.18a**, the PDA microstructures maintained their shape in dimethyl sulfoxide (DMSO) and acetonitrile (ACN), and they exhibited different anisotropic contraction in protic solvents such as polyethylene glycol 200 (PEG 200), methanol (MeOH), and water. In addition, the PDA microstructures exhibited fluorescence transition as well as gel contraction upon exposure to protic solvents (**Fig. 2.18b**). The microstructure exhibited the highest fluorescence in water with the largest gel contraction and showed lower fluorescence as the contraction decreased upon exposure to methanol and PEG 200. Confocal microscopy images of the PDA microstructure in aprotic and protic solvents were obtained, and three-dimensional images were constructed to calculate the volume change (**Fig. 2.18c**). The volume of the PDA microstructure was 50880.8 μm^3 in DMSO ($\alpha = 0$) and 42746.2 μm^3 in ACN ($\alpha = 0.19$). The volume changed to 20268.5 μm^3 in PEG 200 ($\alpha = 0.46$) and 12085.8 μm^3 in MeOH ($\alpha = 0.93$), and the largest volume change of 10019.9 μm^3 (82% of DMSO) occurred when exposed to water ($\alpha = 1.17$) (**Fig. 2.18e**). Confocal orthogonal microscopy images of **Fig. 2.18d** supported that the anisotropic gel contraction of the PDA microstructure was determined from the α value of the immersion solvents. As shown in **Fig. 2.18f**, exposure of the immersion solvent with the higher α generated a greater fluorescence transition of the PDA organogel due to the larger volume contraction. When protic solvents with higher α values, such as MeOH ($\alpha = 0.93$) and water ($\alpha = 1.17$) were introduced to the PDA microstructure, higher fluorescence emissions were observed. The fluorescence emission of the PDA microstructure increased by 3.92 times upon solvent exchange from ACN ($\alpha = 0.19$) to water ($\alpha = 1.17$), while the fluorescence emission change of the microstructures was rarely observed in aprotic solvents with low α values. The α value of the immersion solvent was directly related to gel contraction, fluorescence transition, and resultant volume of PDA organogel.

Table 2.2. Kamlet-Taft solvatochromism parameter. Copyright © 2021 Springer Nature.

Solvent	Hydrogen donor (α)	Hydrogen acceptor (β)	Dipolarity/ polarizability (π*)
Water	1.17	0.18	1.09
Methanol	0.93	0.62	0.6
n-butanol	0.79	0.88	0.47
PEG 200	0.46	0.65	0.915
Acetonitrile	0.19	0.31	0.75
DMSO	0	0.76	1

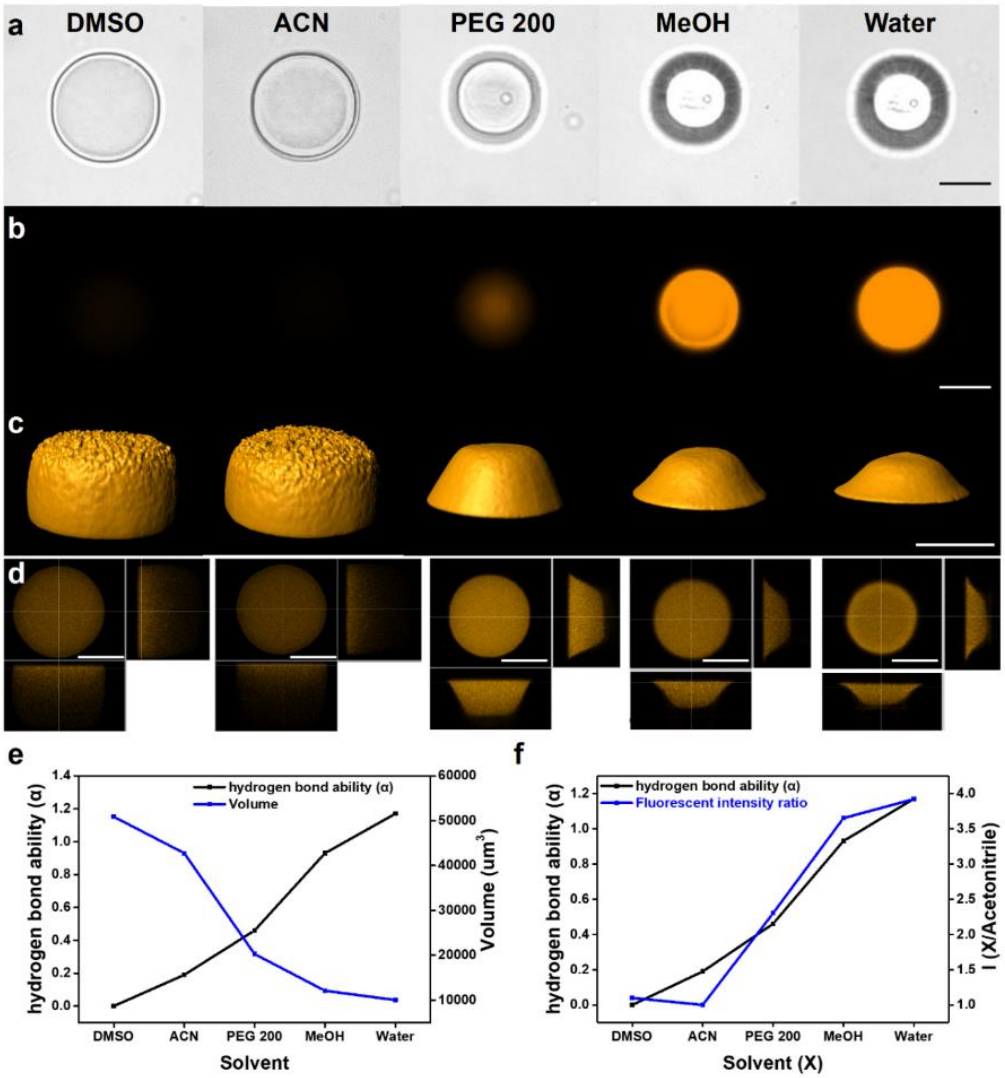

Fig. 2.18. Fluorescence emission change of conjugated PDA organogel microstructure upon the contraction rate. a-d, Bright-field (a), fluorescence (b), 3D reconstructed confocal (c), and orthogonal confocal (d) microscopy images of the conjugated PDA organogel microstructure upon an exposure to DMSO, ACN, PEG 200, MeOH and water. **e,** Volume change of conjugated PDA organogel microstructure according to hydrogen bond ability (α) of immersion solvents. **f,** Fluorescence transition of conjugated PDA organogel microstructure plotted by fluorescent intensity ratio (I_X/I_{ACN}) according to hydrogen bond ability (α) of immersion solvents. Scale bar is 25 μm. Copyright © 2021 Springer Nature.

Using multi-scale simulations, we infer such reversible fluorescence signals are due to the reversible twisting of conjugated PDA backbones[45] and the densification of the gel network occurred during contraction in MeOH. To examine the effects of PDA backbone twisting, we conducted coarse-grained (CG) and AAMD simulations. We constructed the ring-shape crosslinked PDA network model by complete conversions of diacetylene groups and diacrylate groups of 600 HD-DA monomers (**Fig. 2.19**). When the solvent to swell the network model was changed from ACN to MeOH, the radius of gyration

of PDA chains and thus, the void volume reduced (**Fig. 2.20**), resulting in the volume of the network model to contract to ~ 55 % of that in ACN (**Fig. 2.21**).

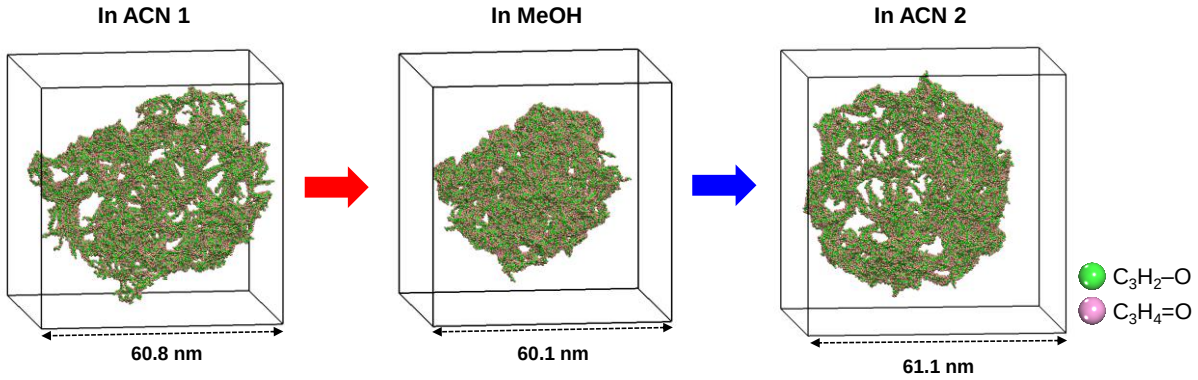

Fig. 2.19. CGMD simulation for contraction and expansion of PDA organogel structure. Final configurations of PDA organogel structure in ACN and MeOH solvents obtained from CGMD simulation. Solvent beads are omitted for clarity. Copyright © 2021 Springer Nature.

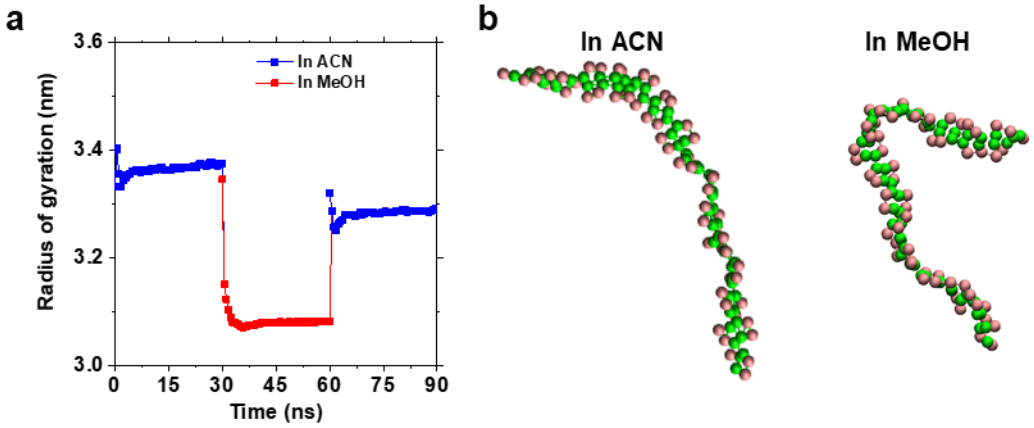

Fig. 2.20. Radius of gyration and molecular structure of PDA in solvent. a, Radius of gyration of PDA in ACN and MeOH solvents obtained from CGMD simulation. **b,** Representative molecular structure of PDA in ACN and MeOH. Structure of PDA was shown stretched and folded in ACN and MeOH, respectively. Green and pink colored beads represent C_3H_2–O and C_3H_4=O group. Copyright © 2021 Springer Nature.

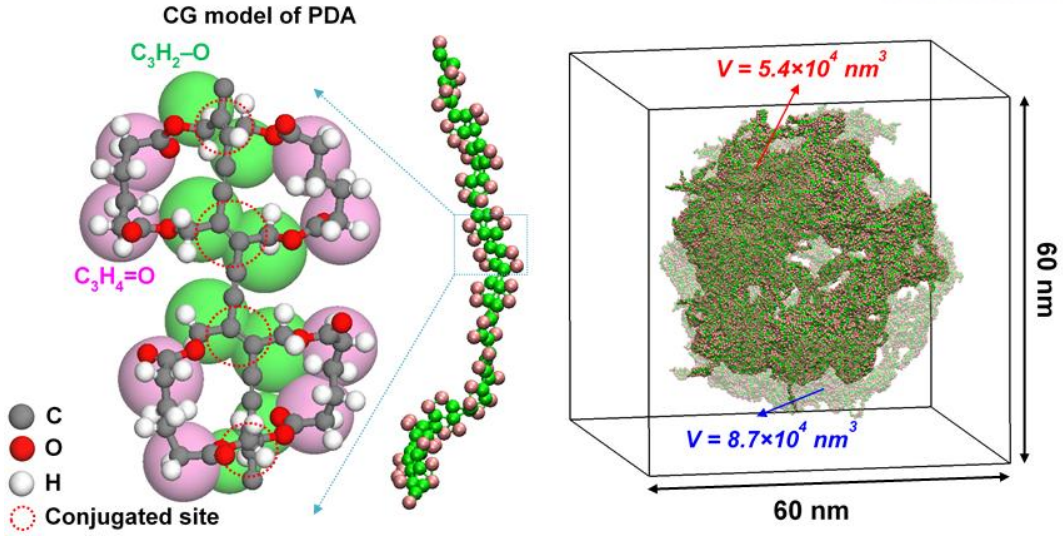

Fig. 2.21. Coarse-grained (CG) model of PDA (left) and configuration of PDA organogel structure in ACN/MeOH solvents (right). Light blue dashed box shows the CG model, composed of 30 diacetylenes. Configuration of PDA organogel in ACN (transparent color) and MeOH (solid color) are shown. Solvents are omitted for clarity. *V* is volume of organogel. Copyright © 2021 Springer Nature.

Solvent-induced conformational changes of the PDA chain were studied using the MD simulation and density functional theory (DFT) calculation. When ACN was replaced by MeOH, PDA chains twisted by decreasing the torsional angle of conjugated backbones (**Figs. 2.22 a and b**), and the twisting of *p*-orbitals increased the relative energy of distorted backbones (**Fig. 2.22c**). A decrease of the torsional angle by the solvent exchange to MeOH increased the HOMO-LUMO gap of conjugated backbones by 0.376 eV (**Fig. 2.23**), which was consistent with the previous study[46].

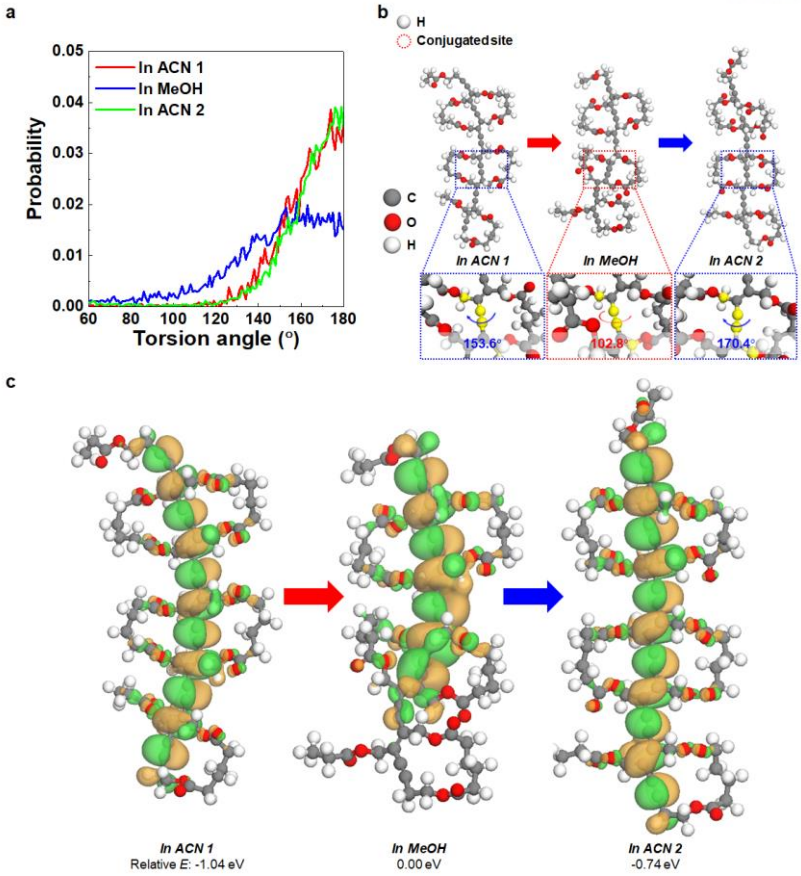

Fig. 2.22. a, Probability distribution of torsion angle of PDA backbone in ACN/MeOH. Solvents were changed sequentially from ACN (ACN 1) to MeOH and back to ACN (ACN 2). **b,** AAMD simulation models of molecular structures of PDA monomer in ACN/MeOH solvents. Blue and red dashed boxes show the torsion angle of PDA backbone. Torsion angle is measured with yellow highlighted carbon atoms. **c,** HOMO isosurfaces and relative energies of PDA molecules from Fig. 2.22b. Relative energies are calculated based on the MeOH case. The green and orange colored isosurfaces represent the positive and negative values of *p*-orbital phase, respectively. Copyright © 2021 Springer Nature.

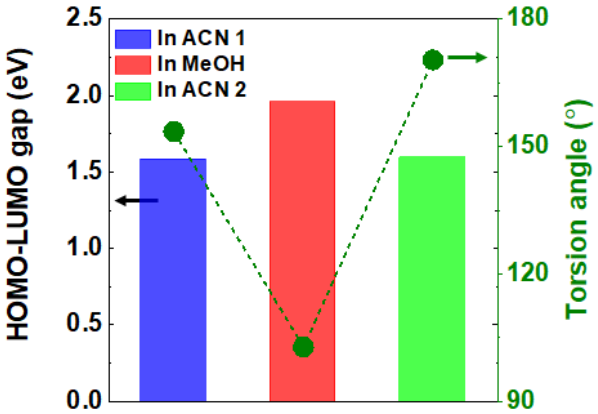

Fig. 2.23. HOMO-LUMO gap and torsion angle of PDA molecule from **Fig. 2.22b** to investigate *p*-orbital twist by solvent exchange. Copyright © 2021 Springer Nature.

Additionally, both simulations and experiments showed similar trends in the shifting of the peak frequency of the Raman scattering. Confocal Raman spectra showed that the triple bonds at 2247.17 cm^{-1} shifted to the higher frequency (2257.04 cm^{-1}), and the double bonds at 1727.83 cm^{-1} moved to the lower frequency (1720.54 cm^{-1}) upon contractions by water (**Fig. 2.24**). Moreover, we calculated the Raman spectra using the part of the PDA structure obtained from the MD simulation according to the two types of solvent (**Fig. 2.25**). For the PDA structure affected by the MeOH solvent, the Raman frequencies corresponding to the vibration modes of double and triple bonded carbons decreased (shifted to the left in **Fig. 2.25a**) and increased (shifted to the right in **Fig. 2.25b**), respectively, compared to the case of ACN solvent. This is consistent with the experimental observations. In general, considering the effect of torsion only, the bond lengths of double- and triple-bonded carbons are decreased, so that the frequencies are increased[46]. However, in our study, the frequencies of double bonded carbon decreased due to the stretch of bond length (~1.380 $Å_{double}$ bond I and ~1.382 $Å_{double}$ bond II in the MeOH solvent, ~1.340 $Å_{double}$ bond I and ~1.358 $Å_{double}$ bond II in the ACN solvent). We believe that this can be attributed to the hydrogen bonding between the oxygen of the acrylate group, which is near the double bond, and MeOH. To confirm this, the Raman frequency of the model system used in this study was also calculated according to the torsion angle (torsion angle: 180° → 90° in **Fig. 2.26**). The frequencies of double and triple bonds both increased and shifted to the right as the torsion angle decreased, which showed the same trend as the previous report[46]. Moreover, the bond lengths of double and triple bonds were decreased (180° torsion angle: 1.381 $Å_{double\ bond\ I}$, 1.381 $Å_{double\ bond\ II}$, and 1.232 $Å_{triple\ bond}$, 90° torsion angle: 1.373 $Å_{double\ bond\ II}$, 1.374 $Å_{double\ bond\ II}$, and ~1.228 $Å_{triple\ bond}$). Therefore, we can conclude that the solvent and torsion effects are dominant in the frequencies of double- and triple-bonded carbons, respectively. Moreover, we predict that the torsion effect of the triple bond of the π-conjugated backbone caused by the protic solvent, such as MeOH, affects the *p*-orbital twist of PDA.

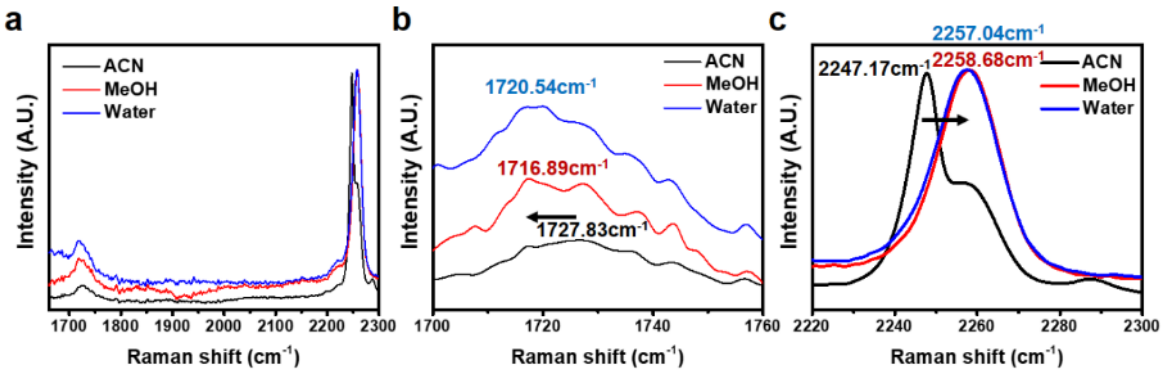

Fig. 2.24. Raman spectroscopy of PDA organogel microstructure upon a solvent exchange. a-c, Full spectral range (a) and magnified regions (b and c) of Raman shift in PDA organogel microstructure.

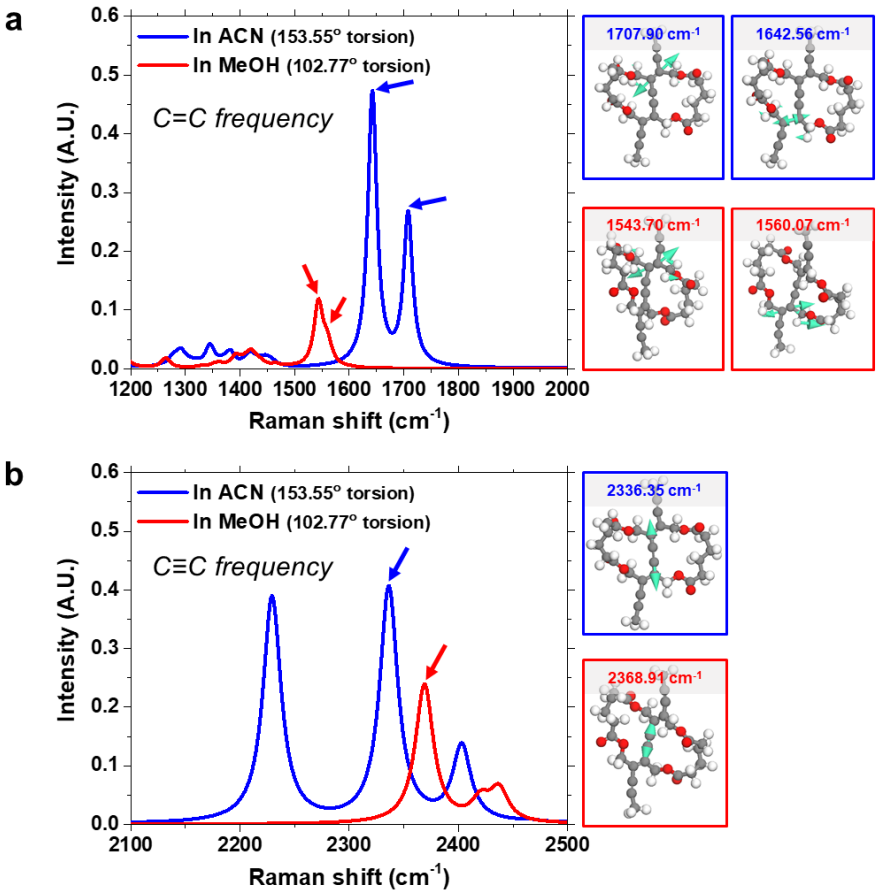

Fig. 2.25. Raman spectra of PDA structure. a,b, Calculated results of Raman spectra of PDA structures for C=C (a) and C≡C (b) frequency regions. The PDA structures are obtained from MD simulation under two types of solvent (*i.e.*, ACN and MeOH). The Raman spectra are calculated under the condition of 298.15 K and 785 nm incident light with Lorentzian broadening (20.0 cm^{-1}). Note that blue and red colored arrows indicate the frequencies of Raman active vibrational modes in the crosslinked PDA ring structure. All Raman active vibrational modes are stretching modes (right hand side of Raman spectra). Copyright © 2021 Springer Nature.

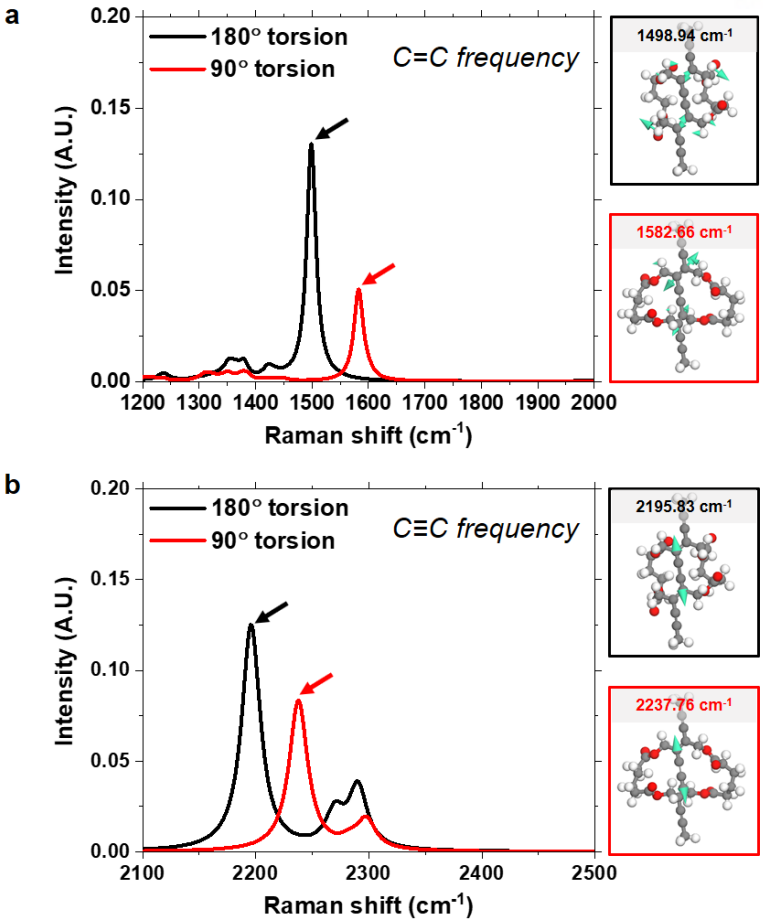

Fig. 2.26. Effect of torsion angle on Raman spectra of PDA. a,b, Calculated results of Raman spectra of PDA structures for C=C (a) and C≡C (b) frequency regions. The PDA structures are constructed according to the two types of torsion angle (*i.e.*, 180º and 90º). The Raman spectra are calculated under the condition of 298.15 K and 785 nm incident light with Lorentzian broadening (20 cm^{-1}). Note that black and red colored arrows indicate the frequencies of Raman active vibrational modes in the crosslinked PDA ring structure. All Raman active vibrational modes are stretching modes (right hand side of Raman spectra). Copyright © 2021 Springer Nature.

When a network model was constructed with fewer acrylate conversion to contract more in MeOH, we observed that the torsional angle further decreased (**Fig. 2.27a**) and the HOMO-LUMO gap increased more (**Fig. 2.27b**). Consistent with simulation results, PDA organogels that were made to contract less in MeOH showed substantially lower fluorescence emission as normalized to PDA density (**Fig. 2.28**). These multiscale molecular simulation results demonstrate that twisting of the conjugated PDA backbone from solvent-induced contraction contributes to the enhanced fluorescence intensity.

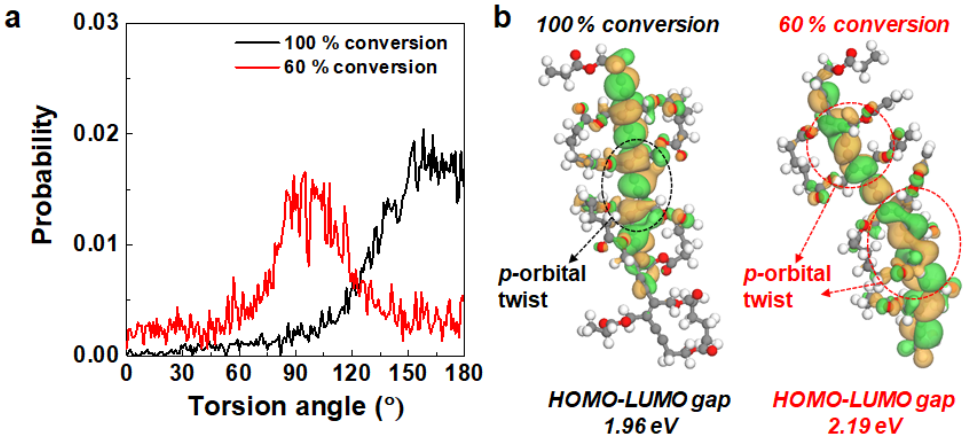

Fig. 2.27. a, Probability distribution of torsion angle of twisted PDA backbone with different number of acrylate conversion sites. **b,** HOMO isosurfaces and HOMO-LUMO gaps of PDA molecules with low (left) and high (right) volume contraction rate. Isosurface value of HOMO is 0.007 e/Å^3. The green and orange colored isosurfaces represent the positive and negative values of p-orbital phase, respectively. Copyright © 2021 Springer Nature.

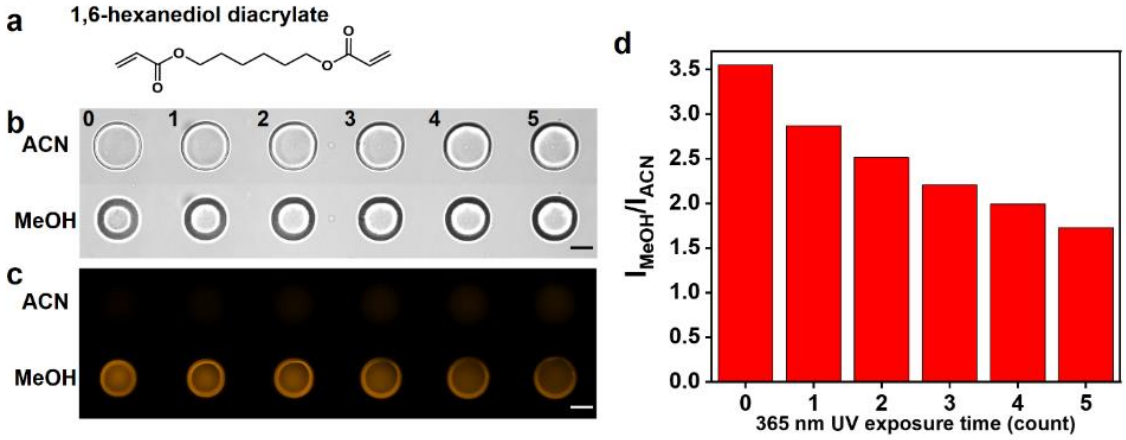

Fig. 2.28. Volume and fluorescence emission intensity change of the conjugated PDA organogel microstructures with different stiffness. PDA organogels were further stiffened with interpenetrating network using 1,6-hexanediol diacrylate. **a,** Chemical structure of 1,6-hexanediol diacrylate. **b,c,** Bright-field (b) and fluorescence (c) microscopy images of six PDA/1,6-hexanediol diacrylate microstructures with different crosslinking density upon a solvent exchange. **d,** Fluorescence intensity ratio (I_{MeOH}/I_{ACN}) of conjugated organogel microstructures upon solvent exchange according to a crosslinking density of 1,6-hexanediol diacrylate controlled by the exposure number of 365 nm UV light. Scale bar is 25 μm. Copyright © 2021 Springer Nature.

Holographic signals displayed by PDA organogels and estimated from a series of numerical studies

We then investigated how network densification combined with chain twisting, both of which resulted from contraction in MeOH, produced the characteristic fluorescence emission displayed by PDA organogels crosslinked without dithering patterns. When the organogels contracted anisotropically in MeOH, in regions devoid of thermal equilibrium formed elastic strain energy. We used finite element analysis (FEA) to estimate the strain field of the surface-attached organogel contracted in MeOH. The shape predicted for the contracted model structure agreed well with observations from laser scanning confocal microscopy (**Fig. 2.29**).

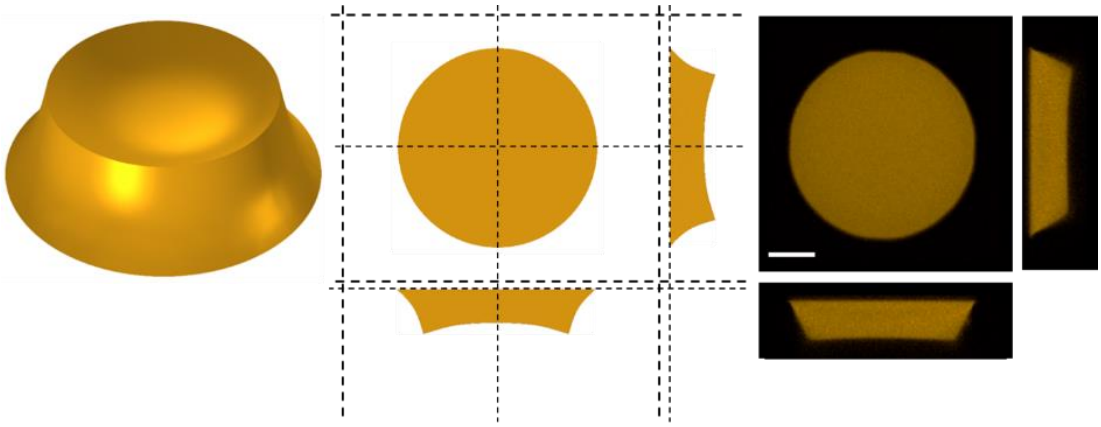

Fig. 2.29. Comparison of contraction simulation result with confocal microscopy image. 3D simulation result (left) shows predicted deformed shape, and each cut plane of simulation result (middle) is matched to confocal microscopy image of contracted gel in MeOH (right). Scale bar is 25um.

Because PDA organogels consist of stiff conjugated backbones and flexible alkyl chains with similar mass fractions, the elastic strain energy generated within the contracted model structure is mainly associated with the twisting of the stiff backbones, which would enhance fluorescence emission. Therefore, we estimated that the local enhancement of fluorescence emission in the contracted model structure would roughly scale with the summation of network densification and local elastic strain energy, $[(1+\varepsilon_{vol}(x,y,z))^{-1}-1]_n+\beta\cdot U_n(x,y,z)$, where ε_{vol} is the volumetric strain, U is the elastic strain energy density calculated from the contracted model structure, and β is the adjustable weight factor. Subscript n indicates that the corresponding value is normalized by its maximum of the model structure. In our microscope, because the depth of field is greater than the entire height of the contracted PDA organogels, the fluorescence expression calculated at each surface-parallel z-plane is integrated along the thickness direction. The patterns seen in the integrated fluorescence expression (**Fig. 2.30b**) resembled those in the microscopy images (**Fig. 2.30a**). We attribute the enhanced fluorescence near the center to elastic strain energy while those in the circumferential areas is due to network densification.

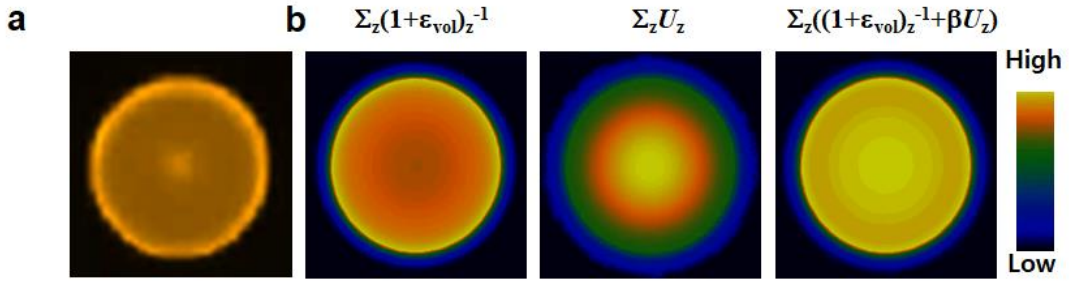

Fig. 2.30. a,b, Organogel crosslinked without dithering pattern into a disk shape and shrunk in MeOH was (a) imaged using epi-fluorescence microscope and (b) simulated using FEA to predict fluorescence expressions resulting from network densification (left), torsional angle reduction (middle), and their combination (right, $\beta = 2$). Copyright © 2021 Springer Nature.

To exploit locally non-uniform fluorescence emission from anisotropic contraction, we created PDA organogels two-dimensionally patterned with varying degrees of volume contraction, expecting more complex fluorescence patterns to emerge. Using 365nm UV light patterned with various dithering shapes such as hexagon, square, rhombus, horizontal, and vertical lines, we created 2D arrays of highly crosslinked vertical *rods* (~ 1 μm diameter) embedded within a lightly crosslinked disk-shape *matrix* (**Fig. 2.31**).

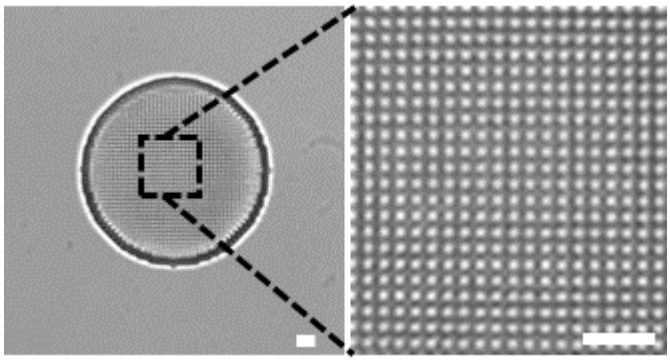

Fig. 2.31. Bright-field microscopy images of PDA organogel microstructure (left) composed of 2D arrays of highly crosslinked rods in a square dithering pattern (right, light areas) embedded in lightly crosslinked matrix (right, dark areas). Copyright © 2021 Springer Nature.

In ACN, the volume expansion ratio of rods and matrix were nearly identical to be one and, therefore, organogels maintained their as-prepared disk shape. Because the refractive index of rods (1.504) was greater than the matrix (1.437) (**Fig. 2.32** and see Methods for refractive index measurement), patterned PDA organogels in ACN exhibit 2D optical heterogeneity where the refractive index alternates along surface-parallel directions but is conserved along the thickness direction (**Fig. 2.33**). Therefore, the organogels act as volume phase holographic gratings (VPHG) that display strong iridescent colors via diffraction (**Figs. 2.34-2.36**).

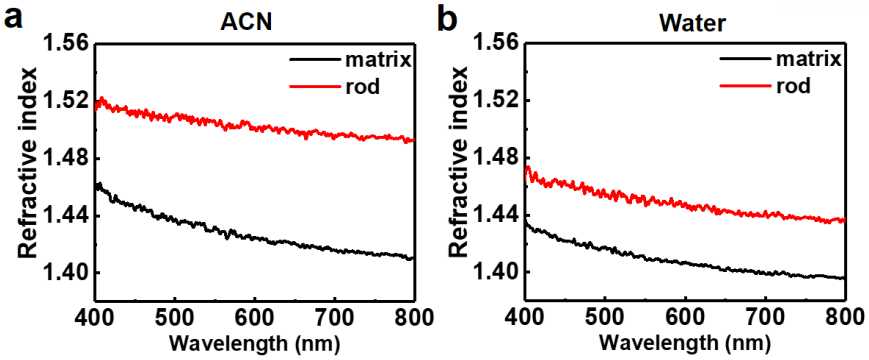

Fig. 2.32. Refractive indices change of rod and matrix in conjugated PDA organogel microstructure upon solvent exchange. a,b, Refractive indices of rod and matrix when exposed to ACN (a) and water (b). Copyright © 2021 Springer Nature.

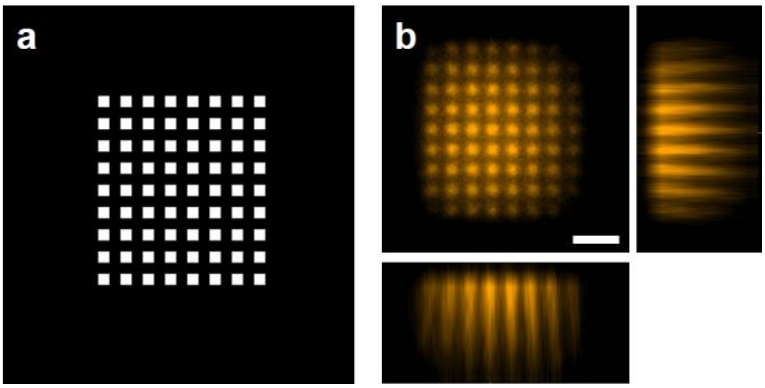

Fig. 2.33. Confocal microscopy image of rod and matrix in conjugated PDA organogel microstructure. a, Square–patterned dithering mask composed of 72 white pixels. **b,** Orthogonal confocal microscopy image of the square–patterned PDA organogel microstructure (Carl zeiss LSM 780, 63×). Scale bar is 10 μm. Copyright © 2021 Springer Nature.

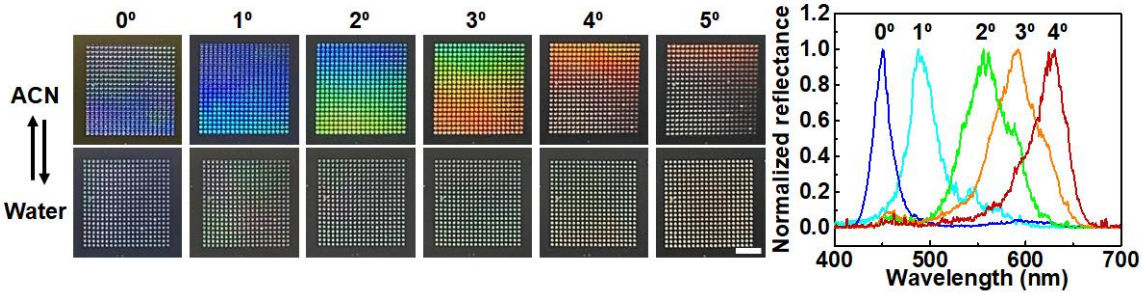

Fig. 2.34. Structural color of the patterned PDA organogel. Structural color of the patterned PDA organogel array was changed as the viewing angle is varied (from left to right, left panel) or as the solvent is exchanged between ACN and water. The spectral change of structural color with different viewing angle is also shown (right panel). Copyright © 2021 Springer Nature.

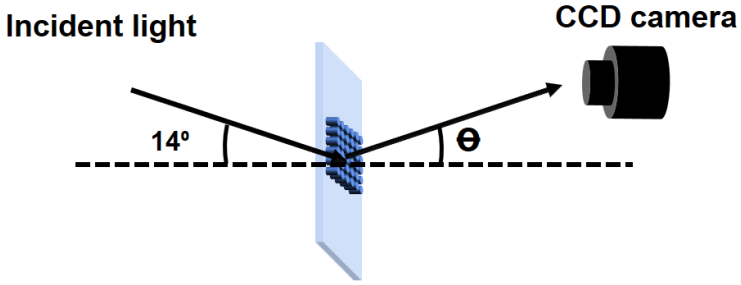

Fig. 2.35. Schematic of the imaging setup for structural color of dithering mask patterned organogel microstructure. Copyright © 2021 Springer Nature.

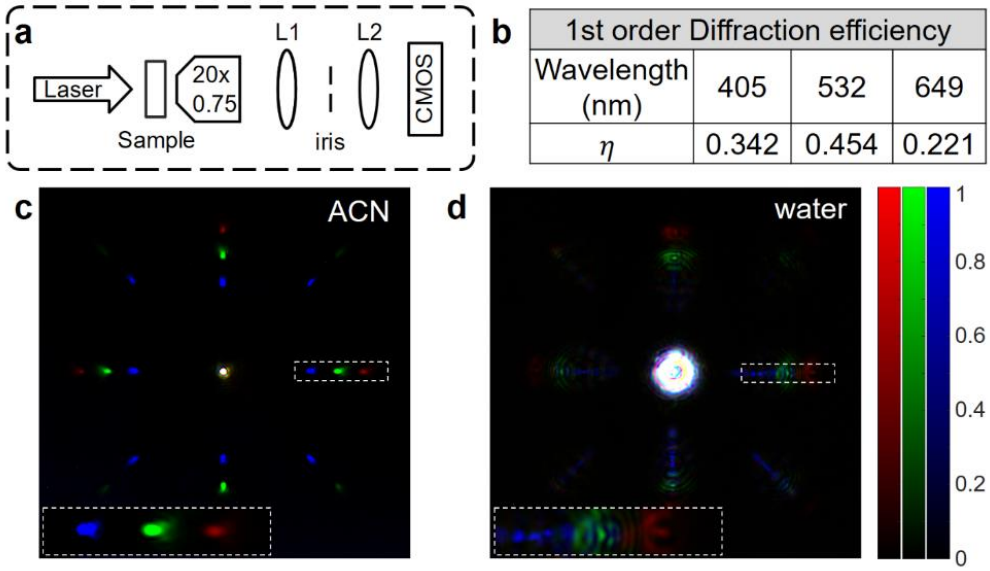

Fig. 2.36. Diffraction from square dithering mask-patterned PDA organogel microstructure. a, Schematic of the diffraction efficiency measuring system. Transmitted and diffracted light were collected by the objective lens (20×/0.75 NA, Olympus) and relayed to the CMOS (CM3-U3-31S4M, Point Grey) camera placed at the Fourier plane by a 4-f lens pair system comprising L1 (f = 250 mm) and L2 (f = 100 mm). An iris was placed at a conjugate image plane to selectively measure light diffracted from a single PDA organogel microstructure. **b,** Diffraction efficiency of the first order diffracted light ($\eta = \sum I_{1st_order} / I_{incident}$) of a PDA organogel microstructure upon immersion to ACN was measured with respect to 405, 532 and 649 nm wavelengths. Here I_{1st_order} is the intensity of the ± 1 diffracted orders in the *x* and *y* directions, and $I_{incident}$ is the intensity of light that is transmitted through empty regions of the sample where there were no PDA organogel structures and only the immersion solvents. **c,d,** Captured diffraction intensity patterns of a PDA organogel microstructure under exposure to ACN (c) and water (d). Diffracted intensity patterns for 649, 532 and 405 nm laser beams were assigned to the RGB colormap, respectively and displayed in a log scale. Insets show a magnified view of a single diffraction order. Copyright © 2021 Springer Nature.

When the immersion solvent was changed to water, the volume expansion ratio of the matrix became smaller than one and that of rods. Furthermore, because the organogel is attached at its bottom surface to a rigid substrate, the in-plane contraction is maximum at the top surface, resulting in bending rods inward. Consequently, non-uniform internal 3D distributions of elastic strain and network densification were generated inside patterned PDA organogels in water (**Figs. 2.37 and 2.38**), which acted as VPHG to display unique fluorescence and bright-field microscopic signals that were specific to dithering patterns (**Fig. 2.39**).

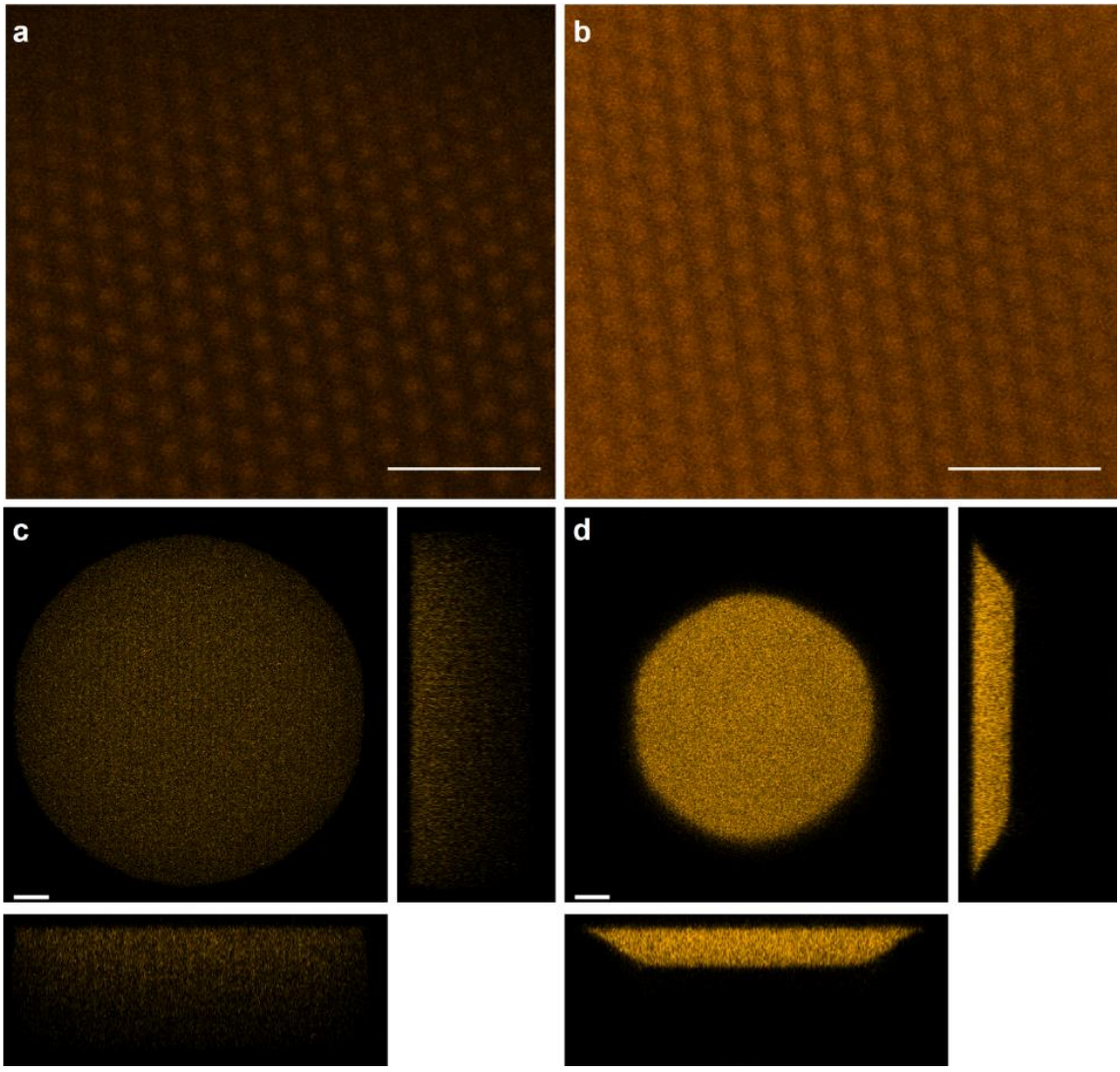

Fig. 2.37. Confocal microscopy images of dithering mask patterned conjugated PDA organogel microstructure. a,b, Hexagon dithering mask patterned PDA organogel microstructure at bottom when exposed to ACN (a) and water (b). **c,d,** Orthogonal confocal microscopy images of hexagon dithering mask patterned PDA organogel microstructure when exposed to ACN (c) and water (d). Scale bar is 10 μm. Copyright © 2021 Springer Nature.

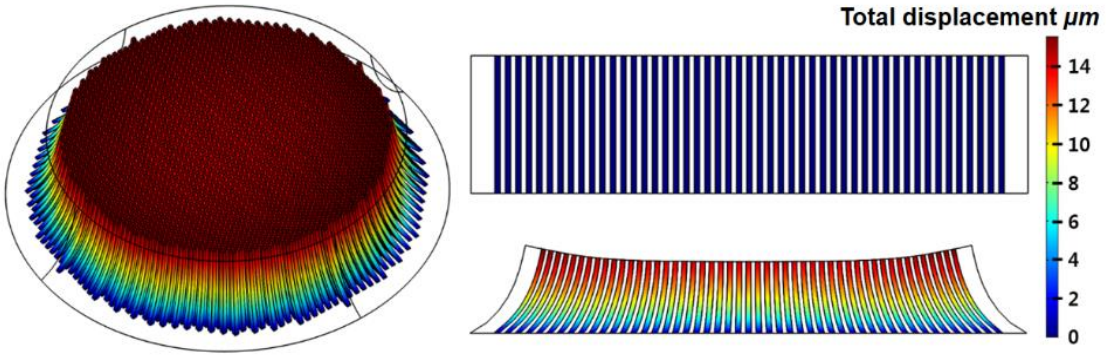

Fig. 2.38. FEA results showing the structure of PDA organogel with arrays of highly crosslinked rods in a square dithering pattern. When organogel contracted in water, a three-dimensional view (left) and a cross-sectional view (bottom) demonstrated deflection of rods towards the center, which were initially aligned along the thickness direction as shown in a cross-sectional view (top). Copyright © 2021 Springer Nature.

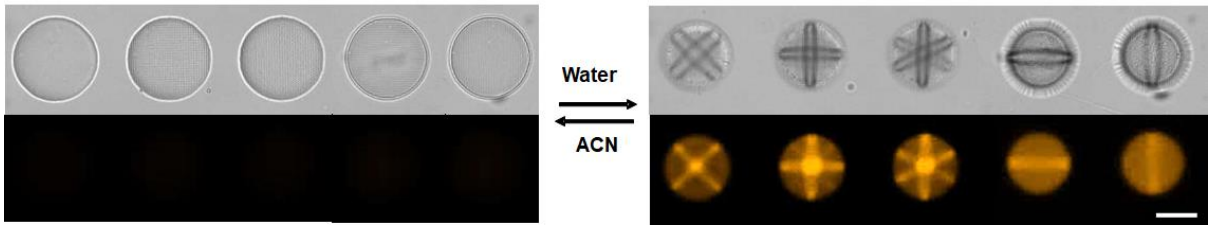

Fig. 2.39. Bright-field (top row) and fluorescence microscopy images (bottom row) of dithering mask patterned PDA microstructure fabricated by five types of masks (rhombus, square, hexagon, and horizontal and vertical line, from left to right) when they were exposed to ACN and water. Scale bar is 50 μm. Copyright © 2021 Springer Nature.

These signals had characteristics of 3D full parallax as seen with varying observation angles, demonstrating their holographic nature (**Fig. 2.40a**). Also, when compared to confocal fluorescence micrographs representing the physical structure of organogels, brightfield micrographs and widefield fluorescence micrographs showed that the light three-dimensionally focused into the shape of a starfish curved around an upper hemisphere is floating above the plateau of physical structure where the fluorescence is emanated. The 3D focused light rapidly evolved during the solvent exchange from ACN to water (**Fig. 2.40b**). The holographic mode can be switched with little crosstalk between the 3D full parallax signals and structural colors upon solvent exchange (**Figs. 2.34 and 2.39**).

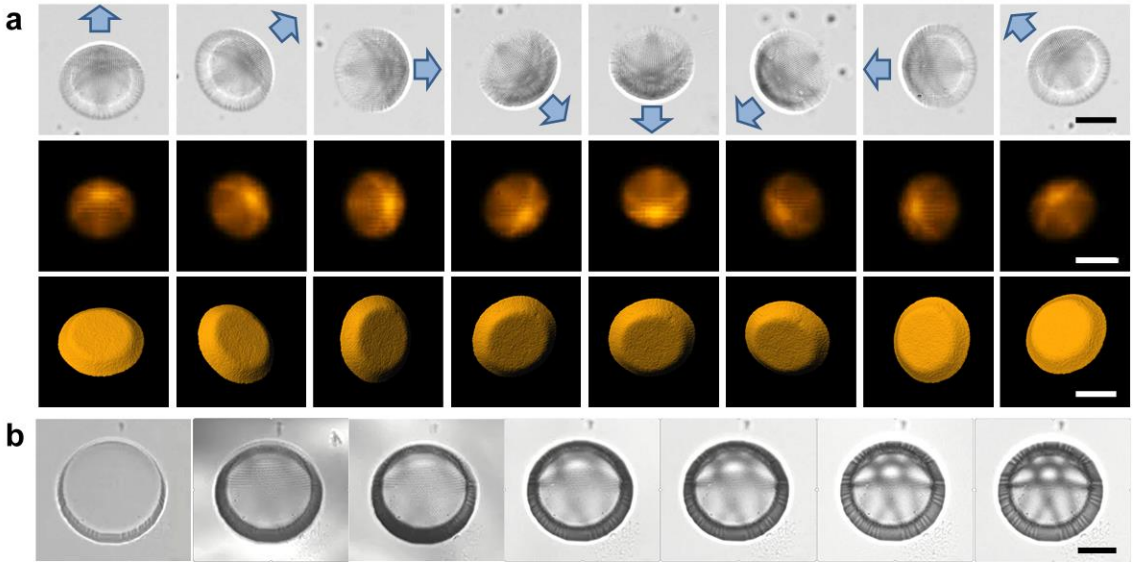

Fig. 2.40. a, Bright-field micrographs (top row), widefield fluorescence micrographs (middle row), and 3D reconstructed confocal fluorescence micrographs (bottom row) of PDA organogels patterned with a hexagon dithering mask. Organogels exposed to water were observed at varying angles (blue arrows indicate viewing angles). **b,** The series of brightfield micrographs showing the temporal evolution of 3D focused light above the physical structure of PDA organogels patterned with a hexagonal dithering mask during the solvent exchange to water. Copyright © 2021 Springer Nature.

Next, we examined whether the local fluorescence emission predicted from elastic strain energy and network densification and the 3D refractive index distribution could correctly explain the unique light signals displayed from patterned PDA organogels in water. We used FEA to predict the deformed shape of a PDA organogel model structure containing a square dithering pattern of highly crosslinked rods (**Fig. 2.41**), which was similar to the LSCM observation (**Fig. 2.42**). We inferred that the rod regions that were irradiated more would have a higher network density than surrounding matrix by roughly a factor of two as estimated from the comparison of initial weak fluorescence intensities between rods and matrix in ACN (**Fig. 2.43**).

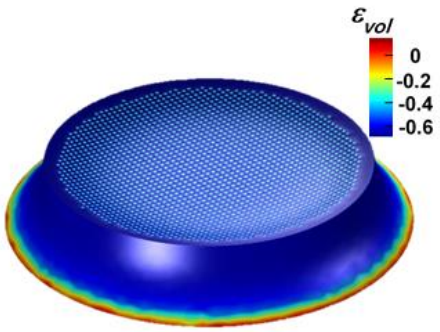

Fig. 2.41. FEA results showing that solvent exchange shrank the organogel patterned with a square dithering mask. Color map indicates volumetric strain. Copyright © 2021 Springer Nature.

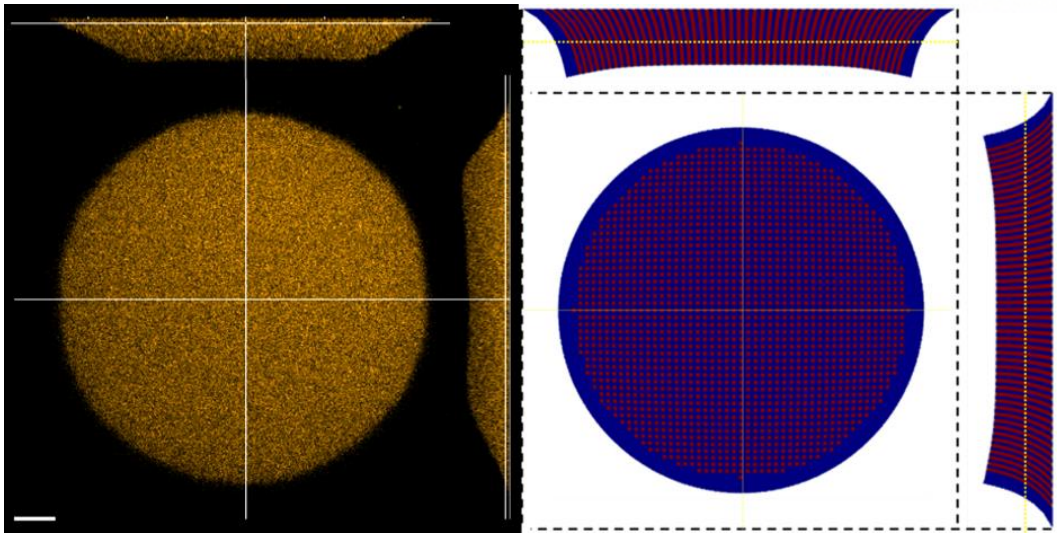

Fig. 2.42. Comparison of confocal microscopy image of dithering mask patterned conjugated PDA organogel microstructure with deformed model structure by FEA. Orthogonal confocal microscopy image (left) of square dithering mask patterned PDA organogel upon exposure to water. Deformed structure modeled by FEA (right) shows bending of rods (red) and contraction of matrix (blue). Scale bar is 10 μm. Copyright © 2021 Springer Nature.

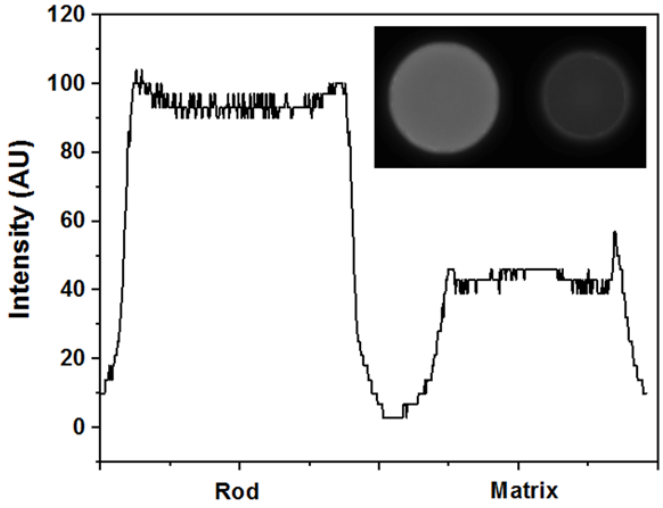

Fig. 2.43. Line profile of initial fluorescence intensity of uniform PDA organogel. Uniform organogels which have same UV dose of rod and matrix in dithering mask patterned PDA organogel microstructure. Inset shows fluorescence image of uniform rod gel (left) and matrix gel (right). Copyright © 2021 Springer Nature.

Based on this estimation, we approximated the locally enhanced fluorescence expression as $\{2[(1+\varepsilon_{vol})^{-1}-1]_n+\beta\cdot U_n\}_r+\{[(1+\varepsilon_{vol})^{-1}-1]_n+\beta\cdot U_n\}_m$, where subscripts *r* and *m* indicate rods and matrix, respectively. To match the fluorescence expression integrated along the thickness direction to microscopic observation, we adjusted β_r while conserving β_m to the value used in the case of organogels

crosslinked without dithering patterns (**Fig. 2.30**), resulting in β_r that is sufficiently greater than β_m (**Fig. 2.44**). We infer that the larger value of β_r is associated with rod regions containing PDA chains that are more densely chemical linked to the network due to a higher acrylate conversion. As organogels contracted, PDA chains in matrix regions with denser chemical links to the networks would rearrange themselves less likely by translation or rotation but more likely by twist or bend, which increases the degree of the torsional angle reduction and enhances the local fluorescence. In addition, similar morphological changes of fluorescence emission were observed in both the model structure and patterned PDA organogels, most apparently the widening of the unique signal, as the volume expansion ratio of matrix regions reduced (**Figs. 2.45-2.47**).

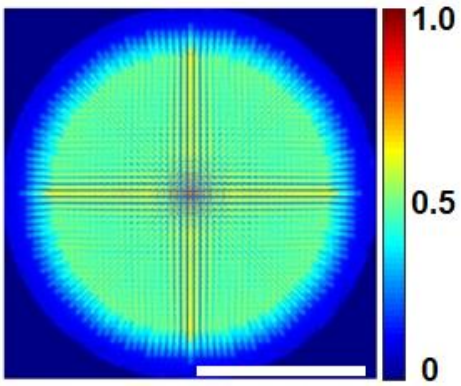

Fig. 2.44. Fluorescence expression predicted for the patterned organogel in FEA results after normalization by the maximum value. A relative contribution of network densification and torsional angle reduction to the fluorescence expression was adjusted separately for rod and matrix to match the fluorescence image shown in **Fig. 2.39**. Copyright © 2021 Springer Nature.

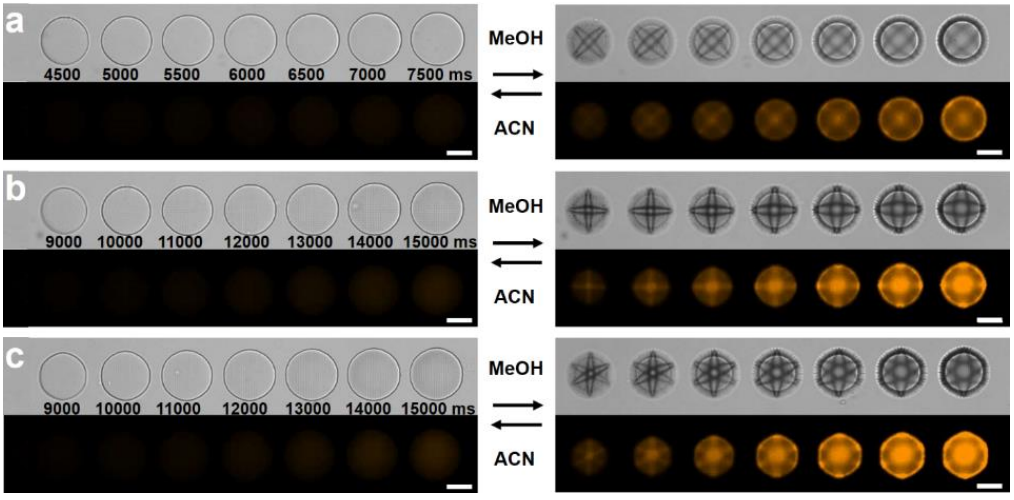

Fig. 2.45. Bright-field and fluorescence microscopy images of dithering mask patterned PDA microstructures having different crosslinking densities upon an exposure of ACN and MeOH. a-c, Rhombus (a), square (b), and hexagon (c) dithering mask were used to fabricate the PDA microstructure. Crosslinking densities was controlled by changing exposure time of 365 nm UV light. Scale bar is 50 μm. Copyright © 2021 Springer Nature.

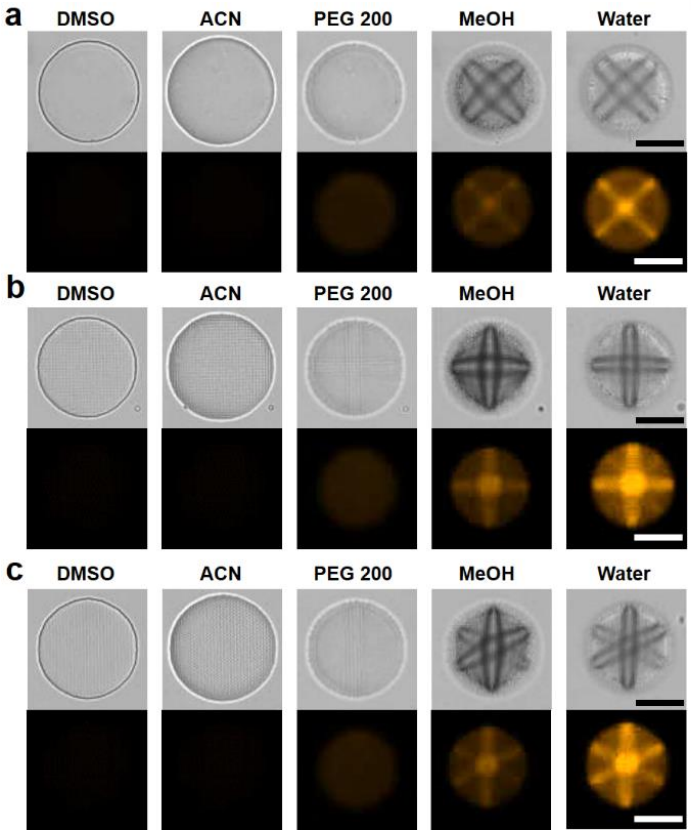

Fig. 2.46. Bright-field and fluorescence microscopy images of PDA organogel microstructures upon exposure to solvents. a-c, Rhombus (a), square (b), and hexagon (c) dithering mask were used to fabricate the PDA microstructure. Scale bar is 50 μm. Copyright © 2021 Springer Nature.

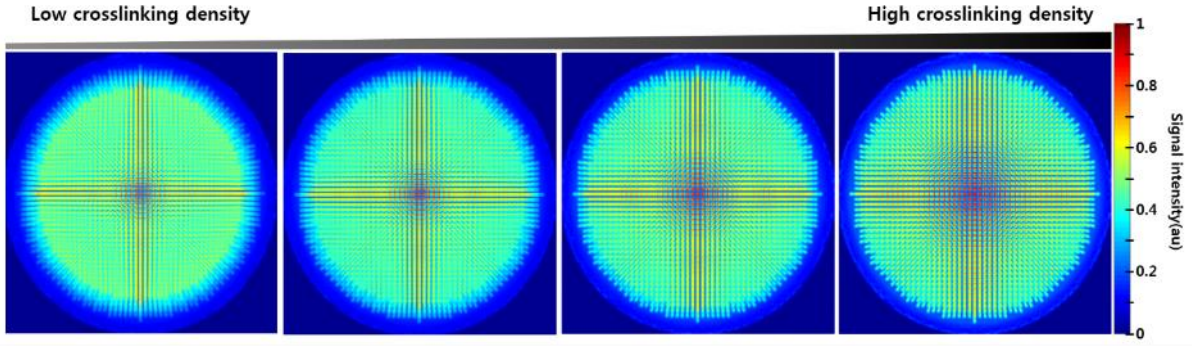

Fig. 2.47. Changing of signal shape with varying contraction level. Modeled fluorescence signals show the strongest intensity at the center of the organogel, and intensity about 0.7 shows along the cross shape. Radius of strong center and width of the cross get larger with higher crosslinking density, lower contraction level. Copyright © 2021 Springer Nature.

We further simulated the light propagation of predicted fluorescence emission through the deformed model structure containing 3D optical heterogeneity. Briefly, the structured spatial profile of the illumination intensity was calculated at each *z*-plane and was then multiplied by the fluorescence expression predicted there (**Fig. 2.48**). We measured refractive indices of monolithic rods and matrix

imbibing ACN or water in thermal equilibrium without geometric constraints (**Fig. 2.32**). Assuming that the reduction was proportional to the level of volumetric contraction, we formulated the refractive index in water as $R_{(r,m)}(x,y,z) = R_{i,(r,m)} - A_{(r,m)}[(1+\varepsilon_{vol}(x,y,z))^{-1}-1]$, where $R_{i,(r,m)}$ is the refractive index measured in ACN and $A_{(r,m)}$ are proportionality constants calculated from the measurement. Using the 3D map of refractive index, we computed the light field propagation through consecutive surface-parallel planes along the thickness direction of the deformed model structure using the angular spectrum method[47-49]. The incident light field $E_{in,n}(x,y)$ was multiplied with the phase delay from the n^{th} z-plane to become the output field $E_{out,n}(x,y) = E_{in,n}(x,y)\cdot\exp(i2\pi\Delta\phi_n(x,y)\,\Delta/\!/\lambda)$, where $\Delta\phi_n(x,y) = R_{(r,m)} - 1.340$ is the difference between the local refractive index with the surrounding media water in the n^{th} z-plane, Δl is the distance between adjacent z-planes, and λ is the wavelength of light. The output field was subsequently propagated to the next $n+1^{th}$ z-plane where it became the incident light field (**Fig. 2.48**). This process of field propagation was repeated consecutively throughout the entire z-planes. At each z-plane, the illumination intensity calculated as the absolute square of the optical field (**Fig. 2.48b**) was multiplied with the fluorescence expression to obtain the fluorescence signal intensity, which was integrated along the thickness direction. The integrated fluorescence signal intensity (**Fig. 2.49a**) clearly displayed the unique fluorescence signal as observed experimentally in **Fig. 2.39.**

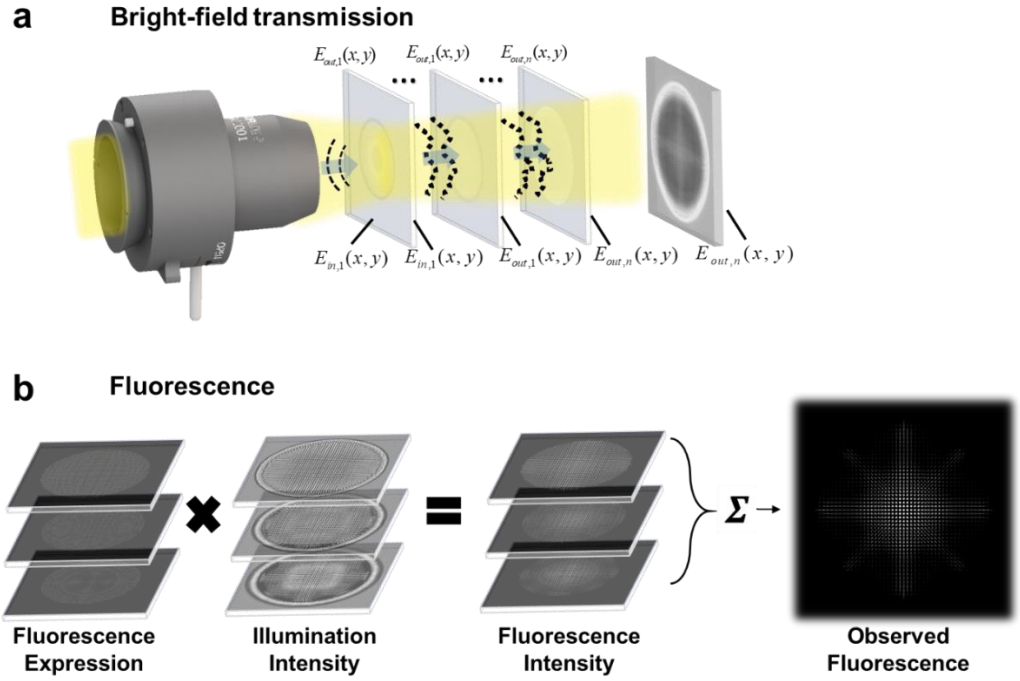

Fig. 2.48. Light propagation simulations. a, The 3D organogel structure was divided into N=90 layers. The local volumetric strain upon exposure to water, obtained by finite element analysis, was used to reconstruct the refractive index distribution of each layer L. The incident beam $E_{\mathrm{in},1}(x,y)$ was modeled by the condenser NA. Propagation of light through the respective layers was calculated using the angular spectrum method. To simulate the bright-field transmitted light, the intensity of the optical

field obtained for the individual plane waves per incident angle, which ranged between ±17.4° to cover the full illumination numerical aperture (NA) of 0.3, were incoherently summed. **b,** The observed fluorescence pattern within the organogel structure was calculated by multiplying the degree of fluorescence expression per layer with the illumination intensity per layer. The degree of fluorescence expression was calculated through FEA simulations as described in the main text. The illumination intensity per layer was calculated using the angular spectrum method as in Fig. 2.48 (a). Copyright © 2021 Springer Nature.

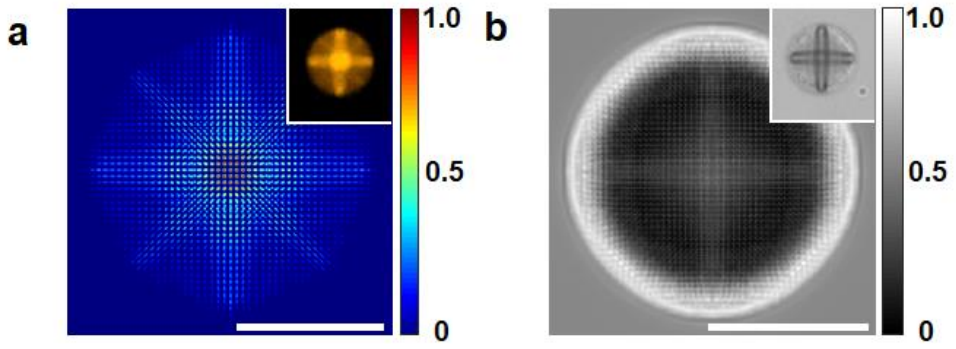

Fig. 2.49. a,b, (a) Expected fluorescence intensity based on fluorescence expression and illumination intensity (inset: fluorescence micrograph) and (**b**) expected bright-field transmitted light distribution (inset: bright-field micrograph) for Fig. 2.41. Copyright © 2021 Springer Nature.

We also simulated the signal generation in the bright-field transmission micrographs. Using the same angular spectrum method, we computed the light propagation from a spatially incoherent light source (corresponding to the LED used in our experiments) that is focused through a condenser onto the deformed model structure with the 3D refractive index map (**Fig. 2.48a**). As shown in **Fig. 2.49b** the simulated transmitted light matched our observations. In light of these results, we concluded that the unique signals in fluorescence and bright-field micrographs originated from non-uniform 3D distributions of volume contraction and refractive index, which were generated by dithering patterns and organogel attachment to a rigid substrate. The structural non-uniformity resulted in the elastic strain, which led to the local enhancement of the fluorescence emission, and the optical heterogeneities resulted in holographic diffraction of light through PDA organogels. Our conclusion is supported by the absence of such holographic signals from free-standing patterned PDA organogels, which upon immersed in water contracted isotropically, and thus, retained 2D optical and structural heterogeneities with structural colors as in ACN (**Fig. 2.50**). Moreover, when surface-attached organogels were made of fluorescence monomer and 1,6-hexanediol acrylate, instead of HD-DA monomer, and patterned with identical dithering patterns, they did not exhibit the unique fluorescence signal, demonstrating the role of twisting conjugated PDA chains (**Fig. 2.51**).

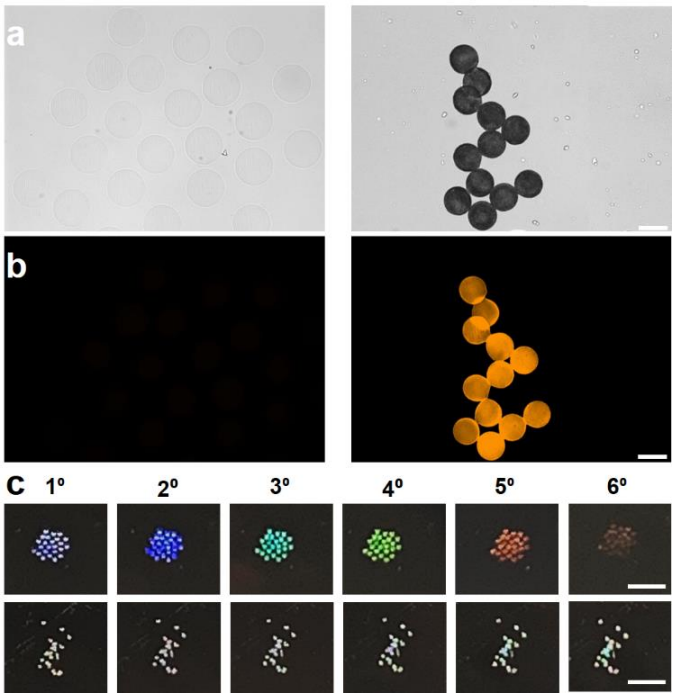

Fig. 2.50. Bright-field, fluorescent and structural color change of dithering mask patterned PDA organogel microparticle. a,b, Bright-field (a) and fluorescence (b) microscopy images of hexagon patterned PDA organogel microparticles when they were exposed to ACN (left) and water (right). **c,** Structural color change of hexagon patterned PDA organogel microparticles upon a solvent exchange from ACN (top) to water (bottom). Scale bar is 100 μm for (a) and (b), and 1 mm for (c). Copyright © 2021 Springer Nature.

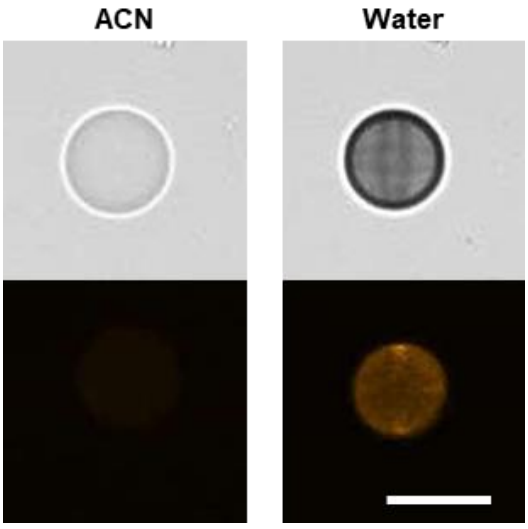

Fig. 2.51. Bright-field and fluorescent pattern change of dithering mask patterned 1,6-hexanediol diacrylate microstructures. Bright-field and fluorescence microscopy image of dithering mask patterned fluorescein o-acrylate attached 1,6-hexanediol diacrylate microstructure with upon exposure to ACN and water. Scale bar is 100 μm. Copyright © 2021 Springer Nature.

Cryptographic systems and flexible applications using PDA organogel microstructure

To examine the feasibility of using patterned PDA organogels as holography-based cryptographic or anti-counterfeiting systems, we created different shapes of PDA organogels with varying dithering patterns and examined their holographic signals under bright-field and fluorescence microscope. PDA organogels with identical shapes but varying dithering patterns were microscopically indistinguishable in ACN. However, when immersed in water, these organogels displayed holographic signals that were unique to the shape of each dithering pattern in both bright-field and fluorescence micrographs (**Fig. 2.52**).

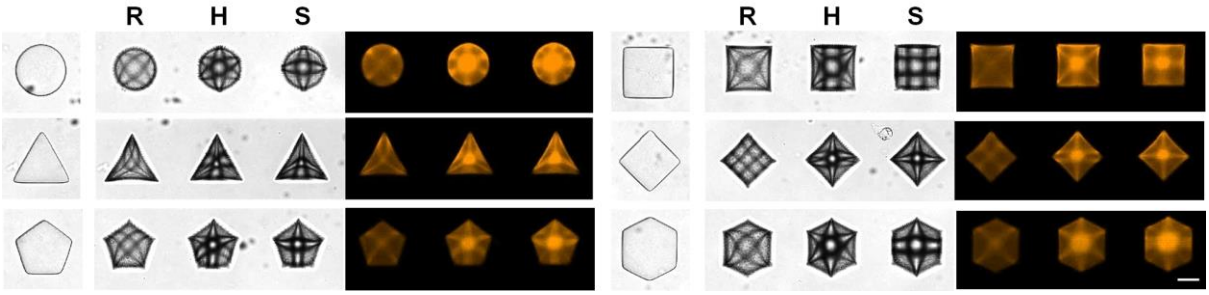

Fig. 2.52. Bright-field and fluorescence microscopy images of different shapes of PDA organogels patterned using one type of dithering mask, either rhombus (R), square (S), or hexagon (H). Copyright © 2021 Springer Nature.

The use of hybrid dithering patterns further enriched the palette of available holographic signals (**Fig. 2.53**). For example, when diamond-shape PDA organogels were patterned in binary using two out of three dithering masks – rhombus, hexagon, and square –the nine combinations were clearly distinguished from each other by the azimuthal profile of fluorescence intensity (**Figs. 2.54-2.56** and see Methods for the azimuthal profile). Using an automated process of dithering lithography, we created an encrypted micro-array consisting of patterned organogels formed at specific locations among unpatterned organogels, displaying the hidden word "UNIST" with unique holographic signals in water (**Fig. 2.57**).

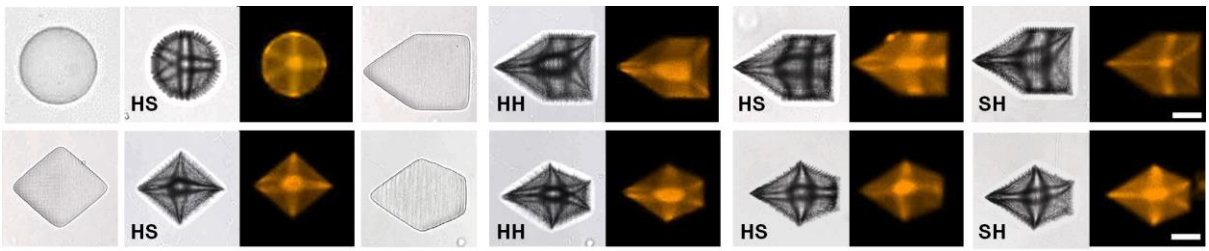

Fig. 2.53. a,b, Bright-field and fluorescence microscopy images of different shapes of PDA organogels patterned using a binary mask composed of any two out of the three masks (rhombus (R), square (S), or hexagon (H)). Holographic signals are unique to the shape of the dithering pattern, forming a wide palette of possible signals. Copyright © 2021 Springer Nature.

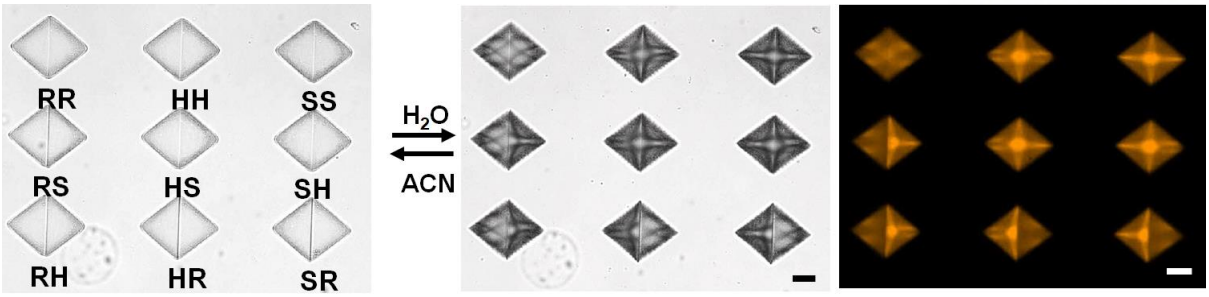

Fig. 2.54. Encryption of multiple patterns in diamond shaped PDA microstructure using binary dithering mask lithography. Copyright © 2021 Springer Nature.

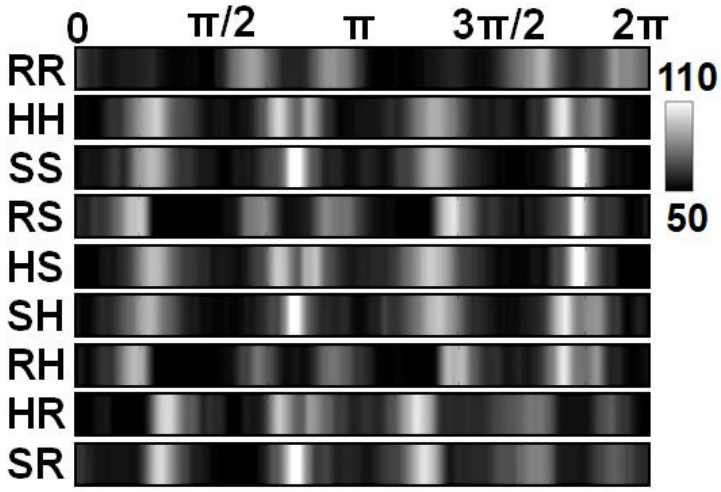

Fig. 2.55. Decryption of 9 distinctive fluorescence patterns in Fig. 2.53 via oval profile. Copyright © 2021 Springer Nature.

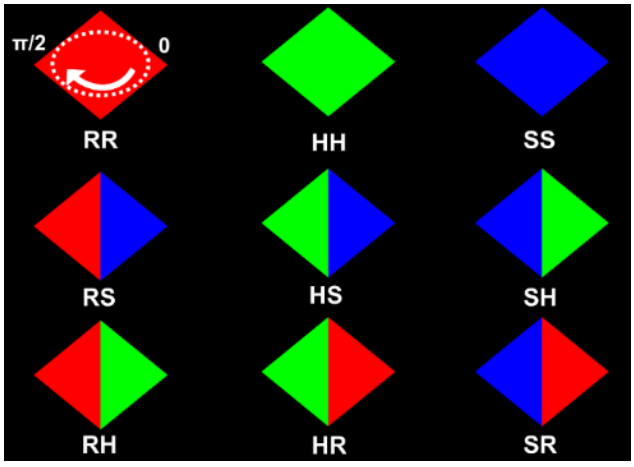

Fig. 2.56. Schematic of binary dithering mask patterning and oval profile of diamond-shaped conjugated PDA organogel microstructures. Nine combinations of binary dithering masks. Rhombus (R), hexagon (H), and square (S) pattern. Copyright © 2021 Springer Nature.

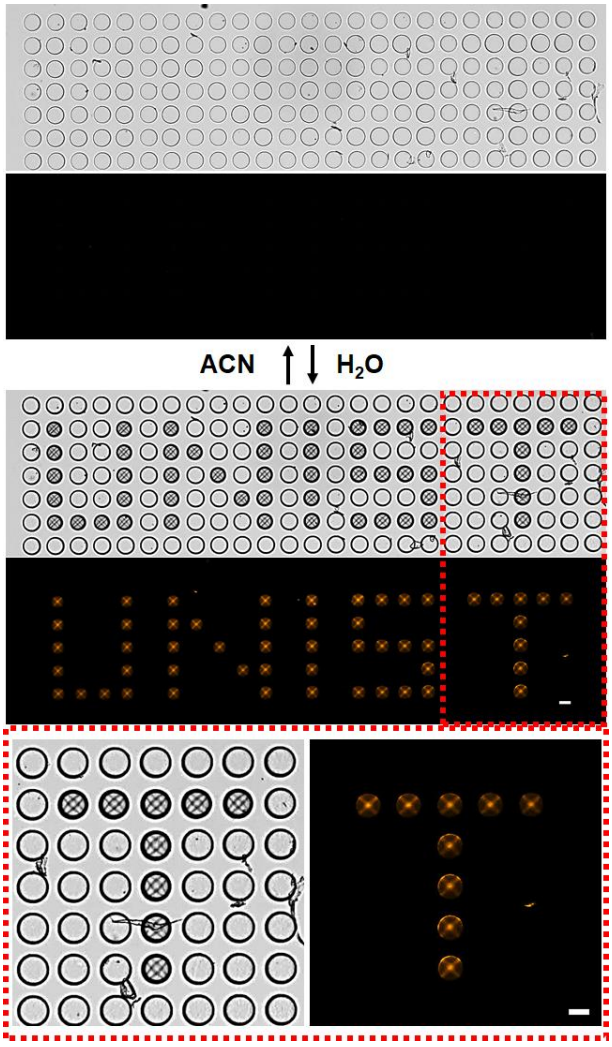

Fig. 2.57. Encryption of letters "U-N-I-S-T" using rhombus dithering mask exhibits unique patterns at individual microstructures (shown in red dotted box). Copyright © 2021 Springer Nature.

A PDA organogel microstructure exhibiting shape morphing and structural color and fluorescence emission change

When the patterned organogels were detached from underlying substrates and exposed to water, they actuated by locally bending along the direction settled by the shape of dithering pattern and showed enhanced fluorescence in regions experiencing large deformations (**Fig. 2.58 and 2.59**).

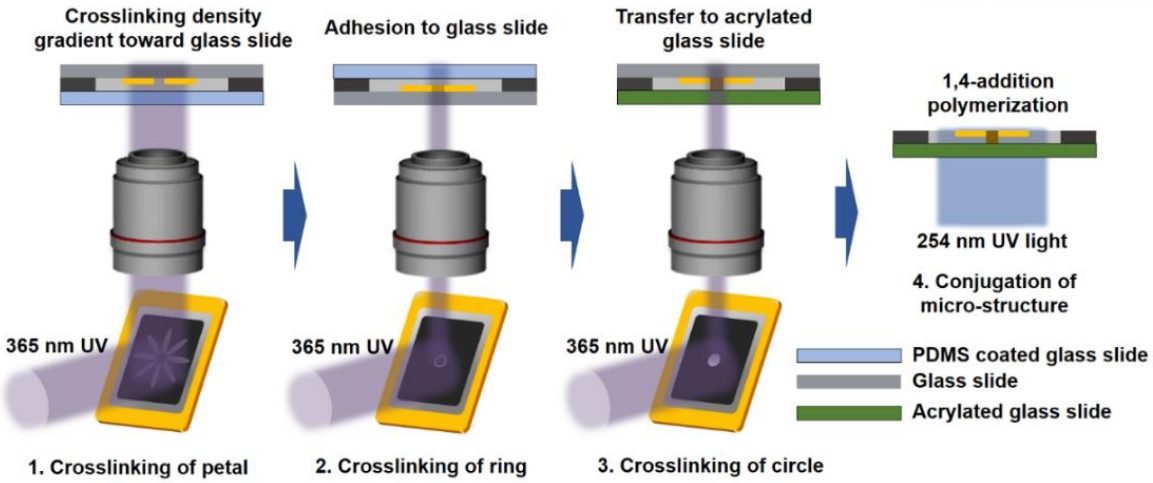

Fig. 2.58. Fabrication process of shape morphing PDA organogel microstructure. Copyright © 2021 Springer Nature.

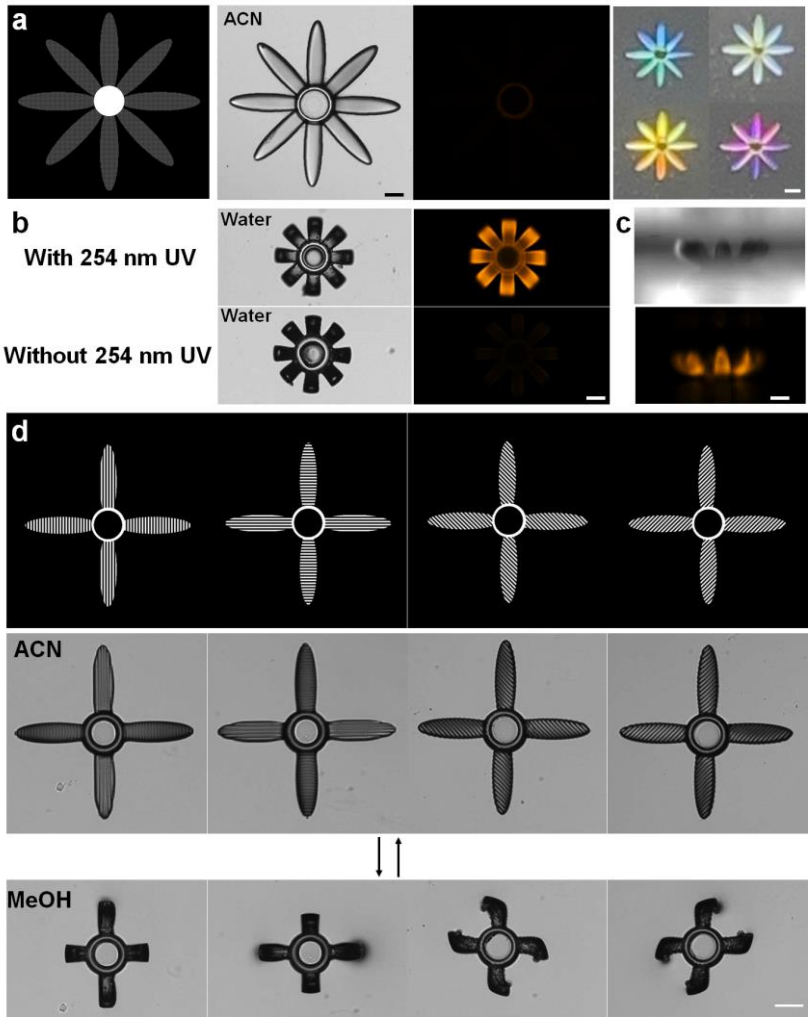

Fig. 2.59. A PDA organogel microstructure reversibly actuating and displaying structural color and fluorescence emission in response to a solvent exchange. a, A dithering mask used for the organogel microstructure (a square dithering pattern for petals) (left), bright-field and fluorescence

micrographs (middle), and structural color displayed by a flower-like PDA organogel upon exposure to ACN (right). **b,** Fluorescence emission of a flower-like PDA organogel irradiated with (top) or without (bottom) 254 nm for diacetylene polymerization. **c,** Bright-field and fluorescence micrographs of a flower like PDA organogel immersed in water (a side-view). **d,** Vertical, horizontal, and diagonal dithering patterns applied to petals of flower-like PDA organogels (top) and corresponding bright-field micrographs (middle and bottom). When exposed to MeOH, petals bent along the direction settled by each dithering pattern, which produced in-plane swelling mismatch. Scale bars are 100 μm. Copyright © 2021 Springer Nature.

In ACN, patterned PDA organogels displayed strong structural colors because the periodicity of the refractive index was conserved along the thickness direction. These structural colors can be reversibly switched on and off in selective areas when micro-arrays of disk-shaped PDA organogels were created with varying directions of periodicity. For example, when a micro-array was created with organogels patterned with horizontal lines on one side and with vertical lines on the other side, structural colors were visible only in one side where the direction of incident light was parallel to that of the periodicity and the other side when the direction of the incident light changed by 90° (**Figs. 2.60 and 2.61**). Contrarily, organogels with bidirectional periodicity, for example, a square dithering pattern, retained both the tone and intensity of structural colors when the direction of incident light changed by 90°. Accordingly, by selectively locating organogels with varying directions of periodicity, we created a microarray that displays the letter changing from T to S (or E) and *vice versa* as the incident light rotates by 90° (**Figs. 2.62 and 2.63**).

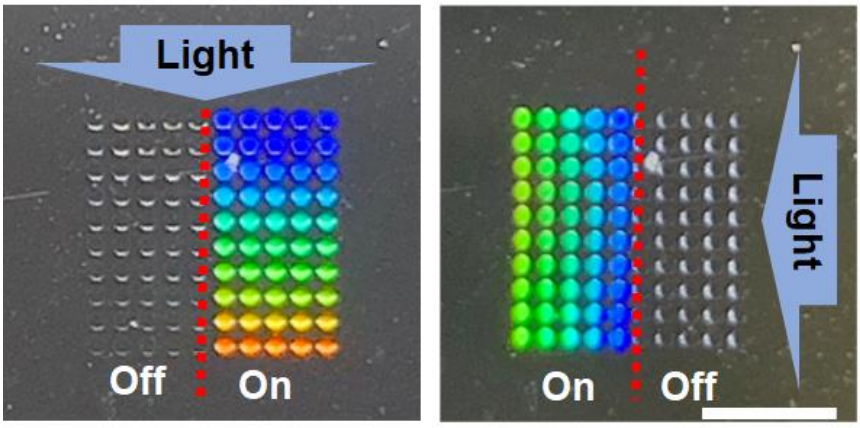

Fig. 2.60. Microarray consisting of organogels patterned with horizontal lines on the right of the red dotted line and vertical lines on the other side display selective structural color depending on the direction of incident light. Copyright © 2021 Springer Nature.

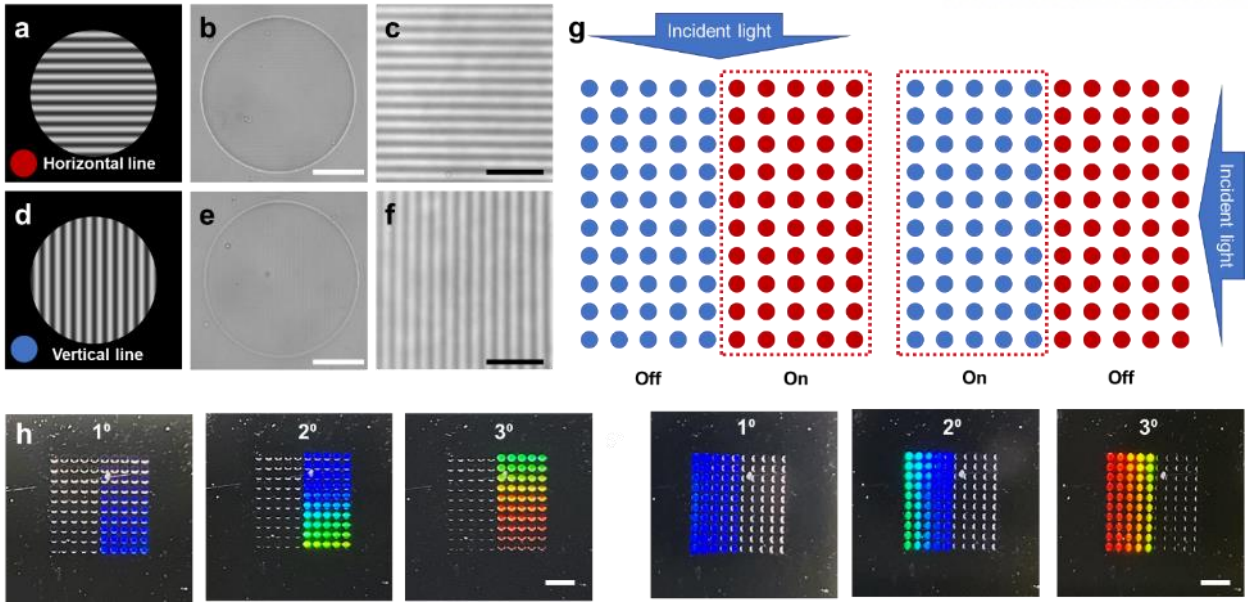

Fig. 2.61. Structural color turn on-off according to the direction of incident light. a, Horizontal lined dithering mask pattern image. **b,c,** Bright-field microscopy images of horizontal lined dithering mask patterned PDA organogel microstructure upon exposure to ACN by 20× (b) and 100 × (c) objective. **d,** Vertical lined dithering mask pattern image. **e,f,** Bright-field microscopy images of vertical lined dithering mask patterned PDA organogel microstructure upon exposure to ACN by 20× (e) and 100 × (f) objective. **g,** Schematic of selective patterning of horizontal and vertical lined dithering mask patterned microarray. **h,** Selective structural color and iridescence according to the direction of incident light. Scale bar: 100 μm (b) and (e), 10 μm (c) and (f) and is 1 mm (h). Copyright © 2021 Springer Nature.

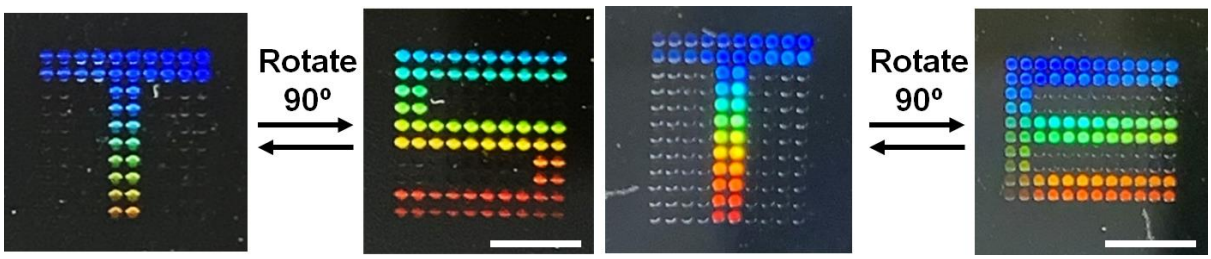

Fig. 2.62. Dynamic flip-flop structural color systems displaying letter changes from T to E and T to S. Copyright © 2021 Springer Nature.

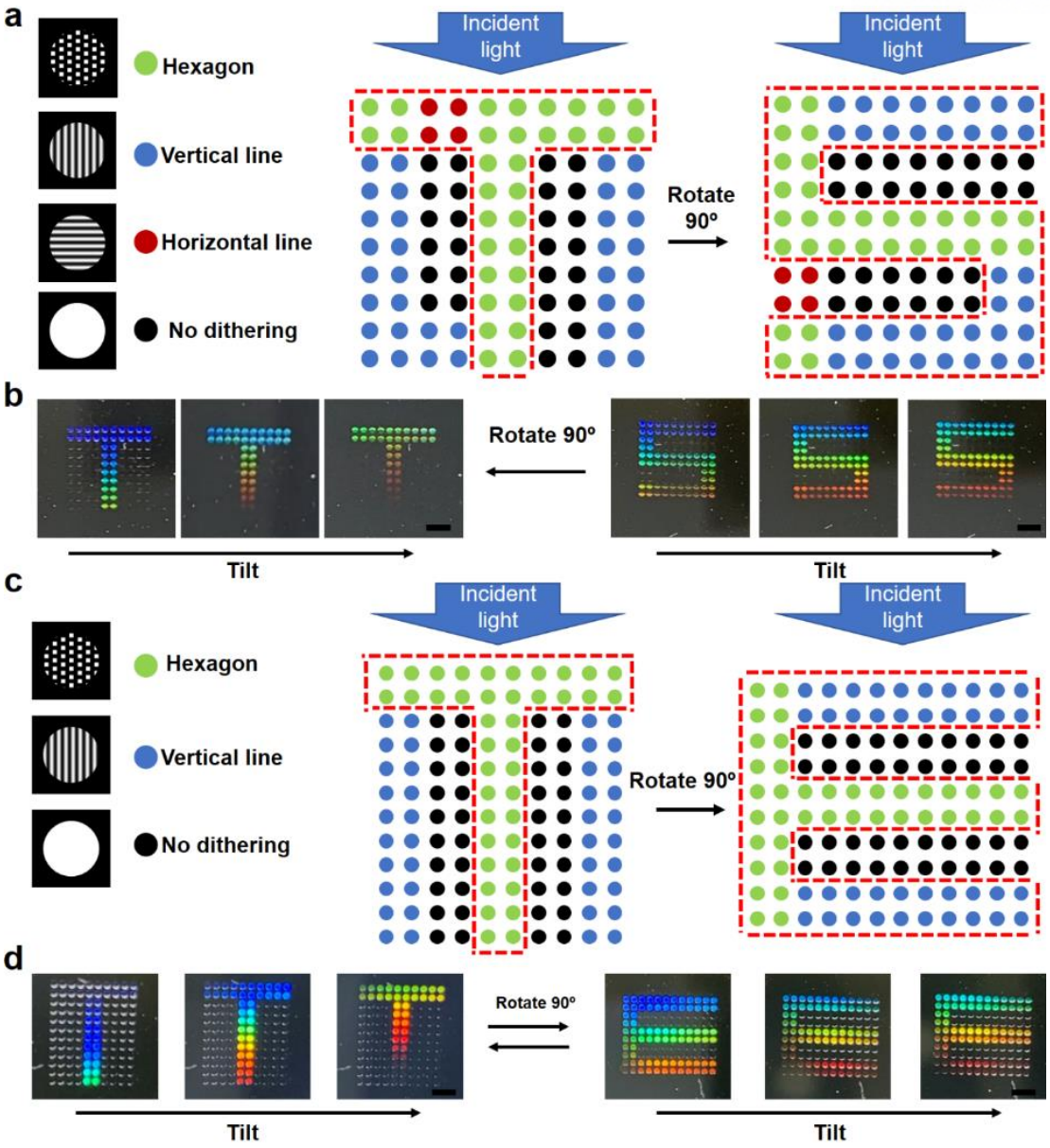

Fig. 2.63. Schematic of letter transition according to the direction of incident light. a, Fabrication of letter transition systems using four types of dithering masks. Hexagon dithering mask pattern (green dot) represents always on. Vertical (blue dot) and horizontal (red dot) dithering mask represents selective on-off of structural color according to the 90 angle of incident light. Black dot dithering mask represent no structural color. **b,** Letters transition from T to S according to the direction of incident light and their iridescence color upon the observation angle. **c,** Fabrication of letter transition systems using three types of dithering masks. Hexagon dithering mask pattern (green dot) represents always on. Vertical line dithering mask (blue dot) represents selective on-off of structural color according to the 90 angle of incident light. Black dot dithering mask represent no structural color. **d,** Letters transition from T to E according to the direction of incident light and their iridescence color upon the observation angle. Scale bar is 1mm. Copyright © 2021 Springer Nature.

Such structural colors were reversibly switched on and off through solvent exchange as well (**Fig. 2.63**). Our holographic microarrays can also be prepared as a flexible free-standing film by embedding microarrays inside conventional photo-curable resin, extending its use in portable systems requiring cryptography or anti-counterfeiting technology (**Fig. 2.64**).

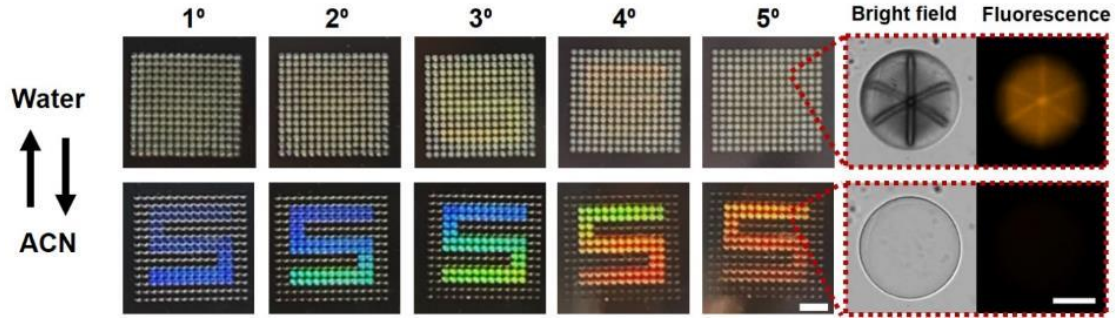

Fig. 2.64. Cryptographic letter system using patterned PDA microstructure. Selective patterning of conjugated PDA organogel for structural color and 1,6-hexanediol diacrylate organogel for blank results in hidden letter encryption. Structural colored letter "S" was displayed upon exposure to ACN. Scale bars are 1 mm (left) and 100 μm (right). Copyright © 2021 Springer Nature.

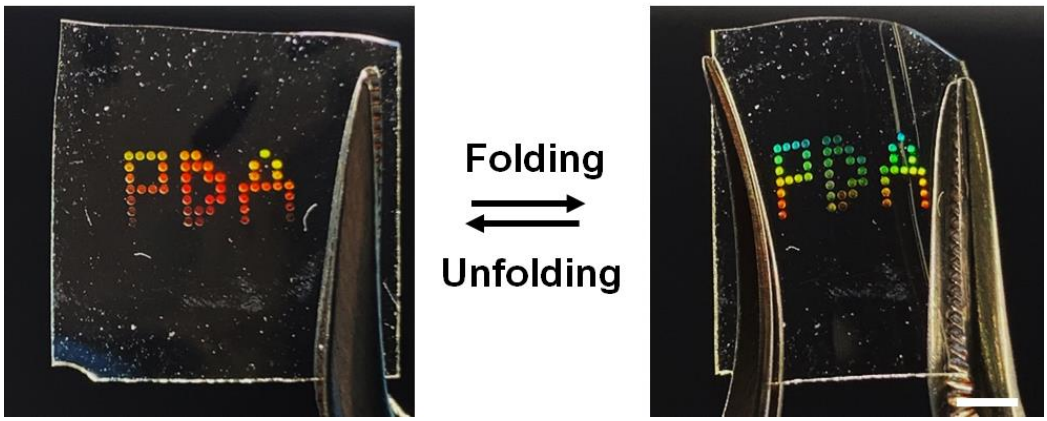

Fig. 2.65. Free-standing flexible films with embedded holographic lettering fabricated using conventional biocompatible PEG-DA resin. Copyright © 2021 Springer Nature.

Encryption of PDA organogel matrix with multiple structural colors

To further demonstrate the practical applicability of our system, we have created the array of square-shaped PDA organogel matrices encrypted with multiple structural colors by changing the shape and pitch of the dithering pattern in each element (**Fig. 2.66**). Due to the wide varieties of the matrix size and the structural color of each element (**Fig. 2.67** and **Fig. 2.68**), the number of codes encryptable in a single organogel matrix is virtually unlimited. For example, when the 5-by-5 organogel matrices were patterned with four structural colors including black indicating no light interference, we can create 4^{25}, or roughly 10^{15} numbers of encryption codes. This number is substantially greater than those reported in previous studies[50-53], where the number of available code was limited by the number of

color-generating materials, *e.g.* fluorescence dyes or inorganic nanoparticles of different types, and the dimensionality of pattern that is typically one in conventional flow lithography[52]. Contrarily, we have used a single material, the HD-DA monomer, to create two-dimensional encryption patterns of multiple (>10) colors, demonstrating the practical applicability of our method. The hidden secondary code was displayed as well by rotating the imaging device or organogel matrices by 90° (**Figs. 2.67-2.70**).

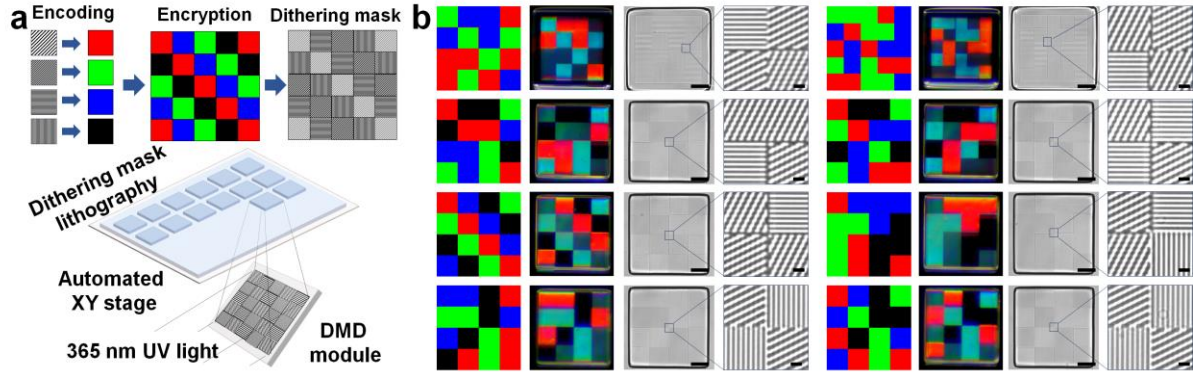

Fig. 2.66. a, A schematic diagram of encryption process that generates a specific dithering pattern in each element of organogel matrix. **b,** Example codes (left), corresponding structural colors displayed by encoded organogel matrices (middle), and their bright-field micrographs (right). Copyright © 2021 Springer Nature.

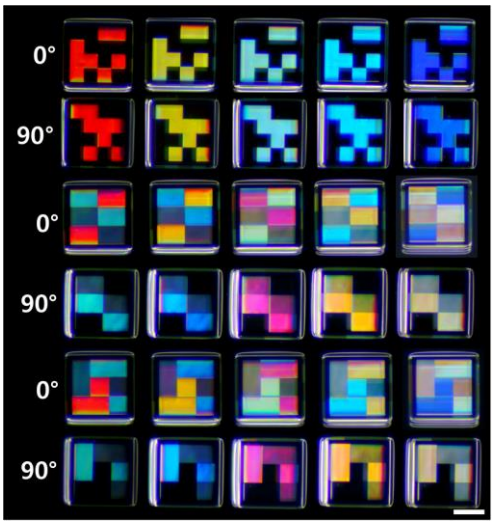

Fig. 2.67. Structural color displayed by encoded organogel matrices with varying matrix size. 0° and 90° indicate the direction of incident light varied by imaging device. Copyright © 2021 Springer Nature.

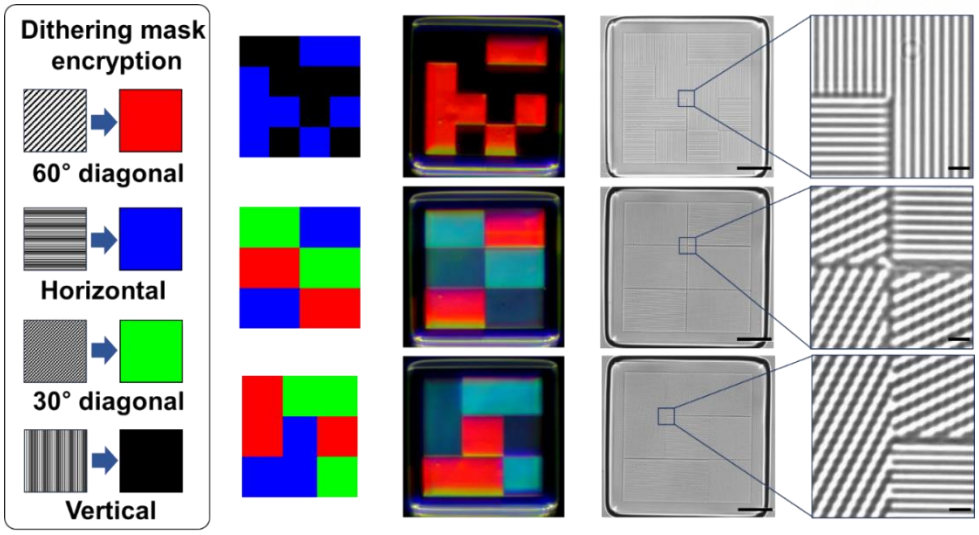

Fig. 2.68. Encrypted information, structural color, bright-field image, and maginified bright-field images of PDA organogel microstructures in Fig. 2.64. Scale bars are 100 μm for bright field images and 5 μm for magnified bright field images. Copyright © 2021 Springer Nature.

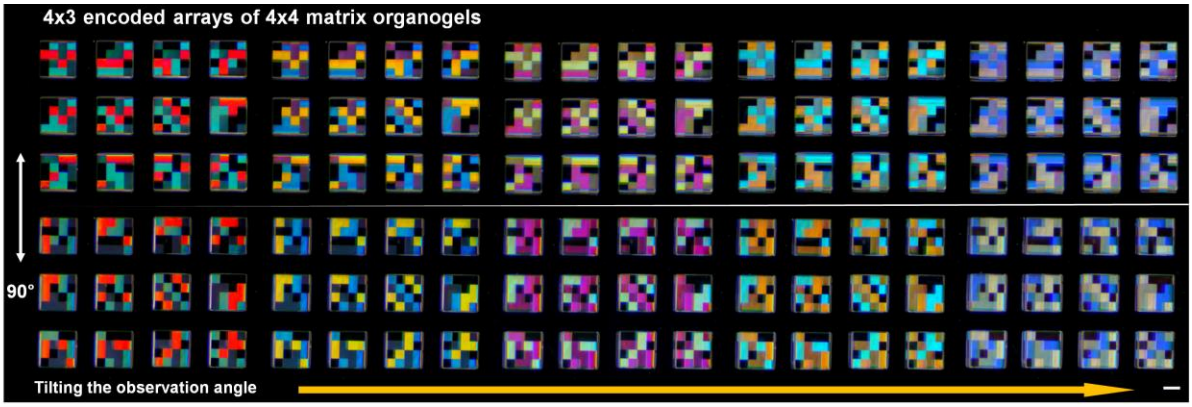

Fig. 2.69. Structural colors displayed by 4×3 micro-array of 4×4 encoded organogel matrices. Scale bars are 200 μm. Copyright © 2021 Springer Nature.

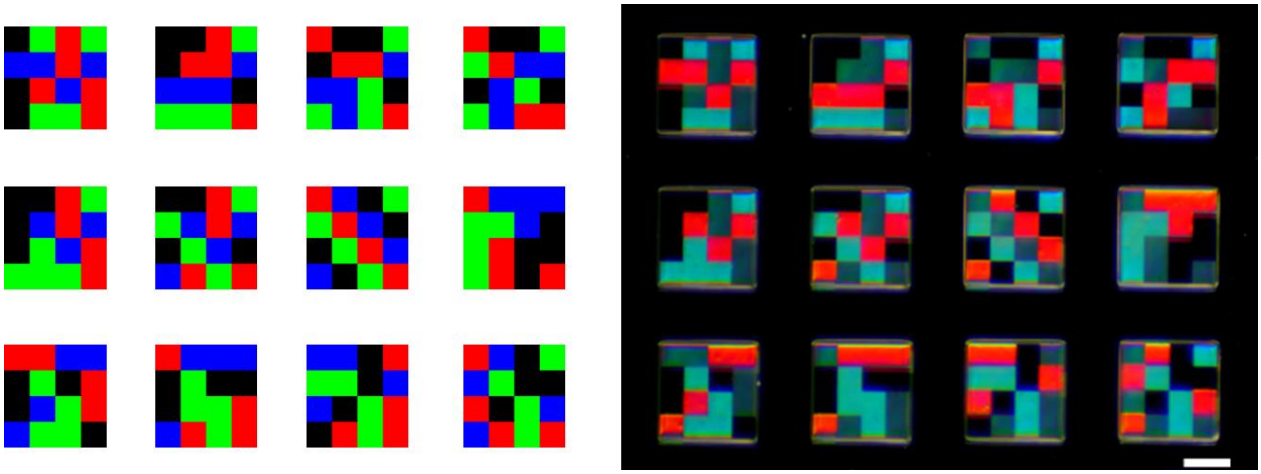

Fig. 2.70. Encrypted information (left) and structural color (right) of PDA organogel microstructures in Fig. 2.66. Scale bar is 200 μm. Copyright © 2021 Springer Nature.

The organogel matrices can be prepared as a large scale flexible free-standing film (**Fig. 2.71**) or free-floating particles (**Fig. 2.72**), demonstrating the broad applicability of our method. Additionally, our method using a fully automated process of dithering lithography can produce ~ 10^5 different codes per hour, demonstrating a high-throughput beneficial for practical use.

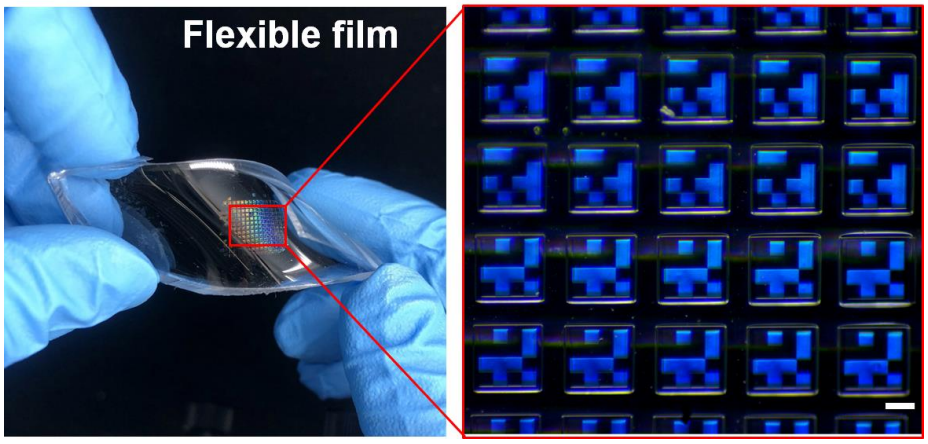

Fig. 2.71. An array of structural color displayed by an imprinted flexible PDMS film. Scale bar is 200 μm. Copyright © 2021 Springer Nature.

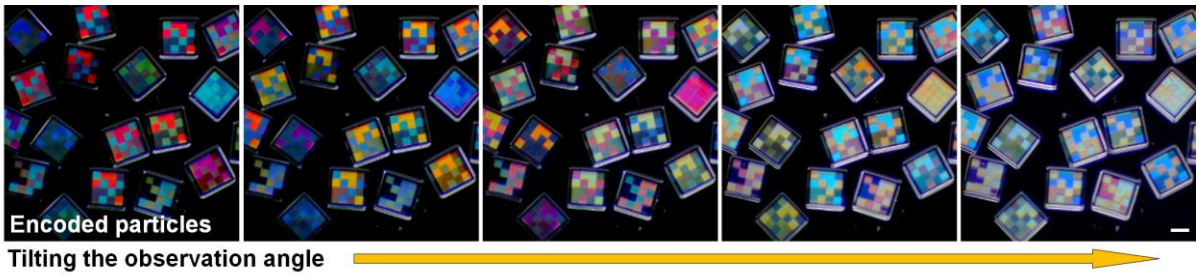

Fig. 2.72. Encoded organogel matrices in the form of free-floating microparticles. Scale bar is 200 μm. Copyright © 2021 Springer Nature.

Finally, we have developed an automated color-encoding process that converts digital color images to dithering patterns (**Fig. 2.73** and See Methods for details). Consequently, multi-color holograms of masterpieces were created with a spatial resolution as high as ~ 8,500 pixels of structural colors per inch (**Figs. 2.74-2.76**). Our PDA organogel is also highly transparent to be used as a transmission volume phase holographic grating (**Fig. 2.77**).

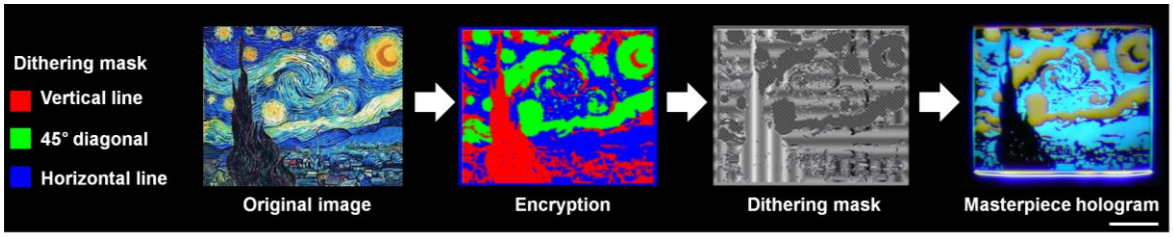

Fig. 2.73. A computer-assisted method to convert digital color images to structural color encrypted holograms. Scale bar is 200 μm. Copyright © 2021 Springer Nature.

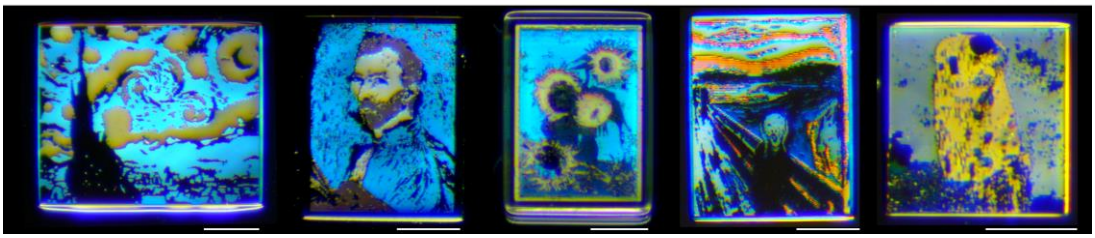

Fig. 2.74. Structural color encrypted PDA organogel micro-particles displaying *The Starry Night*, *Van Gogh self-portrait*, and *Sunflowers* by *Vincent van Gogh*, *The Scream* by *Edvard Munch*, and *The Kiss* by *Gustav Klimt*. Scale bar is 200 μm. Copyright © 2021 Springer Nature.

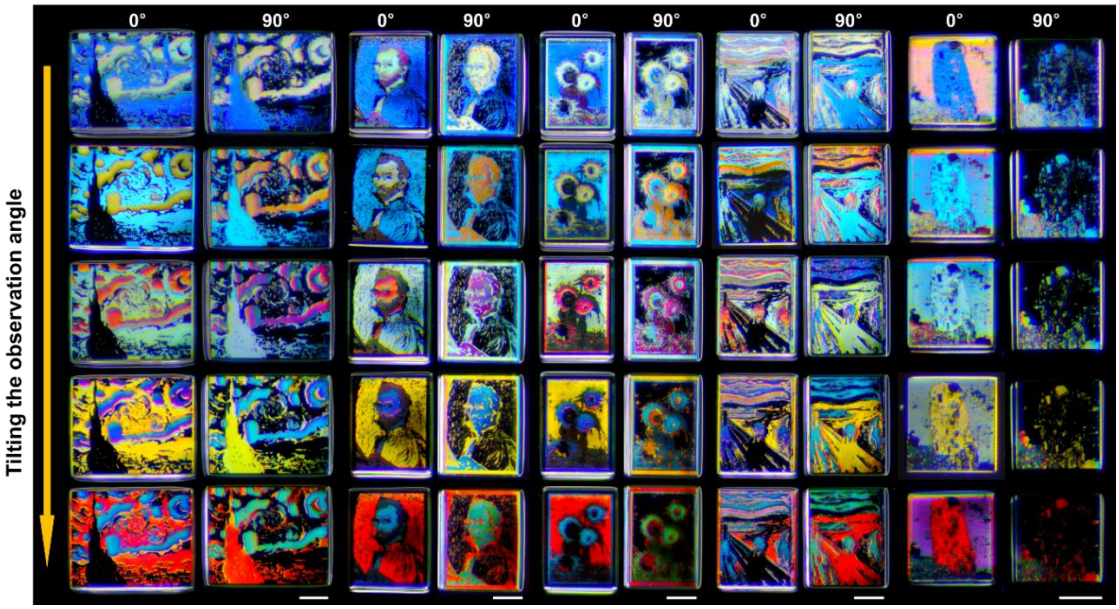

Fig. 2.75. Selective structural color change of masterpiece encrypted microstructures by changing the viewing angle. Scale bar is 200 μm. Copyright © 2021 Springer Nature.

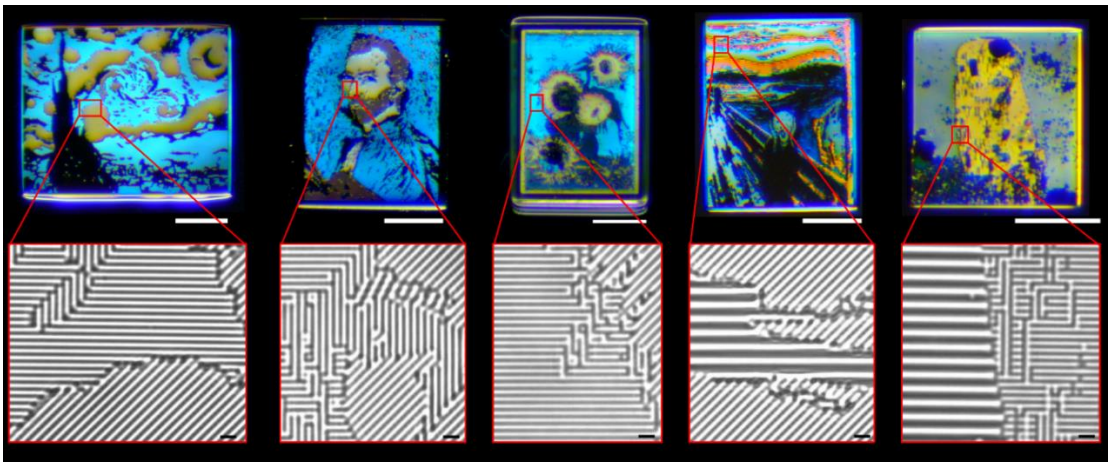

Fig. 2.76. Structural color (top), bright-field (middle), and maginified bright-field (bottom) images of masterpiece encrypted microstructures. Scale bars are 200 μm (top) and 5 μm (bottom). Copyright © 2021 Springer Nature.

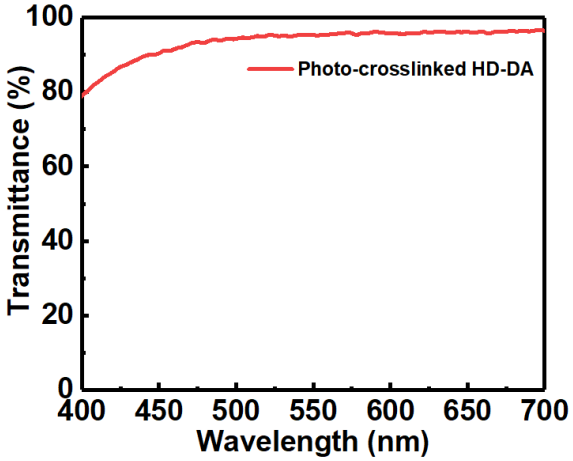

Fig. 2.77. Transmittance of photo-crosslinked HD-DA film. Copyright © 2021 Springer Nature.

In conclusion, we have invented a thin and flexible optical system that has a 2D grating function when expanded in aprotic solvents and 3D refractive index anisotropy when contracted in protic solvents. Our two-dimensionally patterned PDA organogels rapidly and reversibly display either unique 3D full parallax signals or structural colors in different solvents. This ability to reversibly expand and contract the polymeric structure enabled three holographic modes to be displayed in a single architecture, forming new polymeric hologram systems. Such holographic features originated from unique molecular and structural properties of our systems, which were theoretically studied by multiple simulations. Contrary to previous methods using expensive techniques such as an E-beam lithography to create holograms[51], our method is accessible and reproducible due to simple material synthesis, low costs of devices, and visibility using a portable imaging device (**Figs. 2.78-2.80**). Using the method, the organogel microstructures with almost unlimited number of high-resolution structural color codes can be produced with high throughput, demonstrating that our method has brought considerable progress in encryption and anti-counterfeiting technologies.

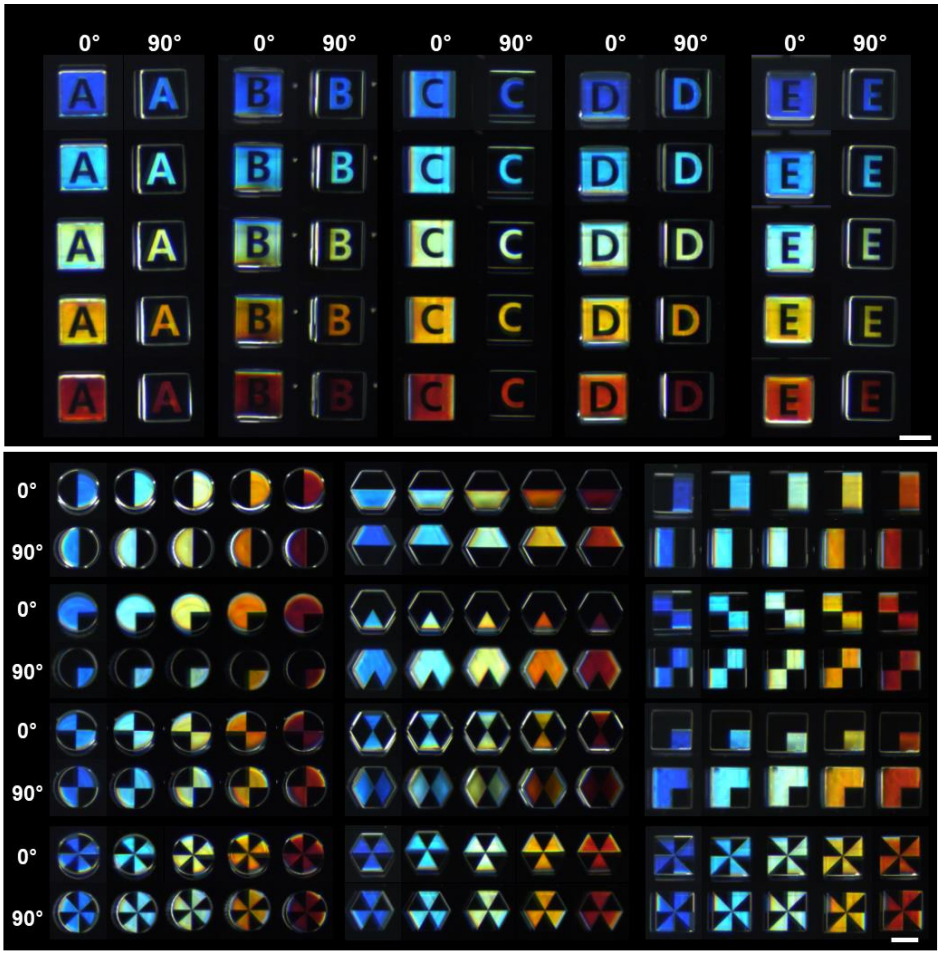

Fig. 2.78. Structural color on-off PDA organogel microstructures patterned with two types of line dithering mask (horizontal and vertical line). The letter encryption (top) and the section-based encryption (bottom) systems. Scale bars are 200 μm. Copyright © 2021 Springer Nature.

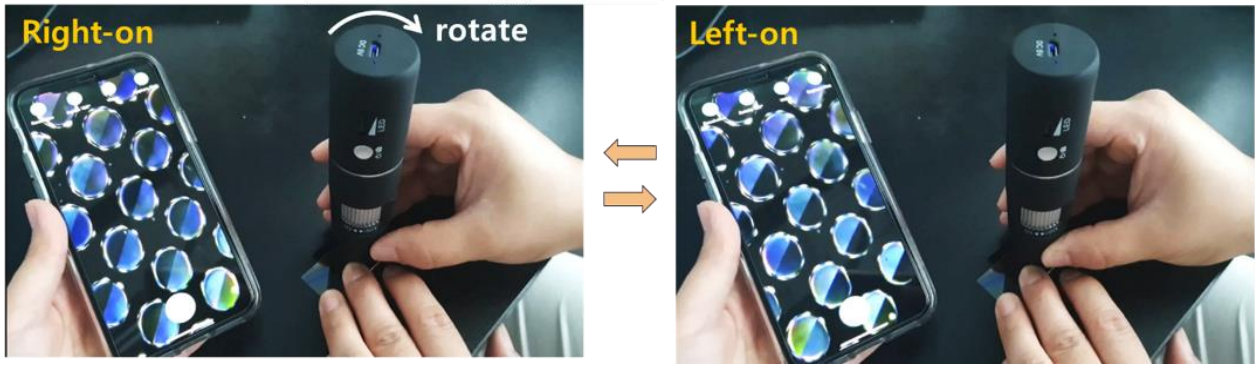

Fig. 2.79. Selective structural color changing of PDA organogels by rotating the portable imaging device. Copyright © 2021 Springer Nature.

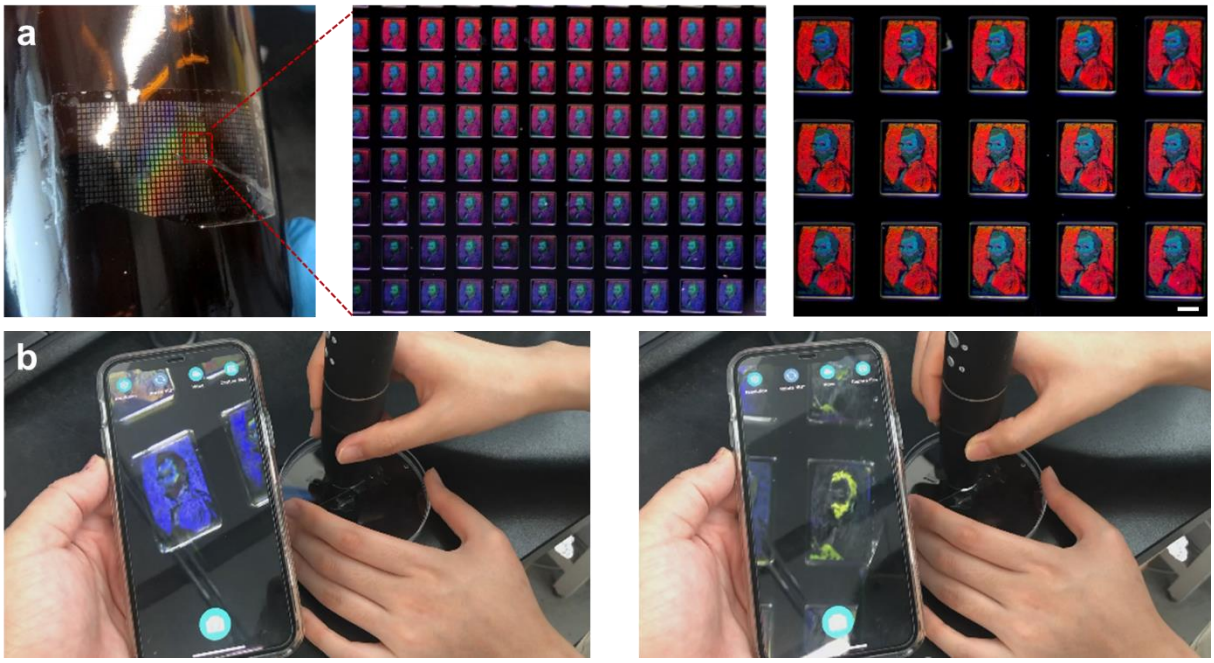

Fig. 2.80. a, A flexible free-standing PDMS film encoded with *Van Gogh self-portrait* hologram and attached to a beer bottle. **b,** A use of a portable device to selectively display structural colors of *Van Gogh self-portrait* holograms. Scale bar in (a) is 200 μm. Copyright © 2021 Springer Nature.

2. 3 Experimental section

Materials. 2,4-hexadiyn-1,6-diol (GFS chemicals, 97 %), tri-ethyl amine (Sigma-Aldrich, 99.5 %), acryloyl chloride (Sigma-Aldrich, 97 %), tetrahydrofuran (THF, Sigma-Aldrich, anhydrous 99.8 %), acetonitrile (Sigma-Aldrich, anhydrous 99.8 %), methanol (Sigma-Aldrich, anhydrous 99.8 %), dimethylsulfoxide (Sigma-Aldrich, 99.5 %), dimethylformamide (Sigma-Aldrich, anhydrous 99.8 %), 1,6-hexanediol diacrylate (Sigma-Aldrich, 80 %) and 2-hydroxy-2-methylpropiophenone (Darocur 1173, Sigma-Aldrich, 97 %). All chemicals were used without further purification.

Fabrication of conjugated PDA organogel microstructures. Conjugated organogel microstructures were fabricated with a customized Digital Micromirror Device (DMD) based mask-less photolithography system. 2,4-hexadiyn-1,6-diacrylate (HD-DA) was mixed with photo-initiator (Darocur 1173) by 9:1 (v/v). The precursor monomer solution was flowed into acrylated PDMS microfluidic channel and crosslinked by DMD patterned 365 nm UV light (11.44mW/ mm^2, SOLIS-365C, Thorlabs) through 20× objective (S plan Fluor ELWD, Nikon). The size and shape of conjugated organogel microstructure was controlled with DMD software (NIS-Element AR4.50.00). Crosslinked diacetylene organogel microstructure was further exposed to 254 nm UV light (2.21mW/ cm^2) for 30 mins to induce 1-4 addition photopolymerization resulting in a conjugated backbone.

Process of dithering mask lithography. Five dithering masks (hexagon, square, rhombus, horizontal

line, and vertical line) were programmed with MATLAB (MathWorks) by changing the periodicity of black and white pixels. Photocrosslinking of HD-DA was achieved by dithering masks patterned 365 nm UV light (11.44mW/ mm^2, SOLIS-365C, Thorlabs) through 20× objective (S plan Fluor ELWD, Nikon) using an inverted microscope (Ti-E, Nikon).

Azimuthal profile of dithering mask patterned PDA organogel microstructures. Oval profile plug-in in Image J was used to numerically evaluate the fluorescent intensity of each pattern by oval orientation from 0 to 2π. The resulting oval profile were graduated with gray-scale color map using MATLAB (MathWorks).

Fabrication process of structural color encrypted microstructures. Four types of dithering patterns (two types of diagonal lines, horizontal lines, and vertical lines) were designed by changing the periodicity of black and white pixels using MATLAB (MathWorks). Then each dithering mask was assigned to red, green, blue and black colors respectively. The colors were randomly arranged in the shape of a chessboard. Finally, using MATLAB (MathWorks), the structural color encoded dithering mask was created by matching the dithering pattern to each color. Structural color encrypted microstructures were fabricated with a customized digital micromirror device (DMD) based mask-less photolithography system using structural color encoded dithering masks. 2,4-hexadiyn-1,6-diacrylate (HD-DA) were mixed with photo-initiator (Darocur 1173) by 9:1 (v/v) and photo-crosslinked on the acrylated glass slide covered with the polydimethylsiloxane (PDMS) coated glass slide by dithering masks patterned 365 nm UV light (11.44mW/mm^2) through 20× objective.

Synthesis of 2,4-hexadiyn-1,6-diacrylate (HD-DA). To a solution of 2,4-hexadiyn-1,6-diol (1.00 g, 9.10 mmol) in tetrahydrofuran (50 mL) and triethylamine (2.29 g, 22.70 mmol) at room temperature, acryloyl chloride (2.47 g, 27.30 mmol) was added dropwise for 30 min. The resulting solution mixture was stirred for 4 h at 25 °C. After being concentrated in vacuo, the residue was dissolved in ethyl acetate and extracted using water three times, dried with $MgSO_4$, and filtered. The solvent was removed under a vacuum, and the residue was further purified using silica gel column chromatography (hexane/ethyl acetate = 5/1) to yield 1.10 g (56%) of the desired diacetylene monomer HD-DA as a transparent yellow liquid. ^{1}H nuclear magnetic resonance (NMR) spectra were recorded on a 400 MHz FT-NMR spectrometer (Bruker). NMR multiplicities are abbreviated as follows: *s* = singlet and *dd* = doublet of doublets. ^{1}H NMR (400 MHz, Chloroform-*d*) δ 6.40 (dd, *J* = 17.3, 1.3 Hz, 2H), 6.07 (dd, *J* = 17.3, 10.5 Hz, 2H), 5.84 (dd, *J* = 10.5, 1.3 Hz, 2H), and 4.76 (s, 4H). ^{13}C nuclear magnetic resonance (NMR) spectra were recorded on a 101 MHz FT-NMR spectrometer (Bruker). ^{13}C NMR (101 MHz, DMSO-d) δ 165.01, 133.28, 127.72, 75.50, 69.74, and 52.62.

Microfluidic device fabrication. Polydimethylsiloxane (PDMS, Sylgard) microfluidic channels were

fabricated through soft lithography[1]. Briefly, PDMS was mixed with a curing agent in a 10:1 ratio and degassed in vacuo for 20 min. The mixture solution was poured onto the SU-8 master and cured at 70 °C for 2 h. A glass slide (Deckglaser, 24 mm × 60 mm) was rinsed through sonication in ethanol and acetone for 15 min, incubated in 1 M NaOH solution for 1 h, and rinsed with deionized water. The PDMS channel and glass slide were treated using an oxygen-plasma process (FEMTO SCIENCE, CUTE-1MPR) for 1 min (100 W, 80 sccm). The PDMS channel was attached to a glass slide and heated at 90 °C for 2 h. A 2% (v/v) solution of 3-(trimethoxysilyl)propyl acrylate (TMSPA) was flowed into the PDMS channel and incubated for 30 min. The PDMS channel was rinsed with ethanol and heated at 90 °C for 30 min in a vacuum oven.

Acrylation of the glass slide. The glass slide was sonicated in ethanol and acetone for 15 min and incubated in 1 M NaOH solution for 1 h. After rinsing with deionized water, the glass slide was incubated in 3-(trimethoxysilyl)propyl acrylate (TMSPA) solution (2% in EtOH) for 30 min. The glass slides were rinsed with ethanol and heated at 90 °C for 30 min in a vacuum oven.

Fabrication process of PDA/1,6-hexanediol diacrylate interpenetrating microstructure. PDA/1,6-hexanediol diacrylate-interpenetrated microstructures were fabricated using a customized digital micromirror device (DMD) based mask-less photolithography system. 2,4-hexadiyn-1,6-diacrylate (HD-DA) was mixed with a photo-initiator (darocur 1173) by 9:1 (v/v). The precursor monomer solution was flowed into the acrylated PDMS microfluidic channel and crosslinked using 365 nm UV light (11.44 mW/mm^2, SOLIS-365C, Thorlabs) through a 20× objective (S plan Fluor ELWD 20× DIC N1, Nikon). The conjugated backbone of the fabricated PDA microstructure was photopolymerized upon irradiation with 254 nm UV light (2.21 mW/cm^2) for 30 min. The uncrosslinked HD-DA was rinsed with ACN, and 1,6-hexanediol diacrylate monomer solution mixed with a photo-initiator in a ratio of 9:1 (v/v) was flowed into the microfluidic channel. The interpenetrating 1,6-hexanediol diacrylate network was crosslinked using 365 nm UV light, and the crosslinking density was controlled by adjusting the exposure number to 365 nm UV light (3.81 mW/mm^2, 300 ms).

Imaging. Bright-field and fluorescence microscopy images were captured through 4× (Plan Fluor, Nikon), 10× (Plan Fluor, Nikon), and 20× objectives (S plan Fluor ELWD, Nikon) using a charge-coupled device (CCD) camera (CoolSNAPTM MYO, Photometrics). Fluorescence microcopy images were obtained using an excitation bandpass filter (483 nm CWL/31 nm Bandwidth, Edmund 25 optics) and emission bandpass filter (535 nm CWL/43 nm Bandwidth, Edmund optics). Confocal microscopy images were obtained using a confocal microscope (LSM 780 configuration 16 NLO, Carl Zeiss) with a 488 nm excitation laser source. Stacked 3D images were reconstructed using the IMARIS software (Bitplane AG). SEM images were obtained using scanning electron microscopy (SEM) (HITACHI S-4800). The structural color images were captured using a CCD camera (iPhone XS, Apple). The angle

of incident light was 14°, and the angle (θ) between the microarray and CCD camera was increased by 1°.

Characterization. UV-Vis absorption spectra were measured using a UV-Vis microspectrometer (CRAIC, 20/20 PV). Fluorescence emission spectra were measured using a laser scanning confocal microscope (FV1000, Olympus). Raman spectra were measured with a confocal laser Raman microscope (RAMANplus, Nanophoton) using 785 nm laser excitation. Raman spectra were recorded using a 300 l mm^{-1} grating and collected using a 50× objective (CFI L Plan EPI CR) with a laser power of 113.41 mW and an exposure time of 24 s. Reflectance spectra were measured using a compact fiber optic spectrometer (KESHET-PHOTON). Refractive indices were measured over the spectral range of 370–1000 nm using an ellipsometer (M-2000V, J. A. Woollam). X-ray photoelectron spectroscopy (XPS, Thermo scientific, ESCA Probe) spectra were acquired with a normal emission geometry using conventional monochromatic Al Kα radiation ($h\nu$ = 1486.6 eV). The pass energy was 50.0 eV. The transmittance spectrum was measured using a UV-Vis spectrometer (Cary 8454, Agilent Technologies).

AFM nanoindentation of PDA organogels. The Young's modulus of the PDA organogel immersed in methanol was measured using an atomic force microscope (AFM, NX-10, Parksystems). We used a gold-coated, silicon nitride cantilever with a tetrahedral tip (BioLever mini, BL-AC40TS-C2, spring constant = 0.09 N/m, Olympus), which, according to the manufacturer, exhibited enhanced sensitivity in measuring the force-distance curve in a liquid environment. The indentation was performed at a maximum loading force of 2.54 nN and a loading speed of 1 μm/sec. The Young's modulus was calculated by fitting the measured force-distance curve to the Hertzian contact model with a conical indenter using a data analysis software (XEI, Parksystems). The calculated Young's modulus was 1.56 ± 0.28 MPa and 0.88 ± 0.07 MPa ($n > 14$) for the PDA organogels uniformly crosslinked to the level of matrix and rod, respectively.

Finite element analysis (FEA). The hygroscopic swelling feature in the COMSOL Multiphysics software (version 5.3a) was used to simulate solvent-induced deformation of the PDA organogel. For rods and matrix, the change in solvent concentration in the model structure upon solvent exchange was calculated based on the volume expansion ratio measured for the PDA organogels crosslinked without dithering patterns to the level of rod or matrix. The volume change of the PDA organogel upon solvent exchange, as measured using laser scanning confocal microscopy, was sufficiently low for the model structure to be considered as a linear elastic material[21]. The dimensions of the model structure before deformation, including the radius of the disk-shaped matrix, the width of rods in a square cross-section, and the height of rods and matrix, which were 30 μm, 1.25 μm, and 30 μm, respectively, closely matched those of the patterned PDA organogel immersed in ACN. The bottom surface of the model structure was set by a fixed constraint, similar to the patterned PDA organogel attached to the glass

substrate.

For the model structure, a steady-state equation of motion in the absence of the body force is

$$(1) \quad 0 = \nabla \cdot (FS)^{\mathrm{T}}$$

where S is the second Piola-Kirchhoff stress tensor and F is the deformation gradient tensor. In the presence of the inelastic strain due to hygroscopic swelling, the constitutive equation for the case of geometric nonlinearity is

$$(2) \quad S = J_{\mathrm{inel}} F_{\mathrm{inel}}^{-1} (C : \varepsilon_{\mathrm{el}}) F_{\mathrm{inel}}^{-\mathrm{T}}$$

where ε is the Green-Lagrange strain tensor, C is the elasticity tensor, J is the determinant of F, and subscripts *el* and *inel* indicate the elastic and inelastic components, respectively. F_{inel} is defined as $I + \varepsilon_{\mathrm{inel}}$, where I is the identity matrix and $\varepsilon_{\mathrm{inel}}$ is the hygroscopic swelling, which can be calculated from the measured values of the volume expansion ratio of PDA organogels (**Fig. 2.29**). Using the definition of the Green-Lagrange strain tensor and the decomposition of the deformation gradient tensor,

$$(3) \quad \varepsilon_{\mathrm{el}} = \frac{1}{2}\left(F_{\mathrm{el}}^{\mathrm{T}} F_{\mathrm{el}} - I\right) \quad \text{and} \quad F_{\mathrm{el}} = F F_{\mathrm{inel}}^{-1}$$

the equation of motion can be solved numerically. The elasticity tensor was calculated from the Young's modulus and Poisson's ratio, which were, respectively, measured using the AFM nanoindentation method as described in the Supplementary Methods and assumed to be 0.33, which is typical for the polymer network with stiff backbones[54].

Fabrication process of free-standing PEG-DA film with embedded PDA organogels. The PDA organogel microstructures were fabricated using a customized digital micromirror device (DMD) based mask-less photolithography system using a hexagon dithering mask. The HD-DA monomer solution was photo-crosslinked by irradiating with 365 nm UV (11.44 mW/mm^2) at the desired positions using LabVIEW, and as a result, PDA organogels exhibiting structural color lettering were fabricated. After removing the uncrosslinked monomer solution using ACN, the PEG-DA resin solution was poured into the PDA organogels. After photo-crosslinking was conducted under 365 nm UV (0.03254 mW/mm^2, 10 s), the PEG-DA films with embedded PDA organogels were detached from the glass slide.

Fabrication of shape-morphing PDA organogel microstructures. 2,4-hexadiyn-1,6-diacrylate (HD-DA) was mixed with a photo-initiator (Darocur 1173) in a 9:1 (v/v) ratio. As shown in **Fig. 2.29**, the precursor HD-DA monomer was dropped on the PDMS-coated glass slide, and a glass slide with a 70

μm thickness spacer was placed over the PDMS-coated glass slide. The petal regions were photo-crosslinked using the desired dithering masks under 365 nm UV (11.44 mW/mm^2) irradiation for 8000 ms, and the synthesized petal-shaped microstructure adhered to a glass slide with a crosslinking density gradient along the thickness direction. After the glass slide was flipped over, an additional crosslinking process was carried out with a ring-shaped mask under 365 nm UV (11.44 mW/mm^2, 2000 ms) to inhibit the detachment of the microstructure from the glass slide when removing the PDMS top. The PDMS-coated glass slide was replaced with the acrylated glass slide, the center region was further photo-crosslinked with a circular mask under 365 nm UV (11.44 mW/mm^2, 2000 ms), and the fabricated microstructure was covalently bound to the acrylated glass slide. Finally, 1,4-addition polymerization of flower-like shape morphing microstructure was carried out upon exposure to 254 nm UV light.

Fabrication process of structural color encrypted microarray systems. Microstructures were fabricated using a LabVIEW controlled DMD based mask-less photolithography system. The precursor monomer solution was photo-crosslinked by irradiating with 365 nm UV while moving an optical stage, and as a result, 12 different types of structural color encrypted microstructures in a 4×3 array were fabricated (**Fig. 5d**). Note that the dithering mask for one microstructure consists of 4 types of dithering patterns (*i.e.*, horizontal, vertical line, and 30° and 60° diagonal line patterns).

Fabrication of the structural color encrypted PDMS film. The surface of the HD-DA microstructures was treated with oxygen plasma (FEMTO SCIENCE, CUTE-1MPR) for 1 min (50 W, 20 sccm) and coated with 1H,1H,2H,2H-pefluorooctyl trichlorosilane through vapor deposition. A mixture of PDMS and a curing agent was poured into a surface-modified HD-DA hologram microstructure array in a 10:1 ratio, and spin coating (500 rpm for 10 s) was performed to prepare a uniform PDMS film. After curing at 70 °C for 2 h, the PDMS film was detached.

Fabrication of the structural color encrypted microparticles. Encrypted microparticles were fabricated in a PDMS microfluidic channel using a stop-flow lithography technique[23]. Briefly, the precursor HD-DA monomer was flowed into a microfluidic channel and photo-crosslinked through the dithering mask patterned 365 nm UV irradiation.

2.4 Conclusion

In conclusion, we developed a conjugated organogel that reversibly displays 3 modes of holograms in a single architecture. Using dithering mask lithography, we realized two-dimensional patterns with varying crosslinking density on a conjugated polydiacetylene. In protic solvents, the organogel contracts anisotropically to develop optical and structural heterogeneities along the third dimension, displaying holograms in the form of three-dimensional full parallax signals, both in fluorescence and bright-field

microscopy imaging. In aprotic solvents, these heterogeneities diminish as organogels expand, recovering the two-dimensional periodicity to display a third hologram mode based on iridescent structural colors. Our study presents a next-generation hologram manufacturing method for multi-level encryption technologies.

2.5 References

1. Kang, Y., Walish, J. J., Gorishnyy, T. & Thomas, E. L. Broad-wavelength-range chemically tunable block-copolymer photonic gels. *Nat. Mater.* **6**, 957-960 (2007).
2. Matsubara, K., Watanabe, M. & Takeoka, Y. A thermally adjustable multicolor photochromic hydrogel. *Angew. Chem. Int. Ed.* **46**, 1688-1692 (2007).
3. Kim, H. *et al.* Structural colour printing using a magnetically tunable and lithographically fixable photonic crystal. *Nat. Photonics* **3**, 534-540 (2009).
4. Honda, M., Seki, T. & Takeoka, Y. Dual Tuning of the Photonic Band-Gap Structure in Soft Photonic Crystals. *Adv. Mater.* **21**, 1801-1804 (2009).
5. Holtz, J. H. & Asher, S. A. Polymerized colloidal crystal hydrogel films as intelligent chemical sensing materials. *Nature* **389**, 829-832 (1997).
6. Sagara, Y. & Kato, T. Mechanically induced luminescence changes in molecular assemblies. *Nat. Chem.* **1**, 605-610 (2009).
7. Chiappelli, M. C. & Hayward, R. C. Photonic Multilayer Sensors from Photo-Crosslinkable Polymer Films. *Adv. Mater.* **24**, 6100-6104 (2012).
8. Wang, Q. M., Gossweiler, G. R., Craig, S. L. & Zhao, X. H. Cephalopod-inspired design of electro-mechano-chemically responsive elastomers for on-demand fluorescent patterning. *Nat. Commun.* **5**, 4899 (2014).
9. Luo, W. *et al.* Steric-repulsion-based magnetically responsive photonic crystals. *Adv. Mater.* **26**, 1058-1064 (2014).
10. Xiao, F. B. *et al.* Smart Photonic Crystal Hydrogel Material for Uranyl Ion Monitoring and Removal in Water. *Adv. Funct. Mater.* **27**, 1702147 (2017).
11. Couturier, J. P., Sutterlin, M., Laschewsky, A., Hettrich, C. & Wischerhoff, E. Responsive Inverse Opal Hydrogels for the Sensing of Macromolecules. *Angew. Chem. Int. Ed.* **54**, 6641-6644 (2015).
12. Asher, S. A., Holtz, J., Liu, L. & Wu, Z. J. Self-Assembly Motif for Creating Submicron Periodic Materials. Polymerized Crystalline Colloidal Arrays. *J. Am. Chem. Soc.* **116**, 4997-4998 (1994).
13. Weissman, J. M., Sunkara, H. B., Tse, A. S. & Asher, S. A. Thermally Switchable Periodicities and Diffraction from Mesoscopically Ordered Materials. *Science* **274**, 959-960 (1996).
14. Campbell, M., Sharp, D. N., Harrison, M. T., Denning, R. G. & Turberfield, A. J. Fabrication

of photonic crystals for the visible spectrum by holographic lithography. *Nature* **404**, 53-56 (2000).

15. Tondiglia, V. P., Natarajan, L. V., Sutherland, R. L., Tomlin, D. & Bunning, T. J. Holographic formation of electro-optical polymer-liquid crystal photonic crystals. *Adv. Mater.* **14**, 187-191 (2002).
16. Orosco, M. M., Pacholski, C., Miskelly, G. M. & Sailor, M. J. Protein-coated porous-silicon photonic crystals for amplified optical detection of protease activity. *Adv. Mater.* **18**, 1393-1396 (2006).
17. Yoon, J., Lee, W. & Thomas, E. L. Thermochromic block copolymer photonic gel. *Macromolecules* **41**, 4582-4584 (2008).
18. Tay, S. *et al.* An updatable holographic three-dimensional display. *Nature* **451**, 694-698 (2008).
19. Zhou, Y., Hauser, A. W., Bende, N. P., Kuzyk, M. G. & Hayward, R. C. Waveguiding Microactuators Based on a Photothermally Responsive Nanocomposite Hydrogel. *Adv. Funct. Mater.* **26**, 5447-5452 (2016).
20. Lim, H. S., Lee, J. H., Walish, J. J. & Thomas, E. L. Dynamic Swelling of Tunable Full-Color Block Copolymer Photonic Gels via Counterion Exchange. *ACS Nano* **6**, 8933-8939 (2012).
21. Kim, S. *et al.* Silk inverse opals. *Nat. Photonics* **6**, 817-822 (2012).
22. Burgess, I. B., Lončar, M. & Aizenberg, J. Structural colour in colourimetric sensors and indicators. *J. Mater. Chem. C* **1**, 6075-6086 (2013).
23. Lee, G. H. *et al.* Chameleon-Inspired Mechanochromic Photonic Films Composed of Non-Close-Packed Colloidal Arrays. *ACS Nano* **11**, 11350-11357 (2017).
24. Jiang, N. *et al.* Laser Interference Lithography for the Nanofabrication of Stimuli-Responsive Bragg Stacks. *Adv. Funct. Mater.* **28**, 1702715 (2018).
25. Zhao, Q. L., Wang, Y. L., Cui, H. Q. & Du, X. M. Bio-inspired sensing and actuating materials. *J. Mater. Chem. C* **7**, 6493-6511 (2019).
26. Liao, J. L. *et al.* Multiresponsive Elastic Colloidal Crystals for Reversible Structural Color Patterns. *Adv. Funct. Mater.* **29**, 1902954 (2019).
27. Watanabe, T. *et al.* Photoresponsive hydrogel microstructure fabricated by two-photon initiated polymerization. *Adv. Funct. Mater.* **12**, 611-614 (2002).
28. Li, J., Liang, G. Q., Zhu, X. L. & Yang, S. Exploiting Nanoroughness on Holographically Patterned Three-Dimensional Photonic Crystals. *Adv. Funct. Mater.* **22**, 2980-2986 (2012).
29. Li, M. G., Humayun, M., Hughes, B., Kozinski, J. A. & Hwang, D. K. A microfluidic approach for the synthesis and assembly of multi-scale porous membranes. *RSC Adv.* **5**, 100024-100029 (2015).
30. Liu, E. Y., Jung, S. & Yi, H. M. Improved Protein Conjugation with Uniform, Macroporous Poly(acrylamide-co-acrylic acid) Hydrogel Microspheres via EDC/NHS Chemistry. *Langmuir*

32, 11043-11054 (2016).

31. Wu, Y., Liang, J., Horkay, F. & Libera, M. Antimicrobial Loading into and Release from Poly(ethylene glycol)/Poly(acrylic acid) Semi-interpenetrating Hydrogels. *J. Polym. Sci. Pol. Phys.* **54**, 64-72 (2016).
32. Beristain, M. F., Estrada, M. R., Ortega, A., Claverie, A. L. & Ogawa, T. Radical stabilization of aromatic diacetylenes (dinaphthylbutadiynes) in the free radical polymerization of methyl methacrylate. *Polym. J.* **48**, 963-967 (2016).
33. Beristain, M. F., Munoz, E. & Ogawa, T. Polymerization of diphenylbutadiyne derivatives in solution by free radical initiator. *J. Macromol. Sci. A* **44**, 605-611 (2007).
34. Beristain, M. F., Bucio, E., Burillo, G., Munoz, E. & Ogawa, T. Study on the interaction of diarylbutadiynes with free radicals: Interaction with propagating radicals of some vinyl monomers. *Polym. Bull.* **43**, 357-364 (1999).
35. Kamoun, E. A., El-Betany, A., Menzel, H. & Chen, X. Influence of photoinitiator concentration and irradiation time on the crosslinking performance of visible-light activated pullulan-HEMA hydrogels. *Int. J. Biol. Macromol.* **120**, 1884-1892 (2018).
36. Deng, K. *et al.* Preparation of poly(methyl acrylate)/TiO_2 composites by potassium diperiodatocuprate initiated grafting copolymerization. *Iran. Polym. J.* **19**, 17-25 (2010).
37. Lee, M.-J. & Lee, B.-D. Prediction of radical reaction stie(s) of polycylic aromatic hydrocarbons by atomic charge distribution calculation using the DFT method. *Tetrahedron Lett.* **51**, 3782-3785 (2010).
38. Kim, J. M. *et al.* A polydiacetylene-based fluorescent sensor chip. *J. Am. Chem. Soc.* **127**, 17580-17581 (2005).
39. Lee, J., Kim, H. J. & Kim, J. Polydiacetylene liposome arrays for selective potassium detection. *J. Am. Chem. Soc.* **130**, 5010-5011 (2008).
40. Lee, J., Jun, H. & Kim, J. Polydiacetylene-Liposome Microarrays for Selective and Sensitive Mercury(II) Detection. *Adv. Mater.* **21**, 3674-3677 (2009).
41. Lauher, J. W., Fowler, F. W. & Goroff, N. S. Single-crystal-to-single-crystal topochemical polymerizations by design. *Acc. Chem. Res.* **41**, 1215-1229 (2008).
42. Day, D. & Lando, J. B. Structure Determination of a Poly(Diacetylene) Monolayer. *Macromolecules* **13**, 1483-1487 (1980).
43. Menzel, H., Mowery, M. D., Cai, M. & Evans, C. E. Vertical positioning of internal molecular scaffolding within a single molecular layer. *J. Phys. Chem. B* **102**, 9550-9556 (1998).
44. Batchelder, D. N. *et al.* Self-Assembled Monolayers Containing Polydiacetylenes. *J. Am. Chem. Soc.* **116**, 1050-1053 (1994).
45. Carpick, R. W., Sasaki, D. Y., Marcus, M. S., Eriksson, M. A. & Burns, A. R. Polydiacetylene films: a review of recent investigations into chromogenic transitions and nanomechanical

properties. *J. Phys.: Condens. Matter* **16**, R679-R697 (2004).

46. Filhol, J. S. *et al.* Polymorphs and Colors of Polydiacetylenes: A First Principles Study. *J. Am. Chem. Soc.* **131**, 6976-6988 (2009).
47. Goodman, J. W. *Introduction to Fourier optics* (Roberts and Company Publishers, 2005).
48. Vyas, U. & Christensen, D. Ultrasound Beam Simulations in Inhomogeneous Tissue Geometries Using the Hybrid Angular Spectrum Method. *IEEE Trans. Ultrason. Ferroelectr. Freq. Control* **59**, 1093-1100 (2012).
49. Yang, J. M., Li, J. W., He, S. L. & Wang, L. H. V. Angular-spectrum modeling of focusing light inside scattering media by optical phase conjugation. *Optica* **6**, 250-256 (2019).
50. X. Y. Duan, S. Kamin, N. Liu, Dynamic plasmonic colour display. *Nat. Commun.* **8**, 14606 (2017).
51. D. D. Wen, J. J. Cadusch, J. Meng, K. B. Crozier, Multifunctional Dielectric Metasurfaces Consisting of Color Holograms Encoded into Color Printed Images. *Adv. Funct. Mater.* **30**, 1906415 (2020).
52. Lee, J. *et al.* Universal process-inert encoding architecture for polymer microparticles. *Nat. Mater.* **13**, 524-529 (2014).
53. Y. Liu *et al.*, Inkjet-printed unclonable quantum dot fluorescent anti-counterfeiting labels with artificial intelligence authentication. *Nat. Commun.* **10**, 2409 (2019).
54. Nolte, A. J., Cohen, R. E. & Rubner, M. F. A Two-Plate Buckling Technique for Thin Film Modulus Measurements: Applications to Polyelectrolyte Multilayers. *Macromolecules* **39**, 4841-4847 (2006).

Chapter 3. Highly Stable Upconverting nanocrystal-Polydiacetylenes nanoplates for Orthogonal Dual Signaling-based Detection of Cyanide

This chapter includes the following contents:

J. Oh, I. Jeon, D. Kim, Y. You, D. Baek, S. J. Kang, and J. Lee*. *ACS Appl. Mater. Interfaces* **12**, 4934-4943 (2020).

3.1 Introduction

Polydiacetylene (PDA), one of the conjugated polymers, has been widely studied for development of bio/chemo-sensor platforms due to its unique optical properties that cause blue-to-red color change and red fluorescent emission in response to external stimuli[1–5]. It is well known that photo-induced polymerization converts diacetylene monomers to blue-colored conjugated PDA via 1,4-addition reaction. PDA generally has an absorption maximum at 650 nm corresponding to blue color. Upon exposure to external stimuli, PDA is known to change color from blue to red with subsequent red fluorescent emission, thereby demonstrating the dual signaling capacity[1,2]. These unique optical transitions are likely triggered by conformational changes in the conjugated backbone of PDA induced by a variety of external stimuli[1-3]. Many selective and sensitive PDA sensor platforms have been extensively studied by utilizing this unique optical property to detect pH[6], temperature[7–10], mechanical stress[11,12], and biological molecules[13,14]. These platforms have been developed to detect various types of targets by fabricating spherical liposomes[1,2,15–18], and mono/bilayers[19,20], or by carrying them in polymer matrices[21,22].

Conventional design principles for the selective PDA sensors have been applied by covalently attaching a receptor moiety to the head group of diacetylene monomers that specifically interacts with the target to prevent non-specific interactions with any analogs[1,2,15–18]. Many researchers have succeeded in developing selective PDA sensor platforms to a certain extent using the above mentioned specific lock-and-key interactions between receptor and target molecules[1,2,13–18]. The design studies of the receptor-target interactions to generate a selective detection capability on PDA sensor systems have mostly focused on chemically or structurally similar target analogs. However, for most PDA sensors, external stimuli such as temperature, mechanical agitation, organic solvents, acids, and bases result in selectivity loss and induce a non-specific blue-to-red color change due to the dissociation of the supramolecular PDA assembly into individual PDA fragments[23]. Recently, protective layer[24] and

electrospun fiber[25,26] methods have been introduced to update the design principle to produce stable PDA sensor platforms. Despite these improvements, however, PDA systems still have critical disadvantages for practical application because they produce non-specific color change when heated[26] , treated with organic solvents[24,25], and under mechanical stresses[11]. Moreover, most PDA systems have an intrinsic disadvantage due to the fluorescence emission efficiency being very low[27], and there have been no practical sensor platforms utilizing both colorimetric and fluorescence signals that can be utilized during the day and at night. Although much effort has been made to develop dual signaling PDA sensor systems[28–30] using organic fluorescent dyes and quantum dots, most sensor platforms are solution-based and not suitable for portable detection systems. Furthermore, organic dyes or quantum dots used in current dual sensor systems are very unstable when exposed to external perturbations such as organic solvents, acids, bases, moisture, light, and heat[31–33]. Therefore, it is imperative to develop a PDA sensor system that is sufficiently stable to maintain its blue phase in harsh environments and exhibits detectable fluorescence and colorimetric signals required for practical and stable dual signaling sensor applications.

Herein, we address this challenge by using a universal PDA sensor platform with a dual signaling capability that makes the supramolecular structure of PDA sufficiently stable to withstand external perturbations and perform selective colorimetric and luminescence change–based dual signaling of CN. The strong intercalation of metal ions and hydrophobic intermolecular interaction have been utilized to build highly stable PDA supramolecules exhibiting an unprecedented optical stability. Upconverting nanocrystals (UCNs) with a superior optophysical stability have also been incorporated into the highly stable PDA sensor system to counter the intrinsically weak fluorescence emissions of PDA systems and enable practical colorimetric and luminescent dual signaling in an orthogonal manner. Lastly, to extend the applicability of UCNs/PDA sensor systems to real field applications, we developed a portable device for CN anion detection based on the recognition of luminescence color changes of these systems. The obtained results clearly demonstrate the validity and effectiveness of our approach and can provide insights into a universal design principle for a stable and practical dual signaling PDA sensor platform to rapidly inspect for CN ions in the drinking water industry under harsh environments.

3.2 Results and Discussion

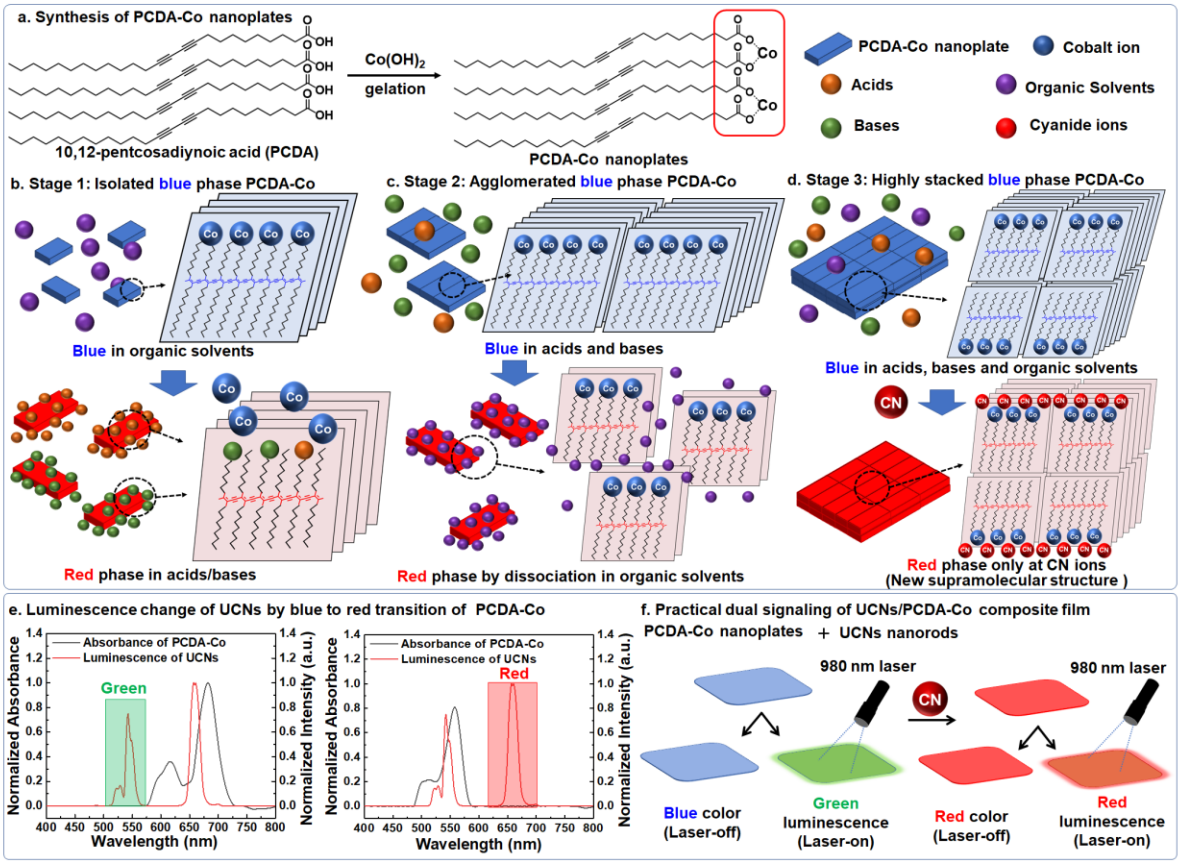

Fig. 3.1. The schematic of fabricating highly stacked PCDA-Co nanoplates. **a,** Synthesis of PCDA-Co with 10,12-pentacosadiynoic acid (PCDA) and cobalt dihydroxide ($Co(OH)_2$). **b,** Stage 1: color change of isolated PCDA-Co nanoplates upon addition of acids, bases, and organic solvents. **c,** Stage 2: Color change of agglomerated PCDA-Co nanoplates upon addition of organic solvents. **d,** Stage 3: Color change of highly stacked PCDA-Co nanoplates upon addition of CN ions. **e,** Absorbance overlap of PCDA-Co supramolecules with luminescence of UCNs. **f,** Dual signaling by luminescence and color change of UCNs/PCDA-Co nanoplate composite film upon addition of CN ions. Copyright © 2020 American Chemical Society.

We synthesized a PDA supramolecular complex having divalent metal cations by intercalating the latter into 10,12-pentacosadiynoic acid (PCDA) diacetylene monomers (**Fig. 3.1a**). Among variety of divalent metal ions, Co^{2+} was used to enhance the stability of the PDA sensor and facilitate its function as a receptor featuring strong interactions with CN anions, which are commonly found in drinking water[34,35]. Cobalt has been used to synthesize antidotes such as hydroxocobalamin, and dicobalt edetate that can efficiently detoxify CN poisoning in blood stream[36]. Cobalt ions rapidly chelate with CN anions to form cobalt-cyanide (Co-CN) complexes, that ultimately produces a nontoxic cyanocobalamin,

which is then excreted in the urine[37,38]. Earlier work has demonstrated that repulsion between the probe and target complexes at the PDA supramolecular structure, induces conformational changes in the conjugated backbone of PDA and also a colorimetric transition (blue to red), as along with a fluorescence emission[1,2,16,17]. We hypothesized that similar conformational changes occur in our PDA-based CN ion detection system. The cobalt moiety at the head group of PDA has strong ionic bond interaction with CN anions and generates high mechanical stress on the assembled conjugated backbone of PDA, causing a blue-to-red color transition.

The ionic bond between the carboxylic groups and metal ions results in PCDA-metal complex supramolecules, the strong hydrophobic interaction of long alkyl chains in PCDA-Co supramolecules is utilized to produce a stackable PCDA-metal supramolecular structure as shown in **Fig. 3.1a**. At stage 1 (**Fig. 3.1b**), each stack of the isolated blue-phase PCDA-Co supramolecules can freely rotate their hydrophobic alkyl chains when treated with acids and bases. Upon exposure to bases, the existing ionic bond between two carboxylate groups and one divalent Co ion is dissociated. A new ionic bond is then generated between one carboxylate group and one monovalent metal ion from the base, resulting in the dissociation of the PCDA-Co supramolecules. In case of exposure to acids, one divalent Co ion in the two carboxylates is replaced by one acidic proton, therefore PCDA-Co supramolecules will collapse. These acid/base-induced alkyl chain rotations ultimately cause the dissociation and collapse of PCDA-Co supramolecules and thus lead to conformational changes in the conjugated backbone of PCDA-Co supramolecules, which are accompanied by a blue-to-red color transition. Organic solvents, however, are unable to induce any color transition because the isolated PCDA-Co supramolecules are already dissociated and stabilized by THF during synthesis. Therefore, no further stress induced by structural perturbations can exist in organic solvents (**Fig. 3.1b**).

During stage 2, the stability of the agglomerated PCDA-Co supramolecular structure is enhanced by the strong hydrophobic intermolecular interaction between isolated PCDA-Co supramolecules, and dissociation into isolated PCDA-Co supramolecules occurs in the presence of organic solvents. The free rotation of alkyl chains when treated with acids and bases is not prevalent at this stage as illustrated in **Fig. 3.1c**. Thus, we expect that agglomerated PCDA-Co supramolecules will remain in blue phase upon treatment with acids and bases but change to red phase in the presence of organic solvents.

At stage 3, intermolecular hydrophobic stacking interactions are maximized, and conformational changes induced by acids/bases or organic solvents are forbidden, which results in highly stacked PCDA-Co supramolecules (**Fig. 3.1d**). These highly stacked PCDA-Co supramolecules are expected to maintain the blue phase upon interaction with acids and bases, organic solvents, and temperature, due to their enhanced stability, however, they change to the red phase under a strong specific interaction between CN and Co ions. We also assume that the latter may create another type of supramolecular

structure, along with color transition from blue to red, because the typical conformational change in the conjugated PDA backbone the rotation of alkyl chain is structurally forbidden in the highly stacked PCDA-Co supramolecular structure that is formed at stage 3.

In addition, we devised a practical dual signaling detection system that overcomes the low fluorescence emission intensity of the PDA system by incorporating UCNs into the PDA supramolecular structure. The resulting UCNs/PCDA-Co nanoplate composite systems display a considerable overlap between the luminescence spectra of UCNs and the absorption spectra of PDA, therefore featuring a practical dual signaling capability based on a colorimetric transition and luminescence change (**Fig. 3.1e**). The initial luminescent green color of the UCNs changes to red when the blue PCDA-Co supramolecules turn red upon reaction with the target CN ions (**Fig. 3.1f**). Furthermore, characteristics of UCNs including the large anti-Stokes shift[39], lack of background autofluorescence[40,41], and high photo-stability[42] in the presence of external environments facilitate the robustness of the PDA sensor platform as a signaling sensor system. In addition, the color change in the PDA due to a local temperature increase triggered by laser irradiation at 980 nm is not expected to occur given the superior thermal stability of PDA supramolecular structure investigated.

Stage 1: Color transition of the isolated PCDA-Co nanoplates in solution

We initially synthesized isolated PCDA-Co supramolecules in solution and examined CN detection capability. Briefly, PCDA dissolved in THF was reacted with the cobalt dihydroxide in water, resulting in viscous PCDA-Co supramolecules (see the Experimental Section for details).

Next, PCDA-Co solution was polymerized by UV irradiation at 254 nm wavelength. The resulting polymerized PCDA-Co supramolecules exhibit nanoplate like morphology (**Fig. 3.2**). A rapid colorimetric transition (from blue to red) was observed in the isolated PCDA-Co nanoplates in solution state, with this change being induced by exposure to CN ions of concentrations as low as 0.5 mM (**Figs. 3.3 and 3.4**). Addition of CN ions resulted in a decrease in the intensity of the absorption peak at 680 nm and appearance of the one at 550 nm (**Fig. 3.3b**). The fluorescence intensity of isolated PCDA-Co nanoplate solution also increased upon the exposure to CN ions (**Fig. 3.3c**).

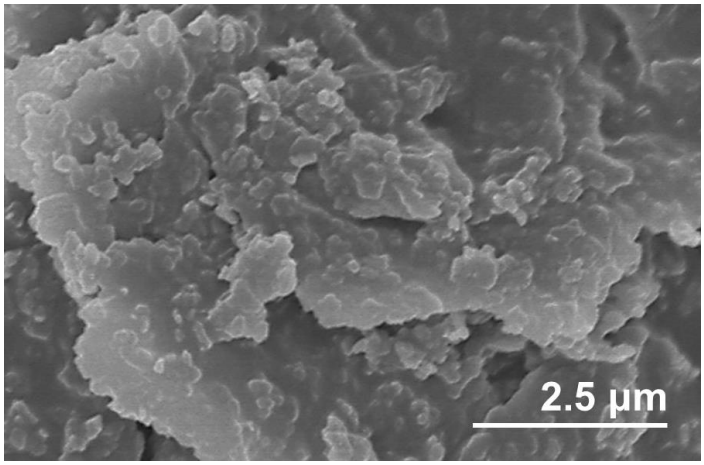

Fig. 3.2. SEM image of isolated PCDA-Co nanoplates. Copyright © 2020 American Chemical Society.

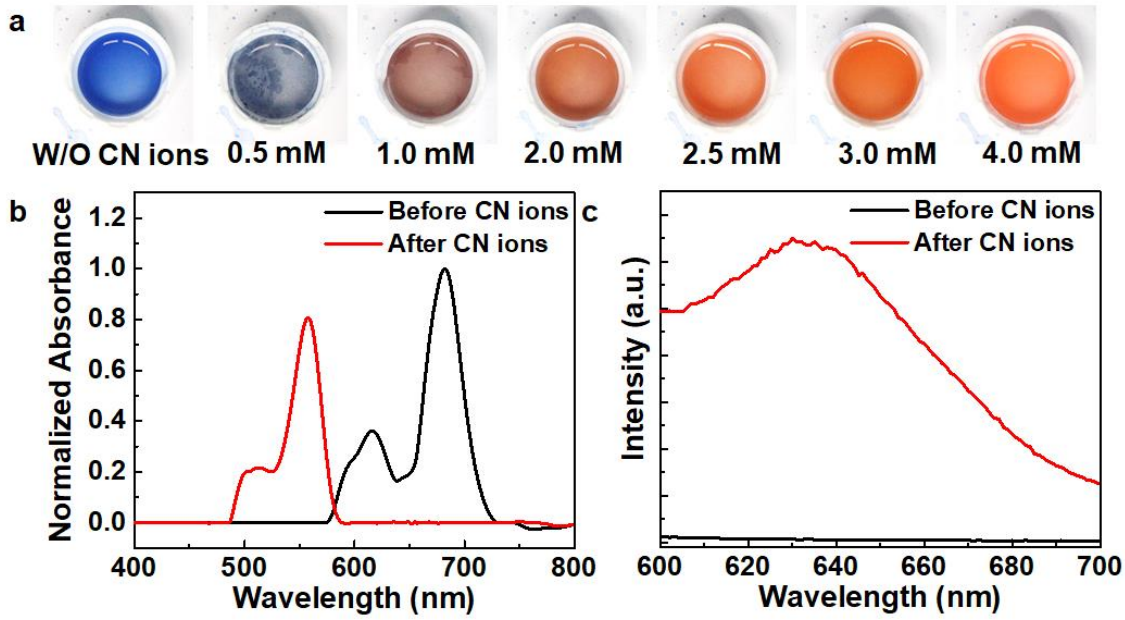

Fig. 3.3. a, Color change observed in isolated PCDA-Co nanoplates ($R_{PCDA/Co}$ = 0.33) in solution upon the addition of various concentrations of CN ions. (B) UV-Vis and (C) fluorescence spectra change in isolated PCDA-Co nanoplates before/after exposure to 4 mM of CN ions (excitation at 480 nm). Copyright © 2020 American Chemical Society.

Fig. 3.4 Rapid color changes observed for isolated PCDA-Co nanoplates in solution after treatment

with CN ions (4 mM).

As hypothesized in the stage 1 of the **Fig. 3.1**, these isolated PCDA-Co nanoplates in solution did not exhibit blue-to-red color transition upon exposure to organic solvents (**Figs. 3.5a and 3.6a**).

However, these isolated PCDA-Co nanoplates exhibited non-specific blue-to-red color transition upon exposure to acids, bases, and thermal stress at 90 °C (**Figs. 3.5b and 3.5c**). The absorbance at 680 nm decreased, while that at 550 nm increased upon exposure to acids, bases, and thermal stress (90 °C) (**Fig. 3.6**). From these observations, we inferred that the intermolecular interaction between individual PCDA-Co nanoplates in THF, was not strong enough to maintain the structure of assembled alkyl chain in PCDA-Co nanoplates, which led to easy rotation of the alkyl chain in presence of acids, bases, and thermal stress.

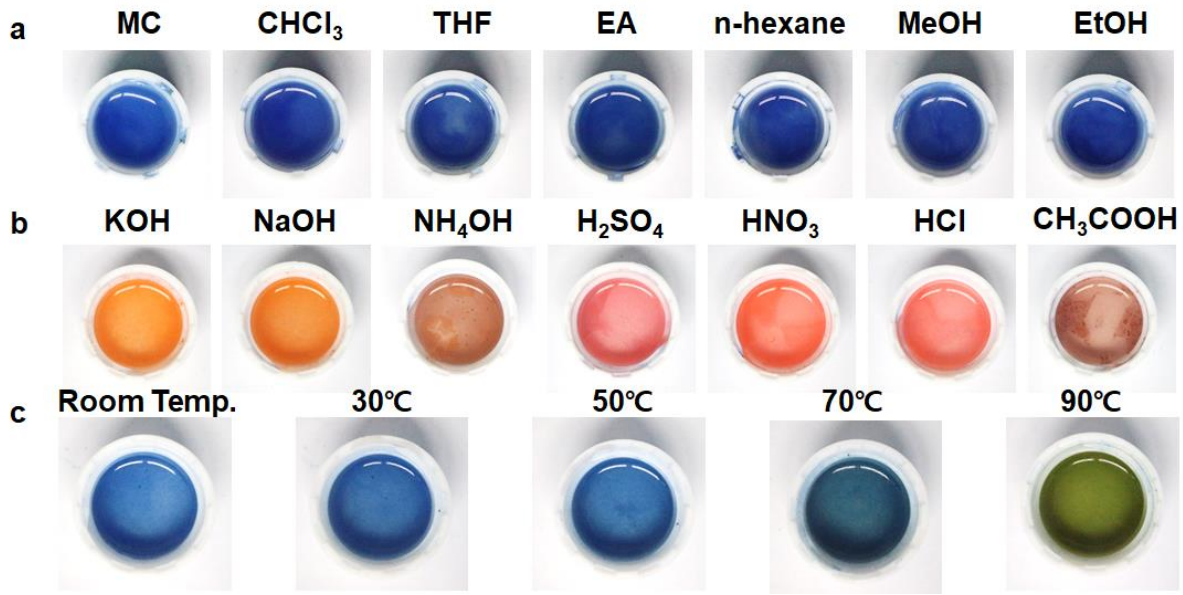

Fig 3.5. a-c, Color change observed in isolated PCDA-Co nanoplates ($R_{PCDA/Co}$ = 0.33) in solution, after introducing (a) organic solvents, (b) 4 mM of acids and bases, and (c) heat. Copyright © 2020 American Chemical Society.

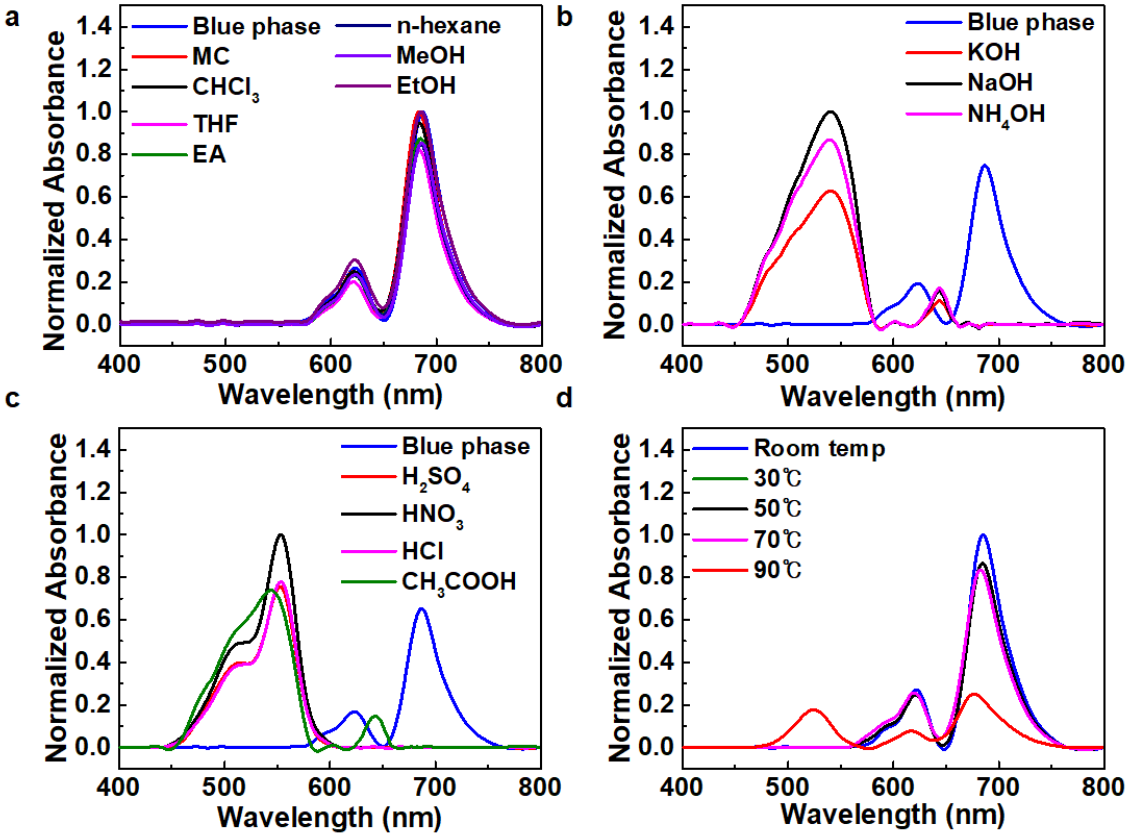

Fig 3.6. a-d, Change in UV-vis absorption intensities of isolated PCDA-Co nanoplates upon treatment with (a) organic solvents, (b) bases, (c) acids, and (d) thermal stress. Copyright © 2020 American Chemical Society.

In order to increase the structural stability of the PCDA-Co nanoplates, we controlled the ratio of ionic bonds between PCDA and cobalt ions by altering their initial molar ratio ($R_{PCDA/Co}$) from 3:1 to 1:3 as shown in **Fig. 3.7**. We hypothesized that the higher ratio of cobalt ions in PCDA, provides stronger ionic bonding to create the highly packed supramolecular structure. However, solutions containing different molar ratios ($R_{PCDA/Co}$) of PCDA-Co nanoplates showed a non-specific color transition upon exposure to acid/bases (**Fig. 3.7**) and exhibited similar characteristic color transitions toward CN ions (**Fig. 3.8**).

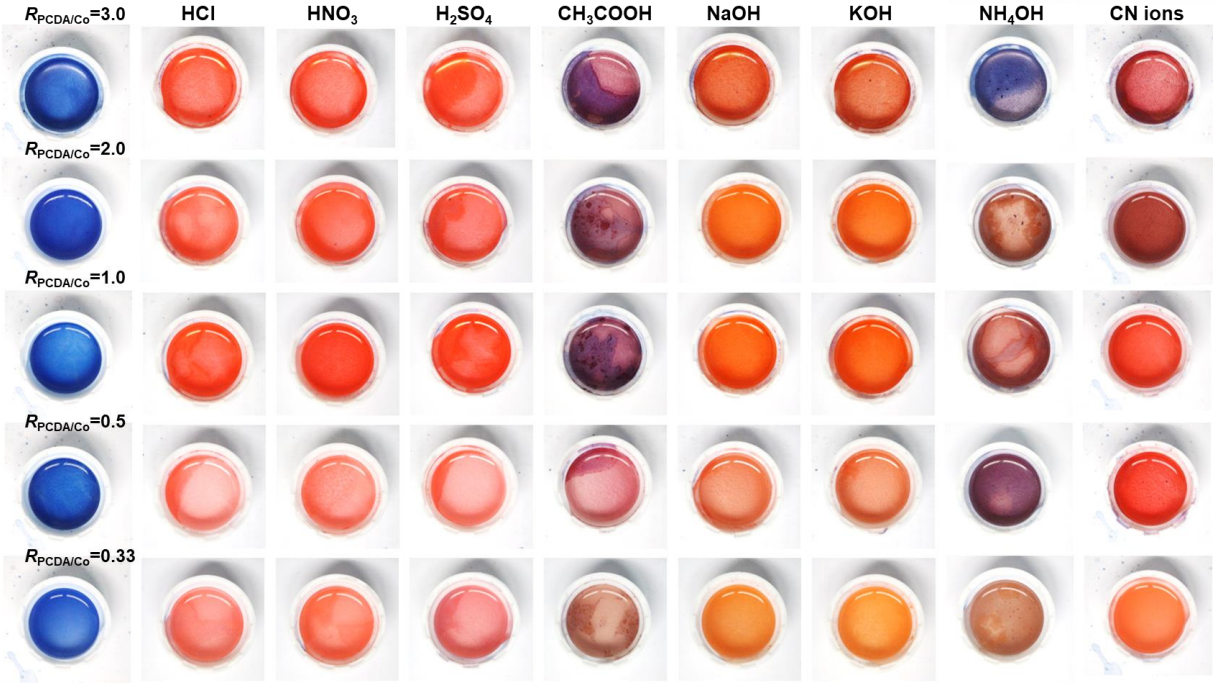

Fig. 3.7. Color changes observed for solution-phase isolated PCDA-Co nanoplates prepared using various $R_{PCDA/Co}$ and treated with acids, bases, and CN ions. Copyright © 2020 American Chemical Society.

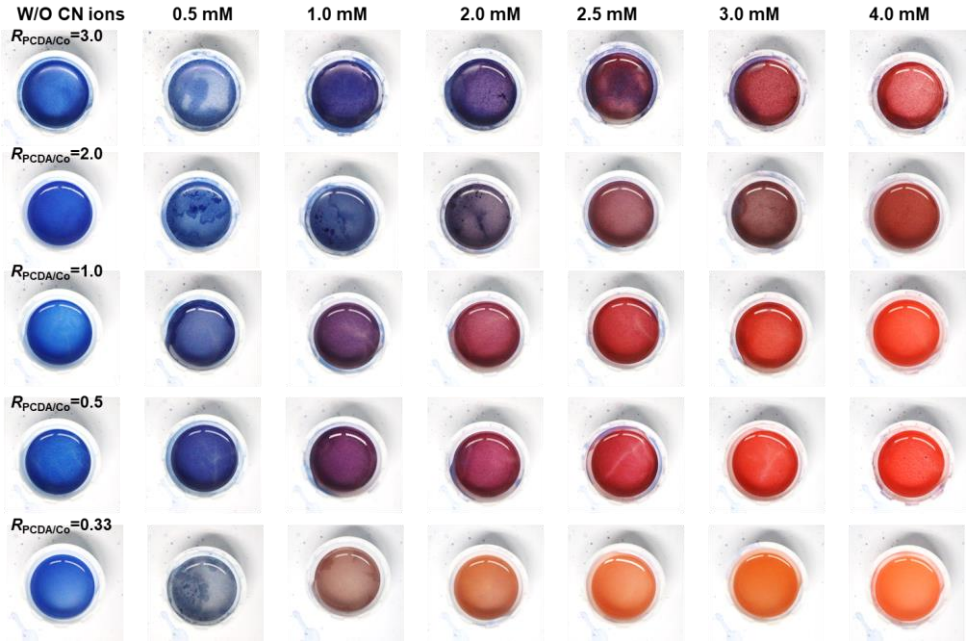

Fig. 3.8. Color changes observed in solution for isolated PCDA-Co nanoplates fabricated using various $R_{PCDA/Co}$ and treated with various concentrations of CN ions. Copyright © 2020 American Chemical Society.

Stage 2: Color transition of the agglomerated PCDA-Co nanoplates in solution

To inhibit alkyl chain rotation in isolated PCDA-Co nanoplates and increase their stability, the intermolecular hydrophobic stacking force of these nanoplates was increased by simply increasing the amount of deionized (DI) water after nanoplate synthesis in THF, which resulted in nanoplate agglomeration (**Fig. 3.9**).

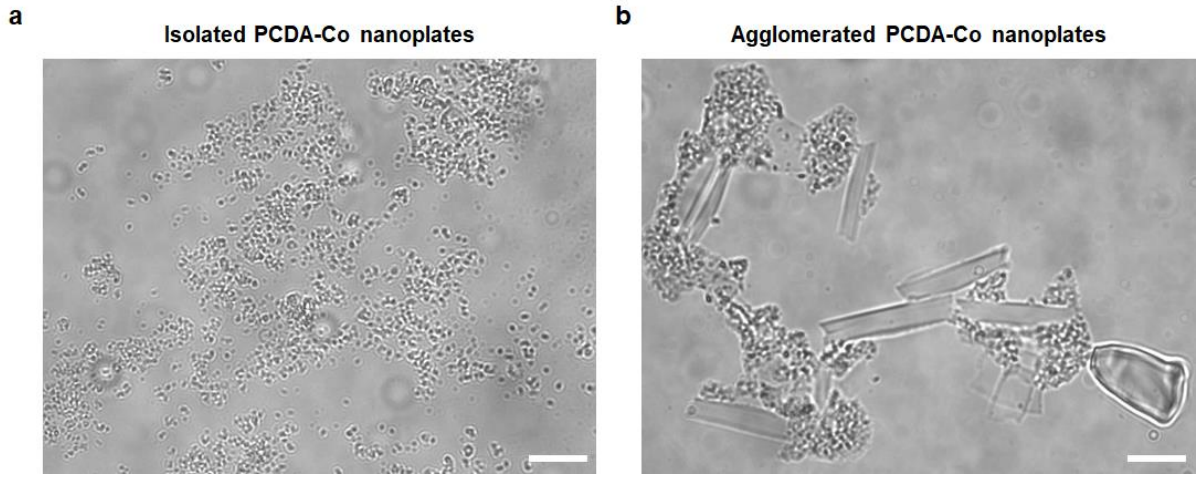

Fig. 3.9. a,b, Bright-field microscopy images of (a) isolated PCDA-Co nanoplates and (b) agglomerated PCDA-Co nanoplates in solution. Scale bars are 10 μm. Copyright © 2020 American Chemical Society.

Interestingly, these agglomerated PCDA-Co nanoplates did not exhibit a blue-to-red color transition upon exposure to bases (**Figs. 3.10a and 3.11a**), organic solvents (hexane, MeOH, EtOH) (**Fig. 3.10b**) and thermal stress (**Fig. 3.10c**), but showed color change upon acid addition (H_2SO_4, HNO_3, HCl, CH_3COOH) and in presence of organic solvents such as methylene chloride (MC), chloroform ($CHCl_3$), THF, and ethyl acetate (EA).

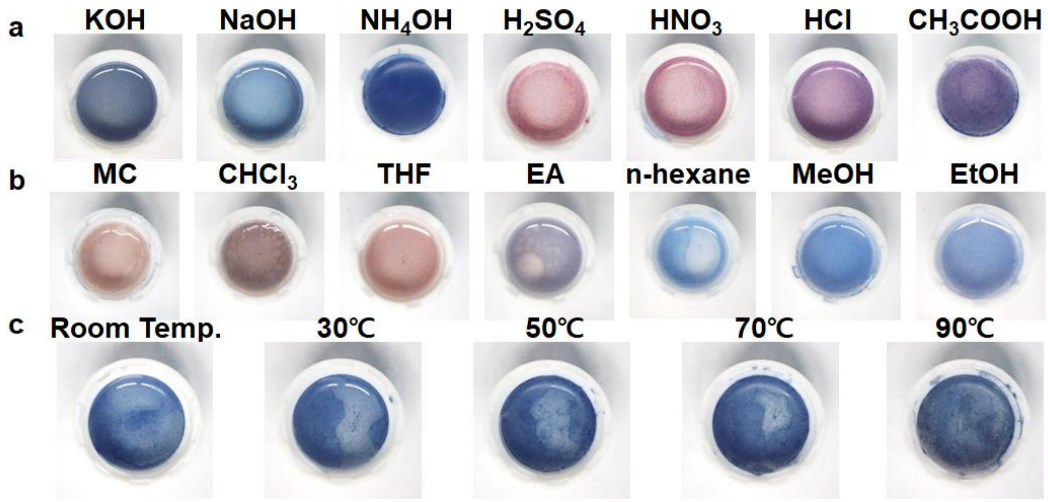

Fig. 3.10. a-c, Color change observed in agglomerated PCDA-Co nanoplates ($R_{PCDA/Co}$ = 0.33) in solution state, upon addition of (a) 4 mM of acids and bases, (b) organic solvents, and (c) heating. Copyright © 2020 American Chemical Society.

The absorbance at 680 nm decreased and 550 nm increased upon exposure to 4 mM of acids (H_2SO_4, HNO_3, HCl, CH_3COOH) and organic solvents (MC, $CHCl_3$, THF, EA) (**Fig. 3.11b and 3.11c**). From these results, we believe that the stability of the isolated PCDA-Co nanoplates increased to some extent because of the enhanced intermolecular hydrophobic interaction between alkyl chains. This structural stability inhibited the exchange of cobalt (II) ions with the cations (K^+, Na^+, $NH4^+$) from bases (KOH, NaOH, NH_4OH) and as a result, agglomerated PCDA-Co nanoplates maintained their conformation of conjugated backbone without color change. However, when these agglomerated PCDA-Co nanoplates are dissolved well in organic solvents such as MC, $CHCl_3$, THF, and EA, they tend to separate into isolated PCDA-Co nanoplates with strong dissociation stress resulting in a conformational change of conjugated backbone with the blue-to-red color transition. Although PCDA-Co did not exhibit optimal stability toward acids, bases, and organic solvents, we concluded that agglomeration, involving an enhancement of the hydrophobic intermolecular stacking interaction of PCDA-Co nanoplates, imparts additional stability.

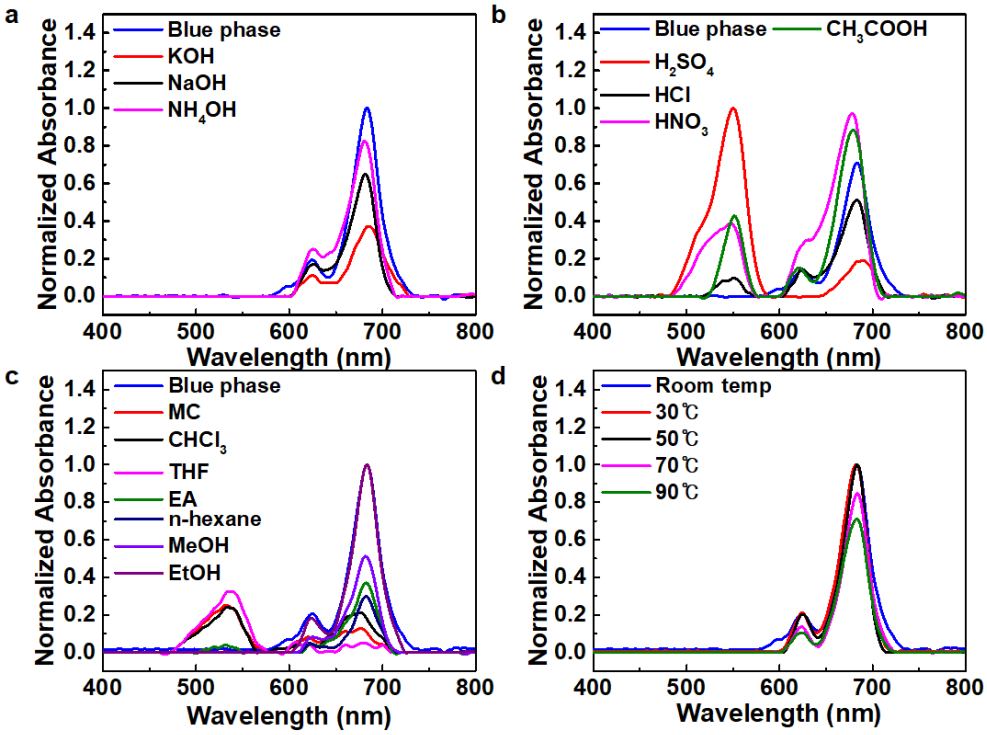

Fig. 3.11. a-d, Changes in UV-vis absorption intensities of isolated PCDA-Co nanoplates in solution upon treatment with (a) bases, (b) acids, (c) organic solvents, and (d) thermal stress. Copyright © 2020 American Chemical Society.

Stage 3: Color transition of the highly stacked PCDA-Co nanoplates in solid film

The previous result of agglomerated PCDA-Co nanoplates provided the possibility to control over the stability of PDA sensor system. However, those agglomerated PCDA-Co nanoplates exhibited non-specific color transition on treatment with acids and several organic solvents. To function as a highly stable and selective PDA sensor system, we enhanced the hydrophobic intermolecular stacking interaction of isolated PCDA-Co nanoplates to completely inhibit the conformational change of the conjugated backbone and the dissociation of PCDA-Co nanoplates. We spin-coated the isolated PCDA-Co nanoplate solution onto a PET film to construct highly stacked PCDA-Co nanoplates. The PCDA-Co nanoplates having various morphologies according to the molar ratios ($R_{PCDA/Co}$) as in **Fig. 3.12**, were prepared and cast onto the PET film as described in **Fig. 3.13**.

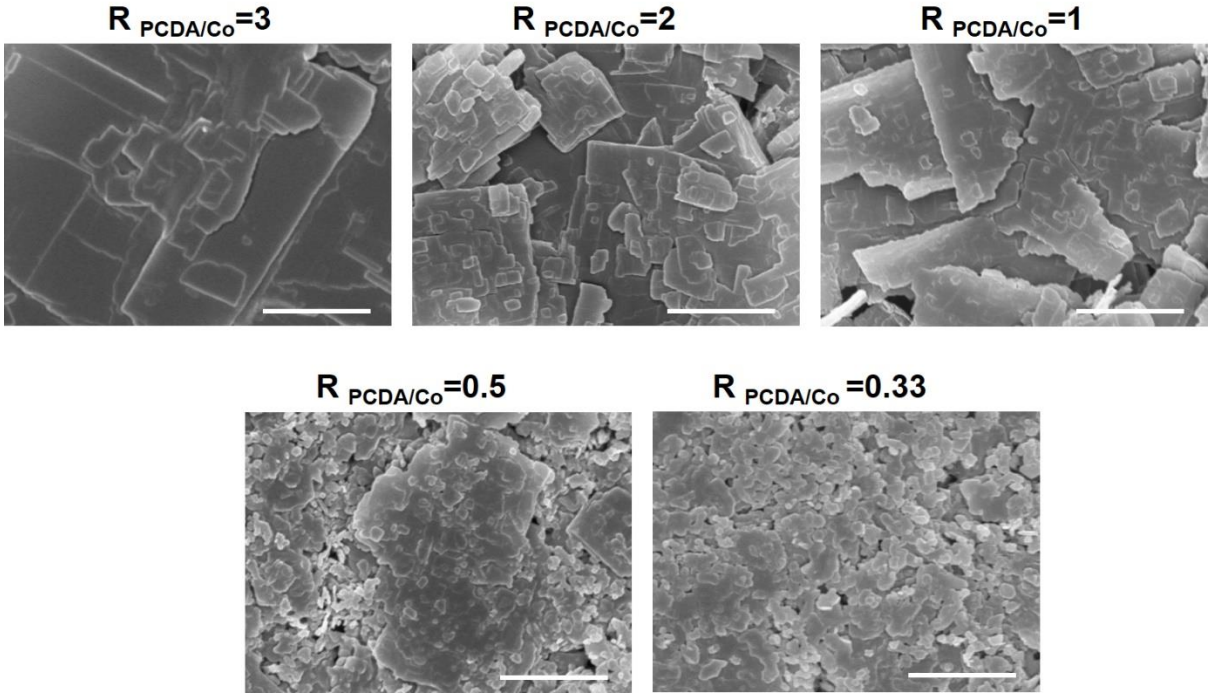

Fig. 3.12. SEM images of isolated PCDA-Co nanoplates in solution based on various initial molar ratio ($R_{PCDA/Co}$). Scale bar = 2.5 μm. Copyright © 2020 American Chemical Society.

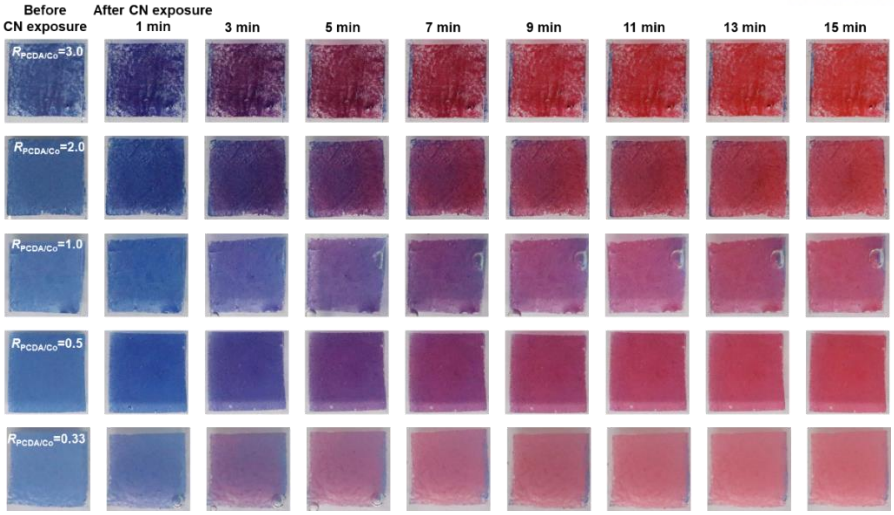

Fig. 3.13. Color changes observed for highly stacked PCDA-Co nanoplates prepared using various $R_{PCDA/Co}$ and exposed to CN ions (25 mM). Copyright © 2020 American Chemical Society.

The PCDA-Co nanoplate solution with higher concentration of cobalt ions ($R_{PCDA/Co}$ = 0.33 and 0.5) exhibited highly uniform coating property on PET film. Surprisingly, PCDA-Co nanoplates film exhibited no color change upon exposure to various acids, bases, organic solvents, thermal stress, and even mechanical stress- folding in half 10 times (**Figs 3.14a-d**). We believe that the methodology given in the design principle led to the formation of highly stable PCDA-Co nanoplates film. Interestingly, the resulting highly stacked PCDA-Co nanoplates exhibited a blue-to-red color transition when treated with CN ions (**Fig. 3.14d**).

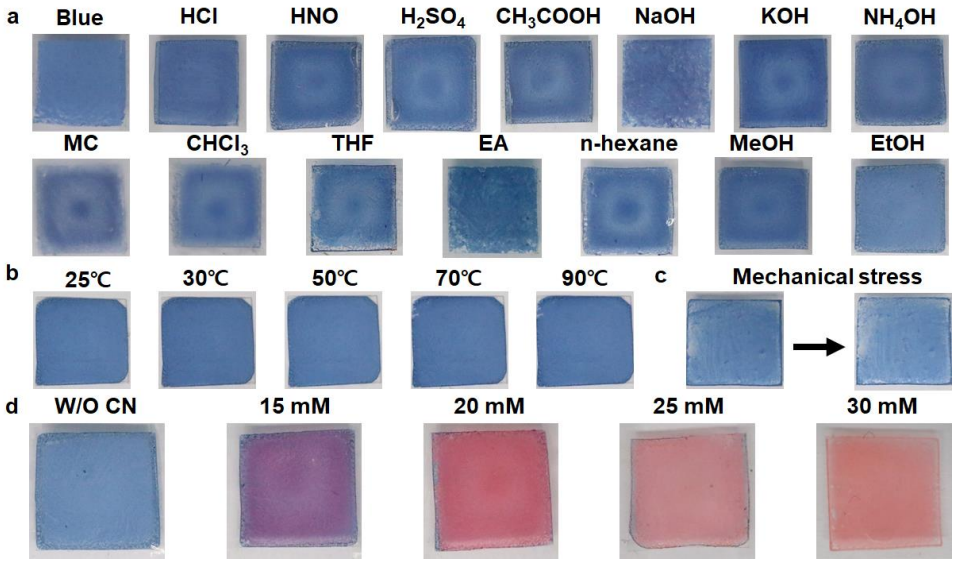

Fig. 3.14. a-d, Color change observed in highly stacked PCDA-Co nanoplates films upon treatment with (a) acids, bases, and organic solvents, (b) heating, (c) mechanical stress (folding in half 10 times), and (d) various concentration of CN ions. Copyright © 2020 American Chemical Society.

Generating PCDA-Co nanoplates films at a particular molar ratio ($R_{PCDA/Co}$ = 0.33), enabled selective detection of CN ions with concentrations down to 15 mM in 5 min. PCDA-Co nanoplates films having different molar ratios ($R_{PCDA/Co}$ = 0.33, 0.5, 1, 2, and 3) also exhibited a blue-to-red color transition with CN ions (**Figs. 3.13 and 3.15**).

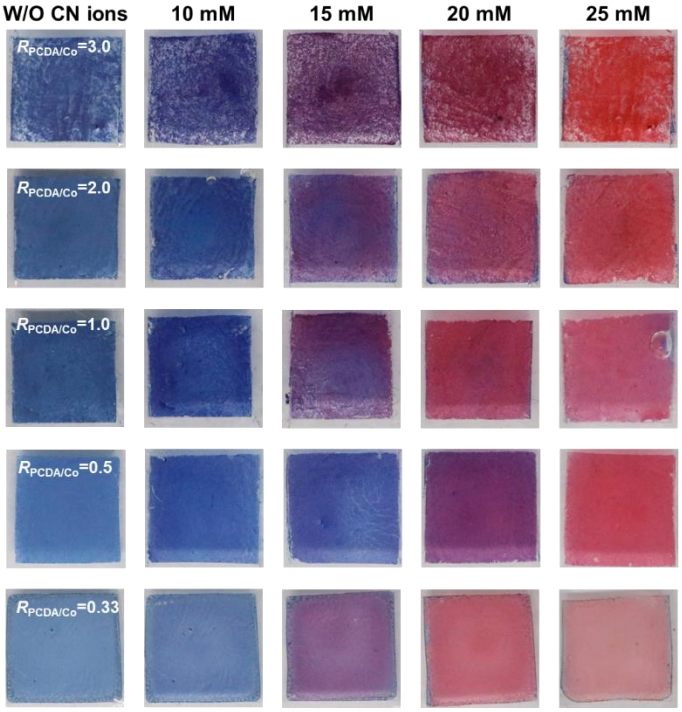

Fig 3.15. Color changes observed for highly stacked PCDA-Co nanoplates prepared using various $R_{PCDA/Co}$ and treated with various concentrations of CN ions. Copyright © 2020 American Chemical Society.

The X-ray photoelectron spectroscopy (XPS) data of the PCDA-Co nanoplates film supported the strong ionic interaction between Co and CN ions (**Fig. 3.16a**). The Co 2p XPS spectrum showed that cobalt molecules were bonded with PCDA molecules and an exposure of CN ions did not affect this bonding. Also, the N 1s XPS spectrum demonstrated the binding energy peak at 398.3 eV after treatment with CN ions, indicating ionic bonding between the CN ions and cobalt molecules in the PCDA-Co nanoplates. Raman spectra further confirm that the interaction between Co and CN ions triggered the changes in conjugation lengths of PCDA-Co nanoplates. The alkyne-alkene bands (2095 and 1450 cm^{-1}) corresponding to the blue phase PCDA-Co nanoplates moved to higher wavenumbers (2120 and 1515 cm^{-1}) representing a typical blue-to-red phase transition of PDAs (**Fig. 3.16b**)[43]. The blue shift in alkyne-alkene bands indicates that the compressive stress was generated in the conjugated backbone of PCDA-Co nanoplates upon exposure to CN ions, ultimately resulting in the blue-to-red color transition of the film. From this result, we assumed that PCDA-Co nanoplates have two different supramolecular

structure changes, one is by the environmental perturbation such as presence of acids, bases, and organic solvents, and the other is by the specific interaction between probe and target.

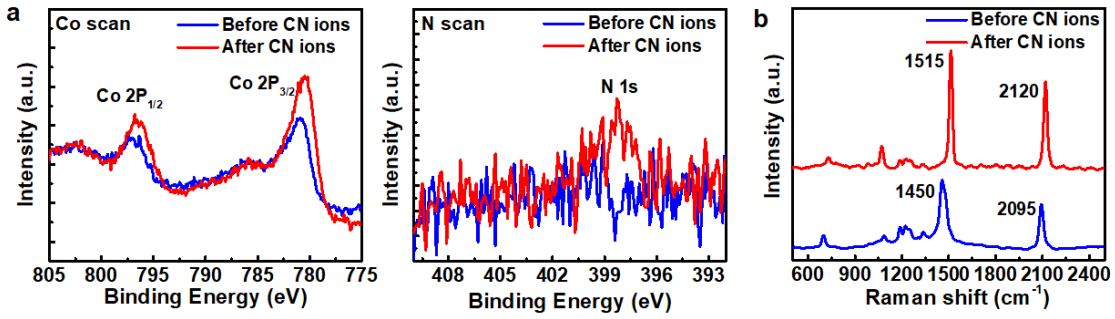

Fig. 3.16. a,b, (a) XPS and (b) Raman spectra of highly stacked PCDA-Co nanoplates film before/after exposure to 15 mM of CN ions. Copyright © 2020 American Chemical Society.

Supramolecular structure change of PCDA-Co nanoplates upon exposure to acids, bases, and organic solvents

To understand the structural changes in the isolated PCDA-Co nanoplates, the agglomerated PCDA-Co nanoplates and the highly stacked PCDA-Co nanoplates, X-ray diffraction (XRD) of each phase of PCDA-Co nanoplates were studied before and after exposure to THF, MeOH, KOH, and H_2SO_4. The isolated PCDA-Co nanoplates in blue phase exhibited six distinct peaks, denoted by the closed circles as shown in Figure 5A. These peaks were obtained at 2θ = 1.68, 3.32, 4.98, 6.64, 8.30, and 9.94 in the range lower than 2θ =12°, and their lattice spacing were calculated by 5.252, 2.658, 1.772, 1.329, 1.064, and 0.889 nm corresponding to those of D_0/n (n = 1–6), indicating the characteristic periodic lamellar structure having the interlayer spacing (D_0) of 5.252 nm[44,45]. These six distinct peaks of isolated PCDA-Co nanoplates did not decrease intensity after exposure with THF and MeOH, and their D_0, the thickness of lamellar structure, was 5.586 nm and 5.381 nm, respectively (**Fig. 3.17a**). Thus, the isolated PCDA-Co nanoplates maintained their crystallinity after exposure to organic solvents. However, the six distinct peaks disappeared after treatment with KOH and H_2SO_4 as shown in **Fig. 3.17a**. The periodic lamellar structure of isolated PCDA-Co nanoplates collapsed, and their crystallinity disappeared upon addition of KOH and H_2SO_4. In case of blue phase agglomerated PCDA-Co nanoplates in solution, the six distinct peaks were measured at 2θ = 1.68, 3.32, 4.96, 6.6, 8.26, and 9.92, and their D_0 were 5.252 nm. The XRD peaks of agglomerated PCDA-Co nanoplates were maintained after exposure to MeOH and KOH, and D_0 values was calculated as 5.130 nm and 5.656 nm, respectively. The blue phase XRD peaks disappeared after exposure to THF and H_2SO_4 indicating the collapse of crystallinity (**Fig. 3.17b**). These XRD results were consistent with the UV-Vis absorbance results of agglomerated PCDA-Co nanoplates in solution, where the agglomerated PCDA-Co nanoplates exhibited color transition only with acids

and organic solvents, which dissolved well with agglomerated PCDA-Co. In case of the highly stacked PCDA-Co nanoplates in blue phase, the six distinct peaks were observed at 2θ = 1.54, 3.14, 4.8, 6.44, 8.12, and 9.78 with an interlayer spacing (D_0) of 5.8051 nm, indicating the periodic lamellar structure. The six distinctive peaks maintained their location and intensity even after treatment with organic solvents, bases, and acids (**Fig. 3.17c**). Surprisingly, these highly stacked PCDA-Co nanoplates exhibited a completely new crystalline structure with an interlayer spacing (D_0) of 4.6441 nm while the isolated PCDA-Co nanoplates maintained their crystalline structure without the collapse in the presence of CN ions (**Fig. 3.17d**). Although the blue-to-red color transition is similar to that observed upon exposure to acids, bases, and organic solvents, the interaction between Co and CN ions is very specific and results in a completely different crystalline structure transition, which allows for the selective detection of CN ions.

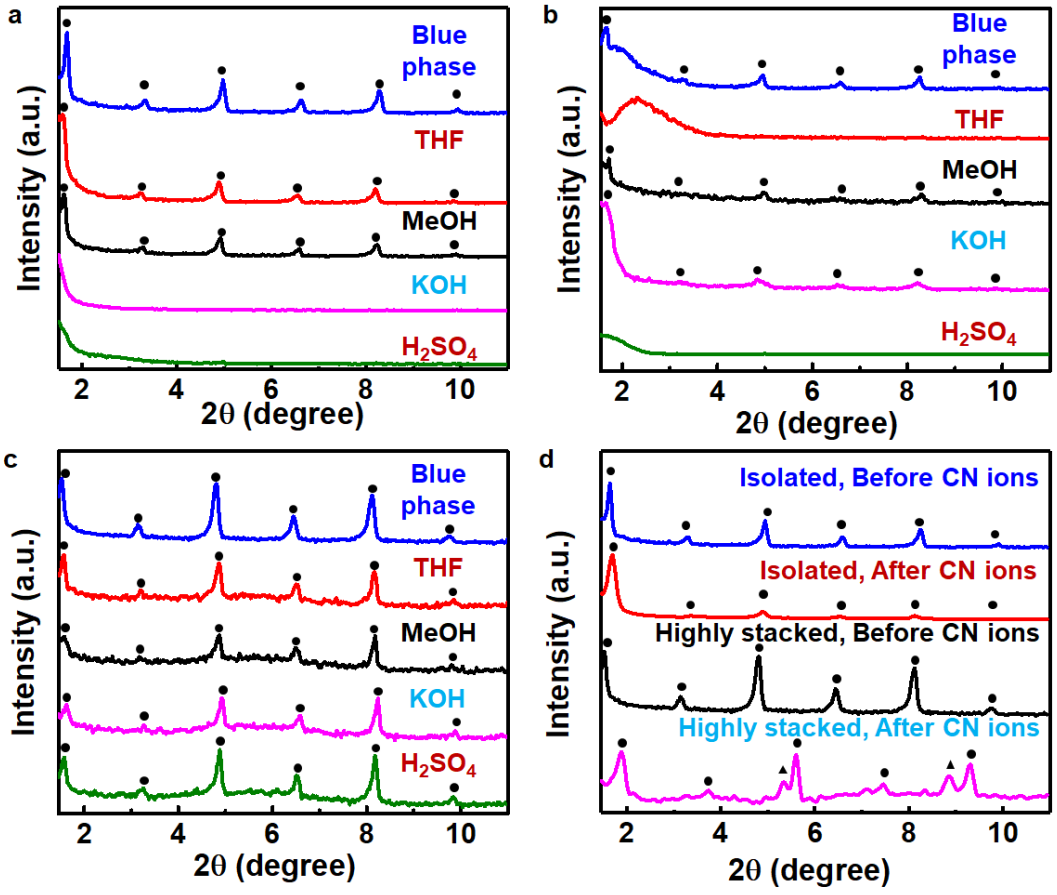

Fig. 3.17. a,b, XRD spectra of (a) isolated PCDA-Co nanoplates, and (b) agglomerated PCDA-Co nanoplates in solution upon treatment with acids, bases, and organic solvents. **c,** XRD patterns of highly stacked PCDA-Co nanoplates in solid film before/after addition of acids, bases and organic solvents. **d,** XRD patterns of isolated PCDA-Co nanoplates and highly stacked PCDA-Co nanoplates before/after addition of CN ions. Copyright © 2020 American Chemical Society.

We further investigated structural changes in isolated PCDA-Co nanoplates, agglomerated PCDA-Co nanoplates, and highly stacked PCDA-Co nanoplates with addition of CN ions. As shown in Figure 6, the blue phase, isolated, agglomerated, and highly stacked PCDA-Co nanoplates exhibit planar shapes. The isolated PCDA-Co nanoplates lost their planar characteristic and converted to dissociated aggregates after exposure to CN ions (**Fig. 3.18a**). However, the agglomerated PCDA-Co nanoplates and the highly stacked PCDA-Co nanoplates maintained their planar characteristics but exhibited a deformed and distorted nanoplate after exposure to CN ions (**Figs. 3.18b and 3.18c**). These results also support the conclusion that the highly stacked PCDA-Co nanoplates exhibited specific morphological transition only in the presence of CN ions compared to isolated PCDA-Co nanoplates.

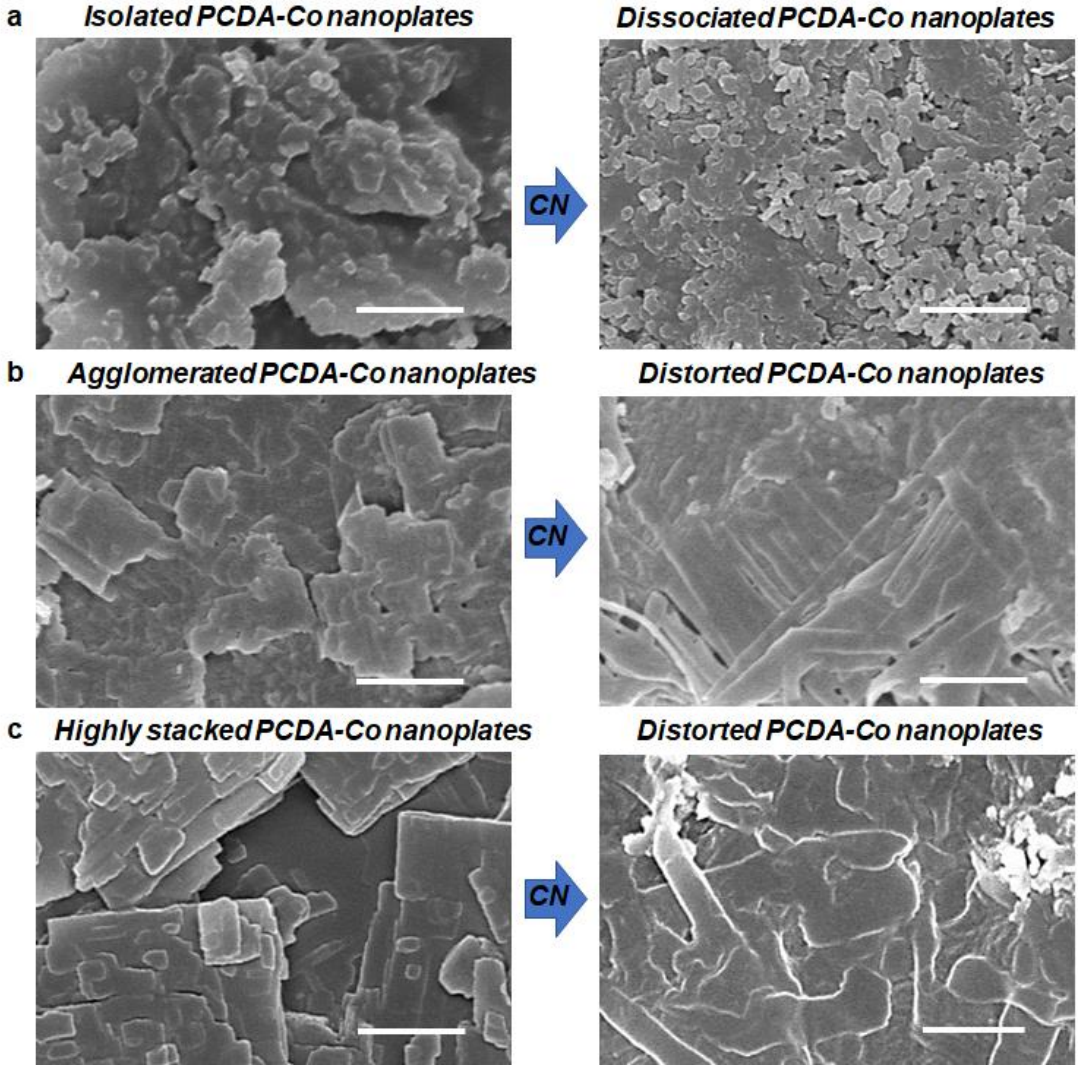

Fig. 3.18. a-c, Changes observed in SEM images of (a) isolated PCDA-Co nanoplates, (b) agglomerated PCDA-Co nanoplates, and (c) highly stacked PCDA-Co nanoplates with molar ratios of PCDA and cobalt ions ($R_{PCDA/Co}$ = 0.33) upon exposure to 15 mM of CN ions. Scale bars = 1.5 μm. Copyright © 2020 American Chemical Society.

Dual signaling capability of UCNs/PCDA-Co nanoplate composites

To realize the practical dual signaling capability, we incorporated UCNs into the highly stacked PCDA-Co nanoplates sensor system. Although there are many potential luminescent material candidates, most organic and inorganic luminescent materials are disadvantageous, due to their instability with external environments such as temperature, solvents, oxygen, and humidity. Lanthanide ion-doped UCNs have a superior optical stability against environmental changes.[46,47] In addition, UCNs release a large anti-stokes shift luminescence at a visible range under near-infrared light (NIR) irradiation, and therefore, 980 nm NIR laser of excitation does not induce any colorimetric interference with the blue-to-red visible color change of PDA. We began with synthesizing hydrophobic *β*-$NaYF_4$:Yb^{3+}/Er^{3+}/Gd^{3+} UCNs, which exhibit a green emission through a hydrothermal method (see the Experimental Section for details). Then, the green luminescent UCNs were dispersed in 12 mM of isolated PCDA-Co nanoplate solution, and the UCNs/PCDA-Co composite solution was coated onto a PET substrate. As shown in SEM image, UCNs were homogeneously incorporated into the highly stacked PCDA-Co nanoplates (**Fig. 3.19**).

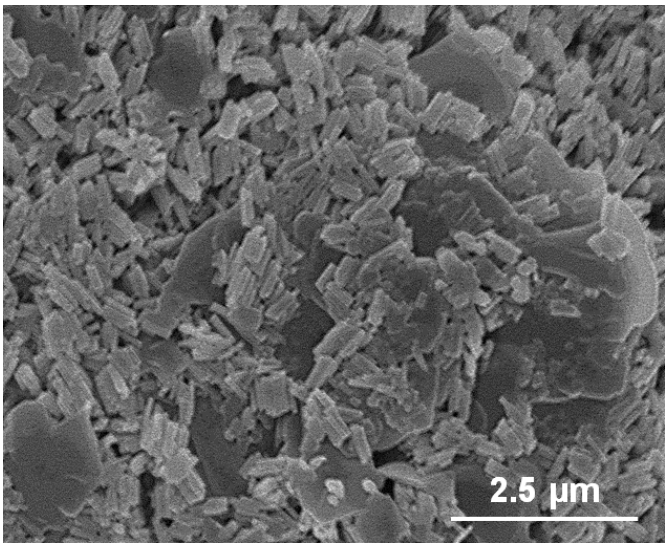

Fig. 3.19. SEM image of UCNs incorporated into highly stacked PCDA-Co nanoplates. Copyright © 2020 American Chemical Society.

The resulting UCNs/PCDA-Co nanoplate composite films exhibited a selective blue-to-red color change and a green-to-red luminescence change in the presence of CN ions and displayed superior optical stability irrespective of any luminescence and color change occurrence when treated with acids, bases, and organic solvents (**Figs. 3.20a and 3.20c**). The above simultaneous color and luminescence change was ascribed to the absorption and luminescence wavelength overlap between highly stacked PCDA-Co nanoplates and UCNs. Upon exposure to CN ions, the luminescence intensity of UCNs at

550 nm decreased, and a green-to-red luminescence change was observed as the PCDA-Co color changed from blue to red, whereas the luminescence intensity at 550 nm was maintained upon exposure to acids, bases, and organic solvents (**Figs. 3.20b and 3.20d**).

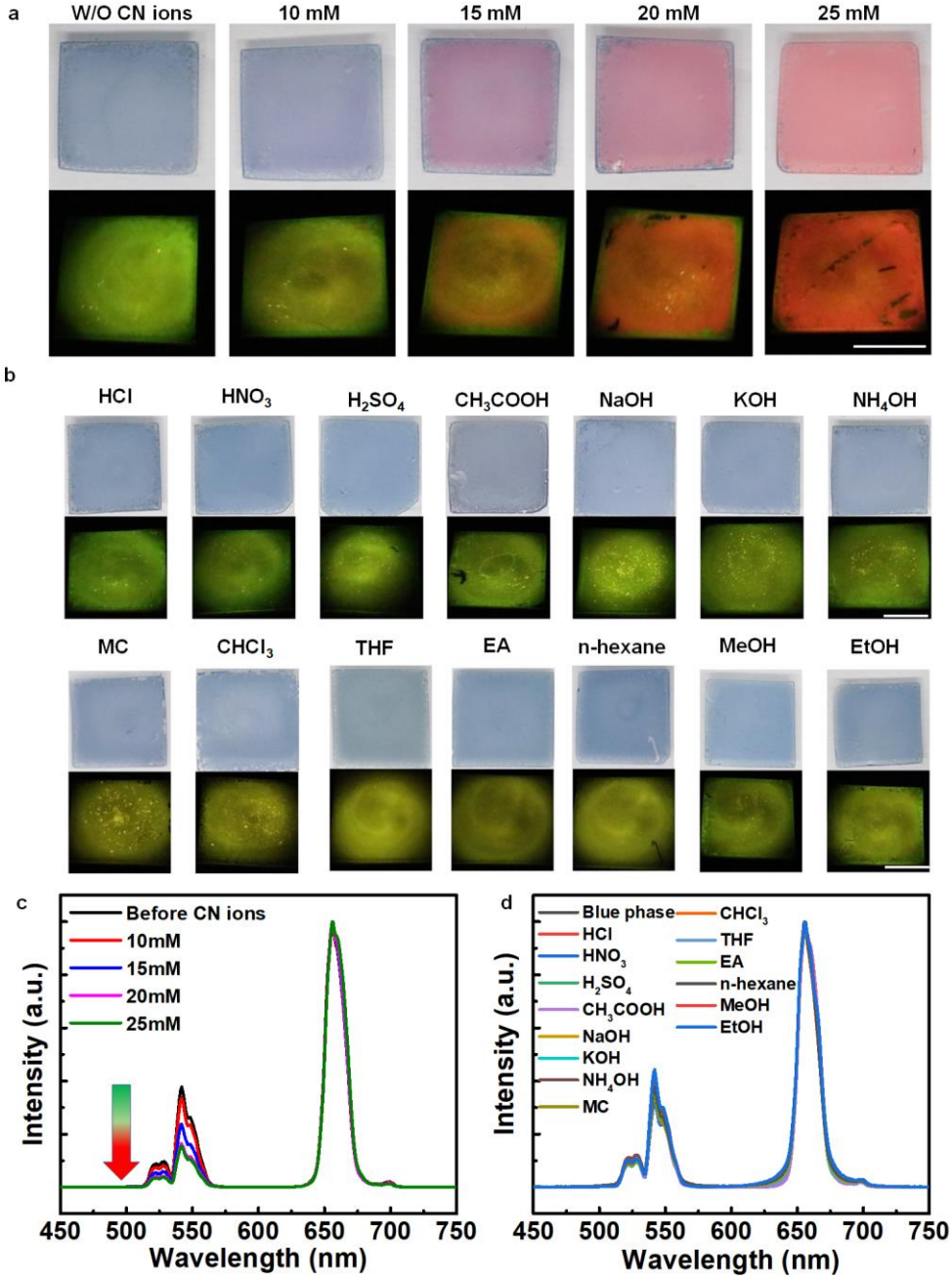

Fig. 3.20. a, Color and luminescence changes of UCNs/PCDA-Co nanoplate composites film upon addition of various concentrations of CN ions. **b,** Changes in the luminescence spectrum of UCNs/PCDA-Co nanoplate composite film upon exposure to various concentrations of CN ions. **c,** Color and luminescence changes of UCNs/PCDA-Co nanoplate composite film upon exposure to various acids, bases, and organic solvents. **d,** Changes in the luminescence spectrum of UCNs/PCDA-Co nanoplate composites film upon treatment with acids, bases, and organic solvents.

To expand the potential utility of the UCNs/PCDA-Co nanoplate composite system, we designed a prototype portable detection system. The portable detection system was composed of a dichroic mirror (FF757-Di01, Semrock), 980 nm NIR laser diode, printed circuit board (PCB), and red-green-blue (RGB) complementary metal-oxide-semiconductor (CMOS) sensor (**Fig. 3.21a**). The UCNs/PCDA-Co nanoplate composite film was irradiated with 980 nm NIR laser through the dichroic mirror and the reflected luminescence from UCNs was analyzed by RGB CMOS sensor. We programed the device in such a way that the LED on the portable device turned green when the luminescence intensity ratio, measured between 650 nm and 550 nm ($E_{650\ nm}/E_{550\ nm}$), becomes greater than 3. This ratio was obtained when the UCNs/PCDA-Co nanoplate composites were exposed to 15 mM of CN ions. Similarly, the LED turned to red light when the luminescence intensity ratio of the composite had $E_{650\ nm}/E_{550\ nm}$ less than 3. As shown in **Fig. 3.21b**, our portable device selectively detected the luminescence change of the UCNs/PCDA-Co composite system when exposed to 15 mM of CN ions.

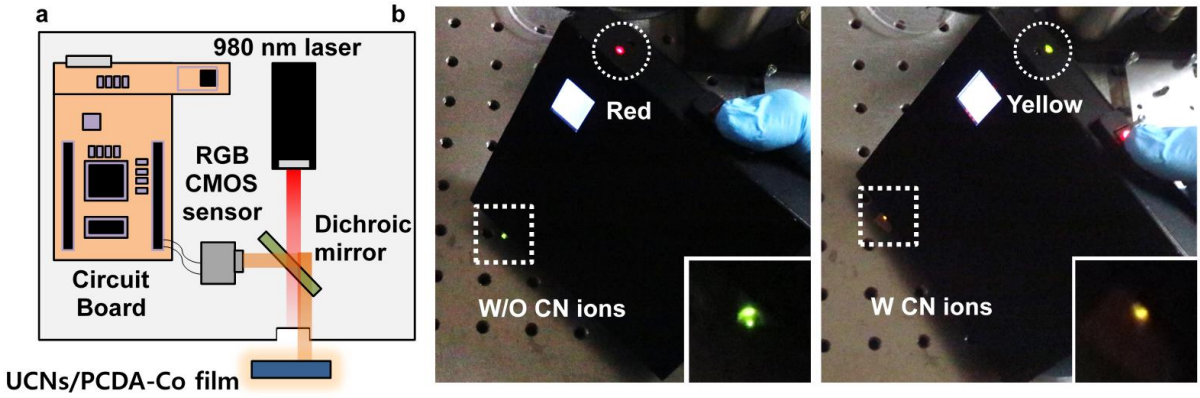

Fig. 3.21. a, Schematic of the portable detection system. **b,** Selective detection of CN ions with the device in (**a)**. Inset images show the luminescence color change of UCNs/PCDA-Co nanoplate composite film after exposure to CN ions (LED is red in the absence of CN ions and green in the presence of CN ions). Scale bar is 0.5 cm. Copyright © 2020 American Chemical Society.

3.3 Experimental Section

Materials. Unless stated otherwise, all chemicals were purchased from Sigma-Aldrich.

Preparation of isolated PCDA-Co nanoplates. To a solution of 14.71 mmol of cobalt hydroxide (Alfa Aesar) in 0.4 mL of DI water, 4.90 mmol of 10,12-pentacosadiynoic acid (PCDA, GFS Chemicals) in 9.6 mL of THF was added dropwise and stirred at room temperature overnight. 50 µl of the resulting PCDA-Co nanoplates organogel was diluted in 2 mL of THF and photo-polymerized under 254 nm UV light irradiation for 6 min. The PCDA-Co nanoplates were isolated by further dilution with 4 mL of THF.

Preparation of agglomerated PCDA-Co nanoplates. DI water (4 mL) was added to the previously synthesized isolated PCDA-Co nanoplate solution, and photo-polymerized with 254 nm UV light irradiation for 6 min.

Preparation of highly stacked PCDA-Co nanoplates film. The same procedure as that described above was followed to synthesize a solution of isolated PCDA-Co nanoplates, 50 μL of which was spin-coated onto PET film (1 cm × 1 cm) using a spin-coater (ACE-200, Dong Ah Tech) (150 rpm for 5 min).

Synthesis of hexagonal phase UCNs. To a solution of NaOH (0.6 g in 3 mL DI water) mixed with 10 mL of ethanol upon vigorous stirring, 10 mL of oleic acid, 4 mL of $RECl_3$ (0.2 M, RE = $Gd^{3+}/Y^{3+}/Yb^{3}/Er^{3+}$ = 30/50/18/2) and 2 mL of NH_4F (2 M) were added. The mixture precursor solution was transferred to a stainless steel autoclave, with subsequent heating at 200 °C for 2 h. After naturally cooling to room temperature, nanocrystals were collected by centrifugation and washed with ethanol and water.

UCNs/PCDA-Co nanoplate composite film. Isolated PCDA-Co nanoplates in solution were synthesized using the abovementioned procedure. Next, 12 mg of UCNs was added to 200 μL of isolated PCDA-Co nanoplate solution, and the mixture were vortexed for 1 min using a vortex mixer (NB-105V, N-Biotek). Finally, the UCNs/PCDA-Co nanoplate composite was spin-coated onto the PET substrate (1 cm × 1 cm) using a spin-coater (ACE-200, Dong Ah Tech) (150 rpm for 5 min).

Characterization. The blue-to-red color change of PCDA-Co were captured using a digital camera (EOS M3, Canon). UV-vis absorption spectra were recorded by a UV-vis spectrometer (Cary 8454, Agilent Technologies). Fluorescence emission of PCDA-Co nanoplates were measured using a fluorescence spectrophotometer (Cary Eclipse, Agilent Technologies). X-ray photoelectron spectroscopy (XPS) data were obtained with a photoelectron spectrometer (K-alpha, Thermo Fisher). Raman spectra were recorded using a confocal Raman microscope (alpha 300s, WITec). Scanning electron microscopy (SEM) images were taken with a scanning electron microscope (S-4800, Hitachi High-Technologies). XRD measurements were recorded with an X-ray diffractometer (D/MAX2500V/PC, Rigaku) at a scanning rate of 1° min^{-1} with the 2θ from 1° to 16°. The photoluminescence spectra of UCNs were recorded with a spectrometer (QE Pro, Ocean Optics) using an external 0–10 W adjustable continuous wave 980 nm laser (MDL-H-980, Changchun New Industries Optoelectronics Tech. Co., Ltd.).

3.4 Conclusion

In summary, we successfully developed a universal design principle for a highly stable PDA sensor platform with an unprecedented stability when faced with environmental perturbation such as acids, bases, organic solvents, and thermal and mechanical stress. The stability of the PDA sensor system was enhanced by (i) rational control of the strong ionic bonds between cobalt ions and PCDA and (ii) maximization of the hydrophobic intermolecular interactions of PCDA-Co supramolecules. UCNs were incorporated into the highly stable PCDA-Co sensor system to selectively detect CN ions via stable dual signaling (colorimetric transition + luminescence color change), and a customized portable detection system was demonstrated. The developed sensor platform can be further employed in diverse PDA sensor systems for use in harsh environments (both night- and daytime) because of the simplicity of its synthesis and unusually high stability. Thus, this work provides insights into ways of overcoming the inherent disadvantages of PDA sensor systems for robust and practical dual signaling sensor applications.

3.5 References

1. Lee, J., Kim, H.-J., Kim, J. Polydiacetylene Liposome Arrays for Selective Potassium Detection. *J. Am. Chem. Soc.* **130**, 5010-5011 (2008).
2. Lee, J., Jun, H., Kim, J. Polydiacetylene–Liposome Microarrays for Selective and Sensitive Mercury(II) Detection. *Adv. Mater.* **21**, 3674-3677 (2009).
3. Chen, X., Zhou, G., Peng, X., Yoon, J. Biosensors and Chemosensors Based on the Optical Responses of Polydiacetylenes. *Chem. Soc. Rev.* **41**, 4610-4630 (2012).
4. Lee, J., Kim, J. Multiphasic Sensory Alginate Particle Having Polydiacetylene Liposome for Selective and More Sensitive Multitargeting Detection. *Chem. Mater.* **24**, 2817-2822 (2012).
5. Dolai, S., Bhunia, S. K., Beglaryan, S. S., Kolusheva, S., Zeiri, L., Jelinek, R. Colorimetric Polydiacetylene–Aerogel Detector for Volatile Organic Compounds (VOCs). *ACS Appl. Mater. Interfaces* **9**, 2891-2898 (2017).
6. Kew, S. J., Hall, E. A. H. pH Response of Carboxy-Terminated Colorimetric Polydiacetylene Vesicles. *Anal. Chem.* **78**, 2231-2238 (2006).
7. Chance, R. R., Baughman, R. H., Müller, H., Eckhardt, C. J. Thermochromism in a Polydiacetylene Crystal. *J. Chem. Phys.* **67**, 3616 (1977).
8. Kim, J.-M., Lee, J.-S., Choi, H., Sohn, D., Ahn, D. J. Rational Design and In-Situ FTIR Analyses of Colorimetrically Reversible Polydiacetylene Supramolecules. *Macromolecules* **38**, 9366-9376 (2005).
9. Park, H., Lee, J.-S., Choi, H., Ahn, D. J., Kim, J.-M. Rational Design of Supramolecular Conjugated Polymers Displaying Unusual Colorimetric Stability upon Thermal Stress. *Adv. Funct. Mater.* **17**, 3447-3455 (2007).

10. Lee, S., Lee, J., Lee, M., Cho, Y. K., Baek, J., Kim, J., Park, S., Kim, M. H., Chang, R., Yoon, J. Construction and Molecular Understanding of an Unprecedented, Reversibly Thermochromic Bis-Polydiacetylene. *Adv. Funct. Mater.* **24**, 3699-3705 (2014).
11. Park, D.-H., Hong, J., Park, I. S., Lee, C. W., Kim, J.-M. A Colorimetric Hydrocarbon Sensor Employing a Swelling-Induced Mechanochromic Polydiacetylene. *Adv. Funct. Mater.* **24**, 5186-5193 (2014).
12. Terada, H., Imai, H., Oaki, Y. Visualization and Quantitative Detection of Friction Force by Self-Organized Organic Layered Composites. *Adv. Mater.* **30**, 1801121 (2018).
13. Chen, X., Hong, L., You, X., Wang, Y., Zou, G., Su, W., Zhang, Q. Photo-Controlled Molecular Recognition of α-Cyclodextrin with Azobenzene Containing Polydiacetylene Vesicles. *Chem. Commun.* 1356-1358 (2009).
14. Seo, S., Lee, J., Choi, E.-J., Kim, E.-J., Song, J.-Y., Kim, J. Polydiacetylene Liposome Microarray Toward Influenza A Virus Detection: Effect of Target Size on Turn-On Signaling. *Macromol. Rapid Commun.* **34**, 743-748 (2013).
15. Jung, Y. K., Kim, T. W., Park, H. G., Soh, H. T. Specific Colorimetric Detection of Proteins Using Bidentate Aptamer-Conjugated Polydiacetylene (PDA) Liposomes. *Adv. Funct. Mater.* **20**, 3092-3097 (2010).
16. Lee, J., Jeong, E. J., Kim, J. Selective and Sensitive Detection of Melamine by Intra/Inter Liposomal Interaction of Polydiacetylene Liposomes. *Chem. Commun.* **47**, 358-360 (2011).
17. Lee, J., Seo, S., Kim, J. Colorimetric Detection of Warfare Gases by Polydiacetylenes Toward Equipment-Free Detection. *Adv. Funct. Mater.* **22**, 1632-1638 (2012).
18. Wang, D.-E., Wang, Y., Tian, C., Zhang, L., Han, X., Tu, Q., Yuan, M., Chen, S., Wang, J. Polydiacetylene Liposome-Encapsulated Alginate Hydrogel Beads for Pb^{2+} Detection with Enhanced Sensitivity. *J. Mater. Chem. A* **3**, 21690-21698 (2015).
19. Charych, D. H., Nagy, J. O., Spevak, W., Bednarski, M. D. Direct Colorimetric Detection of a Receptor-Ligand Interaction by a Polymerized Bilayer Assembly. *Science* **261**, 585-588 (1993).
20. Cheng, Q., Stevens, R. C. Coupling of an Induced Fit Enzyme to Polydiacetylene Thin Films: Colorimetric Detection of Glucose. *Adv. Mater.* **9**, 481-483 (1997).
21. Seo, S., Lee, J., Kwon, M. S., Seo, D., Kim, J. Stimuli-Responsive Matrix-Assisted Colorimetric Water Indicator of Polydiacetylene Nanofibers. *ACS Appl. Mater. Interfaces* **7**, 20342-20348 (2015).
22. Tu, M.-C., Cheema, J. A., Yildiz, U. H., Palaniappan, A., Liedberg, B. Vapor Phase Solvatochromic Responses of Polydiacetylene Embedded Matrix Polymers. *J. Mater. Chem. C* **5**, 1803-1809 (2017).

23. Wu, S., Zhang, Q., Bubeck, C. Solvent Effects on Structure, Morphology, and Photophysical Properties of an Azo Chromophore-Functionalized Polydiacetylene. *Macromolecules* **43**, 6142-6151 (2010).
24. Lee, J., Chang, H. T., An, H., Ahn, S., Shim, J., Kim, J.-M. A Protective Layer Approach to Solvatochromic Sensors. *Nat. Commun.* **4**, 2461 (2013).
25. Yoon, J., Chae, S. K., Kim, J. M. Colorimetric Sensors for Volatile Organic Compounds (VOCs) Based on Conjugated Polymer-Embedded Electrospun Fibers. *J. Am. Chem. Soc.* **129**, 3038-3039 (2007).
26. Chae, S. K., Park, H., Yoon, J., Lee, C. H., Ahn, D. J., Kim, J.-M. Polydiacetylene Supramolecules in Electrospun Microfibers: Fabrication, Micropatterning, and Sensor Applications. *Adv. Mater.* **19**, 521-524 (2007).
27. Lécuiller, R., Berréhar, J., Ganiére, J. D., Lapersonne-Meyer, C., Lavallard, P., Schott, M. Fluorescence Yield and Lifetime of Isolated Polydiacetylene Chains: Evidence for a One-Dimensional Exciton Band in a Conjugated Polymer. *Phys. Rev. B* **66**, 125205 (2002).
28. Li, X., McCarroll, M., Kohli, P. Modulating Fluorescence Resonance Energy Transfer in Conjugated Liposomes. *Langmuir* **22**, 8615-8617 (2006).
29. Kim, H.-J., Lee, J., Kim, T.-H., Lee, T. S., Kim, J. Highly Emissive Self-assembled Organic Nanoparticles having Dual Color Capacity for Targeted Immunofluorescence Labeling. *Adv. Mater.* **20**, 1117-1121 (2008).
30. Kyeong, S., Kang, H., Yim, J., Jeon, S.-J., Jeong, C. H., Lee, Y.-S., Jun, B. H., Kim, J.-H. Quantum Dot-Assembled Nanoparticles with Polydiacetylene Supramolecule Toward Label-Free, Multiplexed Optical Detection. *J. Colloid Interface Sci.* **394**, 44-48 (2013).
31. Folling, J., Belov, V., Kunetsky, R., Medda, R., Schonle, A., Egner, A., Eggeling, C., Bossi, M., Hell, S. W. Photochromic Rhodamines Provide Nanoscopy with Optical Sectioning. *Angew. Chem. Int. Ed.* **46**, 6266-6270 (2007).
32. Kucherak, O. A., Richert, L., Mely, Y., Klymchenko, A. S. Dipolar 3-Methoxychromones as Bright and Highly Solvatochromic Fluorescent Dyes. *Phys. Chem. Chem. Phys.* **14**, 2292-2300 (2012).
33. Wan, S. L., Zheng, Y., Shen, J., Yang, W. T., Yin, M. Z. "On–off–on" Switchable Sensor: A Fluorescent Spiropyran Responds to Extreme pH Conditions and Its Bioimaging Applications. *ACS Appl. Mater. Interfaces* **6**, 19515-19519 (2014).
34. Kulig, K. W. *Cyanide Toxicity*, U.S. Dept. of Health and Human Services, Public Health Service, Agency for Toxic Substances and Disease Registry: Atlanta, GA, 1991.
35. Baskin, S. I., Brewer, T. G. In *Medical Aspects of Chemical and Biological Warfare*, Sidell, F. R., Takafuji, E. T., Franz, D. R., Eds., TMM Publications: Washington, DC, 1997, Chapter 10, p 271.

36. Evans, C. L. Cobalt Compounds as Antidotes for Hydrocyanic Acid. *Brit. J. Pharmacol.* **23**, 455-475 (1964).
37. Frankenberg, L., Sorbo, B. Effect of Cyanide Antidotes on teh Metabolic Conversion of Cyanide to Thiocyanate. *Arch. Toxicol.* **33**, 81-89 (1975).
38. Lee, J. H., Jeong, A. R., Shin, I.-S., Kim, H.-J., Hong, J.-I. Fluorescence Turn-On Sensor for Cyanide Based on a Cobalt(II)−Coumarinylsalen Complex. *Org. Lett.* **12**, 764-767 (2010).
39. Auzel, F. Upconversion and Anti-Stokes Processes with f and d Ions in Solids. *Chem. Rev.* **104**, 139-174 (2004).
40. Wu, S., Han, G., Milliron, D. J., Aloni, S., Altoe, V., Talapin, D. V., Cohen, B. E., Schuck, P. J. Non-Blinking and Photostable Upconverted Luminescence from Single Lanthanide-Doped Nanocrystals. *Proc. Natl. Acad. Sci. USA* **106**, 10917-10921 (2009).
41. Park, Y. I., Kim, J. H., Lee, K. T., Jeon, K.-S., Na, H. B., Yu, J. H., Kim, H. M., Lee, N., Choi, S. H., Baik, S.-I., Kim, H., Park, S. P., Park, B.-J., Kim, Y. W., Lee, S. H., Yoon, S.-Y., Song, I. C., Moon, W. K., Suh, Y. D., Hyeon, T. Nonblinking and Nonbleaching Upconverting Nanoparticles as an Optical Imaging Nanoprobe and T1 Magnetic Resonance Imaging Contrast Agent. *Adv. Mater.* **21**, 4467-4471 (2009).
42. Lu, Y., Zhao, J., Zhang, R., Liu, Y., Liu, D., Goldys, E. M., Yang, X., Xi, P., Sunna, A., Lu, J., Shi, Y., Leif, R. C., Huo, Y., Shen, J., Piper, J. A., Robinson, J. P., Jin, D. Tunable Lifetime Multiplexing Using Luminescent Nanocrystals. *Nat. Photonics* **8**, 32-36 (2014).
43. Koshihara, S., Tokura, Y., Takeda, K., Koda, T., Kobayashi, A. Reversible and Irreversible Thermochromic Phase Transitions in Single Crystals of Polydiacetylenes Substituted with Alkyl-Urethanes. *J. Chem. Phys.* **92**, 7581 (1990).
44. Baek, W., Heo, J.-M., Oh, S., Lee, S.-H., Kim, J., Joung, J. F., Park, S., Chung, H., Kim, J.-M. Photoinduced Reversible Phase Transition of Azobenzene-Containing Polydiacetylene Crystals. *Chem. Commun.* **52**, 14059-14062 (2016).
45. Okaniwa, M., Oaki, Y., Imai, H. Intercalation-Induced Tunable Stimuli-Responsive Color-Change Properties of Crystalline Organic Layered Compound. *Adv. Funct. Mater.* **26**, 3463-3471 (2016).
46. Wang, F., Han, Y., Lim, C. S., Lu, Y., Wang, J., Xu, J., Chen, H., Zhang, C., Hong, M., Liu, X. Simultaneous Phase and Size Control of Upconversion Nanocrystals Through Lanthanide Doping. *Nature* **463**, 1061-1065 (2010).
47. Zhou, J., Zhu, X., Chen, M., Sun, Y., Li, F. Water-Stable $NaLuF_4$-Based Upconversion Nanophosphors with Long-Term Validity for Multimodal Lymphatic Imaging. *Biomaterials* **33**, 6201-6210 (2012).

Chapter 4. Orthogonal dual signaling of Chemical warfare agents using polydiacetylene/upconversion nanocrystals nanocomposites

This chapter includes the published contents:

J. Oh, D. Kim, Y. Shin, H. Cho, and J. Lee*. *Func. Compos. Struct.* **2**, 025003 (2020).

4.1 Introduction

Polydiacetylene (PDA), one of the conjugated polymers, has been extensively studied for the development of various sensor systems because of their unique optical properties such as color change and fluorescence emission[1-4]. Diacetylene molecules are polymerized by 1-4 addition polymerization under 254 nm UV irradiation and blue-phase PDA having an alternating "yne-ene" backbone is generated[5-7]. PDAs undergoes a blue-to-red color transition and fluorescence emission by the conformational change of conjugated backbone by the applied external stimuli[1-3]. They have been fabricated as liposomes[1, 2, 8], films[9, 10], and nanowires[11] to recognize various series of external stimuli such as heat[12, 13], pH[8], mechanical stress[14], and molecular recognition[1, 2, 15-18]. Based on these stimuli-responsive optical property changes of PDAs, a great deal of effort has been devoted to detecting toxic molecules by introducing structurally distinct recognition units into diacetylene monomers. One of the toxic molecules, the Chemical Warfare Agents (CWAs), has been considered a weapon of mass destruction (WMD), and the use of these WMDs is prohibited by customary international humanitarian law (IHL). Nevertheless, to maximize killing capacity, CWAs are often sprayed illegally day and night during the civil war. Therefore, in order to evacuate from contaminated areas where CWAs have been sprayed or to use a proper antidote for people exposed to chemical agents, it is necessary to develop a detection system that selectively and quickly identifies the type of CWAs at night as well as during the day.

In this study, we report UCNs embedded PDA supramolecules capable of rapidly and selectively detecting two CWAs gases using the orthogonal electrophilic and nucleophilic reaction mechanisms of G-series nerve agent (DMMP) and blood agent (ClCN). To selectively recognize DMMP and ClCN, we suggest nucleophilic oxime (OX) modified PCDA-OX and electrophilic benzaldehyde (BA) modified PCDA-BA molecules. We further fabricate PCDA-OX/UCNs and PCDA-BA/UCNs nanocomposite embedded fiber patches that exhibit a dual signaling capability of yellow-to-red luminescence transition and a blue-to-red color change upon exposure to DMMP and ClCN gases,

respectively. In addition, we provide a color standard for the convenient use of military PDA sensors that do not require scientific analysis tools. This design principle of the PDA/UCNs nanocomposite-based sensor system extends the applicability of PDA sensor systems to military use in the development of gas CWAs detection systems.

4.2 Results and Discussion

We begin with synthesizing two diacetylene derivatives, PCDA-OX and PCDA-BA (**Fig. 4.1a**). It is known that OX has an enhanced nucleophilicity by the α-effect of an adjacent nitrogen atom, and they have been used to synthesize an antidote molecule such as 2-pyridine aldoxime methyl chloride (2-PAM) in the treatment of nerve agent poisoning[19]. ClCN, a blood agent, has been known that the toxicity comes from cyanide (CN) ions that were released by the reaction with glutathione in biological systems[20]. The released nucleophilic cyanide strongly binds ferric cation (Fe^{3+}) inside cytochrome oxidase and cause suffocation from lack of oxygen with fatal damage to the respiratory system. Cyanide molecules, a strong nucleophile, are also known to bind with the electrophilic benzaldehyde group producing cyanohydrin molecules. Briefly, a nucleophilic OX attacks electrophilic organophosphonates and electrophilic aldehydes are attacked by nucleophilic cyanides. Therefore, these reaction mechanisms are orthogonal with each other. PDAs system for the selective detection of target CWAs molecules. Multiple substrates such as PET and fiber patch are coated with PCDA-OX and PCDA-BA monomers and PCDA-OX or PCDA-BA coated substrates exhibit blue color through 1-4 addition photo-polymerization of diacetylenes groups under 254 nm UV light irradiation (**Fig. 4.1b**). PCDA-OX or PCDA-BA coated cotton fibers display rapid color change from blue to red when exposed to DMMP or ClCN (**Fig. 4.1c**). We believe that nucleophilic oximes in PCDA-OX probe molecules rapidly react with organophosphonate (OP) of DMMP target molecules and therefore repulsion force between covalently bonded PCDA-OX and DMMP complexes impose a strong conformational change to the conjugated backbone of PDA resulting color transition (**Fig. 4.1d**). In contrast, for ClCN, cyanide anion from the target ClCN molecules act as a nucleophile and react with electrophilic benzaldehyde groups in PCDA-BA probe molecule. In other words, DMMP and ClCN have orthogonal reaction mechanisms in that PCDA-OX acts as a nucleophile for DMMP and PCDA-BA acts as an electrophile for ClCN. In this way, we expect that PCDA-OX and PDCA-BA maintain their initial blue color upon exposure to ClCN and DMMP, respectively. In addition, we incorporate UCNs into the investigated PDA sensor system to realize the dual signaling sensor system to be available at night through a luminescent change of UCNs (**Fig. 4.1e**). The luminescence color of the PDA/UCNs nanocomposite changes from yellow to red according to the absorption change of PDA. These UCNs/PDA nanocomposite systems provide a potential utility for selective detection of CWAs that can be used at night-time.

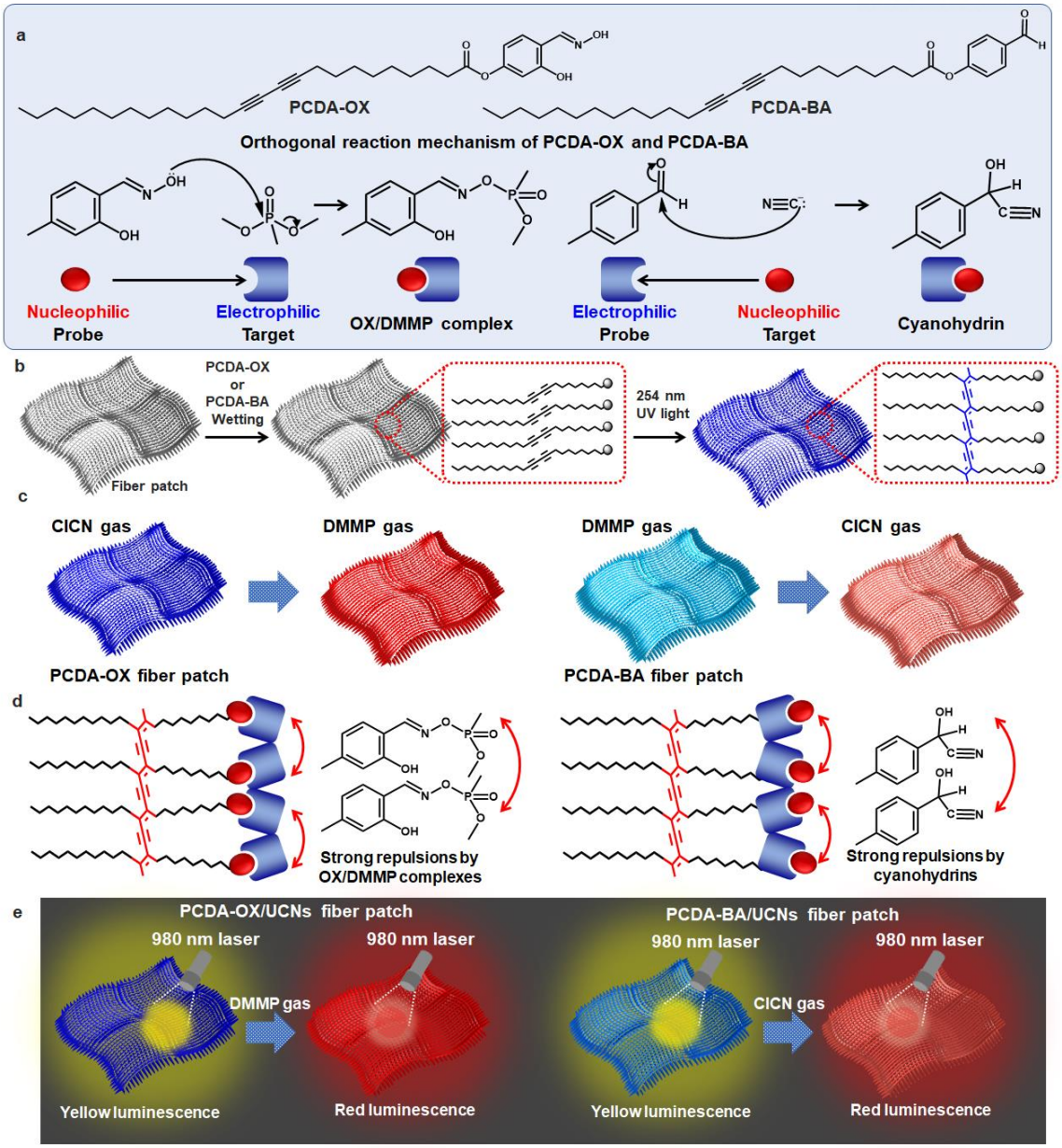

Fig. 4.1. a, Chemical structure of investigated diacetylene PCDA-OX and PCDA-BA (top) and the reaction mechanisms of OX with DMMP (bottom) and BA with ClCN. **b,** Schematic illustration of the fabrication of PCDA-OX or PCDA-BA coated fiber patch. **c,** Selective detection of DMMP and ClCN using PCDA-OX and PCDA-BA fiber patches. **d,** Detection mechanism of PCDA-OX and PCDA-BA. **e,** Schematic illustration of PDA/UCNs nanocomposite fiber patches for night-time detection.

To explain the detection capability of the synthesized PDA molecules, we initially prepared PCDA-OX coated PET film and exposed to the DMMP solution. PET film was coated with PCDA-OX (30 mM in THF) and exposed to 254 nm UV light for 1 min. The resulting blue colored PCDA-OX PET film exhibited rapid color change from blue to red (**Fig. 4.2a**) with absorption change from 650 nm to

550 nm (**Fig. 4.2c**) when exposed to 0.1 ml of DMMP liquid in less than 1 s. To expand the flexibility of the PDA sensor system, PCDA-OX was coated on fiber patch (see the Experimental Section for details). As in **Fig. 4.2b**, PCDA-OX coated fiber patch also exhibited rapid blue to red color transition in less than 1 s upon exposure to DMMP liquid. To test the colorimetric response of the PCDA-OX system, the reflection spectra of PCDA-OX coated cotton fiber was measured before and after the exposure of DMMP liquid. The reflectance intensity at 450 nm decreased with an increase at 650 nm upon exposure to 0.1 ml of DMMP. We further exposed the PCDA-OX fiber patch to DMMP droplet having 100 μm diameter corresponding to the detection limit of conventional CWAs detection papers such as M-8 and M-9. Multiple DMMP droplets were sprayed onto the PCDA-OX fiber patch (see the Experimental Section for details) and the PCDA-OX fiber patch exhibited a blue-to-red color transition (**Fig. 4.2e**). These results showed that our PCDA-OX system successfully detects the CWAs by the detection limit of conventional CWAs detection systems such as M-8 and M-9.

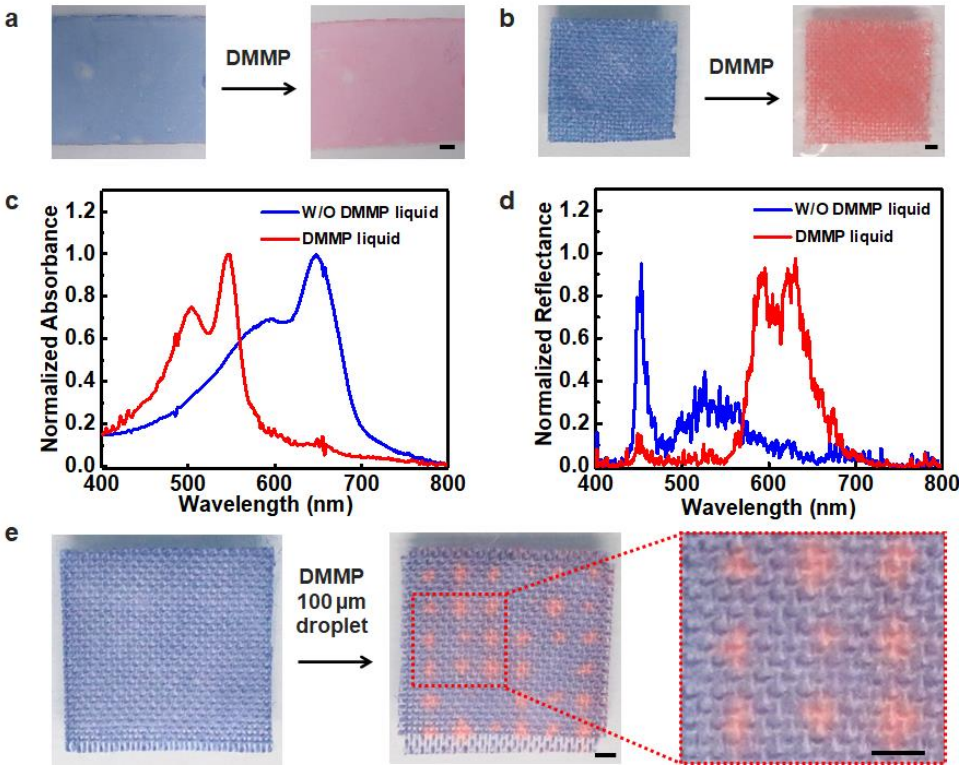

Fig. 4.2. **a,** Color change of PCDA-OX coated PET film after exposure to DMMP liquid (9.23M). **b,** Color change of PCDA-OX cotton fiber patch after exposure to DMMP liquid (9.23M). **c,** Normalized UV-vis absorption spectra of PCDA-OX coated PET film before and after exposure to DMMP liquid (9.23M). **d,** Normalized reflectance spectra of PCDA-OX cotton fiber patch before and after exposure to DMMP liquid (9.23M). **e,** Color change of PCDA-OX fiber patch after exposure to DMMP droplets (Diameter: 100 μm).

To find whether our PDA Sensor systems can detect gaseous CWAs selectively and rapidly, PCDA-OX or PCDA-BA fiber patch was exposed to DMMP gas (390 ppm) and ClCN gas (1720 ppm)

(see the Experimental Section for details). PCDA-OX coated fiber patch exhibited blue to red color transition in 7 s upon exposure to DMMP gas but it appeared no color transition when exposed to ClCN gas. In the case of PCDA-BA fiber patch, blue to red color transition appeared in less than 1s upon exposure to ClCN gas but no color transition was observed when exposed to DMMP gas (**Fig. 4.3a**). These selective color changes were originated from the orthogonal reaction mechanism of DMMP and ClCN in that electrophilic BA has no interaction reaction with electrophilic OP and the nucleophilic OX has no interaction with CN nucleophiles.

It is known that the saturation and brightness of the two colors change according to the ambient light. Therefore, to analyze the color change of the PDA sensor system regardless of a light condition without using scientific analytical tools, we used an angle change of Hue (H) value because the angular difference in hue values does not change in a color wheel according to the amount of light. First, the color of the PDA fiber patch before and after exposure to CWAs (**Figs. 4.3a** (top) and **4.3b** (top)) was averaged using a Korean Standard Color Analysis (KSCA) program (**Figs. 4.3a** (middle) and **4.3b** (middle)). Second, the main H values were extracted and color names were assigned using the KSCP (Korean Standard Color Palette) program. Finally, the position of the colors was displayed on the color wheel, and we measured the degree of angle change between the two colors (**Figs. 4.3a** (bottom) and **4.3b** (bottom)). PCDA-OX fiber patch was assigned as a turbid blue color before and after exposure to ClCN, and the H value of located at 210˚ and 212˚. After exposure to DMMP gas, the name of the color changed to a pale red and the H angle changed by 152˚. For the PCDA-BA fiber patch, the color was named as a pale blue with H value at 208˚, and the H value was slightly changed to 215˚ after exposure to DMMP gas. When the PCDA-BA fiber patch was exposed to ClCN gas, the name of the color was changed to purple pink with H value at 317˚. This H angle-based color analysis offers the color standard of the colorimetric warfare agent sensors and improves the practical military use of the PDA sensor.

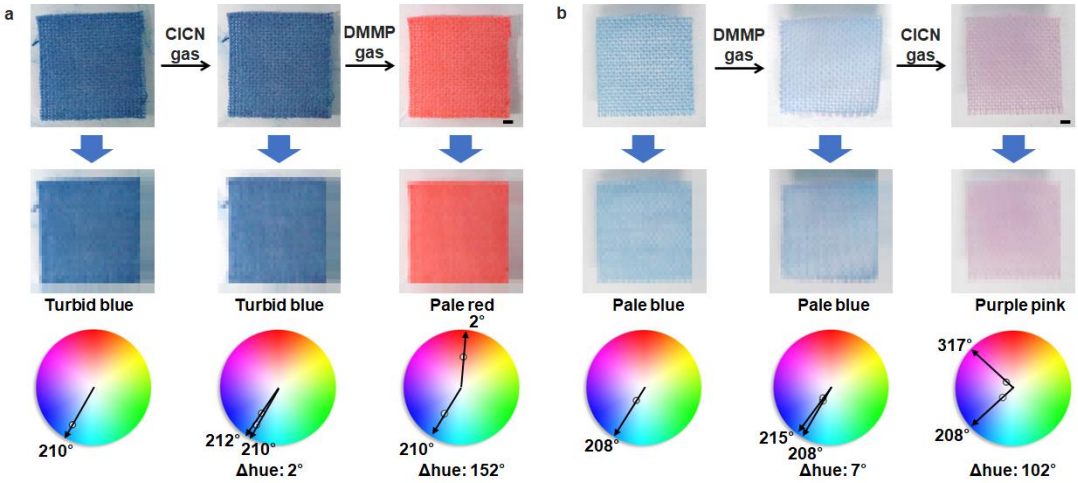

Fig. 4.3. a, CCD images (top), averaged colors and color standard names (middle), and H values on the color wheel (bottom) of PCDA-OX coated fiber patch after exposure to ClCN (1720 ppm) and DMMP

(390 ppm) gases. **b,** CCD images (top), averaged colors and color standard names (middle), and H values on the color wheel (bottom) of PCDA-BA coated fiber patch after exposure to DMMP (390 ppm) and ClCN (1720 ppm) gases.

It is known that CWAs attacks are often carried out at night when it is difficult to respond. For this reason, to develop a robust night-time detection system, we incorporated UCNs into our PDA sensor system. Lanthanide ion-doped UCNs have large anti-stokes shift characteristics emitting visible luminescence upon excitation with 980 nm near-infrared (NIR) laser light[21, 22]. UCNs are a promising candidate luminescence material because they have excellent optical stability upon physicochemical changes[23-25]. We synthesized yellow luminescent hydrophobic β-$NaYF_4$:Yb/Er/Gd UCNs using a hydrothermal method (see the Experimental Section for details). To test the stability of UCNs upon exposure to CWAs, UCNs were embedded into a fiber patch and exposed to DMMP and ClCN gases. UCNs maintained their rod-like morphology (**Fig. 4.4a**) without changing luminescence color after exposure to CWAs (**Figs. 4.4b** and **4.4c**). Figures 4.4d and 4.4e show that the 650 nm luminescence wavelength of UCNs overlaps with the 650 nm absorption wavelength of PCDA-OX in blue phase, and 540 nm luminescence of UCNs overlaps with the 550 nm absorption wavelength of PCDA-OX in red phase. By using these luminescence and absorbance overlap of UCNs with PDA, we expect that blue-to-red color transition of PDA induces luminescence color change of UCNs when exposed to CWAs. We prepared yellow luminescent UCNs/diacetylene monomer mixture solution (30 mM of PCDA-OX or PCDA-BA in THF). A fiber patch was coated with UCNs/diacetylene monomers (PCDA-OX or PCDA-BA) mixture solution and photopolymerized under 254 nm UV light irradiation (see the Experimental Section for details). The resulted PCDA-OX/UCNs or PCDA-BA/UCNs fiber patches were exposed to DMMP and ClCN gases, and the luminescence color changes were measured in the darkroom. PCDA-OX/UCNs fiber patch presented the luminescence color change from yellow to red with blue-to-red color change upon exposure of DMMP gas but no luminescence and color change upon exposure to ClCN gas (**Fig. 4.4f**). PCDA-BA/UCNs fiber patch exhibited a yellow-to-red luminescence color change upon exposure of ClCN gas while they did not show the luminescence change upon exposure of DMMP gas (**Fig. 4.4g**). PCDA-OX/UCNs system exhibited the luminescence color transition with the decrease of the emission at 540 nm wavelength by the absorbance change of PCDA-OX upon exposure to DMMP gas (**Fig. 4.4h**). PCDA-OX/UCNs and PCDA-BA/UCNs sensor system showed selective detection capability of DMMP and ClCN gases through dual-signaling such as color and luminescence change. These results provide the potential utility for the development of dual signaling PDA/UCNs sensor system that can be used at night.

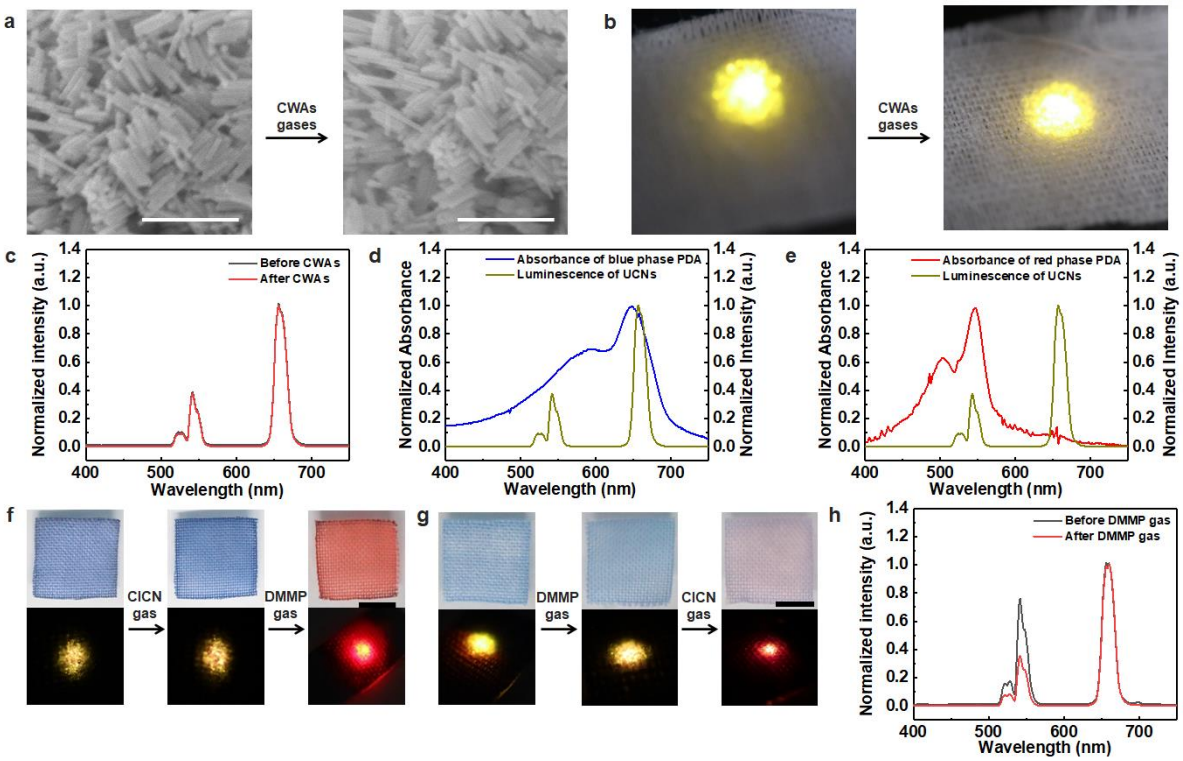

Fig. 4.4. a, SEM images and **b,** luminescence change of UCNs after exposure to ClCN (1720 ppm) and DMMP (390 ppm) gases. **c,** Luminescence spectra change of UCNs coated fiber patch before and after exposure to ClCN (1720 ppm) and DMMP (390 ppm) gases. **d,e,** Luminescence overlap of UCNs with (d) blue phase PCDA-OX and (e) red phase PCDA-OX. **f,** Color (top) and luminescence (bottom) change of PCDA-OX/UCNs fiber patch upon exposure to ClCN (1720 ppm) and DMMP (390 ppm) gases. **g,** Color (top) and luminescence (bottom) change of PCDA-BA/UCNs fiber patch upon exposure to ClCN (1720 ppm) and DMMP (390 ppm) gases. **h,** Luminescence spectra change of PCDA-OX/UCNs fiber patch before and after exposure to DMMP (390 ppm) gas. Scale bar is 1 μm for (A) and 5 mm for (F). Copyright © 2021 IOP Publishing.

4.3 Experimental Section

Materials

10,12-pentacosadiynoic acid (PCDA) was purchased from GFS chemicals. Oxalyl chloride was purchased from TCI chemicals. 4-hydroxy benzaldehyde, 2,4-dihydroxy benzaldehyde (HBA), hydroxylamine hydrochloride, and 2-butanone were purchased from Alfa Aesar. Triethylamine (TEA), dimethylformamide (DMF), dichloromethane, and pyridine were purchased from Sigma-Aldrich. Tetrahydrofuran (THF), ethyl acetate (EA), hexane, and ethanol were purchased from SAMCHUN chemicals. All chemicals were used without further purification.

Preparation of diacetylene monomers

Synthesis of PCDA-HBA. To a solution of 5.33 mmol of PCDA in 20mL of dichloromethane, 15.7 mmol of oxalyl chloride was added dropwise. The mixture solution was stirred for 2hrs. After concentrating in vacuo, the residue was dissolved in 2-butanone and added to a solution containing 5.27 mmol of 2,4-dihydroxy benzaldehyde and 6.17 mmol of TEA in 50 mL of 2-butanone. The mixture solution was stirred overnight and extracted with ethyl acetate (EA). The residue was further purified by column chromatography (hexane:EA = 9:1). ^{1}H NMR (400 MHz, DMSO-d_6) δ 10.21 (s, 1H), 7.69 (d, J = 8.5 Hz, 1H), 6.77 – 6.66 (m, 2H), 2.59 (t, J = 7.4 Hz, 2H), 2.28 (t, J = 6.4 Hz, 4H), 1.70 – 1.16 (m, 32H), 0.86 (t, 3H).

Synthesis of PCDA-OX. To a solution of 2.02 mmol PCDA-HBA in 100mL of ethanol, 4.04 mmol of hydroxylamine hydrochloride solution in 20 mL of DI-water/ethanol (1/1) mixture was added dropwise. The resulting solution was refluxed for 6hrs at 44℃. After concentrating in vacuo, the residue was extracted with ethyl acetate (EA), and further purified by column chromatography (hexane:EA = 5:1). ^{1}H NMR (400 MHz, DMSO-d_6) δ 11.31 (s, 1H), 10.37 (s, 1H), 8.31 (s, 1H), 7.52 (d, J = 8.3 Hz, 1H), 6.67 – 6.58 (m, 2H), 2.56 (t, J = 7.4 Hz, 2H), 2.28 (t, J = 6.3 Hz, 4H), 1.69 – 1.20 (m, 32H), 0.86 (t, 3H).

Synthesis of PCDA-BA. To a solution of 5.33 mmol PCDA in 20 mL of dichloromethane, 15.7 mmol of oxalyl chloride was added dropwise, and a catalytic amount of DMF was added. The resulting solution was stirred for 2 hrs at room temperature. After concentrating in vacuo, the residue was dissolved in THF and added to a solution containing 5.27 mmol of 4-hydroxy benzaldehyde in 20 mL of pyridine. The mixture solution was stirred overnight and extracted with ethyl acetate (EA). The residue was further purified by column chromatography (hexane:EA = 5:1). ^{1}H NMR (400 MHz, DMSO-d_6) δ 10.00 (s, 1H), 7.98 (d, 2H), 7.37 (d, 2H), 2.62 (t, J = 7.4 Hz, 2H), 2.28 (t, J = 6.5 Hz, 4H), 1.74 – 1.20 (m, 32H), 0.85 (t, 3H).

Fabrication of PCDA-OX and PCDA-BA fiber patches. A cotton fiber patch (1 cm x 1 cm) was coated with 30 mM of PCDA-OX in THF. PCDA-OX coated fiber patch were polymerized by 254 nm UV light irradiation for 1 min. PCDA-BA coated fiber patch was fabricated by following the same process. PCDA-BA coated fiber patch was polymerized by 254 nm UV light irradiation for 30 s.

Preparation of 100μm diameter DMMP droplet. DMMP solution was dropped on a PET film using a high-precision dispenser (E2, Nordson). DMMP droplet. The contact angle and radius of DMMP were measured using a drop shape analyzer (DSA100, Krüss). The volume and the diameter of the DMMP were calculated using the measured contact angle and radius. The volume of the DMMP droplet of (0.52 nl) having a diameter of 100 μm was further adjusted by optimizing the voltage (80 V) and stroke value (90%) of the dispenser.

Preparation of DMMP and ClCN gases. DMMP and ClCN solution was vaporized with dry and transferred to the gas storage container. The concentration of DMMP (390 ppm) and ClCN gases (1720 ppm) was controlled using a constant flow regulator.

Synthesis of hexagonal phase UCNs. 10 mL of oleic acid, 4 mL of $RECl_3$ (0.2 M, RE = $Gd^{3+}/Y^{3+}/Yb^{3}/Er^{3+}$ = 30/50/18/2) and 2 mL of NH_4F (2 M) were added to a solution of NaOH (0.6 g in 3 mL di-water) with 10 mL of ethanol upon vigorous stirring. The mixture precursor solution was moved to a stainless steel autoclave and heated for 2 hrs at 200 °C in a vacuum oven. After cooling to room temperature, UCNs were washed with water and ethanol by centrifugation.

Fabrication of PCDA-OX/UCNs and PCDA-BA/UCNs fiber patches. 12 mg of UCNs was added to 200 uL of PCDA-OX or PCDA-BA solution in THF (30 mM), and the mixture solution was vortexed for 1min (NB-105V, N-Biotek). A cotton fiber patch was coated with UCNs/PCDA-OX mixture solution and polymerized by 254 nm UV light irradiation for 1 min. A cotton fiber patch was coated with UCNs/PCDA-BA mixture solution and polymerized by 254 nm UV light irradiation for 30 s.

Characterization. The images of the PCDA-OX and PCDA-BA system were taken using a charge-coupled device (CCD) camera (EOS M3, Canon). UV-vis absorption spectra were measured by a UV-vis spectrometer (Cary 8454, Agilent Technologies). Reflectance spectra were measured using a fiber optic spectrometer (KESHET-PHOTON). Scanning electron microscopy (SEM) images were captured with a scanning electron microscope (S-4800, Hitachi High-Technologies). The photoluminescence spectra of UCNs were recorded with a spectrometer (QE Pro, Ocean Optics) using a 980 nm laser (MDL-H-980, Changchun New Industries Optoelectronics Tech. Co., Ltd.).

4.4 Conclusion

We have developed a rapid and selective DMMP (a G-agent simulant) and ClCN (a blood agent) gas detection systems using PDA/UCN nanocomposite by rationally utilizing the orthogonal reaction mechanism of CWAs. The PCDA-OX/UCNs and PCDA-BA/UCNs rapidly interacted with the organophosphonate and cyanide, causing a selective blue to red color change and yellow to red luminescence change upon DMMP and ClCN. Since the change in luminescence color is observed using an invisible 980 nm NIR laser light, there is no risk of being exposed to the enemy at night, and we further expect the straightness of the coherent laser light enables the development of long-range sensor systems.

4.5 References

1. Lee J, Kim HJ, Kim J. Polydiacetylene liposome arrays for selective potassium detection. *J. Am. Chem. Soc.* **130**, 5010-11.
2. Lee J, Jun H, Kim J. Polydiacetylene-Liposome Microarrays for Selective and Sensitive Mercury(II) Detection. *Adv. Mater.* **21**, 3674-77 (2009).
3. Chen XQ, Zhou GD, Peng XJ, Yoon J. Biosensors and chemosensors based on the optical responses of polydiacetylenes. *Chem. Soc. Rev.* **41**, 4610-30 (2012).
4. Lee J, Kim J. Multiphasic Sensory Alginate Particle Having Polydiacetylene Liposome for Selective and More Sensitive Multitargeting Detection. *Chem. Mater.* **24**, 2817-22 (2012).
5. Ahn DJ, Kim JM. Fluorogenic polydiacetylene supramolecules, Immobilization, micropatterning, and application to label-free chemosensors. *Acc. Chem. Res.* **41**, 805-16 (2008).
6. Chance RR. Chromism in Polydiacetylene Solutions and Crystals. *Macromolecules.* **13**, 396-8 (1980).
7. Mosley DW, Sellmyer MA, Daida EJ, Jacobson JM. Polymerization of diacetylenes by hydrogen bond templated adlayer formation. *J. Am. Chem. Soc.* **125**, 10532-3 (2003).
8. Kew SJ, Hall EAH. pH response of carboxy-terminated colorimetric polydiacetylene vesicles. *Anal. Chem.* **78**, 2231-8 (2006).
9. Kim JM, Chae SK, Lee YB, Lee JS, Lee GS, Kim TY, et al. Polydiacetylene supramolecules embedded in PVA film for strip-type chemosensors. *Chem. Lett.* **35**, 560-1 (2006).
10. Lee J, Seo S, Kim J. Colorimetric Detection of Warfare Gases by Polydiacetylenes Toward Equipment-Free Detection. *Adv. Funct. Mater.* **22**, 1632-8 (2012).
11. Bai F, Sun ZC, Lu P, Fan HY. Smart polydiacetylene nanowire paper with tunable colorimetric response. *J. Mater. Chem.* **22**, 14839-42 (2012).
12. Kim JM, Lee JS, Choi H, Sohn D, Ahn DJ. Rational design and in-situ FTIR analyses of colorimetrically reversibe polydiacetylene supramolecules. *Macromolecules.* **38**, 9366-76 (2005).
13. Park H, Lee JS, Choi H, Ahn DJ, Kim JM. Rational design of supramolecular conjugated polymers displaying unusual colorimetric stability upon thermal stress. *Adv. Funct. Mater.* **17**, 3447-55 (2007).
14. Park DH, Hong J, Park IS, Lee CW, Kim JM. A Colorimetric Hydrocarbon Sensor Employing a Swelling-Induced Mechanochromic Polydiacetylene. *Adv. Funct. Mater.* **24**, 5186-93 (2014).
15. Chen X, Hong L, You X, Wang Y, Zou G, Su W, et al. Photo-controlled molecular recognition of alpha-cyclodextrin with azobenzene containing polydiacetylene vesicles. *Chem Comm.* 1356-8 (2009).
16. Seo S, Lee J, Choi EJ, Kim EJ, Song JY, Kim J. Polydiacetylene liposome microarray toward influenza a virus detection: effect of target size on turn-on signaling. *Macromol. Rapid Commun.* **34**, 743-8 (2013).

17. Oh J, Jeon I, Kim D, You Y, Baek D, Kang SJ, et al. Highly Stable Upconverting Nanocrystal-Polydiacetylenes Nanoplates for Orthogonal Dual Signaling-Based Detection of Cyanide. *ACS Appl. Mater. Interfaces.* **12**, 4934-43 (2020).
18. Wang DE, Wang YL, Tian C, Zhang LL, Han X, Tu Q, et al. Polydiacetylene liposome-encapsulated alginate hydrogel beads for Pb2+ detection with enhanced sensitivity. *J. Mater. Chem. A.* **3**, 21690-8 (2015).
19. Jokanović M. Handbook of toxicology of chemical warfare agents, (Ed, Gupta RC), Academic Press, Boston, 2015.
20. Aldridge WN. The Conversion of Cyanogen Chloride to Cyanide in the Presence of Blood Proteins and Sulphydryl Compounds. *Biochem. J.* **48**, 271-6 (1951).
21. Auzel F. Upconversion and anti-Stokes processes with f and d ions in solids. *Chem. Rev.* **104**, 139-73 (2004).
22. Lu YQ, Zhao JB, Zhang R, Liu YJ, Liu DM, Goldys EM, et al. Tunable lifetime multiplexing using luminescent nanocrystals. *Nat. Photonics.* **8**, 33-7 (2014).
23. Wang F, Han Y, Lim CS, Lu YH, Wang J, Xu J, et al. Simultaneous phase and size control of upconversion nanocrystals through lanthanide doping. *Nature.* **463**, 1061-5 (2010).
24. Haase M, Schafer H. Upconverting Nanoparticles. *Angew. Chem.* **50**, 5808-29 (2011).
25. Bogdan N, Vetrone F, Ozin GA, Capobianco JA. Synthesis of Ligand-Free Colloidally Stable Water Dispersible Brightly Luminescent Lanthanide-Doped Upconverting Nanoparticles. *Nano Lett.* **11**, 835-40 (2011).

Chapter 5. Summary and Future Perspectives

5.1 Summary

In this dissertation, photonic systems displaying novel optical properties were introduced for diverse applications such as three-dimensional (3D) displays, anti-counterfeiting systems, and optical sensors. We studied novel photonic systems exhibiting multi-modal holographic signals and chemosensors having high stability and dual optical signals through the rational design of novel diacetylene molecules and the introduction of upconversion nanoparticles.

In chapter 1, various photonic systems with unusual optical properties such as bio-inspired photonic systems and metamaterials systems were introduced. Moreover, we explained the limitation of conventional metasurface holograms and the need for novel dynamic holograms with multiple optical signals for use in various research fields such as optical sensors, dynamic gratings, and light control devices.

In chapter 2, we have invented a novel polydiacetylene (PDA) hologram system that has a 2D grating function when expanded in aprotic solvents and 3D refractive index anisotropy when contracted in protic solvents. Our polymeric hologram systems reversibly display either unique 3D full parallax signals or structural colors according to the type of solvents. This ability to reversibly expand and contract the polymeric structure enabled three holographic modes to be displayed in a single architecture, forming new polymeric hologram systems. Such holographic features were theoretically studied by DFT calculations, MD, and FEA simulations. Moreover, we presented a variety of encryption applications and our method has made considerable progress in anti-counterfeiting technologies. Based on our results, we believe that our method and system can open new avenues in the development of thin structures to actively manipulate light and will form the basis of self-signaling 4D printing materials.

In chapter 3, we successfully developed a universal design principle for a highly stable PDA sensor platform with unprecedented stability when faced with environmental perturbation such as acids, bases, organic solvents, and thermal and mechanical stress. The stability of the PDA sensor system was enhanced by (i) rational control of the strong ionic bonds between cobalt ions and PCDA and (ii) maximization of the hydrophobic intermolecular interactions of PCDA-Co supramolecules. UCNs were incorporated into the highly stable PCDA-Co sensor system to selectively detect CN ions via stable dual signaling (colorimetric transition + luminescence color change), and a customized portable detection system was demonstrated. The developed sensor platform can be further employed in diverse PDA sensor systems for use in harsh environments (both night- and daytime) because of the simplicity of its synthesis and unusually high stability. Thus, this work provides insights into ways of overcoming the inherent disadvantages of PDA sensor systems for robust and practical dual signaling sensor applications.

In chapter 4, we have developed a rapid and selective DMMP (a G-agent simulant) and ClCN (a blood agent) gas detection systems using PDA/UCN nanocomposite by rationally utilizing the orthogonal reaction mechanism of CWAs. The PCDA-OX/UCNs and PCDA-BA/UCNs rapidly interacted with the organophosphonate and cyanide, causing a selective blue to red color change and yellow to red luminescence change upon DMMP and ClCN. Since the change in luminescence color is observed using an invisible 980 nm NIR laser light, there is no risk of being exposed to the enemy at night, and we further expect the straightness of the coherent laser light enables the development of long-range sensor systems.

To conclude, we investigated novel photonic systems exhibiting multi-modal holograms or dual optical signals. We anticipate that our two universal design principles, which are established through the above-mentioned four chapters, can be utilized to expand other responsive systems effectively and to develop novel systems exhibiting unprecedented optical signals for diverse photonics applications.

5.2 Future Perspectives

Based on the rational design of organic molecules and projection micro-stereolithography, several responsive systems are suggested in this chapter, for more developed and advanced polymer systems with unusual properties.

First, we suggest responsive PDA organogel systems displaying efficient fluorescence emissions, using the newly synthesized diacetylene resin. These resins having photocurable moiety at the one end and functional moiety at the other end displays different fluorescence transition upon a contraction according to the intermolecular interactions between the functional moieties. We believe that these different fluorescence capabilities of PDA organogels enable novel anticounterfeiting applications in response to solvent exchange.

Second, we suggest a novel responsive organogel exhibiting shape-morphing and structural color transition. Based on the rational design of functional resins capable of large negative thermal expansion, we would like to develop shape-morphing origami via projection micro-stereolithography. It would be possible to construct thermo-responsive origami that can be transformed into any desired shape and displays structural color change for diverse applications such as tissue engineering and soft robotics.

Lastly, by combining nano-scale lithography and molecular design of functional resin, we hope to realize the advanced polymer system that controls the propagation of acoustic waves in response to external stimuli. We believe that our methods can open avenues in the development of polymeric structures to actively control acoustic waves for transformation acoustics applications.

Acknowledgements (감사의 글)

2011년에 울산과학기술원에 학부생으로 입학한 후 어느덧 10년이라는 시간이 흘렀습니다. 10년이라는 긴 시간 동안 학교와 함께 성장하여 맺은 결실을 바탕으로 드디어 사회에 나갈 준비를 하고 있습니다.

무엇보다도 먼저 저의 지도 교수님이신 이지석 교수님께 깊은 감사의 말씀 올립니다. 모든 면에서 미성숙하고 부족했던 20대 초반의 제가 무사히 박사학위를 받을 수 있도록 연구뿐만이 아니라 인생을 살아가는 데 꼭 필요한 부분까지 여러 방면에서 많은 가르침을 주시고, 연구가 무엇인지, 항상 연구자로써 갖춰야 할 자세를 솔선수범해서 보여주시며, 힘든 일이 있을 때마다 길을 알려주시고 인생의 조언을 아끼지 않으신 이지석 교수님께 진심으로 감사드립니다. 이지석 교수님을 만나 뵙고 교수님의 지도 아래에 연구할 수 있었던 것이 제 인생의 행운이라 생각합니다. 교수님께 받은 가르침들 잊지 않고, 더욱 정진하여 자랑스러운 제자가 될 수 있게 노력하겠습니다.

그리고 바쁘신 와중에도 기꺼이 박사 졸업 논문 심사위원을 맡아 주신 곽상규 교수님, 고현협 교수님, 이창영 교수님, 김정욱 교수님께도 진심으로 감사의 말씀 올립니다. 대학원 재학 중 공동연구의 기회를 주시고 아낌없는 조언과 지도를 해 주신 것에 감사드립니다. 그 과정에서 연구에 관해 더 많은 것을 배울 수 있었고, 이를 토대로 한층 더 성장할 수 있었습니다. 조언해주신 부분들 잊지 않고 더욱 노력하여 발전하는 사람이 되겠습니다.

연구실 생활을 하며 많은 일을 함께한 연구실 식구들에게 감사를 전합니다. 2015년도에 연구실 1기로 만나서 벌써 7년째 함께 달려온 동기이자 친구 인규, 취미가 비슷해 항상 즐겁게 대화했던 영훈이, 연구실을 위해 고생하는 랩장 창일이, 그리고 졸업한 석사 후배들인 수빈이, 다정이, 성현이를 비롯한 1, 2기 원년 멤버들 감사합니다. 첫 랩장을 하면서 부족한 부분이 많아서 미안했고, 그럼에도 불구하고 잘 따라주어서 정말 고마웠습니다. 그리고 첫 부사수이자 AMHOLO로 돌아온 상균이, 농구부 후배이자 추억이 많고 항상 열심히 하는 부사수 도원이에게도 감사합니다. 열정적이고 힘이 되는 좋은 동생들을 부사수로 만나서 많은 것을 배우고 얻어갑니다. 또한 함께 연구를 진행한 다혜와 혜리에게도 감사합니다. 누구보다 꼼꼼하고 자신의 일에 열정적인 다혜와 항상 실험실 일을 자기 일처럼 솔선수범해주는 혜리에게도 많은 것을 배웠고 정말 고맙습니다. 항상 열정적으로 실험하던 석사졸업생 윤경이를 비롯해, 희수, 병천이, 종규, 채영이, 종범이에게도 감사합니다. 전부가 하고자 하는 일들 모두 이루길 바랍니다.

또한, 2010년 울산과학기술원 학부생 시절부터 박사가 되기까지 10년이라는 시간 동안 함께 성장한 친구들에게도 감사의 말 전합니다. 화학공학과에서 학부생 시절부터 많은 추억을 함께하였고 104동 6층에서 6년간 힘들 때마다 정말 많은 부분 함께 고민하고 열정적으로 연구에 관해 토의하던 이태경 박사와 조수원 박사 고맙습니다. 그리고 14년 전 고등학교 1학년 때 만나서 함께 울산과학기술원에서 학부와 대학원까지 함께한 이승진 박사에게도 고맙습니다. 또한, 학부 시절에 인연이 닿아 박사과정 동안 많은 추억을 쌓으며 함께 성장해온 오세혁 박사, 변성준, 이한솔 박사에게도 감사합니다. 그리고 학부생부터 석사까지 함께 헬스장에서 운동하며 연구의 꿈을 같이 키우다 지금은 미국에서 공부 중인 박범수에게도 감사를 전합니다. 또한 긴 시간 동안 나를 지지하고 응원해준 윤종환, 이상용, 이창훈, 김호영, 배병진, 윤기훈, 김대왕, 최종관, 안하솜, 전민찬에게도 감사합니다.

그리고 학위 과정 시작할 때 만나서 지난 6년간 많은 일이 있었지만, 변함없이 사랑으로 곁을 지켜준 사랑하는 여자친구 유영이에게 정말 고맙고 사랑한다는 말을 전하고 싶습니다. 힘든 일이 있을 때마다 함께 고민해주고 격려해주고 응원해줘서 무사히 학위 과정을 마칠 수 있었습니다. 진심으로 고맙고, 사랑합니다.

마지막으로 항상 믿음과 사랑으로 저를 지지해주시고 응원해주신 사랑하는 어머니, 아버지와 동생 나현이에게도 진심으로 감사하고 사랑한다는 말씀을 전하고 싶습니다. 오랫동안 공부하는 아들을 위해 항상 응원해주시고 믿어 주셔서 감사합니다. 더 열심히 노력하여 자랑스러운 아들, 오빠가 되겠습니다.

Appendix-Research achievements

Honors and Awards

[1] **Grand Prize** in the 27th Samsung Humantech Paper Award (2021)

[2] **Excellent Paper Presentation Award-Virtual Lightning Talk Session** by The Polymer Society of Korea (2021)

[3] **Outstanding Graduate Student Award for Excellence** by the department of Energy and Chemical Engineering, UNIST (2020)

[4] **Academic Award for Excellent Presentation** by The Korean Society for Composite Materials (2019)

Publication

Peer-reviewed Journal Papers

[1] **J. Oh**, D. Baek, T. K. Lee, D. Kang, H. Hwang, E. M. Go, I. Jeon, Y. You, C. Son, D. Kim, M. Whang, K. Nam, M. Jang, J.-H. Park, S. K. Kwak*, J. Kim*, and J. Lee*. Dynamic multimodal holograms of conjugated organogels via dithering mask lithography. *Nature Materials* **20**, 385-394 (2021)

[2] Y. Shin, I. Jeon, Y. You, K. Song, T. K. Lee, **J. Oh**, I. Son, D. Baek, D. Kim, H. Cho, H. Hwang, T. Kim, S. K. Kwak, J. Kim*, and J. Lee*. Facile Microfluidic Fabrication of 3D Hydrogel SERS Substrate with High Reusability and Reproducibility via Programmable Maskless Flow Microlithography. *Adv. Optical Mater.* **8**, *2001586* (2020)

[3] **J. Oh**, D. Kim, Y. Shin, H. Cho, and J. Lee*. Orthogonal dual signaling of chemical warfare agents using polydiacetylene/upconversion nanocrystals nanocomposites. *Func. Compos. Struct.* **2**, 025003 (2020)

[4] **J. Oh**, I. Jeon, D. Kim, Y. You, D. Baek, S. J. Kang, and J. Lee*. Highly Stable Upconverting Nanocrystal–Polydiacetylenes Nanoplates for Orthogonal Dual Signaling-Based Detection of Cyanide. *ACS Appl. Mater. Interfaces* **12**, 4934-4943 (2020)

Conference Papers

[1] **J. Oh,** I. Jeon, D. Kim, Y. You, D. Baek, and J. Lee*. Highly stable upconverting nanocrystal-polydiacetylenes sensor for orthogonal dual signaling-based detection of cyanide. Electronic Poster. KSCM (2019).

[2] **J. Oh**, and J. Lee*. Dynamic Polydiacetylene Organogel Microstructure Fabrication Using Photolithography Technique. Electronic Poster. PSK (2018)

[3] **J. Oh**, and J. Lee*. Rapid dynamic fluorescent transition of polydiacetylene organogel microstructure fabricated by photolithography. Electronic Poster. PSK (2018)

[4] **J. Oh**, I. Jeon, and J. Lee*. Rapid cyclic fluorescent transition of polydiacetylene organogel microstructure fabricated by photolithography. Electronic Poster. PRCR (2018)

[5] **J. Oh**, Y. You, and J. Lee*. Selective detection of cynide ion with polydiacetylene supramolecules. Electronic Poster. KSIEC (2018)

[6] **J. Oh**, I. Jeon, S. Jeong, and J. Lee*. Optofluidic polydiacetylene of microstructure synthesis. Electronic Poster. IUPAC-FAPS (2017)

[7] **J. Oh**, D. Kim, Y. You, and J. Lee*. Novel polydiacetylene microstructure synthesis platform for label free on-chip biosensor. Electronic Poster. IUPAC-PSK40 (2016)

[8] **J. Oh**, D. Kim, S. Jeong, and J. Lee*. Novel polydiacetylene microstructure synthesis platform for label free on-chip biosensor. Electronic Poster. KSIEC (2016)

[9] S. Ahn, **J. Oh**, S. Shin, and J. Lee*. Full color tactile sensor fabrication. Electronic Poster. IUPAC Photochem (2016)

[10] **J. Oh**, I. Jeon, S. Ahn, D. Kim, J. Lee. Smart Microparticle Fabrication Using Flow Lithography. Review paper. Polymer Science and Technology 26 (2), 155-162 (2015)

Patent

[1] J. Lee, **J. Oh.** Photocurable composition, method for manufacturing micro-structure and micro-structure manufactured thereby. Korea-10-2019-0101814.

[2] J. Lee, **J. Oh,** I. Jeon, D. Kim. Colorimetric sensor material for detection of blister agents. Korea-10-2020-0158633.

[3] J. Lee, **J. Oh,** I. Jeon, D. Kim. Colorimetric sensor material for detection of V types of nerve agents. Korea-10-2020-0158634.

[4] J. Lee, **J. Oh,** I. Jeon, D. Kim. Colorimetric fiber patches for detection of G types of nerve agents. Korea-10-2020-0158635.

[5] J. Lee, I. Jeon, **J. Oh,** D. Kim. Colorimetric fiber patches for detection of V types of nerve agents. Korea-10-2020-0158636.

[6] J. Lee, I. Jeon, **J. Oh,** D. Kim. Colorimetric fiber patches for detection of blister agents. Korea-10-2020-0158637.
